

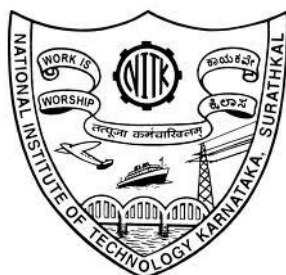
GROWTH AND CHARACTERIZATION OF DC MAGNETRON SPUTTERED Ni-Ti INTERMETALLIC AND NEAR EQUIATOMIC THIN FILMS

Thesis

Submitted in partial fulfillment of the requirements for the degree of
DOCTOR OF PHILOSOPHY

by

B. NAVEEN KUMAR REDDY



DEPARTMENT OF PHYSICS

NATIONAL INSTITUTE OF TECHNOLOGY KARNATAKA,
SURATHKAL, MANGALORE - 575 025

July 2018

Dedicated to my Parents, Wife and Friends

DECLARATION

By the Ph.D. Research Scholar

I hereby declare that the Research Thesis entitled **Growth and characterization of DC magnetron sputtered Ni-Ti intermetallic and near equiatomic thin films** which is being submitted to the National Institute of Technology Karnataka, Surathkal in partial fulfillment of the requirements for the award of the Degree of Doctor of Philosophy in Physics *is a bonafide report of the research work carried out by me.* The material contained in this Research Thesis has not been submitted to any University or Institution for the award of any degree.

B. Naveen Kumar Reddy

Reg. No.: 110679PH11F01

Department of Physics

Place: NITK-Surathkal

Date: July, 2018

CERTIFICATE

This is to certify that the Research Thesis entitled **Growth and characterization of DC magnetron sputtered Ni-Ti intermetallic and near equiatomic thin films** submitted by B. NAVEEN KUMAR REDDY (Reg. No.: 110679PH11F01) as the record of the research work carried out by him, *is accepted as the Research Thesis submission* in partial fulfillment of the requirements for the award of degree of Doctor of Philosophy.

Prof. N.K. Udayashankar

(Research Guide)

Chairman - DRPC

(Signature with Date and Seal)

ACKNOWLEDGEMENT

“Work hard and leave the rest to God” therefore, it is most appropriate that I begin by expressing my gratitude to Almighty for having blessed me with the opportunity, strength to pursue my Ph.D and for blessing me with the skill and abilities to carry out this research work.

The ideal teacher urges his students to go forward and does not suppress them; he opens the way but does not take them to the place. I am indeed grateful to my advisor, Prof. N.K. Udayashankar for his guidance and encouragement. His technical expertise has helped me to broaden my professional perspective and view of research. His passion for research is contagious and very inspiring. His philosophical way of framing research in fundamental and logical manners has taught me how to effectively conduct advanced research. I am indeed grateful to Prof. N.K. Udayashankar for his cooperation, support and insightful questions which helped me to define my research topic.

I am grateful to the members of my Research Progress Assessment Committee (RPAC) Dr. S.M. Murigendrappa (Department of Mechanical Engineering) and Prof. H.D. Shashikala (Department of Physics) for their comments and suggestions during every stage of my dissertation work.

I am thankful to Dr. M.N. Satyanarayana (H.O.D), Dr. H.S. Nagaraja, Dr. Deepak Vaid, Dr. Partha Pratim Das, Dr. Karthick Tarafder, Dr. T.K. Shajahan and Dr. Kishore Sridharan for their kind support.

I would like to thank non-teaching staff of the Department of Physics for their constant cooperation and support.

I would like to acknowledge the Satyabama University, Manipal University, Avansa Technologies, IIT Kanpur and Sinsil International for providing me various characterization facilities.

Special thanks to my friend Mr. M.R. Kiran for always being there for me and participating in research discussions. I appreciate his logical thinking and support in framing my thesis.

I would like to extend my gratitude to my colleagues, Dr. Vikas, Dr. Hidayath Ulla, Dr. Boominathan Sellarajan, Kiran P, Brian Jeeven Fernandes, Ramana Reddy P,

Mahendra K, Suchitra S.M, Martha Ramesh, Subhashini, Soumalya Bhattacharya, Akhila B, I. Ramesh Reddy, M. Vijay and others at NITK for their cooperation and encouragement.

It is also a pleasure to acknowledge the support of all those who helped me directly and indirectly in carrying out this work. For sure I would not have been able to come to an end without them and the energy I got from all the activities I could undertake with them.

I am grateful to the authorities of National Institute of Technology Karnataka for giving me the opportunity for doing research in the Department of Physics. I am also grateful to the Ministry of Human Resource Department (MHRD)-Government of India for awarding research scholarship.

The last but not the least, I want to thank my parents for their constant love and trust, that has always been the impetus for me to achieve this. I would like to express my love and gratitude to my wife, Dr. Shruthi for being my support system through thick and thins.

Finally, this thesis would not have been possible without the tremendous support and encouragement from my dearest friend Kasi Vishwanath, who has always encouraged me to follow my dreams and happiness in my life.

Thank you!!!

Place: NITK-Surathkal

B. NAVEEN KUMAR REDDY

Date: January, 2018

“No experiments are useless.” – Thomas Alva Edison

ABSTRACT

In recent years NiTi thin films have attracted much attention as intelligent and functional materials because of their unique properties such as shape memory effect. Shape memory alloy thin films possess several desirable properties such as high power to weight (or force to volume) ratio, and ability to recover large transformation stress and strain upon heating and cooling, pseudoelasticity (or superelasticity), high damping capacity, good chemical resistance and biocompatibility, etc. In spite of the development of advanced deposition techniques for NiTi thin films, some unresolved issues still remain, which limit precise control of composition during the deposition. In order to standardize these deposition techniques, an advanced understanding of the underlying process-property relationships are essential. This thesis mainly describes the growth and characterization of DC magnetron sputtered intermetallic, and near equiatomic NiTi alloy thin films. The correlation between deposition parameters and material properties has been established. In this thesis work, we have mainly investigated the influence of post-deposition conditions (annealing temperature and/or aging time) on NiTi thin film micro-structure, surface morphology, mechanical and surface properties. Based on XRD, it was concluded that annealed and aged intermetallic and near equiatomic NiTi thin films were crystallized, resulting in the form of various dominant phases along with intermetallic precipitates. The surface morphology of the investigated intermetallic and near equiatomic NiTi thin films from FESEM characterization was found to vary significantly with respect to annealing temperature and/or aging time. Topographical structures can be altered by varying the annealing temperature and/or aging time. The surface mean height (R_a), root mean square (RMS) and maximum peak to valley height (P-V) values have been obtained by AFM characterization. Nanoindentation tests on annealed and aged intermetallic and near equiatomic NiTi thin films were performed at room temperature. The hardness and elastic modulus values of deposited films increase probably due to formation of the intermediate metastable states by the incomplete alloying process. X-ray photo electron spectroscopy (XPS) was used to study the composition and surface chemistry of the annealed films. From HR-XPS investigations, it was observed that annealed and/or aged intermetallic and near equiatomic NiTi thin films had higher affinity to form Titanium dioxide (TiO_2) layer on the film surface leaving a Nickel enriched matrix immediately behind the metal oxide layer along with carbide precipitates.

Keywords: Intermetallic, Near equiatomic, Annealing, Aging, Nanoindentation, XPS.

CONTENTS

1	Introduction	1
1.1	Historical background of shape memory alloys	4
1.2	Phenomena of phase transformation in shape memory alloys	5
1.3	Shape memory effect (SME)	10
1.4	Superelasticity or Pseudoelasticity	12
1.5	Ni-Ti phase diagram	14
1.6	Thin film deposition process	18
	1.6.1 Physical vapor deposition	20
	1.6.2 Sputtering	20
	1.6.3 DC magnetron sputtering process	20
1.7	Literature survey	23
1.8	Objectives of the present work	32
1.9	Organization of the Thesis	33
2	Experimental methods	35
2.1	Experimental procedure	35
	2.1.1 Target and substrate cleaning process	35
	2.1.1.1 Substrate cleaning process	35
	2.1.1.2 Target cleaning process	36
	2.1.2 Sputter parameter optimization	37
	2.1.3 Sputter deposition process	37
2.2	Flow chart for sputter deposition process and characterization phase	39
2.3	Characterization techniques	40
	2.3.1 X-ray diffraction (XRD)	40
	2.3.1.1 Bragg's law	41
	2.3.2 Field emission scanning electron microscope (FESEM)	43
	2.3.2.1 Energy dispersive X-ray spectroscopy	45
	2.3.3 Atomic force microscopy (AFM)	46
	2.3.3.1 AFM Components	46

2.3.3.2	Modes of operation	47
2.3.3.3	Contact mode	47
2.3.3.4	Non-contact mode	49
2.3.3.5	Tapping mode or Intermittent contact mode	50
2.3.4	Nanoindentation	53
2.3.4.1	Load-displacement curves	53
2.3.4.2	Oliver and Pharr analysis	54
2.3.5	X-ray photoelectron spectroscopy (XPS)	58
2.3.5.1	Basic principles of the photoemission process	59
3	The effect of annealing temperature on the structural, morphological, mechanical and surface properties of intermetallic NiTi alloy thin films	69
3.1	Introduction	69
3.2	Experimental	70
3.2.1	Growth of intermetallic NiTi alloy thin films	70
3.2.2	Thin film characterization	71
3.3	Results and discussion	72
3.3.1	Structural analysis	72
3.3.2	Surface morphology	75
3.3.3	Surface topography analysis	76
3.3.4	Nanoindentation	78
3.3.5	X-ray photoelectron spectroscopy analysis	80
3.3.5.1	Ni (2p) spectra	81
3.3.5.2	Ti (2p) spectra	83
3.3.5.3	O (1s) spectra	85
3.3.5.4	C (1s) spectra	86
3.4	Conclusions	88
4	Aging time correlation in DC magnetron sputtered Ni₆₀Ti₄₀ thin films	89
4.1	Introduction	89
4.2	Experimental	91

4.3	Thin film characterization	91
4.4	Results and discussion	91
4.4.1	Structural analysis	91
4.4.2	Surface morphology	94
4.4.3	Surface topography analysis	96
4.4.4	Nanoindentation	97
4.4.5	X-ray photoelectron spectroscopy analysis	101
4.4.5.1	Ni (2p) spectra	102
4.4.5.2	Ti (2p) spectra	104
4.4.5.3	O (1s) spectra	105
4.4.5.4	C(1s) spectra	106
4.5	Conclusions	108
5	Influence of annealing temperature on the structural, morphological, mechanical and surface properties of near equiatomic NiTi thin films	111
5.1	Introduction	111
5.2	Experimental	112
5.3	Thin film characterization	113
5.4	Results and discussions	113
5.4.1	Structural analysis	113
5.4.2	Surface morphology	115
5.4.3	Surface topography analysis	117
5.4.4	Nanoindentation	118
5.4.5	X-ray photoelectron spectroscopy analysis	122
5.4.5.1	Ni (2p) spectra	124
5.4.5.2	Ti (2p) spectra	125
5.4.5.3	O (1s) spectra	127
5.4.5.4	C (1s) spectra	128
5.5	Conclusions	130
6	Aging time correlation in DC magnetron sputtered near equiatomic NiTi thin films	131

6.1	Introduction	131
6.2	Experimental	132
6.3	Thin film characterization	132
6.4	Results and discussions	133
6.4.1	Structural analysis	133
6.4.2	Surface morphology	135
6.4.3	Surface topography analysis	137
6.4.4	Nanoindentation	139
6.4.5	X-ray photoelectron spectroscopy analysis	143
6.4.5.1	Ni (2p) spectra	146
6.4.5.2	Ti (2p) spectra	148
6.4.5.3	O (1s) spectra	149
6.4.5.4	C (1s) spectra	151
6.5	Conclusions	152
7	Summary and future directions	153
7.1	Summary	153
7.1.1	The effect of annealing temperature on the structural, morphological, mechanical and surface properties of intermetallic NiTi alloy thin films	153
7.1.2	Aging time correlation in DC magnetron sputtered Ni ₆₀ Ti ₄₀ thin films	155
7.1.3	Influence of annealing temperature on the structural, morphological, mechanical and surface properties of near equiatomic NiTi thin films	156
7.1.4	Aging time correlation in DC magnetron sputtered near equiatomic NiTi thin films	157
7.2	Future directions	158
	References	161
	List of Publications	191
	Curriculum Vitae	193

LIST OF FIGURES

S. No.	Title	Page No.
Figure 1.1	Temperature-induced phase transformation of an SMA without mechanical loading	6
Figure 1.2	Schematic of the shape memory effect of an SMA showing the detwinning of the material with an applied stress	6
Figure 1.3	Schematic of the shape memory effect of an SMA showing the unloading and subsequent heating to austenite under no load condition	7
Figure 1.4	Temperature-induced phase transformation in the presence of applied load	8
Figure 1.5	A pseudoelastic loading path	9
Figure 1.6	Schematic of a pseudoelastic stress-strain diagram	9
Figure 1.7	Schematic of a stress-temperature phase diagram for an SMA	10
Figure 1.8	Stress-strain-temperature data exhibiting the shape memory effect for a typical NiTi SMA	11
Figure 1.9	Phase diagram and two possible pseudoelastic loading paths	12
Figure 1.10	A typical SMA pseudoelastic loading cycle	13
Figure 1.11	Time-temperature-precipitation diagram for a Ti-52 at% Ni alloy	15
Figure 1.12	Ni-Ti alloy phase diagram	16
Figure 1.13	Sputtering process in a sputter down configuration	21
Figure 1.14	Scheme of the sputtering deposition process	22
Figure 2.1	(a) Before cleaning (b) After cleaning	36
Figure 2.2	(a) Before cleaning (b) After cleaning	36
Figure 2.3	DC magnetron sputtering system	38
Figure 2.4	Position of magnetron guns in the vacuum chamber	38
Figure 2.5	Plasma during sputtering process	38

Figure 2.6	(a) Nickel sputtering target with erosion zone (b) Titanium sputtering target with erosion zone	40
Figure 2.7	As-deposited NiTi thin films	40
Figure 2.8	Reflection of X-rays from different atomic planes, illustrating the Bragg's law	42
Figure 2.9	X-ray diffractometer (Model: Rigaku Miniflex-600)	43
Figure 2.10	Schematic details of Field emission scanning electron microscope	44
Figure 2.11	Field Emission Scanning Electron Microscope (Model: SUPRA 55, CARL ZEISS GERMANY)	44
Figure 2.12	Block diagram of AFM components	47
Figure 2.13	AFM in contact mode	48
Figure 2.14	Force versus distance curve (Moss and Sinha 2003)	48
Figure 2.15	AFM in non-contact mode	51
Figure 2.16	Resonance curve of cantilever (a) above the surface, (b) close to the surface	51
Figure 2.17	Atomic Force Microscope (Model: AFM-NTMDT)	52
Figure 2.18	Atomic Force Microscope (Model: Bruker Innova)	52
Figure 2.19	Schematic representation of load-displacement curve in Oliver-Pharr method	54
Figure 2.20	A schematic of the cross-section through an indentation with various dimensions	56
Figure 2.21	Nanoindeter (ASMEC Universal nanomechanical Tester (ZHN))	58
Figure 2.22	An electron energy diagram for a Ni ²⁺ cation showing the absorption of a photon and resultant expulsion of a 2p level photoelectron	60
Figure 2.23	(a) Simplified schematic following a photoelectron (e ⁻) through a PHI 5000 VersaProbe II spectrometer. (b) The expanded view of the energy analyzer setup in spectrum mode employing the CHA. Under these conditions the	62

photoelectrons enter the energy analyzer at point A and travel between two negatively charged plates. The grey lines represent possible pathways these electrons may travel through the energy analyzer. Only the photoelectrons with the selected pass energies will exit the analyzer at point B and enter the detector. (c) The expanded view of the energy analyzer setup in imaging mode employing the SMA. The presence of the mesh hemispherical electrode and additional slit allows for specific photoelectron BE's to be selected allowing for high-resolution images to be collected

Figure 2.24	(a) The survey spectrum collected from a polycrystalline NiO powder sample containing a small C impurity. The elemental concentrations in at.% for the Ni, O and C species are also presented	60
Figure 2.24	(b) The high resolution Ni 2p spectrum taken for the same NiO sample. The electronic structural features arising from j-j coupling (Ni 2p _{3/2} , Ni 2p _{1/2}), multiplet splitting and shake up interactions are clearly visible	64
Figure 2.25	X-ray Photoelectron Spectrometer (Model: PHI 5000 Versaprobe II, FEI Inc.)	68
Figure 3.1	XRD patterns of intermetallic NiTi thin films annealed at (a) 350 °C (b) 450 °C (c) 550 °C and (d) 650 °C	74
Figure 3.2	FESEM micrographs of intermetallic NiTi thin films annealed at (a) 350 °C (b) 450 °C (c) 550 °C and (d) 650 °C	75
Figure 3.3	AFM (3D surface morphology) micrographs of sputter deposited intermetallic NiTi thin films vacuum annealed for 1 hour at (a) 350 °C (b) 450 °C (c) 550 °C and (d) 650 °C	77
Figure 3.4	Load-displacement curves from nanoindentation experiments performed on the intermetallic NiTi thin films deposited at room temperature and vacuum annealed for 1 h at four different temperatures	79

Figure 3.5	XPS survey spectrum obtained for intermetallic NiTi thin films annealed at (a) 350 °C (b) 450 °C (c) 550 °C and (d) 650 °C	81
Figure 3.6	Gaussian de-convoluted HR-XPS spectrum for Ni (2p) of intermetallic NiTi thin films annealed at (a) 350 °C (b) 450 °C (c) 550 °C and (d) 650 °C	83
Figure 3.7	Gaussian de-convoluted HR-XPS spectrum for Ti (2p) of intermetallic NiTi thin films annealed at (a) 350 °C (b) 450 °C (c) 550 °C and (d) 650 °C	84
Figure 3.8	Gaussian de-convoluted HR-XPS spectrum for O (1s) of intermetallic NiTi thin films annealed at (a) 350 °C (b) 450 °C (c) 550 °C and (d) 650 °C	86
Figure 3.9	Gaussian de-convoluted HR-XPS spectrum for C (1s) of intermetallic NiTi thin films annealed at (a) 350 °C (b) 450 °C (c) 550 °C and (d) 650 °C	87
Figure 4.1	X-ray diffraction patterns of intermetallic NiTi thin films (a) as-deposited (b) vacuum annealed at 600 °C for 1 h (c) vacuum annealed at 600 °C for 1 h followed by aging at 500 °C for 2 h (d) vacuum annealed at 600 °C for 1 h followed by aging at 500 °C for 4 h and (e) vacuum annealed at 600 °C for 1 h followed by aging at 500 °C for 6 h	93
Figure 4.2	4.2 FESEM planar micrographs of intermetallic NiTi thin film vacuum annealed at 600 °C for 1 h followed by aging at 500 °C for (a) 2 h (b) 4 h and (c) 6 h	95
Figure 4.3	FESEM cross-sectional micrographs of intermetallic NiTi thin film vacuum annealed at 600 °C for 1 h followed by aging at 500 °C for (a) 2 h (b) 4 h and (c) 6 h	95
Figure 4.4	AFM (3D surface morphology) micrographs of sputter deposited intermetallic NiTi thin film vacuum annealed at 600 °C for 1 h followed by aging at 500 °C for (a) 2 h (b) 4 h	97

and (c) 6 h

Figure 4.5	Load-displacement plots of intermetallic NiTi thin films deposited at room temperature and vacuum annealed at 600 °C for 1 h followed by aging at 500 °C for 2 h, 4 h and 6 h	100
Figure 4.6	Ni (2p) HR-XPS spectrum recorded for intermetallic NiTi thin films annealed at 600 °C for 1 h followed by aging at 500 °C for (a) 2 h (b) 4 h and (c) 6 h	103
Figure 4.7	Ti (2p) HR-XPS spectrum recorded for intermetallic NiTi thin films annealed at 600 °C for 1 h followed by aging at 500 °C for (a) 2 h (b) 4 h and (c) 6 h	105
Figure 4.8	Gaussian de-convoluted HR-XPS spectrum for O (1s) of intermetallic NiTi thin films annealed at 600 °C for 1 h followed by aging at 500 °C for (a) 2 h (b) 4 h and (c) 6 h	106
Figure 4.9	Gaussian de-convoluted HR-XPS spectrum for C (1s) of intermetallic NiTi thin films annealed at 600 °C for 1 h followed by aging at 500 °C for (a) 2 h (b) 4 h and (c) 6 h	108
Figure 5.1	XRD patterns of near equiatomic NiTi thin films annealed at (a) 350 °C (b) 450 °C (c) 550 °C and (d) 650 °C	114
Figure 5.2	Cross sectional FESEM micrographs of near equiatomic NiTi thin films annealed at (a) 350 °C (b) 450 °C (c) 550 °C and (d) 650 °C	116
Figure 5.3	AFM (3D surface morphology) micrographs of sputter deposited near equiatomic NiTi thin film vacuum annealed for 1 h at (a) 350 °C (b) 450 °C (c) 550 °C and (d) 650 °C	118
Figure 5.4	Load-displacement curves from nanoindentation experiments performed on the near equiatomic NiTi thin films deposited at room temperature and vacuum annealed for 1 hour at four different temperatures (a) 1.5 mN (b) 2 mN and (c) 2.5 mN	121

Figure 5.5	XPS survey spectrum obtained for near equiatomic NiTi thin films annealed at (a) 350 °C (b) 450 °C (c) 550 °C and (d) 650 °C	123
Figure 5.6	Gaussian de-convoluted HR-XPS spectrum for Ni (2p) of near equiatomic NiTi thin films annealed at (a) 350 °C (b) 450 °C (c) 550 °C and (d) 650 °C	125
Figure 5.7	Gaussian de-convoluted HR-XPS spectrum for Ti (2p) of near equiatomic NiTi thin films annealed at (a) 350 °C (b) 450 °C (c) 550 °C and (d) 650 °C	126
Figure 5.8	Gaussian de-convoluted HR-XPS spectrum for O (1s) of near equiatomic NiTi thin films annealed at (a) 350 °C (b) 450 °C (c) 550 °C and (d) 650 °C	128
Figure 5.9	Gaussian de-convoluted HR-XPS spectrum for C (1s) of near equiatomic NiTi thin films annealed at (a) 350 °C (b) 450 °C (c) 550 °C and (d) 650 °C	129
Figure 6.1	X-ray diffraction patterns of near equiatomic NiTi thin films (a) as-deposited (b) vacuum annealed at 600 °C for 1 h (c) vacuum annealed at 600 °C for 1 h followed by aging at 500 °C for 2 h (d) vacuum annealed at 600 °C for 1 h followed by aging at 500 °C for 4 h and (e) vacuum annealed at 600 °C for 1 h followed by aging at 500 °C for 6 h	134
Figure 6.2	Cross sectional FESEM micrographs of near equiatomic NiTi thin film vacuum annealed at 600 °C for 1 h followed by aging at 500 °C for (a) 2 h (b) 4 h and (c) 6 h	136
Figure 6.3	AFM (3D surface morphology) micrographs of sputter deposited near equiatomic NiTi thin film vacuum annealed at 600 °C for 1 h followed by aging at 500 °C for (a) 2 h (b) 4 h and (c) 6 h	138
Figure 6.4	Load-displacement curves from nanoindentation experiments performed on the near equiatomic NiTi thin films deposited at room temperature and vacuum annealed at	141

	600 °C for 1 h followed by aging at 500 °C for 2 h, 4 h and 6 h. (a) 1.5 mN (b) 2 mN and (c) 2.5 mN	
Figure 6.5	The average Hardness and Elastic modulus as a indentation depth of the near equiatomic NiTi thin films deposited at room temperature and vacuum annealed at 600°C for 1 h followed by aging at 500°C for 2 h, 4 h and 6 h. (a) 1.5 mN (b) 2 mN and (c) 2.5 mN.	142
Figure 6.6	XPS survey spectrum obtained from near equiatomic NiTi thin film vacuum annealed at 600 °C for 1 h followed by aging at 500 °C for (a) 2 h (b) 4 h and (c) 6 h	144
Figure 6.7	XPS depth profile analysis of the aged near equiatomic NiTi thin film vacuum annealed at 600 °C for 1 h followed by aging at 500 °C for (a) 2 h (b) 4 h and (c) 6 h	145
Figure 6.8	Gaussian de-convoluted HR-XPS spectrum for Ni (2p) of near equiatomic NiTi thin film vacuum annealed at 600 °C for 1 h followed by aging at 500 °C for (a) 2 h (b) 4 h and (c) 6 h	147
Figure 6.9	Gaussian de-convoluted HR-XPS spectrum for Ti (2p) of near equiatomic NiTi thin film vacuum annealed at 600 °C for 1 h followed by aging at 500 °C for (a) 2 h (b) 4 h and (c) 6 h	149
Figure 6.10	Gaussian de-convoluted HR-XPS spectrum for O (1s) of near equiatomic NiTi thin film vacuum annealed at 600 °C for 1 h followed by aging at 500 °C for (a) 2 h (b) 4 h and (c) 6 h	150
Figure 6.11	Gaussian de-convoluted HR-XPS spectrum for C (1s) of near equiatomic NiTi thin film vacuum annealed at 600 °C for 1 h followed by aging at 500 °C for (a) 2 h (b) 4 h and (c) 6 h	151

LIST OF TABLES

S. No.	Title	Page No.
1.1	Survey and classification of thin-film deposition technologies	19
3.1	Deposition conditions for intermetallic NiTi thin films	71
3.2	Structural parameters of intermetallic NiTi thin films	74
3.3	Various roughness parameters of the intermetallic NiTi thin films with same scan area	76
3.4	The hardness and elastic modulus parameters of intermetallic NiTi thin films annealed at four different temperatures	80
3.5	Surface elemental composition evaluated from XPS survey spectrum of intermetallic NiTi thin films	82
4.1	Various roughness parameters of the intermetallic NiTi thin films with same scan area	97
4.2	The hardness and elastic modulus parameters of intermetallic NiTi thin film vacuum annealed at 600 °C for 1 h followed by aging at 500 °C for different times	99
4.3	Surface elemental composition evaluated from an XPS survey spectrum of intermetallic NiTi thin film vacuum annealed at 600 °C for 1 h followed by aging at 500 °C for different times	102
5.1	Various parameters of the near equiatomic NiTi thin films annealed at 350, 450, 550 and 650 °C	118
5.2	The hardness, elastic modulus, depth recovery ratio, and wear resistance parameters of near equiatomic NiTi thin films annealed at four different temperatures for different loads	122
5.3	Surface elemental composition evaluated from an XPS survey spectrum of near equiatomic NiTi thin films	123
6.1	Various roughness parameters of the near equiatomic NiTi thin films with same scan area	139
6.2	Surface elemental composition evaluated from an XPS survey spectrum of near equiatomic NiTi thin film vacuum annealed	144

at 600 °C for 1 h followed by aging at 500 °C for different times

LIST OF ABBREVIATIONS

Ni-Ti	Nickel-Titanium
MEMS	Micro Electro Mechanical Systems
SMA	Shape Memory Alloy
SME	Shape Memory Effect
SE	Superelasticity
A	Austenitic Phase
M	Martensitic Phase
R	Intermediate Phase
M_s	Martensitic Start Temperature
M_f	Martensitic Finish temperature
A_s	Austenitic Start Temperature
A_f	Austenitic Finish temperature
XRD	X-ray Diffraction
FESEM	Field Emission Scanning Electron Microscope
EDS	Energy Dispersive X-ray Spectroscopy
AFM	Atomic Force Microscope
XPS	X-ray Photoelectron Spectroscopy
HRXPS	High Resolution X-ray photoelectron Spectroscopy
T-T-T	Time-Temperature-Transformation
CVD	Chemical Vapor Deposition
PVD	Physical Vapor Deposition
DC	Direct Current
UHV	Ultra High Vacuum
FWHM	Full Width Half Maximum
BE	Binding Energy
KE	Kinetic Energy
G.P. Zone	Guinier Preston Zone
B19'	Martensitic phase
B2	Austenite Phase (Parent Phase)

NOMENCLATURE

Symbols	Description
λ	Wavelength
β	Integral Half Width
θ	Bragg Angle
ε	Lattice Strain
D	Crystalline Size
d	Interplanar Distance
K	Shape Factor
γ	Correction Factor
K_c	Spring Constant
Q	Quality Factor
P	Load
H	Hardness
S	Stiffness
h	Displacement
E_r	Reduced Modulus
A_c	Contact Area
h_c	Constant Depth
ν_s	Poisson's Ratio

CHAPTER 1

OVERVIEW

Chapter 1 is divided into two sections. First, it gives a brief overview of the NiTi shape memory alloy thin films. This section is dedicated to the phenomena involving the phase transformation in shape memory alloy thin films, the shape memory effect (SME) and the superelasticity (SE). A short background of the NiTi phase diagram, thin film deposition process and the sputtering process is presented. In the second section, a brief literature review related to growth and characterization of NiTi thin films, composition control, the crystallization of the films and phenomena associated, the oxidation behavior, as well as film/substrate interfacial reactions and the role of the thickness on the properties of the NiTi films are presented. Overall, chapter 1 gives a detailed account of the sputtering process for the growth and characterization of the intermetallic (Ni-rich) and near equiatomic shape memory alloy thin films. The chapter also includes the objectives and organization of the thesis.

1 INTRODUCTION

During the last two decades, certain smart, structural and functional materials have captivated great attention due to their potential scientific, engineering and technological importance (Choudhary and Kaur 2016, Levi et al. 2008, Chopra 2002, Chen and Shen 1997). Among them, shape memory alloys (SMAs) have been widely used as ‘smart’ functional materials due to their inimitable properties of shape memory effect (SME), pseudoelasticity (superelasticity), high power to weight ratio, high damping capacity, good chemical resistance, and bio-compatibility (Otsuka and Ren 2005, Acar et al. 2015, Cheng et al. 2004, Tillmann and Momeni 2015). SMAs possess these unusual properties due to a temperature dependent martensitic phase transformation from a low symmetry state (martensite) to a high symmetric state (austenite) (Otsuka and Ren 2005). These effects (SME) have been found in materials

such as metals, ceramics, polymers. Among all the materials NiTi based shape memory alloys have been investigated and found many commercial applications (Van Humbeeck 1999, James and Hane 2000). In recent times, NiTi thin film SMA has been recognized as a promising and high performance material in the field of micro-electro-mechanical system (MEMS) applications, since it can be patterned with standard lithography techniques and fabricated in batch process (Krulevitch et al. 1996, (Miyazaki and Ishida 1999, Wolf and Heuer 1995, Kahn et al. 1998, Fu et al. 2001). NiTi based thin films are potentially desirable for microscale devices such as accelerometers, gyroscopes, microphones, micro pressure sensors, micrscanners, optical switches for applications in the fields of automotive, aerospace, biomedical, industrial process control, electronic instrumentation, telecommunications, and military applications (Sreekumar et al. 2007, Varadan and Varadan 2000, Wu and Schetky 2000).

In case of SMA thin film, the work output per volume exceeds that of other micro-actuator mechanisms (Kahn et al. 1998, Wolf and Heuer 1995). However, there are some potential problems interconnected with NiTi thin films including low energy efficiency, low dynamic respond speed, large hysteresis, and fatigue problems (Nemat-Nasser and Guo 2006, Wagner et al. 2008).

The phase transformation in SMA thin film is also accompanied by substantial changes in the physical (structural), chemical, mechanical, optical and electrical properties such as yield stress, elastic modulus, hardness, damping, shape recovery, electrical resistivity, thermal conductivity, thermal expansion coefficient, surface roughness, vapor permeability and dielectric constant, etc. (Fu et al. 2001, Fu et al. 2004). The design and fabrication of microsensors and microactuators can fully depend on the above mentioned changes (Winzek et al. 2004).

NiTi based thin films are most frequently used thin film SMA materials and typically prepared using sputtering method (Fu et al. 2004, Fu et al. 2005, Miyazaki and Ishida 1999, Wolf and Heuer 1995). The sputtered NiTi thin films are sensitive to metallurgical factors such as alloy composition, contamination, thermomechanical treatment, annealing and aging process, etc. These factors can greatly influence the transformation temperature, shape memory behavior and superelasticity of NiTi thin films. In addition to that sputtering conditions (target power, gas pressure, deposition

temperature, etc.) and the application conditions (loading conditions, ambient temperature and environment, heat dissipation, heating/cooling rate, strain rate, etc.) also effect the transformation temperature, shape memory behavior and superelasticity of NiTi thin films (Krulevitch et al. 1996, Miyazaki and Ishida 1999, Ishida et al. 1996).

NiTi thin films can be sputter deposited at room temperature or higher temperature (substrate temperature). NiTi thin films usually exhibit amorphous nature at room temperature, thus, post sputtering annealing usually higher than 450°C is a must because SMA effect can occur only in crystalline material form. However, martensite transformation and superelasticity of NiTi thin films are sensitive to post-annealing and/or aging temperature and time (Lehnert et al. 2000, Surbled et al. 2001). To conserve thermal processing budgets and to reduce the reaction between film and substrate the lowest possible annealing or aging temperature is a must (Isalgue et al. 1999). Post annealing and aging process for long term should be avoided since it could trigger dramatic changes in film microstructure (i.e., precipitation mechanical properties and shape memory effect.

There are still many important issues unresolved in NiTi thin film characterization:

- Substrate effects, nucleation and growth mechanisms of NiTi thin films.
- Effects of precipitation (Kajiwara 1996) and point defects and dislocations.
- Nano crystalline structure and grain (micron & nano) size effect on shape memory effect and phase transformation (McKelvey and Ritchie 2000).
- The refinement of grain size can strongly modify the structural and thermodynamic properties, and improvement of mechanical properties of SMAs.
- Film thickness effect (to optime the shape memory effect a minimum thickness is required). Surface oxide and oxygen diffusion layer will have dominant effect if the NiTi film is too thin (Ishida and Sato 2003).
- Formation of film structure and its control, and the effect on shape memory effect (Miyazaki et al. 2000).
- Internal and external/stress on the arrangement of martensite variants, stress induced martensite and its shape memory phenomenon, etc. (Wang et al. 2001, Wuttig et al. 1999).

- Surface chemistry, surface adsorption and biocompatibility of TiNi films with small grain size.

The research work leading to this thesis is an effort to understand some of these unsolved issues and to make progress in the growth and characterization of NiTi thin films.

1.1 HISTORICAL BACKGROUND OF SHAPE MEMORY ALLOYS

In 1890s the discovery of martensite in steels by Adolf Martens was a major step towards the discovery of shape memory alloys. The martensitic transformation as observed in the Fe-C system, was established as an irreversible process. The first recorded shape memory transformation observation was by Chang and Read in 1932. In 1938, the pseudoelastic behavior of the Au-Cd alloy was discovered. In 1949 Kurdjumov and Khandros, explained the reversible transformation of martensite in CuZn and CuAl alloys based on experimental observations of the thermally reversible martensitic structure (Kurdjumov and Khandros 1949). In 1951 Chang and Read found that deformed Au-Cu alloys would return to their original shape when heated (Chang and Read 1950). The same effect was noted in In-Ti alloys by Basinski and Christian in 1954. The alloys that exhibited the reversible martensitic transformation remain unutilized until 1962. In 1963, the shape memory effect of the equiatomic NiTi alloy was observed by Buehler et al. at the U.S. Naval Ordnance Laboratory (NOL); hence the NiTi alloys are usually known as “*Nitinol*” (Nickel-Titanium Naval Ordnance Laboratory) (Buehler et al. 1963).

The name Shape Memory Effect (SME) was given to the associated shape recovery behavior. The discovery of *Nitinol* spearheaded active research interest into SMAs and many commercial applications have been developed. During the 1970s, several bio-medical applications appeared, but it was not until the 1990s that NiTi stents (a metal or plastic tube inserted into the lumen of an anatomic vessel) made a major commercial breakthrough. SMAs had found a variety of additional applications in air conditioning vents, electronic cable connectors, valves, etc.

1.2 PHENOMENA OF PHASE TRANSFORMATION IN SHAPE MEMORY ALLOYS

Within the typical effective temperature range, SMAs have two phases, one is the high temperature phase called *austenite* (A) and the other is the low temperature phase called *martensite* (M), each with a different crystal structure and therefore possesses different properties. Austenite (Cubic) has a different crystal structure from martensite (tetragonal, orthorhombic or monoclinic). The transformation from one phase to another phase occurs by shear lattice distortion but not by diffusion of atoms. This type of transformation is called as martensitic transformation. Each martensitic crystal formed has different orientation diffraction, called a *variant*. The martensitic variants can exist in two forms: twinned martensite (M^t), which is a combination of “self-accommodated” martensitic variants, and detwinned or reoriented martensite in which a specific variant is dominant (M^d). The reversible phase transformation from austenite (parent phase) to martensite (product phase) and vice versa is the basis for the unique behavior of SMAs.

Upon cooling in the absence of an applied load, the crystal structure changes from austenite to martensite and are termed the *forward transformation*. The arrangements of variants occur in a way that the average microscopic shape change is negligible and it leads to twinned martensite. When the material is heated from the martensitic phase, the crystal structure transforms back to austenite and this is called as *reverse transformation*, during which there is no associated shape change. The transformation between the crystal structures of twinned martensite and austenite for an SMA is shown in Fig. 1.1. There are four characteristic temperatures associated with the phase transformation. Under zero load, during the forward transformation, austenite, begins to transform to twinned martensite at the *martensitic start temperature* (M_s) and completes transformation to martensite at the *martensitic finish temperature* (M_f). The transformation is complete and the material is fully in the twinned martensitic phase at this stage. During heating the reverse transformation initiates at the *austenitic start temperature* (A_s) and the transformation is completed at the *austenitic finish temperature* (A_f). It is possible to detwin the martensite by

reorienting a certain number of variants (Fig. 1.2) when a load is applied to the material in the twinned martensitic phase.

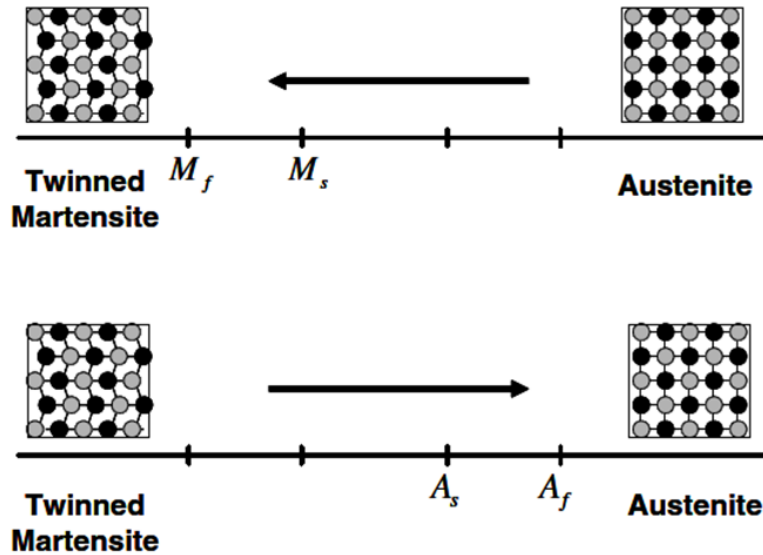


Figure 1.1 Temperature-induced phase transformation of an SMA without mechanical loading (Kumar and Lagoudas 2008).

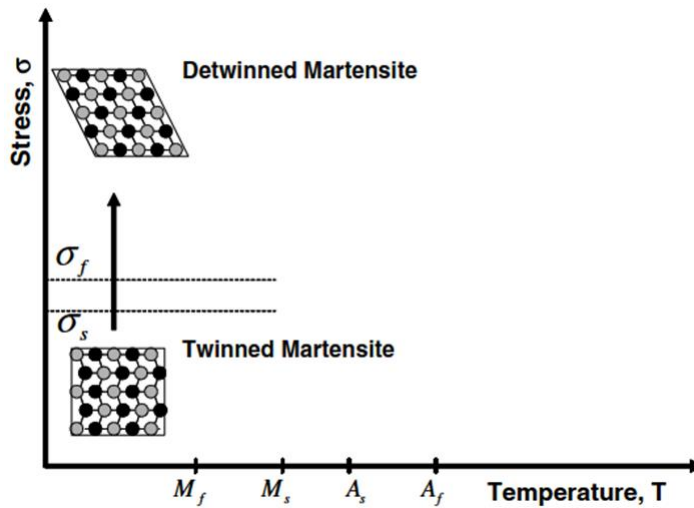


Figure 1.2 Schematic of the shape memory effect of an SMA showing the detwinning of the material with an applied stress (Kumar and Lagoudas 2008).

When the load is released, the detwinning process results in a macroscopic shape change, where the deformed configuration is retained. A subsequent heating of the SMA to a temperature above A_f will result in a reverse phase transformation and results in to complete shape recovery (Fig. 1.3). When the materials cool back to a

temperature below M_f , it leads to the formation of twinned martensite without associated shape change.

The above mentioned process is referred to as the *Shape Memory Effect (SME)*. To start the detwinning process the subjected load must be sufficiently large. The minimum stress required for detwinning initiation is named as the detwinning start stress (σ_s). Sufficient higher load will lead to complete detwinning of martensite where the corresponding stress level is called the detwinning finish stress (σ_f). If a material cooled with a mechanical load greater than σ_s applied to the austenitic phase, there occurs the formation of detwinned martensite with a shape change. The material attains shape recovery by reheating the material while the load is still applied. The schematic of the above described loading path is shown in Fig. 1.3. The phase transformation temperatures mainly depend on the magnitude of the applied load, thus, higher transformation temperatures obtained with higher values of applied load. As a consequence, in stress-temperature space the transformation regions representing the $A \rightarrow M^d$ and $M^d \rightarrow A$ transformations have a positive slope. The transformation temperatures increase with an increase in the magnitude of the load, irrespective of the nature of applied load (tension or compression).

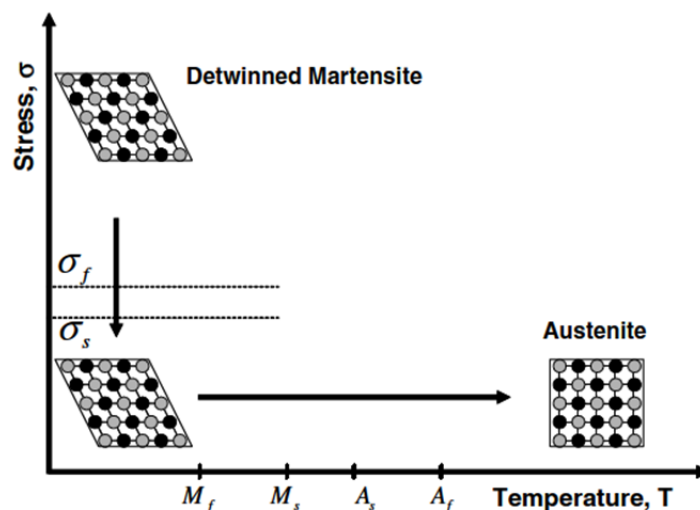


Figure 1.3 Schematic of the shape memory effect of an SMA showing the unloading and subsequent heating to austenite under no load condition (Kumar and Lagoudas 2008).

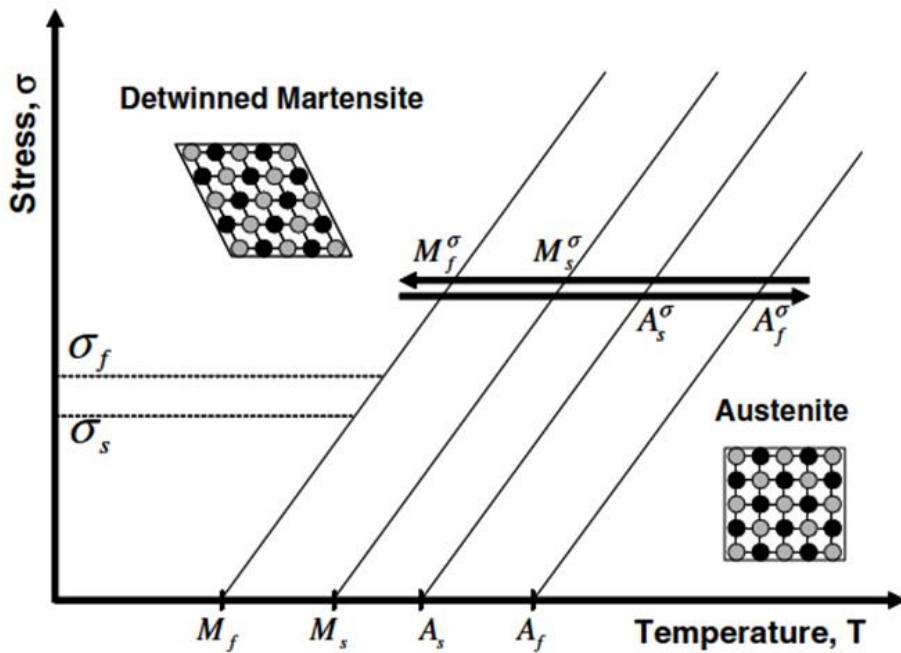


Figure 1.4 Temperature-induced phase transformation in the presence of applied load (Kumar and Lagoudas 2008).

The new transformation temperatures under an applied uniaxial tensile with a corresponding stress, σ , are represented as M_f^σ , M_s^σ , A_s^σ and A_f^σ for martensitic finish, martensitic start, austenitic start and the austenitic finish temperatures, respectively. Transformations can attain not only by thermally induced, but also by applying a sufficient high mechanical load to the material in the austenitic phase. The applied load leads to fully detwinned martensite created from austenite. A complete shape recovery is observed upon unloading to austenite when the temperature of the material is A_f . This type of behavior in material named as pseudoelastic effect and is shown schematically in Fig. 1.5. The associated macroscopic shape change due to the applied load is captured in the resulting stress-strain diagram and it is shown in the Fig. 1.6. The martensitic stress levels at which the transformation initiates and completes are denoted by σ^{M_s} and σ^{M_f} , respectively. In the same way, as the SMA is unloaded, the stress levels at which the material initiates and completes its reverse transformation to austenite are denoted by σ_{A_s} and σ_{A_f} , respectively. If the material in the austenitic phase is tested above the M_s temperature and below the A_f temperature, only partial shape recovery could be observed.

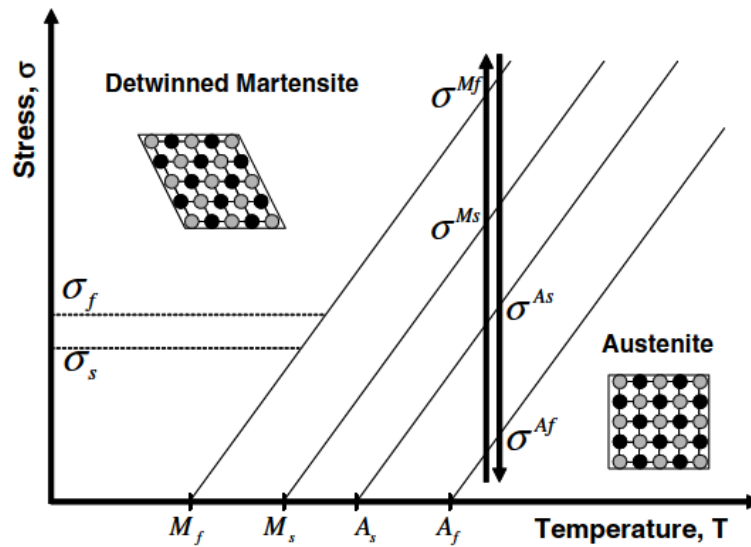


Figure 1.5 A pseudoelastic loading path (Kumar and Lagoudas 2008).

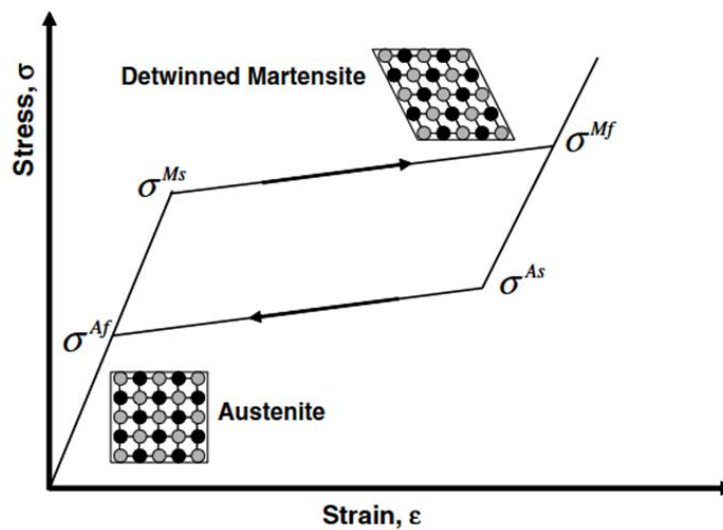


Figure 1.6 Schematic of a pseudoelastic stress-strain diagram (Kumar and Lagoudas 2008).

Schematic representation of the different phases of the SMA, including the austenitic phase and both the twinned (self-accommodated) and detwinned martensite along with the transition zones in a stress-temperature diagram as shown in Fig. 1.7. The diagram which shows the different phases in a stress-temperature space for a given SMA with fixed composition is called the *phase diagram*. The construction of the phase diagram involves the interpretation of the SMA material response subjected to

various thermomechanical loading paths. These loading paths result in shape memory thermal actuation under load and pseudoelastic behavior.

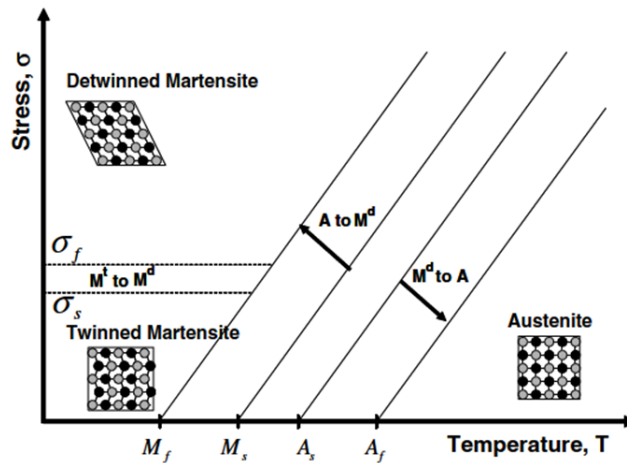


Figure 1.7 Schematic of a stress-temperature phase diagram for an SMA (Kumar and Lagoudas 2008).

1.3 SHAPE MEMORY EFFECT (SME)

An SMA exhibits the shape memory effect during the deformation in twinned martensitic phase and then unloads at a temperature below A_s . When it is subsequently heated above A_f , the SMA will regain its original shape by transforming back into the parent austenitic phase. Fig. 1.8 represents experimental data (stress-strain-temperature for a typical NiTi specimen tested under uniaxial loading. The uniaxial stress σ and the corresponding strain ε is the change in the length of the specimen along the direction of applied load, normalized by the original length.

As shown in Fig. 1.8 starting from the parent phase (at point A), the stress-free cooling of austenite below the forward transformation temperatures (M_s and M_f) results in the formation of twinned martensite (point B). The reorientation process is initiated, when the twinned martensite is subjected to an applied stress that exceeds the stress start level (σ_s), and it leads to the growth of certain favorably oriented martensitic variants that grow at the expense of other less favorable variants. The stress level for reorientation of the variants is extremely lower than the permanent plastic yield stress of martensite. The detwinning process completes at a stress level,

σ_f , and it is categorized by the end of the plateau in the $\sigma - \epsilon$ as shown in Fig. 1.8. Subsequently the detwinned martensitic state is retained when the material is elastically unloaded from C to D.

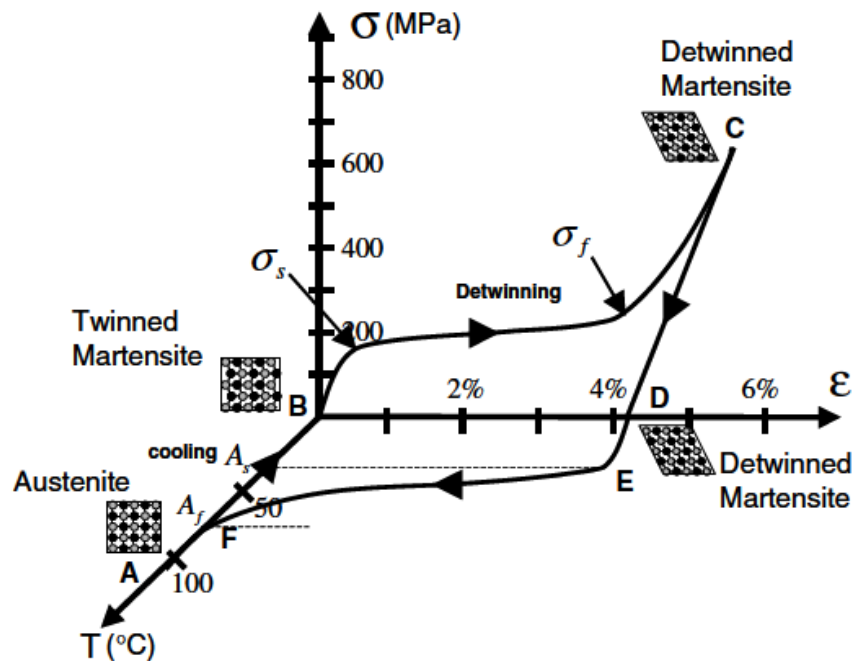


Figure 1.8 Stress-strain-temperature data exhibiting the shape memory effect for a typical NiTi SMA (Kumar and Lagoudas 2008).

Upon heating in the absence of stress the SMA material shows the reverse transformation initiation when the temperature reaches A_s , (at E) and it is completed at a temperature of A_f (point F), above which only the parent austenitic phase exists. In the absence of permanent plastic strain generated during detwinning, the SMA original shape is regained (indicated by A). The recovered strain as a result of the phase transformation from detwinned martensite to austenite is labelled as the transformation strain (ϵ'). The subsequent cooling to martensite will again result in the formation of self-accommodated twinned martensitic variants with no associated shape change, and the whole cycle of the SME can be repeated. This phenomenon is called *one-way shape memory effect*, or simply SME. This is due to the shape recovery during heating after the material has been detwinned by an applied mechanical load.

1.4 SUPERELASTICITY OR PSEUDOELASTICITY

In general, the term superelasticity or pseudoelasticity describes the rubber like behavior. The rubber like effect occurs due to the reversible phase transformation caused by a thermomechanical loading path. The super elastic behavior of SMA is associated with stress-induced transformation, which leads to strain generation during loading and at temperature above A_f upon unloading there would be strain recovery. The thermomechanical loading path starts at a sufficiently high temperature where austenite subsists; Under an applied load it develops a state at which detwinned martensite is stable, and finally returns to the original state (austenite).

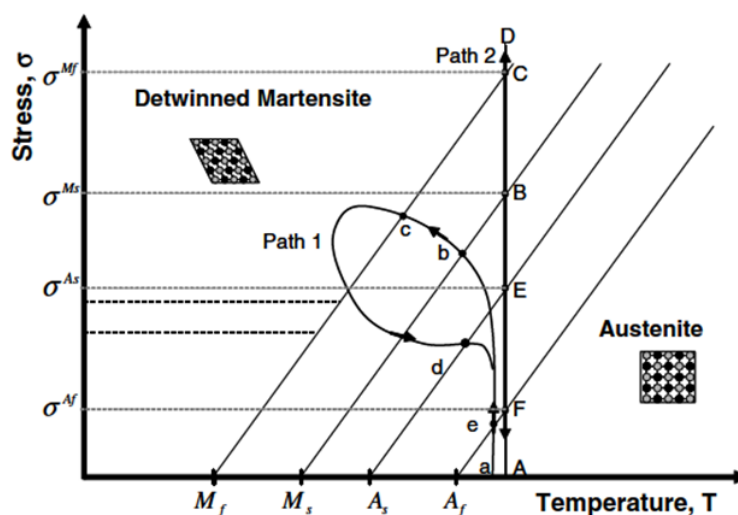


Figure 1.9 Phase diagram and two possible pseudoelastic loading paths (Kumar and Lagoudas 2008).

Further it return to zero stress state ($a \rightarrow b \rightarrow c \rightarrow d \rightarrow e \rightarrow a$) as shown in Fig. 1.9 As path 1. Generally, a pseudoelastic test is conducted at a nominally constant temperature above A_f and the loading path is as shown in Fig. 1.9 As path 2. To explain the pseudoelastic behavior in detail, consider the thermomechanical loading path ($A \rightarrow B \rightarrow C \rightarrow D \rightarrow E \rightarrow F \rightarrow A$) as shown in Fig. 1.9 and which starts at zero stress at a temperature above A_f . The corresponding σ - ϵ experimental data for the loading path is shown in Fig. 1.10. When a mechanical load is applied on SMA the austenite phase undergoes elastic loading ($A \rightarrow B$). At a particular load level, the loading path intersects the surface on the phase diagram for initiation of martensitic transformation. This marks the stress level (σ^{Ms}) for the initiation of transformation into martensite.

The transformation path proceeds further (B→C), to the stress level (σ^{Mf}) where the loading path intersects the M_f transformation surface, showing the end of the transformation.

The martensitic transformation finishing point associated with the elastic loading of the martensitic phase is shown by a distinct change in slope of the $\sigma - \varepsilon$ curve. Due to an increase in the stress there is no martensitic transformation only the elastic deformation of detwinned martensite (C→D). If the stress is released progressively by unloading, the transformation elastically unloads along the path (D→E).

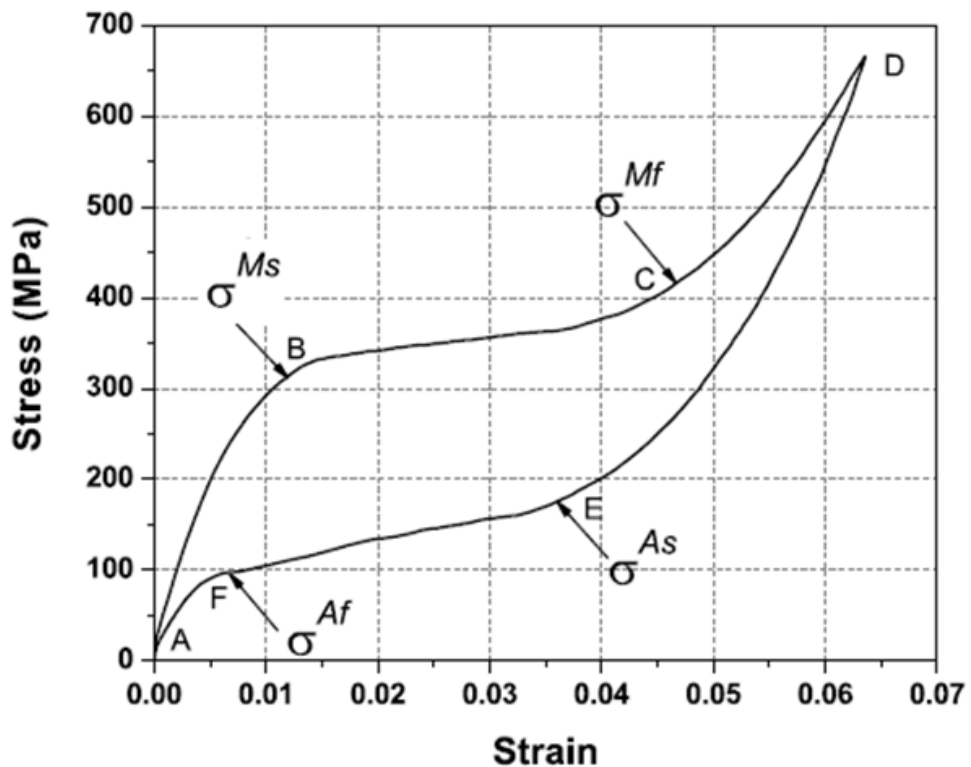


Figure 1.10 A typical SMA pseudoelastic loading cycle (Kumar and Lagoudas 2008).

The unloading path intersects the austenitic start surface (at σ^{As}), which causes martensite to return to austenite at point E. The strain recovery due to phase transformation takes place at the end of unloading. The end of the transformation reverts to austenite phase denoted on the $\sigma - \varepsilon$ curve rejoins the elastic region of austenite (point F) and later the material elastically unloads to A. the complete

pseudoelastic cycle results in a hysteresis, on the $\sigma - \varepsilon$ space, represents the energy dissipation in the transformation cycle. The phase transformation stress levels and hysteresis size levels differ depending on the SMA material and testing conditions.

1.5 Ni-Ti PHASE DIAGRAM

Phase diagram is a graphical representation of the physical state of a substance (solid, liquid or gas) and the temperature and pressure of a substance. NiTi based alloys are ordered intermetallic compounds based on the equiatomic composition of 50 at.% or 55 wt.% of Ni. The Ni-Ti phase diagram typically exists as a metastable phase down to room temperature. The NiTi phase diagram has been controversial for more than 30 years before the current form was established as shown in Fig. 1.12. At first Laves and Wallbaum in 1939 studied the presence of a single phase “NiTi” near the equiatomic composition at higher temperatures (Laves and Wallbaum 1939). Duwez and Taylor in 1950 studied the decomposition of NiTi into Ti_2Ni and $TiNi_3$ phases at 800°C (and at 650°C) (Duwez and Taylor 1950). In 1955, Poole and Hume-Rothery investigated the solubility limit “NiTi” phase above 900°C that the boundary on Ti-rich side is close to 50Ni, and is very steep, while on Ni-rich side the solubility decreases greatly with lowering temperature (Poole and Hume-Rothery 1955). In 1971 Wasilewski et al. found a new phase Ti_2Ni_3 and proposed a phase diagram, which contains a peritectoid reaction at 625°C and also observed that the solubility range of the “NiTi” phase is very narrow at 500°C or below (Wasilewski et al. 1971). Koskimaki et al. in 1969 found a plate-shaped precipitates in specimens which were aged at temperatures below 625°C and named it as “X-phase”. Upon prolonged aging they found that “TiNi” eutectoidally decomposes into Ti_2Ni and $TiNi_3$ and X-phase (Koskimaki et al. 1969). However, the difficulties related to presence of “X-phase” and “ Ti_2Ni_3 ” phase straightened out by the works (diffusion-controlled transformations at higher temperatures for a Ti-52Ni alloy) by Nishida et al. in 1986 (Nishida et al. 1986). As a result, they found that three phases Ti_3Ni_4 , Ti_2Ni_3 and $TiNi_3$ was confirmed by EDS and appeared depending upon aging temperature and time. They proposed that Ti_3Ni_4 phase appeared at lower aging temperature and shorter aging time, $TiNi_3$ phase at higher aging temperature and longer aging time, and Ti_2Ni_3 phase at intermediate temperature and time. The preexisted Ti_3Ni_4 phase is

absorbed in the matrix by prolonged aging and also there is an increase in the number and size of Ti_2Ni_3 phase. Similarly, the preexisted Ti_2Ni_3 phase is absorbed in the matrix by prolonged aging and also there is an increase in number and size of $TiNi_3$ phase. They proposed that the Ti_3Ni_4 and Ti_2Ni_3 phases are intermediate phases and diffusional transformations occur in the following order with respect to increase in aging temperature and time.

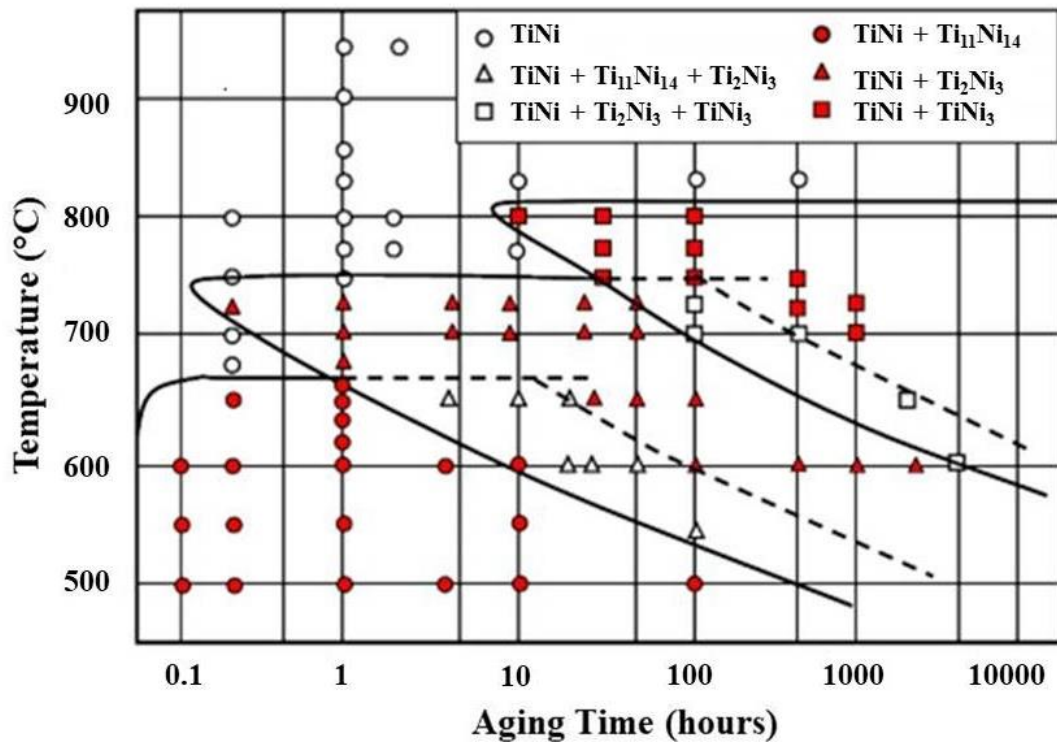


Figure 1.11 Time-temperature-precipitation diagram for a Ti-52at%Ni alloy (Otsuka and Ren 2005).

These transformations are summarized by TTT (time-temperature-transformation) diagram as shown in Fig.1.11. The TTT diagram also unveils upper temperature limit for the Ti_3Ni_4 phase at $680^{\circ}C$. Kainuma et al. in 1987 determined the TTT diagram for Ti-54Ni and Ti-56Ni alloys in addition to the Ti-52Ni alloy (Kainuma et al. 1987). They also examined the solubility limit of the TiNi phase on Ni-rich side, and

confirmed the correctness of the solubility limit proposed by Wasilewski et al. in 1971. By considering the above all the most reliable phase diagram in the central portion of the Ti-Ni system is obtained and it is shown in the Fig. 1.12.

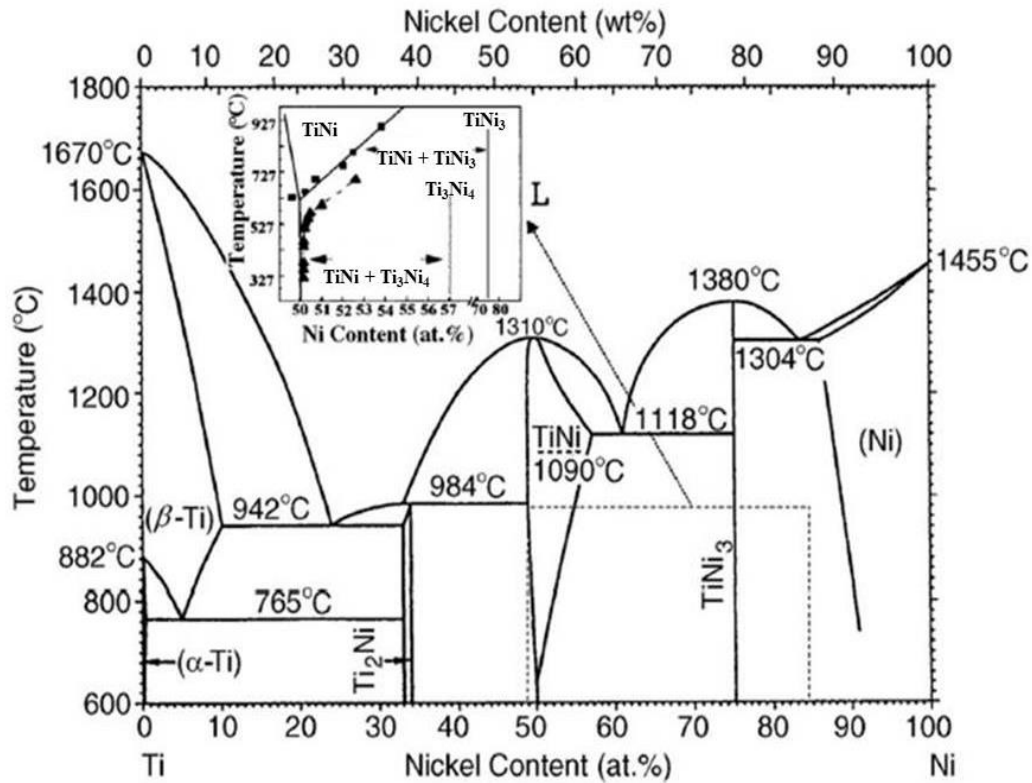


Figure 1.12 Ni-Ti alloy phase diagram (Otsuka and Ren 2005).

Ti-Ni alloys are divided into Ni-rich and Ti-rich alloys. In bulk state, Ti₃Ni₄ precipitates can be used to improve shape memory characteristics in Ni-rich side, unless the Ni content is very close to 50% (say <50.5%). On the other side, in Ti-rich side Ti₂Ni precipitates cannot be utilized, because the solubility limit on this side is almost vertical. However, in crystallized thin films the situation is different via amorphous state, which is a non-equilibrium state. As-deposited films exhibits amorphous nature when the substrate (glass or silicon) temperature is lower than 473 K. Crystallization temperature typically depend upon composition, and that of Ti-50.4at%Ni and Ti-51.1at%Ni is reported to be 756 K (Miura and Nakanishi 1986). Upon heat-treatment the grain size of crystallized films are usually less than 4 μm

(Ishida and Martynov 2002), and mostly 1 μm or so, which is one order of magnitude smaller than those of bulk materials.

Sekiguchi et al. in 1982 produced Ti-Ni thin film by using vacuum deposition method (Sekiguchi et al. 1982). Kim et al. in 1986 prepared the Ti-Ni amorphous films with three compositions by magnetron sputtering technique, and observed R-phase and X-phase precipitates (now known as Ti_3Ni_4 phase) in Ti-56Ni alloy after crystallization (Kim et al. 1986). However, the martensitic transformation was not observed due to lack of near equiatomic composition. After that in 1990 many researchers have prepared Ti-Ni thin films by sputter deposition for MEMS applications (Walker et al. 1990, Busch et al. 1990, Busch and Johnson 1990, Chang et al. 1990, Ikuta et al. 1990, Kuribayashi et al. 1990, Jardine et al. 1990). Walker et al. and Busch et al. noticed the importance of crystallization process to realize martensitic transformations, and observed shape memory effect (Walker et al. 1990, Busch et al. 1990). Miyazaki et al. investigated the shape memory effect by taking strain-temperature curves under constant load and DCS measurements for Ti-50.4Ni and Ti-51.4Ni alloys (Ishida et al. 1994). Su et al. examined damping effect in Ti-Ni films on Si substrate (Su et al. 1994).

Ti-Ni thin films exhibit good mechanical properties, if the grain size is remarkably small (fine) (Miyazaki and Ishida 1999). The transformation behavior depends on composition and is similar to the bulk materials, whereas near equiatomic Ti-Ni exhibits a single $\text{B2} \rightarrow \text{B19}'$ transformation, while Ni-rich Ti-Ni exhibits two-stage $\text{B2} \rightarrow \text{R} \rightarrow \text{B19}'$ transformation, because Ti_3Ni_4 precipitates suppress $\text{B2} \rightarrow \text{B19}'$ transformation relative to $\text{B2} \rightarrow \text{R}$ transformation, as in the case for bulk materials. In Ni-rich alloys the microstructures, transformation behavior and mechanical behavior for Ni-rich Ti-Ni thin films are same as those in bulk materials (Kawamura et al. 1995, Ishida et al. 1996). Superelasticity (Hou and Grummon 1995), one-way shape memory effect (Gyobu et al. 1999, Sato et al. 1998) and two way shape memory effect (Ishida and Martynov 2002, Miyazaki and Ishida 1999, Ishida and Miyazaki 1999) were investigated in detail in Ni-rich alloys.

In this thesis work, we report our preparation of intermetallic (Ni-rich) and near equiatomic NiTi thin films using DC magnetron sputtering method. It has been observed that in the case of intermetallic NiTi thin films (Ni-60at.%, Ti-40at.%

composition), Films, annealed at various temperatures (350°C, 450°C, 550°C and 650°C) exhibited Ni₃Ti phase as major phase and also exhibited Ni-rich precipitates such as B19' (Martensite phase), Ni₄Ti₃ and NiTi₂. In the case of aging at different times (2 h, 4 h and 6 h) intermetallic NiTi thin films exhibited different phases such as NiTi, Ni₃Ti and Ni₂Ti due to incomplete alloying process.

In the case of near equiatomic NiTi thin films (write composition), films annealed at various temperatures (350°C, 450°C, 550°C and 650°C) exhibited the austenite, Martensite, Ni₄Ti₃ and Ni₃Ti phases. Moreover, in the case of aging at different times (2 h, 4 h and 6 h) near equiatomic NiTi thin films exhibited R-phase as major phase and also other phases such as Ni₄Ti₃, NiTi₂, NiTi (Austenite), NiTi (Martensite) and Ni₃Ti.

1.6 THIN FILM DEPOSITION PROCESS

A thin film is formed by a layer of material ranging from fractions of a nanometer (monolayer) to several micrometers in thickness. The controlled synthesis of materials is a fundamental step and this process is referred to as deposition. Thin solid films were first prepared by electrolysis in 1838. Bunsen and Grove prepared metallic films back in 1852 by means of chemical reaction. In 1857 Faraday obtained first metallic thin films by thermal evaporation method using metals. Generally, thin-film deposition technologies are of two types, purely physical such as evaporative methods or purely chemical such as gas and liquid phase chemical processes. The thin film processes that are based on glow discharges and reactive sputtering combine with physical and chemical reactions; these overlapping processes can be categorized as physico-chemical methods.

A classification scheme based on thin-film deposition technologies according to evaporative glow discharge, gas-phase chemical, and liquid-phase chemical processes as shown in Table 1.1. Certain film deposition processes such as oxidation are not deposition processes, but included because of their great importance in solid-state technology. In our work, the intermetallic and near equiatomic NiTi thin films have been prepared using DC magnetron sputtering method, which is a variant of PVD processes.

Table 1.1 Survey and classification of thin-film deposition technologies.

1. Evaporative methods <ul style="list-style-type: none"> ➤ Vacuum Evaporation <ul style="list-style-type: none"> ❖ Conventional vacuum evaporation ❖ Molecular-beam epitaxy (MBE) ❖ Electron-beam evaporation ❖ Reactive evaporation 	
2. Glow-discharge processes	
<ul style="list-style-type: none"> ➤ Sputtering <ul style="list-style-type: none"> ❖ Diode sputtering ❖ Reactive sputtering ❖ Bias sputtering ❖ Magnetron sputtering ❖ Ion beam deposition ❖ Ion beam sputter deposition ❖ Reactive ion plating ❖ Cluster beam deposition (CBD) 	<ul style="list-style-type: none"> ➤ Plasma Processes <ul style="list-style-type: none"> ❖ Plasma-enhanced CVD ❖ Plasma oxidation ❖ Plasma anodization ❖ Plasma polymerization ❖ Plasma nitridation ❖ Plasma reduction ❖ Microwave ECR plasma CVD ❖ Cathodic arc deposition
3. Gas-phase chemical processes	
<ul style="list-style-type: none"> ➤ Chemical Vapor Deposition (CVD) <ul style="list-style-type: none"> ❖ CVD epitaxy ❖ Atmospheric-pressure CVD (APCVD) ❖ Low-pressure CVD (LPCVD) ❖ Metalorganic CVD (MOCVD) ❖ Photo-enhanced CVD (PHCVD) ❖ Laser-induced CVD (PCVD) ❖ Electron-enhanced CVD 	<ul style="list-style-type: none"> ➤ Thermal Forming Processes <ul style="list-style-type: none"> ❖ Thermal oxidation ❖ Thermal nitridation ❖ Thermal polymerization ❖ Ion implantation
4. Liquid-phase chemical techniques	
<ul style="list-style-type: none"> ➤ Electro Processes <ul style="list-style-type: none"> ❖ Electroplating ❖ Electroless plating ❖ Electrolytic anodization ❖ Chemical reduction plating ❖ Chemical displacement plating ❖ Electrophoretic deposition 	<ul style="list-style-type: none"> ➤ Mechanical Techniques <ul style="list-style-type: none"> ❖ Spray pyrolysis ❖ Spray-on techniques ❖ Spin-on techniques ❖ Liquid phase epitaxy

1.6.1 Physical vapor deposition

Physical Vapor Deposition (PVD) processes are atomistic deposition processes in which the material is vaporized from a solid or liquid source, transported in the form of a vapor through a vacuum or low pressure, gaseous (or plasma) environment to the substrate where it condenses in to a film. PVD processes are used to deposit the films with thicknesses in the range of a few nanometers to thousands of nanometers. Generally PVD deposition rates are 10-100 Å (1-10 nanometers) per second. PVD processes can be used to deposit films of elements and alloys as well as compounds using reactive deposition processes.

1.6.2 Sputtering

Sputtering is a non-thermal vaporization process where surface atoms are physically ejected from a solid surface by momentum transfer from an atomic-sized energetic bombarding particle which is usually a gaseous ion accelerated from a plasma. Sputter deposition can be executed by energetic ion bombardment of a solid surface in a vacuum using an ion gun or low pressure plasma (< 5 mTorr) where the sputter particles undergo few or no gas phase collisions in the space between the target and the substrate. Sputtering can also be performed in higher plasma pressure (5-30 mTorr) where kinetic particles sputtered ejected from the sputtering target are “thermalized” by gas phase collisions before they reach the substrate surface. The plasma used in sputtering confined near the sputtering surface may occupy the region between the source and the substrate. The sputtering source can be an element, alloy, mixture, or a compound and the material is evaporated with the bulk composition of the target.

1.6.3 DC magnetron sputtering process

Magnetron sputtering has developed rapidly over the last two decades to the point where it has become proven as the process of choice for the deposition of a wide range of industrially important coatings. Magnetron sputtering makes significant impact in application areas such as hard, wear-resistant coatings, low friction

coatings, corrosion-resistant coatings, decorative coatings and coatings with specific optical, or electrical properties (Kelly and Arnell 2000). Magnetron sputtering is probably the most widely used variant of DC sputtering. Some of the advantages of magnetron sputtering is one or two orders of magnitude higher ion current (i.e. higher deposition rates) and reduced operating pressure (i.e. higher energy of deposited atoms) compared to simple DC sputtering process (Ohring 2002).

In DC magnetron sputtering, permanent magnets are arranged in a suitable configuration behind the target plate. The magnetic field lines penetrate the target and form a closed path on its front surface. The parallel component of the magnetic field strength with respect to the target surface is typically a few hundred gauss measured on the target front surface. Electrons launched slightly off the target normal will initially execute a helical motion along the magnetic field emanating normal to the target. Encountering the region of the parallel component of the magnetic field, also denoted the magnetron component, the electrons are forced to drift in an orbit back to the target. By solving the equations of motion for the electrons one finds that the electrons follow cycloidal trajectories near the target along the space confined by the magnetic field lines. Thus, in the presence of the magnetic field, the secondary electrons make more ionizing collisions close to the target and thereby increase the flux of bombarding ions (i.e. higher ion current), resulting in a higher deposition rate.

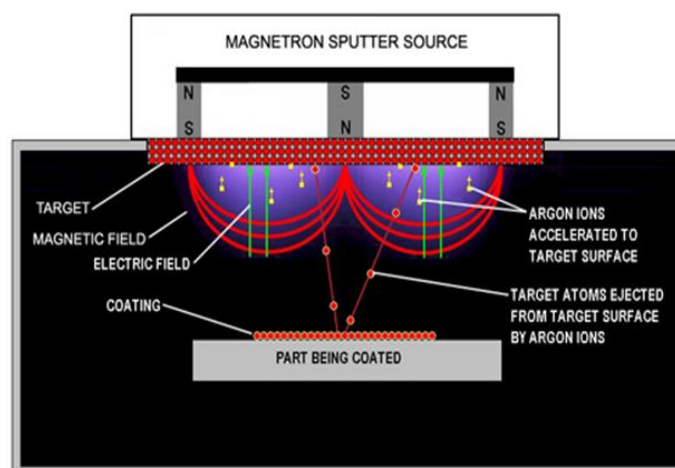


Figure 1.13 sputtering process in a sputter down configuration (Image source: Marca Coating Technology, LLC, Scarborough, ME, www.marca coating.com).

The magnetron current-voltage characteristic is usually $I \propto V^n$ with n close to 10 (without the magnetic field $n \sim 1$) (Helmersson et al. 2006). The significantly increased ionization efficiency makes it possible to reduce the operating pressure and still maintain a stable discharge and a reasonable high ion current. Typical magnetron sputtering pressures are 10^{-2} -1 Pa, which result in a mean free path of the sputtered atoms in the range of 1-100 cm. Thus, compared to simple DC sputtering, the sputtered atoms collide less with the gas atoms, whereby the loss of sputtered atoms to the chamber walls is lowered (increasing the deposition rate). Furthermore, the sputtered atoms preserve most of their initial kinetic energy before hitting the substrate, which is of great importance to the resulting film microstructure. Besides the increased plasma density and a lower operating pressure, the magnetic field also prevents electrons emitted at the target from bombarding the substrate, thereby limiting high substrate heating effects.

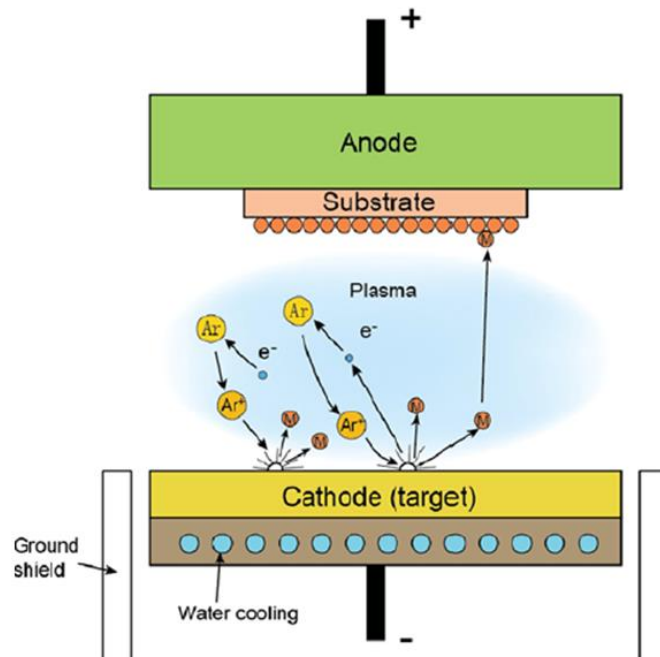


Figure 1.14 Scheme of the sputtering deposition process (Image source: <https://www.slideshare.net/HotLookingCoolGuy/sputtering-process>).

Generally, the deposition rate in a magnetron deposition system is proportional to the DC power dissipated in the magnetron. The significantly increased deposition rate attainable by magnetron sputtering (compared to simple DC sputtering) is often very

desirable. For example, the impurity level in the deposited samples is lower (at a given background pressure) due to a higher flux of target atoms with respect to impurity atoms onto the substrate. Further, a high deposition rate makes magnetron sputtering attractive for industrial applications. However, a drawback of magnetron sputtering is the creation of an erosion crater on the target, denoted the “race track”, where the density of secondary electrons is highest due to the confinement by the magnetic field. This irregular erosion results in a typical target material utilization of only 20-30%. Recently, target utilizations of about 50% have been achieved by optimizing the shape of the magnetic field by use of profiled magnets.

As mentioned above, magnetron sputtering benefits from electron and plasma confinement close to the cathode. But too much confinement may be undesirable if insufficient plasma is dispersed into the direction of the anode/substrate to promote ion bombardment for a desired modification of the growing film. A solution to this problem is to alter the magnet configuration so that, for example, the center magnet is a little weaker than the outer ones. This is an *unbalanced* magnetron configuration, characterized by not all the field lines being closed between the central and outer poles, allowing some field lines to be directed towards the substrate. The unbalanced magnetron configuration enables some of the secondary electrons to follow these field lines, and the plasma is no longer strongly confined to the target region, but is also allowed to flow out towards the substrate. Thus, in addition to providing a high flux of sputtered atoms from the target, an unbalanced magnetron also acts as an effective ion source for substrate bombardment (Kelly and Arnell 2000).

1.7 LITERATURE SURVEY

Thomas et. al in 1982 prepared NiTi alloy thin films in the amorphous state using electron irradiation and a high voltage electron microscope (Thomas et al. 1982). Even though the films were in amorphous state, this was a monumental step in the development of thin film shape memory alloy thin films. The production of shape memory alloy thin films was critical because crystallization of these films allows the progress of films with mechanical properties. In the year 1983, Sekiguchi et al. prepared crystallized NiTi thin films using vacuum deposition technique and

confirmed shape memory effect (SME) in NiTi thin films (Sekiguchi et al. 1982). Four years later, Kim et al. in 1986 used magnetron sputtering to grow films with Ti-56 Ni alloy composition. Although the film's composition was not close the preferred equiatomic composition and did not exhibit martensitic transformation, their work mainly focused on the sputter deposition technique to develop reliable and adequate shape memory alloy thin films (Otsuka and Ren 2005).

The main challenge in the development of shape memory thin films has been the control of the microstructure including stoichiometry and precipitates as well as anisotropy. Since 1990, various physical vapour deposition (PVD) techniques have been used to fabricate NiTi thin films. After the first reports on the deposition of NiTi by magnetron sputtering other processes like Ion beam sputtering, ECR sputtering, Laser ablation, Pulsed laser deposition, Flash evaporation, Electron beam deposition and Vacuum plasma spraying have been used. The most common PVD process is the magnetron sputtering technique, since it allows the deposition at the rate of about 10 $\mu\text{m}/\text{h}$ combined with a relatively simple process equipment. The main challenge remains the deposition of NiTi films with definite stoichiometry and high purity. It was found that in general, in the deposited films, the content of titanium is considerably smaller than in the used sputtering targets.

Davi Johnson in 1991 prepared shape memory alloy thin films using vacuum sputter deposition technique and revealed that the composition and heat treatment of the film are contaminated by oxygen and other species and these affect the transition temperature. It has been observed that the shape memory effect in free standing thin films is comparable to that of bulk NiTi. Higher work output per unit volume of NiTi is achieved with electrostatic or piezoactuators. Actuators in the few-micrometer size domain are possible and have desirable features for electrical and optical activation (Johnson 1991). Miyazaki and Ishida in 1994 investigated shape memory characteristics using DSC and thermomechanical tests. Upon cooling, the solution-treated films showed a single peak in the DSC curve indicating transformation (single stage) from B2 to the martensitic phase, while age-treated films showed double peaks indicating two-stage transformation, i.e., from B2 to the R-phase, then to the martensitic phase. They had also observed that the transformation temperature and strain increased with increasing applied stress (Miyazaki and Ishida 1994). Wolf and

Heuer in 1995 fabricated TiNi (51.7 at% Ti-48.3 at% Ni) films on silicon substrates using RF sputter deposition and produced shape memory effect at 60°C. They created NiTi diaphragms using microfabrication technique, which showed shape memory microactuation and other desirable mechanical properties (Wolf and Heuer 1995).

Ishida et al. in 1996 investigated the stress-strain curves for the annealed films over a wide temperature range (143-473 K) using a tensile tester. All the films showed yielding followed by a plateau region in the stress-strain curves. The strain in the plateau region partly or completely recovered on unloading at high test temperatures (superelasticity), whereas, at low test temperatures, the strain remained after unloading, but partly or completely recovered after subsequent heating (shape memory effect) (Ishida et al. 1996b). Stemmer et al. in 1997 investigated the reaction between shape memory NiTi thin films and silicon observed that a reaction layer is formed during the 525°C post-deposition crystallization anneal of the sputter-deposited NiTi, and consists of several phases: Ti₂Ni, a nickel silicide, and a ternary titanium nickel silicide (Stemmer et al. 1997).

Tsuchiya and Davies in 1998 revealed that R-phase and martensitic transformations in NiTi shape memory alloy thin films are noticed without high temperature annealing. The experimental data obtained from GIXA (Grazing incidence X-ray angles) compared with theoretical simulation and the results indicated that the SMA films were of near equiatomic composition and of density close to the theoretical value for NiTi (Tsuchiya and Davies 1998). Musil and Vlcek observed new physical properties of nanocomposite coating materials, not attainable in polycrystalline films with grains greater than 100 nm. They also described the concept of attaining a new generation of hard nanocomposite coatings with high toughness (Musil and Vlcek 1998).

Ishida et al. in 1999 measured the stress-strain curves and the results showed that the deposited thin films possess sufficient ductility and strength for practical use. Ti-48.3at.%Ni thin film annealed at 773 K for 300 s displays an elongation as large as 20% contrary to bulk specimens. However, the ductility was found to be affected by annealing conditions. Films, annealed at 873 K for 3.6 ks do not show any ductility. It was found that the improvement of ductility is ascribed to the suppression of the grain boundary precipitation of Ti₂Ni (Ishida et al. 1999).

Ohta et al. in 2000 revealed that as-deposited film showed strong adhesion to Si, and poor adhesion to SiO₂ and photoresist. The phase transformation behavior was investigated by differential scanning calorimetry DSC. The transformations of crystal structures of film were examined by temperature controlled XRD and shape recovery behavior was confirmed by immersing it in hot water with a temperature of about 370 K (Ohta et al. 2000). Lehnert et al. in 2000 prepared Ni/Ti multilayers based on the appropriate annealing of SMA thin films. The influence of increasing annealing temperature on the transformation behavior in thin films is investigated by differential scanning calorimetry. The corresponding microstructure is studied by transmission electron microscopy. They observed that the sputter deposited NiTi films made up from multilayers may possess an intrinsic “two-way” shape-memory effect (Lehnert et al. 2000). Ho and Carman in 2000 presented a novel method for depositing NiTi thin film by DC sputtering. This process involved mainly heating the target and does not require compositional modification of the NiTi target. The film possessed transformation temperatures very close to that of the target. The films deposited from hot targets have compositions similar to the target while films deposited from cold targets were Ti deficient. The graded films exhibit the two-way shape memory effect (Ho and Carman 2000).

Surbled et al. in 2001 prepared amorphous NiTi thin films which were subjected to heat treatment higher than 600 K. Thin film SMAs showed strong dependence of the transformation temperatures on heat treatment conditions and composition. Unlike Ni-rich films, the transformation temperatures of Ti-rich films are above the ambient temperature and largely depended on annealing temperatures from 600 to 1200 K (Surbled et al. 2001). Frantz et al. studied the shape memory properties of NiTi thin films deposited on silicon. It is cleared from the results that transformation temperatures above room temperature can be obtained from a Ni-rich NiTi film by using interdiffusion of nickel and silicon (Frantz et al. 2002).

Fernandes et al. in 2002 prepared NiTi thin films and after annealing these films showed the martensitic phase at room temperature. From DSC analysis it is not only confirmed that the possibility of having martensite at room temperature but also showed that M_f at 15°C. These results relied on the fact that the precipitation of Ni₃Ti that took place at high temperature could contribute to local relative depleting in Ni,

equivalent to a Ti enrichment which is responsible for higher M_s and M_f temperature ranges (Fernandes et al. 2002). Lehnert et al. investigated the martensitic phase transformation in Ti-rich NiTi thin films by differential scanning calorimetry and transmission electron microscopy. The annealing temperature range maintained from crystallization temperature to 900°C. By increasing the annealing temperature and/or time, multiple phase transformations, transformations via an R-phase or direct martensite/austenite transformations were observed. They observed that the transformation temperatures could be shifted over a wide range by adjusting the film composition from 48 to 54 at.% Ti. The corresponding transformation curves, grain structure as well as the nature and amount of precipitates were investigated. Films, heated above about 500°C do not require annealing process. In this case, as-deposited films have a very fine-grained and homogeneous microstructure (Lehnert et al. 2002). Ishida and Sato investigated the thickness effect on the shape memory behavior of Ti-50.0at.%Ni thin films. They found that the transformation strain and residual strain under a constant stress are very sensitive to the film thickness when the thickness is less than the average grain size, 5 μm (Ishida and Sato 2003). Kurumada et al. determined the structure of NiTi shape memory alloy nanoparticles by high-resolution electron microscopy. They found that lattice images of an R-phase particle suggested the existence of a Ni-rich Guinier-Preston zone (G.P. zone) (Kurumada et al. 2004). To achieve the shape memory effect Sanjabi et al. deposited the NiTi thin films at room temperature and annealed at 500°C. Transformation temperature evolutions are found to be qualitatively comparable to that of bulk material (Sanjabi et al. 2005). Cho et al. in 2005 prepared Ti/Ni multilayer thin film by a dual d.c. magnetron sputter-deposition method and compared with NiTi amorphous thin film fabricated by an alloy target sputter deposition method. The multilayer thin film exhibited shape memory effect at 673 K where as NiTi amorphous thin films were not crystallized. They found that at 873 K the heat treated Ti/Ni multilayer thin films showed the shape memory effect equivalent to that of the heat-treated NiTi amorphous thin films when the heat treatment temperature was above 873 K (Cho et al. 2005). Huang and Liu in 2005 investigated the Si substrate orientation and SiO₂ buffer layer influence on the surface morphology of deposited NiTi based films. Post annealing results showed homogeneous island distribution. The AFM studies revealed that RMS

surface roughness is closely related to the mean island size and island distribution. The larger the mean island size, the higher the RMS surface for homogeneous island distribution roughness but in case of the inhomogeneous island distribution RMS value always higher (Huang and Liu 2005).

Fu et al. in 2005 were employed X-ray photoelectron spectroscopy (XPS) to study the surface chemistry of the films and interfacial structure of the Si/TiNi system. After long-time aging, carbon content at the sample surface drastically increased and Ni dropped below the XPS detection limit. Depth profiling shown that considerable inter-diffusion occurred between TiNi film and Si substrate and also titanium silicides formed at the interface (Fu et al. 2005a).

Ramirez et al. in 2006 found that the equiatomic amorphous NiTi crystallizes by polymorphic mechanisms and also observed that there is a direct correlation between the average crystal size and the processing temperature. They have successfully characterized the crystallization process and its influence on the martensitic transformation behavior of NiTi thin films (Ramirez et al. 2006).

Wang and Vlassak in 2006 measured the temperature dependence of the crystallite nucleation and growth rates for amorphous NiTi thin films. They proposed a simple mechanism that suppresses heterogeneous nucleation, allowing the grains to grow in a channeling mode. By controlling the nucleation and growth rates, excellent control over the microstructure of the films could be obtained (Wang and Vlassak 2006).

Martins et al. in 2006 investigated texture development during the growth of NiTi thin films using in-situ X-ray diffraction (XRD). The texture evolution during deposition is affected by the substrate type and the ion bombardment of the growing film. Electrical resistivity measurements exhibited different behaviour during phase transformation for the Ni-Ti film deposited on various substrates (Martins et al. 2006).

Kumar et al. in 2006 prepared Ti₄₀Ni₆₀ thin films using an equiatomic alloy target onto silicon substrates. The influence of second phase segregation and superlattice formation and their effect on the electron diffraction patterns have been discussed. Hardness and Young's modulus have been determined as per the standard Oliver-Pharr analysis (Kumar et al. 2006).

Martin et al. in 2007 investigated the effect of a TiN layer deposited on top of the SiO₂/Si(1 0 0) substrate prior to the deposition of the NiTi films. They observed from

the in-situ XRD results that a preferential growth of (1 1 0) oriented grains of the NiTi B2 phase with a top most layer formed mainly by (1 1 1) oriented grains. It has been confirmed that the NiTi films deposited on top of a TiN layer where a dominating orientation could not be identified exhibit a different behaviour. In this, the (1 1 0) oriented grains of the NiTi B2 phase dominate at small thicknesses while (2 1 1) oriented grains take over at larger thicknesses. The different crystallographic orientations of the NiTi thin films influence their phase transformation behavior (Martins et al. 2007).

Raju et al. in 2008 sputter deposited Ni-rich NiTi thin films on Si (1 0 0) substrates at 300°C. The NiTi thin films were solution treated at 700°C for 30 min followed by aging at 400 and 500°C for 5 h. Films, aged at 400 °C exhibits nanocrystalline grains and three phases viz. B2 (austenite), R and Ni₃Ti₂ whereas the film aged at 500°C shows micron sized grains and two phases viz. R and Ni₃Ti₂. The hardness and elastic modulus obtained from Oliver and Pharr analysis found to be lower for the film aged at 400°C than at 500°C which is due to the additional transformation strain during indentation loading and its recovery during unloading in the film aged at 400°C (Raju et al. 2008).

Martins et al. in 2008 prepared near equiatomic NiTi films by magnetron co-sputtering from NiTi and Ti targets on heated substrates ($\approx 470^\circ\text{C}$) has been studied by in situ X-ray diffraction. They obtained different crystallographic orientations by changing the substrate. In the case of films deposited on Si (1 0 0), a (1 1 0) fiber texture is observed in the B2 phase. However, when using a MgO (100) substrate preferential stacking of (1 0 0) planes of the B2 phase parallel to the film surface was observed. NiTi films deposited on a TiN layer (≈ 15 nm) which is deposited on top of a SiO₂/Si (100) substrate. They observed a crossover from (1 1 0) oriented grains dominating at small thicknesses, to (2 1 1) oriented grains taking over at larger thicknesses (Martins et al. 2008).

Lee et al. in 2009 reported the effects of crystallization temperature on the phase transformation behavior of NiTi thin films. With increasing crystallization temperature, the film stress dropped abruptly. Smaller grains were initiated as crystallization temperatures increased. These results showed that, along with thermal

stress, microstructure contributes to the phase transformation behavior, whereas smaller grains may subdue the conversion to martensite (Lee et al. 2009).

Sanjabi et al. in 2009 investigated the influence of the sputtering parameters on the quality of the film and shape memory effect. In spite of composition control, at higher Ar gas pressure, the transformation temperature occurred below room temperature. At low gas pressure, phase transformations showed similar behavior as a function of film composition to NiTi bulk materials (Sanjabi et al. 2009).

Kumar et al. in 2010 studied the effect of substrate and annealing temperatures on mechanical properties of Ti-rich NiTi films. NiTi thin films deposited at two substrate temperatures *viz.* 300 and 400°C. The mechanical properties of the films were found to be the same in the as-deposited as well as annealed conditions for both substrate temperatures. The mechanical properties were found to remain unchanged in amorphous state. However, these properties showed an increase with increasing annealing temperature in crystalline state (Kumar et al. 2010).

Geetha Priyadarshini et al. in 2011 prepared Ni-rich NiTi alloy thin films by radio frequency magnetron sputtering using elemental Ni and Ti as sputter targets. The results showed that due to the lack of surface mobility of the adatoms at the room temperature, the films were smooth and amorphous, with a crystallite size of 15 nm with a porous morphology. At higher substrate temperatures, an increase in the surface diffusion leads to the formation of partially crystalline, rougher films with a denser, compact, fibrous grain microstructure. Ni-rich precipitates such as Ni₄Ti₃, Ni₂Ti, Ni₃Ti and a small amount of the NiTi phase were ascribed to the localized heating and cooling within the grains (Geetha Priyadarshini et al. 2011).

Chung and Chun in 2011 fabricated an uncooled far infrared (IR) imaging sensor micro array using Ni-rich NiTi shape memory alloy films. Micro cantilever arrays were patterned by the photolithographic technique. After aging treatments and thermo mechanical training, the films display typical R-phase transition near room temperature. The thermo mechanical sensitivity of the NiTi film was found higher than that of bi-material films after the two-way shape memory (TWSM) training (Chung and Chan 2011).

Kumar et al. in 2012 grown NiTi thin films of different thickness on silicon (1 0 0) substrates using DC magnetron co-sputtering. NiTi thin films revealed incomplete,

constrained and complete austenite to martensite phase transformation for the films having lower (≤ 300 nm), intermediate (0.6-1.1 μm) and higher (2.3 μm) thickness, respectively. They proposed that the constrained or incomplete transformation arises due to the special constraints introduced by the inter diffusion of film, higher number of grain boundaries and increased level of the intrinsic defects (Kumar et al. 2012).

Sharma and Mohan in 2013 observed from XRD studies that as-deposited films were amorphous in nature whereas annealed films showed poly-crystalline nature with austenite phase as the dominant phase. XPS results showed that in the case of as-deposited films Ni content present on the surface of the films, whereas annealed films did not show any nickel. They concluded from HR-XPS investigations that annealed films have higher tendency to form titanium dioxide layer on the surface of the films than as-deposited NiTi films (Sharma and Mohan 2013).

Hou et al. in 2014 prepared Ni-rich, near equiatomic, and Ti-rich composition of NiTi thin films using biased target ion beam deposition technique. Atomic force microscopy disclosed that films are consistently ultra-smooth over the broad range of compositions. After heat-treatment, the films exhibited B2 and B19' crystal structures and thus possessed potential for martensitic phase transformation, which is the prerequisite for functional shape memory behavior (Hou et al. 2014).

Pan et al. in 2014 conducted nanoindentation tests on sputter deposited NiTi thin film, which exhibits different mechanical responses induced by varied indenter shapes. Under the peak load of 500 μN , the depth recovery ratios are 100% and 68% measured by spherical and Berkovich indentations, respectively. The different response is due to the varied stress distribution beneath two types of indenters. Large plastic deformation hinders the reverse phase transition (R \rightarrow A) in Berkovich indentation, resulting lower recovery. Moreover, essential variance in indentation size effect for NiTi film was shown comparing to traditional metals and phase transition subsidized significantly to the abnormal hardness evolution (Pan et al. 2014).

Tillmann and Momeni in 2015 observed that Ti-rich and near equiatomic NiTi coatings showed a different phase transformation behavior due to the existence of different kinds of precipitations. Ti-rich coatings possess higher hardness due to the lower degree of crystallization and the existence of Ti_2Ni precipitations. Due to the high degree of crystallization of B2 austenite phases, near equiatomic thin films

possessed a lower hardness. Because of the higher volume fraction of the B2 austenite phase near equiatomic NiTi thin films have shown a better wear resistance behavior. Ti-rich NiTi thin films have poor wear resistance due to the existence of a multiphase microstructure and Ti₂Ni precipitations (Tillmann and Momeni 2015).

Priyadarshini et al. in 2016 observed from glancing incidence X-ray diffraction studies that the NiTi thin films exhibited the co-existence of B2 and B19' crystal structures and thus possessed potential for martensitic phase transformation. High resolution transmission electron microscopy was used to observe thermally-induced martensitic twin bands within the nano-grains. X-ray photoelectron spectroscopy was used to investigate the surface elemental composition and also to understand the chemical state of NiTi thin films. Martensitic transformation below room temperature was confirmed by the differential scanning calorimetric measurements. Due to the deformation mechanism governed by grain boundary absorption of the localized strain in nanometer scale, the NiTi films processed at high substrate temperature have shown higher hardness values when compared to the film deposited under the influence of bias voltage (Priyadarshini et al. 2016).

Kauffmann-Weiss et al. in 2017 investigated the growth of binary NiTi thin films on single crystalline MgO substrates using sputter deposition technique. The results showed that deposition at elevated temperatures and controlled heat treatments allow to produce epitaxially grown and smooth NiTi films that exhibit reversible one or two-step martensitic transformations (Kauffmann-Weiss et al. 2017).

1.8 OBJECTIVES OF THE PRESENT WORK

NiTi based films are the most frequently used thin film SMA materials and they are typically prepared using sputtering method. Laser ablation, ion beam deposition, arc plasma ion plating, plasma spray and flash evaporation were also reported but with some intrinsic problems, such as non-uniformity in film thickness and composition, low deposition rate, or non-batch processing, incompatibility with MEMS process, etc. Transformation temperatures, shape memory behaviors and super elasticity of the sputtered NiTi films are sensitive to metallurgical factors (an alloy composition, contamination, thermo-mechanical treatment, annealing and aging process, etc.).

The aim of this PhD thesis is to study the growth and characterization of DC magnetron sputtered intermetallic and near equiatomic NiTi thin films. This study mainly focused to establish a clear relationship between the various physical properties of intermetallic and near equiatomic NiTi thin films.

The objectives of the proposed research investigation are as follows:

1. To study the growth and characterization of DC magnetron sputtered intermetallic and near equiatomic NiTi thin films.
2. To study the effect of annealing temperature and/or aging time on sputtered intermetallic, and near equiatomic NiTi thin films.
3. To study the structural properties of sputtered intermetallic, and near equiatomic NiTi thin films.
4. To study the morphological properties of sputtered intermetallic, and near equiatomic NiTi thin films.
5. To study the mechanical properties of sputtered intermetallic, and near equiatomic NiTi thin films.
6. To study the surface properties of sputtered intermetallic, and near equiatomic NiTi thin films.

1.9 ORGANIZATION OF THE THESIS

The thesis consisted of seven principal chapters and it is organized as follows:

- (1) Chapter 1 is divided into two sections. First, it gives a brief overview of the NiTi shape memory alloy thin films. This section is dedicated to the phenomena involving the phase transformation in shape memory alloy thin films, the shape memory effect (SME) and the superelasticity (SE) are also described. A short background of the NiTi phase diagram, thin film deposition process and the sputtering process is presented. In the second section, a brief literature review related to growth and characterization of NiTi thin films, composition control, the crystallization of the films and phenomena associated, the oxidation behavior, as well as film/substrate interfacial reactions and the role of the thickness on the properties of the NiTi films are presented. Overall, chapter 1 gives a detailed account of the sputtering process for the growth and characterization of the

intermetallic (Ni-rich) and near equiatomic shape memory alloy thin films. The chapter also includes the objectives and organization of the thesis.

- (2) Chapter 2 gives the brief description of DC magnetron sputtering process, which is employed to grow the intermetallic (Ni-rich) and near equiatomic NiTi thin films. This is followed by a concise description of different characterization techniques, namely XRD, FESEM, AFM, nanoindentation and XPS.
- (3) Chapter 3 begins with a discussion of growth and characterization of DC magnetron sputtered intermetallic NiTi alloy thin films. Also, it contains the studies based on the effect of annealing temperature on the structural, morphological, mechanical and surface properties of intermetallic NiTi thin films.
- (4) Chapter 4 consists of the studies based on the effect of aging temperature on the structural, morphological, mechanical and surface properties of intermetallic NiTi thin films.
- (5) Chapter 5 consists of the studies based on the effect of annealing temperature on the structural, morphological, mechanical and surface properties of near equiatomic NiTi thin films.
- (6) Chapter 6 consists of the studies based on the effect of aging time on the structural, morphological, mechanical and surface properties of near equiatomic NiTi thin films.
- (7) Chapter 7 gives the conclusions of the present work. Furthermore, the scope for future research work in this area is also discussed.

CHAPTER 2

EXPERIMENTAL METHODS

This chapter gives the brief description of DC magnetron sputtering technique (Plasma Vapor Deposition (PVD) process), which is employed to grow the intermetallic and near equiatomic NiTi thin films. This is followed by a concise description of experimental procedure and different characterization techniques, namely XRD, FESEM, AFM, Nanoindentation and XPS.

2.1 EXPERIMENTAL PROCEDURE

The whole process of NiTi thin film fabrication and experimental process can be divided into three phases:

- 2.1.1 Substrate and target cleaning process
- 2.1.2 Sputter parameter optimization
- 2.1.3 Sputter deposition process

2.1.1 Target and substrate cleaning process

Before any substrate can be used, it must be adequately cleaned. The proper cleaning technique depends on the nature of the substrate, the nature of the contaminants, and the degree of cleanliness required. Expected contaminants include those from manufacturing procedures, human contact (such as a protein), and airborne dust, lint, and oil particles. The substrate surface must be made clean enough that contaminants do not interfere with the adherence of a vacuum deposited film.

2.1.1.1 Substrate cleaning process

In the present work, the NiTi thin films have been prepared on silicon (1 0 0) substrates at room temperature with separate elemental targets Ni and Ti. Silicon substrates (of size 10 mm x 10 mm) are cleaned primarily by a solvent cleaner, followed by a deionized water (DI) rinse, subsequently with a mild acid clean and finally cleaned with DI rinse and blow dry.

2.1.1.2 Target cleaning process

Titanium: The Titanium targets were cleaned by using following chemical solution.

Chemical composition: 30 ml Hydrochloric acid (HCl) + 10 ml Hydrogen fluoride (HF) + 10 ml Nitric acid (HNO₃) + 50 ml water (H₂O).

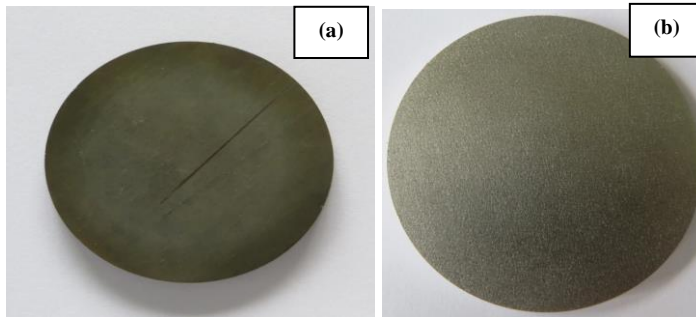


Figure 2.1 (a) Before cleaning (b) After cleaning.

Nickel: The Nickel targets were cleaned by using following chemical solution.

Chemical composition: 10 g Copper Sulphate (CuSO₄) + 50 ml Hydrochloric acid (HCl) + 50 ml Ethanol (CH₃CH₂OH or C₂H₆O) + 50 ml Water (H₂O).

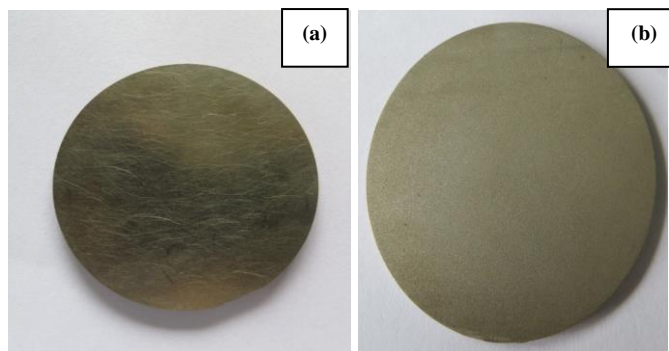


Figure 2.2 (a) Before cleaning (b) After cleaning.

Before fixing to the magnetron guns the metal targets can be cleaned using a four step process. First the target should be wiped using a lint-free lab cloth (towel) soaked in acetone, followed by a similar wipe with Isopropyl alcohol (C₃H₈O or C₃H₇OH or CH₃CHOHCH₃) and finally wipe with deionized water. After the final wipe, the target should be baked (heated) out in air for 30 minutes at 100°C.

2.1.2 Sputter parameter optimization

This work is mainly based on the DC magnetron sputtering process, a physical vapor deposition (PVD) technique which is extensively used in thin film fabrication. In order to obtain the desirable thin film by DC magnetron sputtering process it requires the optimized combination of deposition parameters. The common practice is to repeat the experiments systematically under varied and controlled conditions. However, only certain deposition parameters are involved and in each of the research approaches the parameters are different. The materials used in are also different and the optimizations are done for different applications. In the present investigation, conditions were seen to give rise to desirable structural, morphological, mechanical and surface properties of intermetallic and near equiatomic NiTi thin films. The features of the thin layer formed on the substrate depend on the deposition parameters such as gas flow rate, sputter power, deposition time, gas pressure and substrate to target distance, etc.

2.1.3 Sputter deposition process

NiTi based thin films has been recognized as a promising and high performance material in the field of micro-electro-mechanical-systems (MEMS) applications and they are typically prepared using sputtering method (Fu et al. 2001). In this work, NiTi thin films were deposited using a custom made DC magnetron sputtering system (V.R. Technologies, Bangalore, India) in a lab environment at room temperature. As can be seen in Fig. 2.3, the sputtering system is equipped with two convergent sputtering targets. Configuration of the flange used in the study is two separate targets Ni and Ti with a purity of 99.99% (target size: 50.8 mm x 3.18 mm). The sputter chamber was evacuated to a base pressure, lower than 1.5×10^{-5} mbar using diffusion pump and rotary pump. The pressure in the vacuum chamber was measured using digital Pirani-Penning gauge combinations. To maintain the NiTi thin film deposition it is very important to calibrate and control sputtering parameters carefully, because the values of these parameters tend to either drift after a period of service time or change during deposition. These parameters include Ar gas pressure, gas flow rate, rotation speed, voltage and current of the power supply. The Ar gas pressure with

purity 99.99% was used as a sputtering medium with a constant flow rate of 30 sccm (Standard Cubic Centimeters per Minute). The argon gas pressure was controlled by the proportioning solenoid valve and measured using (AALBORG GFC 17) mass flow controller. The NiTi thin films were deposited on silicon (1 0 0) substrates of dimension 10 mm x 10 mm. Before, every sputter deposition the targets were presputtered 15 minutes to remove the surface oxide layer and also to ascertain the same state of the target. To obtain the uniform film composition the substrate holder was rotated axially at 10 rpm (revolutions per minute). The target to substrate distance was maintained at approximately 50 mm for all depositions.



Figure 2.3 DC magnetron sputtering system.

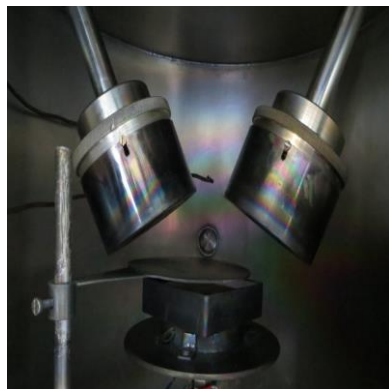
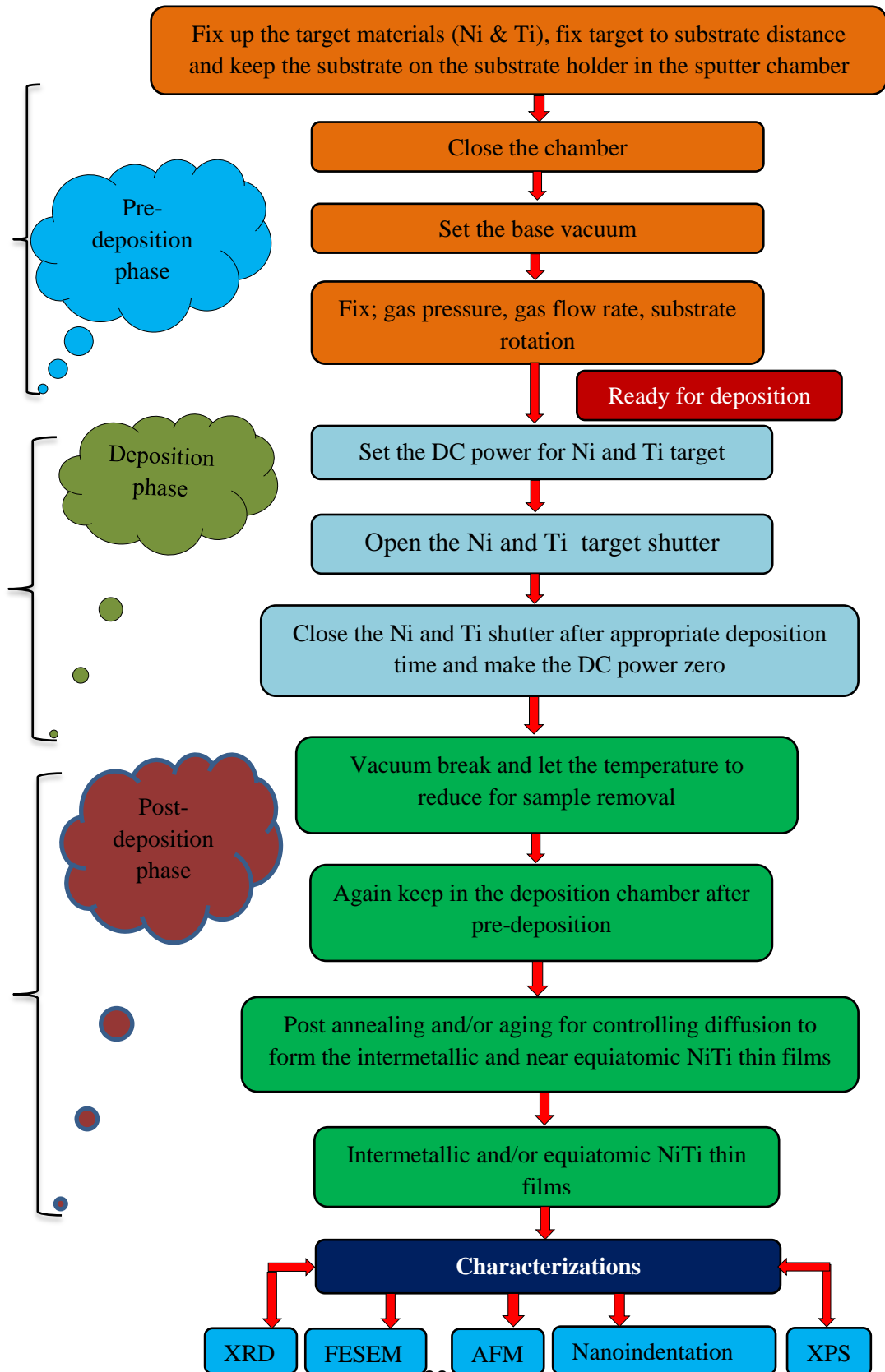


Figure 2.4 Position of magnetron guns in the vacuum chamber.



Figure 2.5 Plasma during sputtering process.

2.2 FLOW CHART FOR SPUTTER DEPOSITION PROCESS AND CHARACTERIZATION PHASE



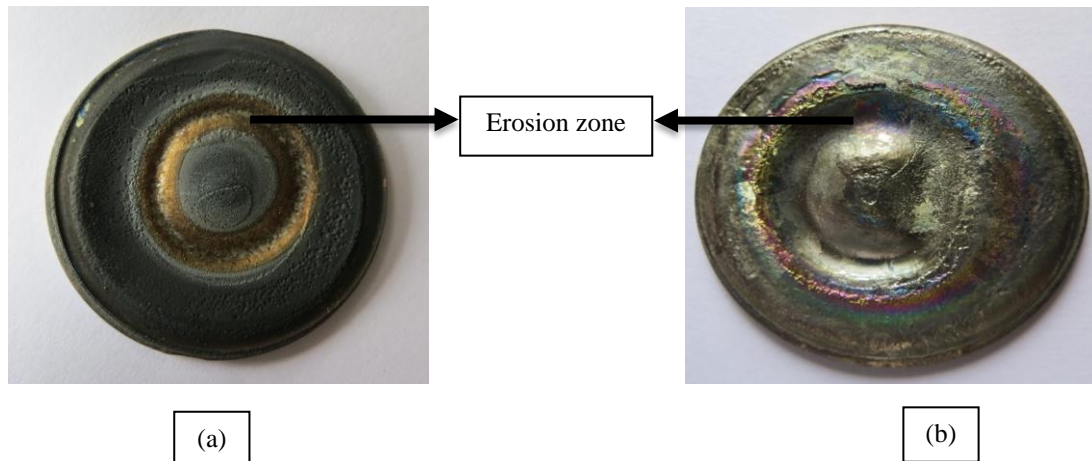


Figure 2.6 (a) Nickel sputtering target with erosion zone (b) Titanium sputtering target with erosion zone.

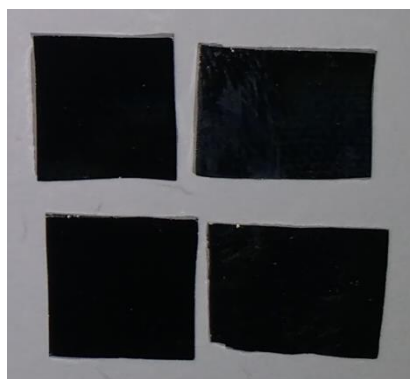


Figure 2.7 As-deposited NiTi thin films.

2.3 CHARACTERIZATION TECHNIQUES

2.3.1 X-ray diffraction (XRD)

X-rays were discovered in 1895 by the German physicist Wilhelm Roentgen and who had named it X-radiation to signify an unknown type of radiation. X-rays are electromagnetic radiation of shorter wavelength. The unit of measurement in the X-ray region is the angstrom (\AA), equal to 10^{-8} cm, and wavelengths approximately in the range 0.5-2.5 \AA . X-rays are produced whenever high-speed electrons collide with a metal target. X-ray tube must possess (a) a source of electrons, (b) a high accelerating voltage, and (c) a metal target. Furthermore, since most of the kinetic energy of the electrons is converted into heat in the target, the latter must be water-cooled to prevent its melting. All X-ray tubes contain two electrodes, an anode (the

metal target) maintained at ground potential, and a cathode, maintained at a high negative potential, normally of the order of 30,000-50,000 volts (V) for diffraction work. In 1912 when the German physicist von Laue revealed that, if crystals were composed of regularly spaced atoms which might act as scattering centers for X-rays, and if X-rays were electromagnetic waves of wavelength about equal to the interatomic distance in crystals, then it should be possible to diffract X-rays by means of crystals. Later W.H. Bragg and W.L. Bragg in the year 1912 successfully analyzed the Laue experiment and was able to express the necessary conditions for diffraction in simpler mathematical form than that used by von Laue.

2.3.1.1 Bragg's law

Bragg's law is a special case of Laue diffraction gives the angles for coherent and incoherent scattering from a crystal lattice. When X-rays are incident on an atom, they make the electronic cloud move as does any electromagnetic wave. The movement of these charges re-radiates waves with the same frequency, blurred slightly due to a variety of effects; this phenomenon is known as Rayleigh scattering (or elastic scattering). The scattered waves can themselves be scattered but this secondary scattering is assumed to be negligible.

A similar process occurs upon scattering neutron waves from the nuclei or by a coherent spin interaction with an unpaired electron. These re-emitted wave fields interfere with each other either constructively or destructively, producing a diffraction pattern on a detector or film. The resulting wave interference pattern is the basis of diffraction analysis and is called Bragg diffraction.

In a crystalline solid, the scattered waves from lattice planes separated by the interplanar distance d . When the scattered waves interfere constructively, they remain in phase since the path length of each wave is equal to an integer multiple of the wavelength. This can be denoted as $2d\sin\theta$, where θ is the scattering angle. Because of the cumulative effect of reflection by successive crystallographic planes of the crystalline lattice the effect of the constructive or destructive interference intensifies.

$$2d\sin\theta = n\lambda \quad (2.1)$$

where n is the order of diffraction and λ is the wavelength of the incident wave. This equation is useful to calculate wavelength, crystal plane separation or diffraction

angle. By measuring the intensity of scattered waves as a function of scattering angle a diffraction pattern would be obtained. A diffraction pattern is obtained by measuring the intensity of scattered waves as a function of scattering angle. Very strong intensities known as Bragg peaks in the diffraction pattern are obtained at the points where the scattering angles satisfy the Bragg condition.

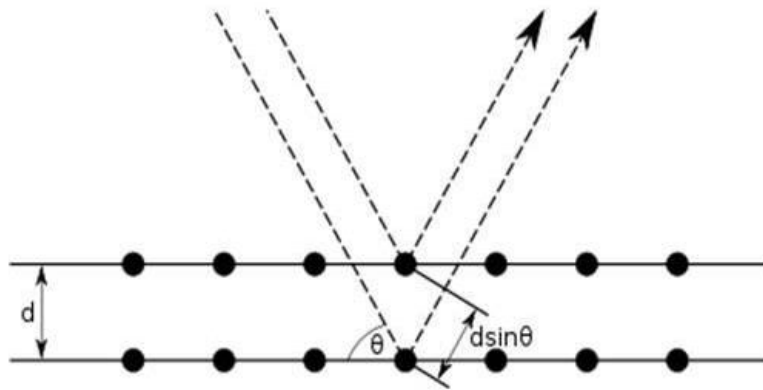


Figure 2.8 Reflection of X-rays from different atomic planes, illustrating the Bragg's law.

(Imagesource:https://www.google.co.in/search?q=bragg%27s+law+diagram&tbm=isch&source=iu&ictx=1&fir=wdlTFrxUKE4H1M%253A%252CN9JRP0WvpmcyM%252C_&usg=__AgGig2bx6lfd5uxUdtT7n2h5xo%3D&sa=X&ved=0ahUKEwiVwuOl3KrbAhUBWX0KHR0kBvAQ9QEIXTAL#imgrc=SUiCzzUDzlcx0M:)

In this thesis work, XRD of NiTi (Intermetallic and near equiatomic) thin films was carried out using Rigaku Miniflex-600 tabletop X-ray diffractometer to verify the amorphous and crystalline (phases) nature. Data were collected using $\text{CuK}\alpha$ ($\lambda=1.54056 \text{ \AA}$) radiation in the diffraction angle (2θ) range from 20° - 80° with a scanning rate of 0.5° per minute with scan step size of 0.05° . The X-ray tube was operated at 40 kV and 15 mA.



Figure 2.9 X-ray diffractometer (Model: Rigaku Miniflex-600)

2.3.2 Field emission scanning electron microscope (FESEM)

FESEM is widely used technique to get topographical features, surface morphology, crystal structure, crystal orientation, presence and location of defects as well as dimension, shape and density of the particles (Goldstein et al. 1981). In FESEM, electrons are liberated from a source and are accelerated in a high electrical field gradient within the high vacuum column (10^{-4} - 10^{-10} torr). The accelerated beam of electrons (monoenergetic) having energies in the range of a few hundred of eV to tens of keV, these primary electrons, is focused with the help of electromagnetic lenses to produce a narrow scan beam that bombards the object. Secondary electrons are emitted from each spot on the object. These are detected to produce an electronic signal. The surface of the sample is scanned over an area. The obtained signal conveys information about the morphology of the sample. Some of these electrons get scattered elastically from the coulomb field of the nucleus, whereas some electrons inelastically scattered from the electrons of the host atoms giving secondary or auger electrons. These auger electrons bare characteristic of the element from which they are emitted (Goldstein et al. 1981). The secondary electrons, detected by a detector every position of the incident electron beam, are used to form an image. The collected signal is amplified and is made to form a synchronous image on a cathode ray tube. A camera is used to capture the image or it may be digitized and processed on a

computer. A schematic diagram of typical scanning electron microscope is given in Figure 2.10.

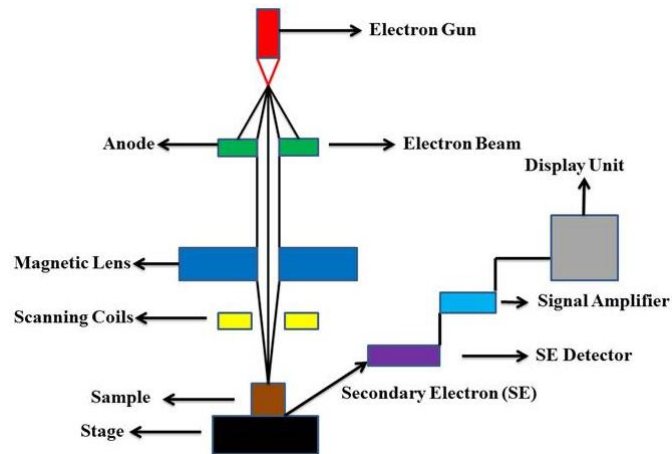


Figure 2.10 Schematic details of Field emission scanning electron microscope.
(Imagesource:<http://shodhganga.inflibnet.ac.in/bitstream/10603/70233/5/chapter2.pdf>)



Figure 2.11 Field Emission Scanning Electron Microscope (Model: SUPRA 55, CARL ZEISS-GERMANY).
(Imagesource:<http://www.mse.ntu.edu.sg/Research/create/Documents/Equipment%20Details-FESEM%20Supra%2055.pdf>)

In this technique, the sample should be conductive. The surface of nonconductive samples is made conductive, usually by coating a thin layer of gold. The beam current and the final spot size determine the depth and resolution of field of the image respectively, which are adjusted with one or more condenser lenses and the probe forming objective lenses. The electrons interact with the sample from a few nanometers to several microns of the surface of the sample depending on the beam parameters and the sample type. Primarily, electrons are emitted from the sample as either backscattered or as secondary electrons, and are detected by the scintillation photomultiplier detector. Secondary electrons have the energy of 3-5 eV and are generally used for the visualization of surface morphology and roughness, as they can spot the exact position of the beam on the sample surface and give morphological information with high resolution (Goldstein et al. 1981).

In this thesis work, the morphological and microstructural features of DC magnetron sputtered intermetallic, and near equiatomic NiTi thin films were investigated with a FESEM (SUPRA 55, CARL ZEISS-GERMANY).

2.3.2.1 Energy dispersive X-ray spectroscopy

Energy Dispersive X-ray Spectroscopy (EDX, EDS, EDXS or XEDS) is an analytical technique used to identify the elemental composition of a sample. This equipment is attached to the SEM to allow for elemental analysis of the sample under investigation. EDS is non-destructive technique and possesses a sensitivity of >0.1% for elements heavier than Carbon (C). EDS works mainly based on detecting X-rays those are ejected by a sample placed in a source of an electron beam. A high energy beam of charged particles (electrons or protons) excites the atoms in the sample that subsequently produce characteristic X-rays to discharge the excess energy.

In an equilibrium state, an atom within the sample contains ground state (or unexcited) electrons in discrete energy levels or electron shells bound to the nucleus. The incident high energy beam excites an electron in the inner shell and ejects it from the shell while creating an electron hole where the electron was. An electron exists in outer or higher energy shell fills the electron hole. The difference in energy between the higher energy shell and the lower energy shell would be released in the form of an X-ray. The number and energy of emitted X-rays can be collected from a specific

area/point in the sample measured by an energy dispersive spectrometer. As the emitted energies of the X-rays are characteristic of the energy difference between the two electron shells and of the atomic structure of the element, then EDS allows measuring the elemental composition of the sample.

2.3.3 Atomic force microscopy (AFM)

Atomic Force Microscopy (AFM) is one of the Scanning Probe Microscopy (SPM) based techniques. It was invented in 1986 by G. Binnig, C.F. Quate and Ch. Gerber (Binnig and Rohrer 1987). To measure the surface morphology and properties of a sample, AFM uses a sharp tip that is connected to a cantilever. The cantilever is bent in positive and negative directions depending on the attractive or repulsive forces exerted during the interaction between the tip and the sample.

In AFM a constant force is applied between the probe and a sample as the probe is raster scanned across the sample surface. A three dimensional image is constructed by monitoring the motion of the tip. Unlike Scanning Tunneling Microscopy (STM), AFM does not require a conducting surface to scan the sample surface. Using this instrument insulators, organic materials, biological macromolecules, polymers, ceramics, and glasses can be imaged under different environmental conditions (Binns 2010).

2.3.3.1 AFM Components

Figure 2.12 shows a block diagram of AFM components. Piezoelectric material, a force transducer, and a feedback controller are basic components of AFM. Piezoelectric materials are electromechanical transducers; they convert electrical potential to mechanical motion. These materials are used to control the motion of the probe as it scan across the surface. The force between the probe and surface is measured using force transducers. The voltage of the transducer varies when the probe comes into contact with the surface. The output of the transducer increases as the probe applies higher force on the sample.

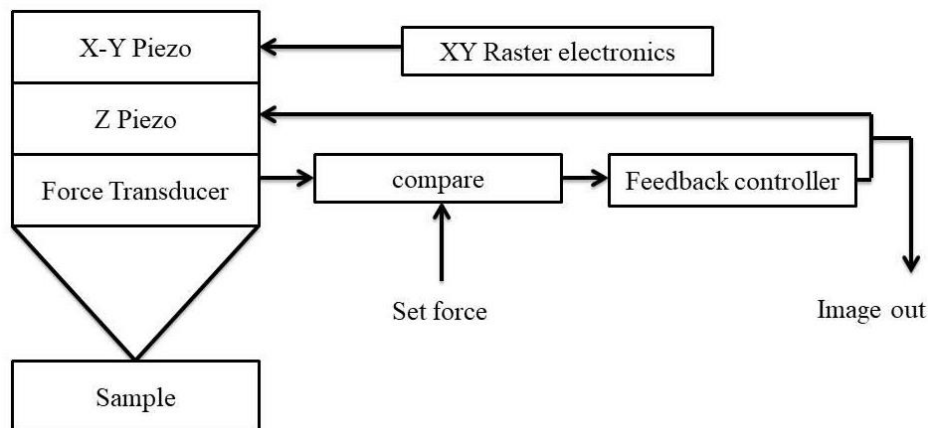


Figure 2.12 Block diagram of AFM components (Rajathadripura. (2014). "Characterization of Hybrid Electronic Materials Using Atomic Force Microscopy" (2014). LSU Master's Theses. 1172).

2.3.3.2 Modes of operation

The AFM can be operated in three modes based on the application. In general, these operating modes are categorized as contact (also called static) mode, dynamic (non-contact) mode and tapping (intermittent) mode. The detailed description of the above mentioned modes is as follows.

2.3.3.3 Contact mode

Figure 2.13 represents AFM operated in contact mode. In contact mode, the tip is brought closer to the sample surface. The tip mechanically contacts the sample surface with the application of force. As the tip moves closer to the surface, a repulsive force is generated between sample and tip. Contact mode is also known as variable deflection mode (Meyer 1992). The cantilever used in contact mode is relatively soft with a spring constant (K_c) between 0.05 and 1.00 N/m. The magnitude of force applied on the sample by the cantilever is in the range of 10^{-7} to 10^{-6} N (Grothe and Park 2000). Sample damages are relatively high in this mode due to the large amount of lateral forces exerted on the sample surface.

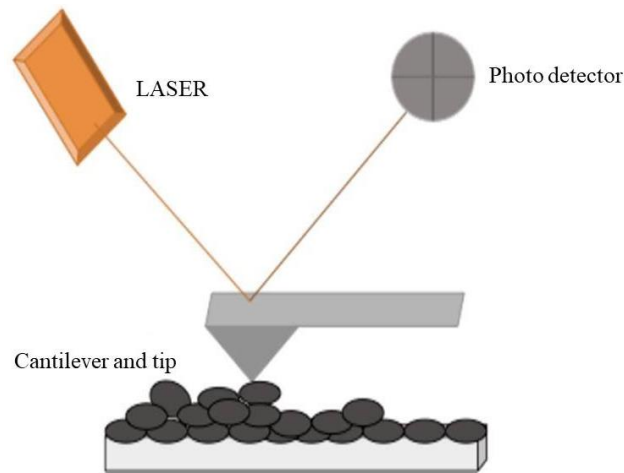


Figure 2.13 AFM in contact mode (Rajathadripura. (2014). "Characterization of Hybrid Electronic Materials Using Atomic Force Microscopy" (2014). LSU Master's Theses. 1172).

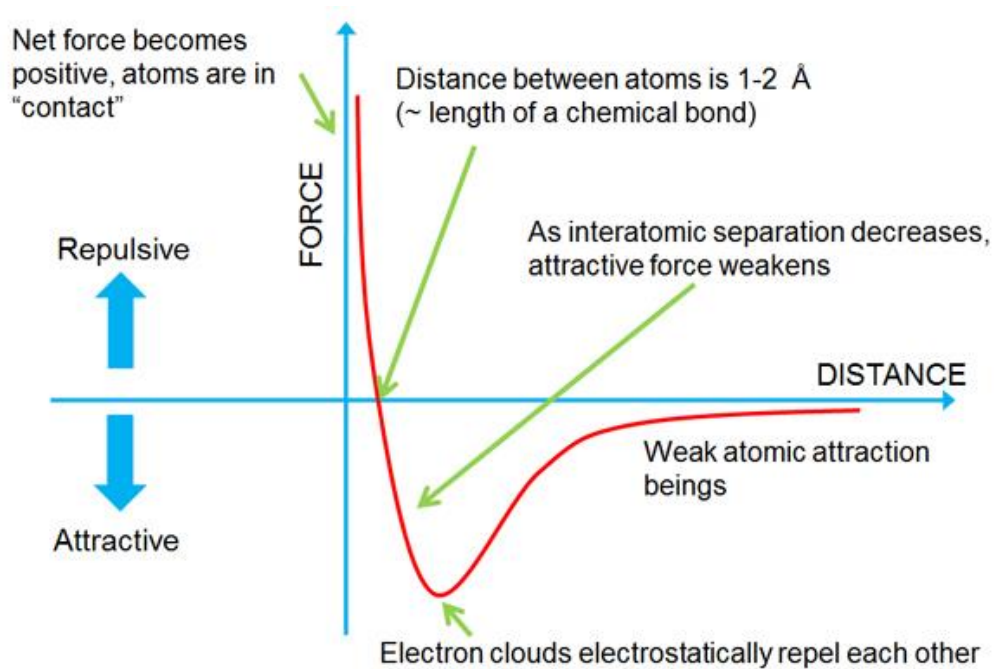


Figure 2.14 Force versus distance curve (Moss and Sinha 2003).

Figure 2.14 represents the force versus distance curve of contact mode AFM. As the Van der Waals force becomes positive, the atoms are in contact. When atoms in the tip and the sample are brought together, and when the distance between them is large, they tend to attract to each other. However, when they are brought very close, the

electron clouds of the tip and sample atoms begin to repel each other electrostatically. Electrostatic repulsion weakens the attractive force between atoms as the interatomic distance continues to decrease. In addition to Van der Waals forces some of the other forces present in contact mode AFM are those exerted by the cantilever and capillary forces.

2.3.3.4 Non-contact mode

Martin et al. developed non-contact AFM in 1987 (DeLong et al. 2008). In non-contact mode (NC mode), the cantilever is oscillated above the sample surface in a resonant frequency with very low or constant amplitude of the order of few nanometers (<10 nm). This mode is also called oscillatory mode or dynamic mode. Here, the cantilever is oscillated at a resonant frequency. Depending upon the forces between the tip and sample, the cantilever resonant frequency changes. Tip-sample interaction in NC-mode is attractive as shown in the Fig. 2.15. NC-mode can be classified into amplitude mode (AM) and frequency mode (FM) of operation. In the Amplitude mode (AM) of operation, the amplitude of the cantilever is kept constant, and the frequency remains close to its resonant frequency (which is fixed). When the tip is brought close to the sample surface, the tip sample interaction leads to changes in amplitude and phase of the cantilever. This mode is usually used to scan in liquid conditions. A high quality factor (Q) for the tip is necessary to obtain a high signal-to-noise ratio. High quality factor value can be achieved only in ultra-high vacuum (UHV) conditions, so this method is more suitable to a vacuum environment.

In the Frequency mode (FM) of operation, the cantilever is oscillated at resonance and continuously tracks the resonant frequency. The oscillation frequency of the cantilever changes with the change in resonant frequency due to tip-sample interaction. Using FMAFM high atomic resolution images of sample surfaces can be obtained; it is generally operated in UHV conditions. In NC-AFM, as the tip approaches the sample the amplitude and phase of the cantilever

Changes, which results in a new frequency (f_{eff}) and new spring constant (K_{eff}) due to Van der Waals forces between tip and sample. The distance between tip and surface changes as Δd with changes in amplitude and phase as shown in the Fig. 2.15. At the

resonant frequency of the cantilever, the amplitude changes as ΔA , and the feedback loop compensates for Δd .

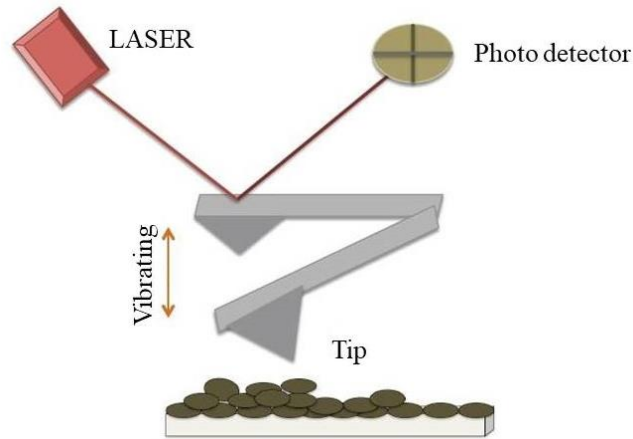


Figure 2.15 AFM in non-contact mode (Rajathadripura. (2014). "Characterization of Hybrid Electronic Materials Using Atomic Force Microscopy" (2014). LSU Master's Theses. 1172).

2.3.3.5 Tapping mode or Intermittent contact mode

This technique is similar to non-contact mode, where the cantilever is oscillated at a resonant frequency with higher amplitude with respect to the surface of the sample. Amplitude is usually kept constant in this mode. Therefore, this imaging technique is also known as amplitude modulation AFM (AM-AFM). Figure 2.16 illustrates the resonance curve of a cantilever above the surface and close to the surface of a sample (specimen). Tapping mode operates in the repulsion force region with periodic tapping on the sample surface. This technique is used to obtain high resolution images of easily deformable material and loosely held substrates, which is difficult to image with regular AFM techniques. It also solves the problems with lateral forces and drag on the surface as the tip is touching only for a short interval of time. Atomic resolution images of inorganic surfaces and high resolution images of polymers, isolated proteins, protein membranes can be obtained using this mode (San Paulo and Garcia 2001).

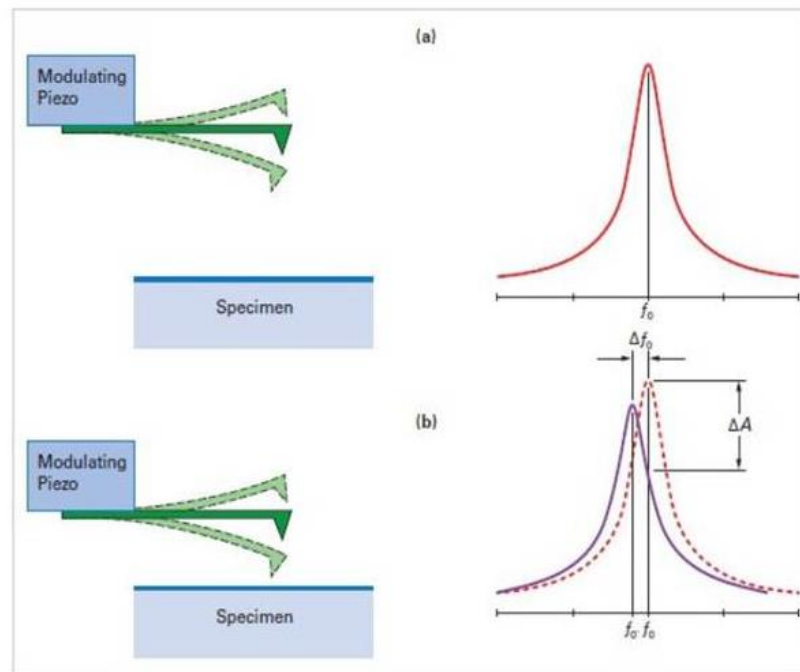


Figure 2.16 Resonance curve of cantilever (a) above the surface, (b) close to the surface (“Atomic force microscope and method for imaging surfaces with atomic resolution” 1988).

Tapping mode is performed with an amplitude modulation detector and a lock-in amplifier. Tapping mode can be performed in air, liquid, and vacuum. A strong cantilever and considerably large oscillation amplitude is required while using tapping mode in air in order to overcome attractive capillary forces by the restoring force of the cantilever spring. The difference between amplitude and set-point determines the force between tip and sample and also determines the image. Tapping mode in liquid is used to scan biological samples (Tesfai et al. 2008).

By immersing the sample and the tip in liquid, adhesive capillary sample-tip problems can be reduced. The frequency of oscillation is kept constant near the resonance of the tip when force is applied on the cantilever by PZT (Piezoelectric tube). Piezoelectric tube comprises of X-Y piezoelectric ceramics and z-piezoelectric transducer. At this oscillation, the tip approaches the sample surface until the amplitude value is reduced to the set point value. Thus sample damages are minimized. The piezoelectric drive adjusts the Z axis (vertical) position by keeping the oscillation amplitude at the set point. The changes in Z position of the tip are plotted as the XY position of the tip to obtain a height image.

In the present thesis work, the AFM studies of the effect of annealing temperature on intermetallic NiTi thin films have been conducted using AFM Model: NT- MDT under semi contact mode at Satyabama University, India as shown in Fig. 2.17.



Figure 2.17 Atomic Force Microscope (Model: AFM-NTMDT) (Image source: <https://www.ntmdt-si.com/products/modular-afm/ntegra-ii>)

In this thesis work, the AFM studies for Chapter 4, 5 and 6 have been conducted using AFM Model: Bruker Innova under tapping mode at Manipal University, India as shown in Fig. 2.18.



Figure 2.18 Atomic Force Microscope (Model: Bruker Innova).

(Imagesource:https://www.google.co.in/search?q=innovairis&tbm=isch&source=iu&ictx=1&fir=IDDvBEd5DiqHZM%253A%252CUChFa2jGZ0QbwM%252C_&usg=__gCy8ne8Arb0r7SwdFK4RHdZa5M%3D&sa=X&ved=0ahUKEwjTo5u246rbAhWJfn0KHx13CqsQ9QEILzAB#imgrc=3ZUXqpr9X2IOoM:)

2.3.4 Nanoindentation

Nanoindentation is a widely adopted method to measure the elastic, plastic, and time-dependent mechanical properties including the hardness and Young's modulus of thin films and small volumes of bulk materials. Nanoindentation is effectively a very high resolution hardness test. The most commonly employed method to determine the modulus and hardness of the indented material are the Oliver and Pharr method first proposed in 1992 (Oliver and Pharr 1992, Giannakopoulos et al. 1994, Giannakopoulos and Suresh 1999, Tabor 2000, Dao et al. 2001, Cheng and Cheng 2004, Oliver and Pharr 2004a, Ganneau et al. 2006, Fischer-Cripps 2011). This has become the standard procedure to extract elastic modulus and hardness of the specimen material from load-displacement measurements (Oliver and Pharr 2004, Schuh 2006, Li and Vlassak 2009, Fischer-Cripps 2011). In nanoindentation tests, a specified load (μN - mN range) is applied to an indenter of known geometry in contact with the sample. The penetration depth (nm - μm range) is then measured as the load is applied through the use of a hard indenter tip, typically diamond.

2.3.4.1 Load-displacement curves

Nanoindentation load-displacement curves (often known as P - h or P - δ curves) are the materials response reflected in the continuous measurement of the depth of penetration while the load is increasing from zero to the maximum load (loading curve) and then decreasing from maximum load to zero (unloading curve). According to Page and Hainsworth, the mechanical response of the sample material impressed by a harder indenter during the indentation cycle provides a "micromechanical fingerprint" of the material (Page and Hainsworth 1993). The obtained fingerprint has two portions; the loading portion of the curve which provides information on the materials response to strain, such as elastic, plastic and in some case phase transformation deformation and the unloading portion of the curve, which represents the elastic recovery of the material while the applied load is being removed. A material's response to the applied load in this initial stage, of loading is elastic and in this stage if the applied load is removed the deformation will be reversible and non-permanent. Eventually, when the applied load is large enough and passes the initial

stage, a finite numbers of atomic bonds are broken by the movement of dislocations and some atoms will form bonds with new neighbours. If bond breaking occurs for a large number of atoms and they move relative to each other, they cannot return to their original position even if the stress is removed, therefore the strain is permanent and it is called plastic deformation (Jones 2001, Callister Jr and Rethwisch 2012). During the nanoindentation test, depending on a material's response to strain, the transition between elastic and plastic deformation can be different and can occur at various loads for different materials. When the indentation reaches the maximum applied load and plastic deformation has already taken place then during the load removal, the elastic recovery of the sample forms the unloading portion of the curve.

2.3.4.2 Oliver and Pharr analysis

Although there are many analytical techniques (Doerner and Nix 1986, Oliver and Pharr 1992, Hainsworth et al. 1996, Cheng and Cheng 2000, Bull 2002, Cheng and Cheng 2004) to determine the load-displacement data from nanoindentation; the most popular one was first suggested by Oliver and Pharr (Oliver and Pharr 1992). According to this procedure, the hardness and Young's modulus can be determined from the indentation curve during one cycle of loading and unloading (Oliver and Pharr 2004).

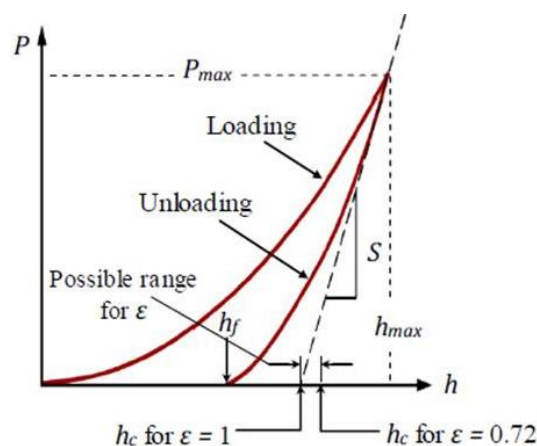


Figure 2.19 Schematic representation of load-displacement curve in Oliver-Pharr method (Oliver and Pharr 1992).

The accuracy of these measurements (hardness and modulus) is extremely dependent on the measurement of four important quantities which can all be determined from the load-displacement curve; the maximum load (P_{max}), the displacement at peak load (h_{max}), the initial elastic unloading stiffness (also known as contact stiffness, S) and most importantly the final displacement after complete unloading (h_f) (Oliver and Pharr 2004). A typical load-displacement curve for an indentation experiment is shown in Fig. 2.19.

To extract the mechanical properties from symmetrical indenters, Oliver and Pharr expanded on the method of Doerner and Nix (Doerner and Nix 1986) which is only valid for the flat punch approximation based on the fact that the initial part of the unloading curve is almost linear (Bhushan and Li 2003). In general, both methods are based on the relationship developed by Sneddon (Sneddon 1965). In the Sneddon relationship, the indentation contact stiffness was derived as follows (Oliver and Pharr 1992):

$$S = \frac{2}{\sqrt{\pi}} E_r \sqrt{A_c} \quad (2.2)$$

In this equation, A_c is the contact area and E_r is the reduced modulus. Later Pharr, Oliver and Brotzen (Pharr et al. 1992) proved that the equation can be applied to wide range of tips with different shapes. Ultimately, Oliver and Pharr determined that the unloading curves are better described by a power law relation (Oliver and Pharr 1992, Oliver and Pharr 2004).

$$P = \alpha (h - h_f)^{m_i} \quad (2.3)$$

In equation (2.2) α and m_i is power-law fitting parameters and the values are determined from experimental data. The power law exponent m varies in the range of 1.2 to 1.6 and it is related to the geometry of the indenter (Bolshakov et al. 1994, (VanLandingham 2003, Oliver and Pharr 2004). The initial slope of the tangent line to the unloading curve (the stiffness of the elastic contact) is expressed by evaluating the derivative at the peak load and peak depth of equation (2.2):

$$S = \left(\frac{dP}{dh} \right)_{h=h_{max}} = \alpha m (h_{max} - h_f)^{m-1} \quad (2.4)$$

By assuming the displacement around the indentation tends to sink-in as shown in Fig. 2.19 or that pile-up is negligible and that it does not affect the contact area (A_c), Equation (2.3) can be used to calculate the contact depth (h_c) under the maximum load. For this assumption $h_c = h_{\max} - h_s$ and h_s is given by:

$$h_s = \varepsilon \frac{P_{\max}}{S} \quad (2.5)$$

then h_c can be considered by:

$$h_c = h_{\max} - \varepsilon \frac{P_{\max}}{S} \quad (2.6)$$

In equation (2.5) $\varepsilon = 0.72, 0.75$ and 1 for conical, paraboloid of revolution and flat-ended cylindrical punch geometry respectively (VanLandingham 2003).

For an ideal indenter that does not itself deform significantly, a function, $f(d)$, relating the projected contact area, A_c , to the penetration depth, h_c , is given by:

$$A_c = f(h_c) = \pi h_c^2 \tan^2 \alpha \quad (2.7)$$

The term is the half angle of the indenter and for a Vickers or Berkovich indenter the equivalent cone angle is $70.296^\circ \approx 70.3^\circ$, therefore the corresponding projected area is simplified to $A_c = 24.5 (h_c)^2$.

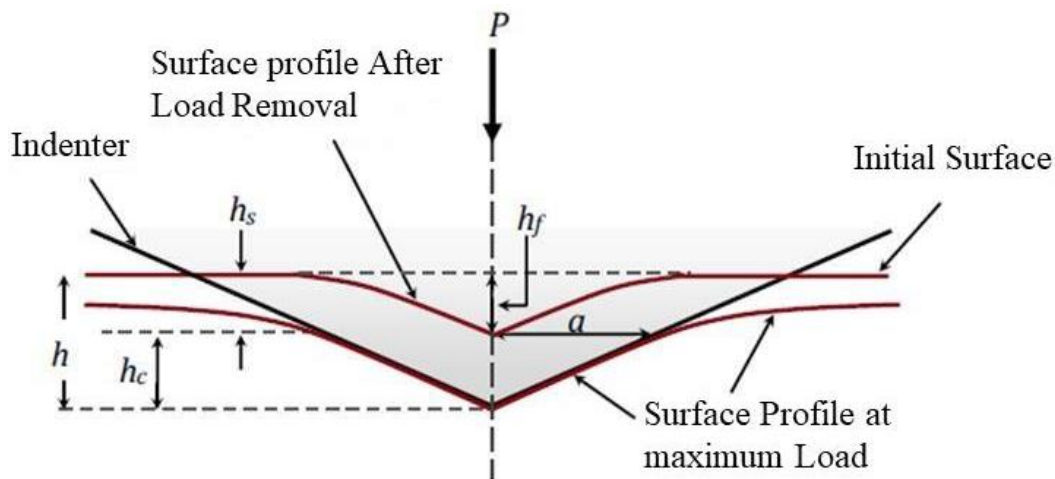


Figure 2.20 A schematic of the cross-section through an indentation with various dimensions (Oliver and Pharr 1992).

Consequently, based on the standard hardness definition and using the load-displacement curve's data, once the supported load and contact area are determined, hardness can be found as below:

$$H = \frac{P_{\max}}{A_c} \quad (2.8)$$

P_{\max} is the maximum indentation force and A_c is the contact area at that force. This is essentially an empirical formula and the hardness value will depend on properties such as the yield strength and work hardening parameters.

Effects of non-rigid indents on the load-displacement behavior can be considered by defining a reduced modulus, E_r also known as the contact modulus, which is given by:

$$\frac{1}{E_r} = \frac{1-\nu_s^2}{E_s} + \frac{1-\nu_i^2}{E_i} \quad (2.9)$$

The terms E_s and ν_s are the Young's modulus and Poisson's ratio of the sample, and E_i and ν_i are the Young's modulus and the Poisson's ratio for the indenter (1140 GPa and 0.07 for diamond) respectively. The reduced modulus, E_r , accounts for the fact that the measured displacement includes contributions from both the sample and the indenter (Oliver and Pharr 1992, Tsui et al. 1996).

By rearranging the equation (2.2), the elastic modulus of the specimen can be obtained as below:

$$E_r = \frac{1}{\beta\gamma} \frac{\sqrt{\pi}}{2} \frac{S}{\sqrt{A_c}} \quad (2.10)$$

The geometrical factor β is a non-dimensional correction factor which has been introduced to the original stiffness equation (King 1987). The correction factor, γ , was introduced by Hay and colleagues by applying a simple modification to the ideal Sneddon solution based on finite element analysis as well as analytical analysis as below (Hay et al. 1999). The γ factor accounts for the radial deformation, which was not included in the Sneddon flat punch approximation.

$$\gamma = \pi \frac{\frac{\pi}{4} + 0.155 \cot \phi \frac{(1-2\nu)}{4(1-\nu)}}{\left(\frac{\pi}{2} - 0.831 \cot \phi \frac{(1-2\nu)}{4(1-\nu)} \right)^2} \quad (2.11)$$



Figure 2.21 Nanoindenter (ASMEC Universal nanomechanical Tester (ZHN)). (Imagesource:<https://www.zwick.com/en/hardness-testers-for-instrumented-indentation-tests/zhn-nanoindenter>).

In this equation for the Berkovich indenter, is equal to 70.32° which is the equivalent cone angle of the indenter tip and ν is the Poisson ratio of the indented material. When using a Berkovich indenter, if the γ correction factor is assumed to be 1, the elastic modulus of a material with a Poisson ratio of 0.25 is overestimated by about 8%. In this thesis work, the nanoindentation studies performed on intermetallic and near equiatomic NiTi thin films using ASMEC Universal Nanomechanical Tester (ZHN) at Avansa Technology & Services, Kanpur, India as shown in Fig. 2.21.

2.3.5 X-ray photoelectron spectroscopy (XPS)

Photoelectron Spectroscopy (PES) is based on the photoelectric effect (Hertz 1887, Hallwachs 1889, Einstein 1905, Siegbahn et al. 1970) in which electrons are emitted through electromagnetic radiation. In X-ray Photoelectron Spectroscopy (XPS), as the name states, X-rays are causing the emission of photoelectrons (PE). Compared to Ultraviolet Photoelectron Spectroscopy (UPS) where the energy of the radiation is only a few tens of eV, the energy of X-rays is in the order of a few thousand eV. Therefore UPS is only able to excite electrons from the outer valence band, while XPS excites electrons from the outer and inner core shells of the molecule. XPS and UPS are both surface sensitive non-destructive methods to probe the first layers. The

information depth of XPS is roughly in the order of up to 10 nm (depending on the material), but is most sensitive in the first 4 nm (Briggs and Seah 2003).

Auger lines are also recorded during XPS measurements. Auger electrons are emitted by a three electron process. First a core hole is created (e.g. in the *K*-shell) and this hole is filled by a second electron from an outer shell (e.g. *L1*). During this relaxation process energy is released which can be used to emit an electron (e.g. *L2,3*) with a lower binding energy (E_B) than the second electron. Unfortunately the N KLL and Ti LMM Auger lines overlap and an evaluation is very difficult. Also XPS provides a better quantification of the peak areas than AES.

2.3.5.1 Basic principles of the photoemission process

In XPS the photoelectric effect is used to investigate the binding energy (E_B) of the electrons in the sample. The molecules in a sample are exposed to X-rays with a definite energy, $h\nu$. If the energy is high enough, electrons can be emitted from the sample. Not only are the number of emitted electrons detected, but also their kinetic energy E_{kin} . E_B can be calculated in a first approximation as the difference between the photon energy $h\nu$, E and ϕ :

$$E_B = h\nu - E_{kin} - \phi \quad (2.12)$$

where ϕ is the work function, i.e. a potential including surface potential of the sample and a correction factor to the actual referencing point for E_B (Briggs and Seah 2003). The latter is not only characteristic for each element but also for its electronic surrounding. Therefore this method can be used to investigate quantitatively the elemental composition and its chemical environment. While it is easy to detect qualitatively even traces of elements below 1%, it is quite difficult to determine a quantitative concentration rate within the order of $\pm 1\%$. Calibration measurements done with Rutherford Back Scattering (RBS, have to be performed to receive such high accuracy. The XPS device, used in this work, consists of a UHV chamber that contains an x-ray source, e.g. an aluminum K_α X-ray source (1489.6 eV), an electron analyzer and a sample holder.

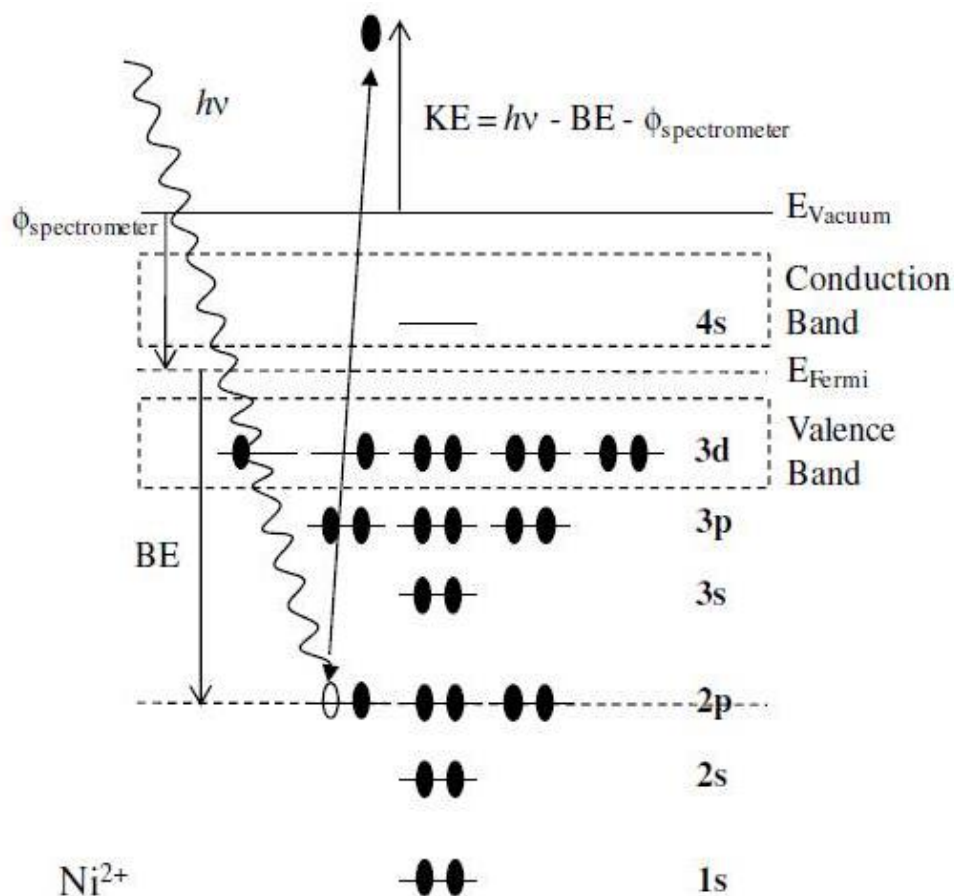


Figure 2.22 An electron energy diagram for a Ni^{2+} cation showing the absorption of a photon and resultant expulsion of a 2p level photoelectron (Payne, B.P. (2011). “X-ray Photoelectron Spectroscopy Studies on the Oxidation Processes of Nickel, Chromium and their Alloys” Ph.D. Dissertation, The University of Western Ontario).

In general, X-rays having energies in the 1-2 keV range will penetrate several hundred nm into a surface ionizing atoms to that depth. In order for the resultant photoelectrons to be detected, they first must escape from the surface without interacting with overlaying atoms; which may lead to loss of KE (inelastic scattering). The probability that a photoelectron will reach the surface without losing any of its KE can be approximated using the Beer-Lambert Law:

$$I_d = I_0 e^{-d/\lambda} \quad (2.13)$$

where I_d is the photoelectron intensity originating from atoms at depth d , I_0 is the signal emanating from the surface atoms and λ is the electron inelastic mean free path

(IMFP). The IMFP represents the average distance a photoelectron can travel before undergoing inelastic scattering and is dependent on both the material properties (i.e. density) and electron KE. If a Gaussian probability distribution is assumed, then 95% of the photoelectrons detected would have been produced within a depth of 3λ . Typical IMFPs for the metal 2p core photoelectrons for transition metals and their oxides are calculated to be on the order of 1.1 – 1.8 nm (using Al K_{α}) (Tanuma et al. 1988, Powell and Jablonski 2005) resulting in an information depth between 3.3-5.4 nm for these systems. Photoelectrons ejected from a sample surface are focused towards the entrance slit of a combined concentric hemispherical (CHA) and spherical mirror (SMA) energy analyzer. Prior to entering the analyzer the energies of the photoelectrons are retarded to a fixed pass energy (E_p). To monitor the photoelectron counts as a function of BE (spectrum mode) the CHA is used. Once inside the CHA the photoelectrons travel between two curved plates (hemispheres) having focusing potentials $-V_1$ and $-V_2$ (Fig. 2.23(b)). The instrument transmission function is defined as the fraction of the total number of photoelectrons collected at the sample surface that pass through the CHA into the detector. The transmission function is dependent on the CHA slit width, CHA radius and the initial KE of the photoelectrons. The absolute resolution (ΔE) of the instrument is defined by the full width at half maximum (FWHM) of the resultant photoelectron peaks. The absolute resolution of the instrument increases with decreasing pass energy. Any increase in spectral resolution results in a loss of photoelectron signal due to a higher dispersion of the electrons around the exit slit.

To collect chemical state images on the surface of the sample the SMA is employed. Similar to the CHA portion of the analyzer the SMA has two hemispherical electrodes. The main differences between the two analyzers are that an inner mesh electrode and an additional energy selecting slit are employed in the SMA design.

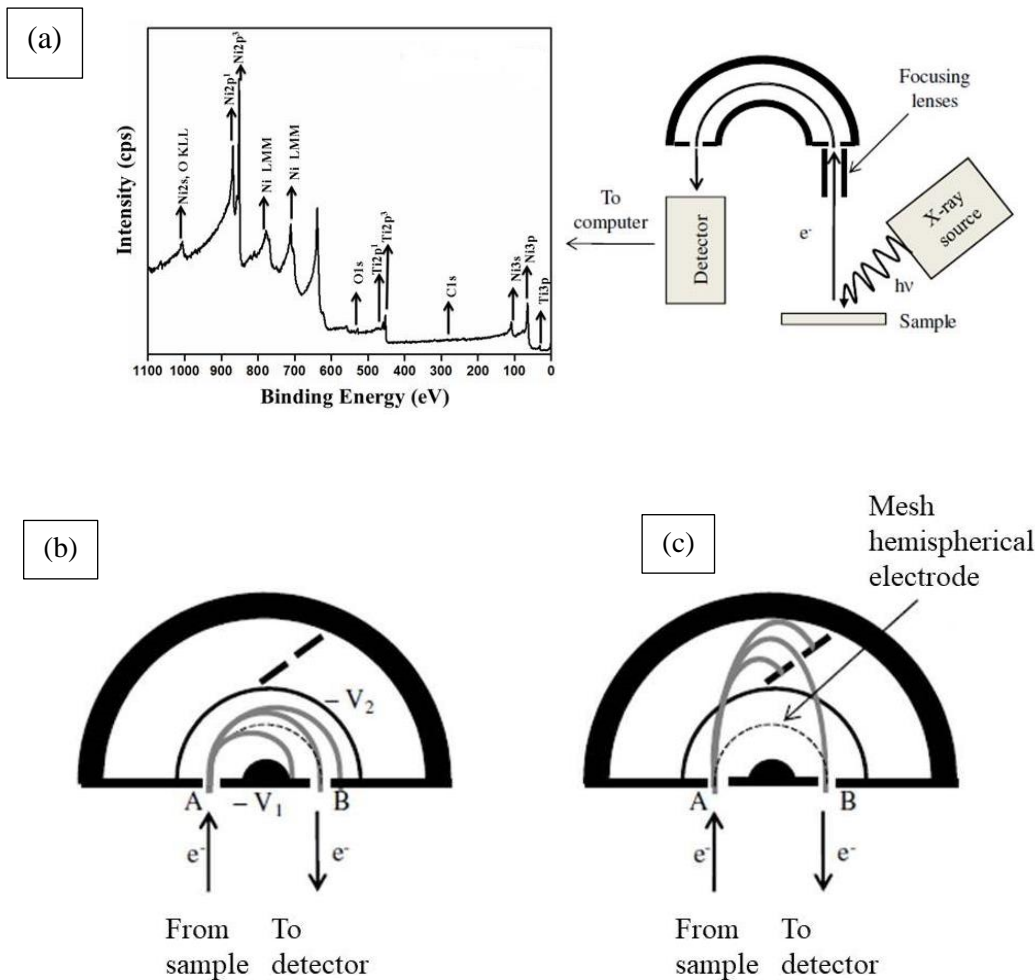


Figure 2.23 (a) Simplified schematic following a photoelectron (e^-) through a PHI 5000 VersaProbe II spectrometer. (b) The expanded view of the energy analyzer setup in spectrum mode employing the CHA. Under these conditions the photoelectrons enter the energy analyzer at point A and travel between two negatively charged plates. The grey lines represent possible pathways these electrons may travel through the energy analyzer. Only the photoelectrons with the selected pass energies will exit the analyzer at point B and enter the detector. (c) The expanded view of the energy analyzer setup in imaging mode employing the SMA. The presence of the mesh hemispherical electrode and additional slit allows for specific photoelectron BE's to be selected allowing for high-resolution images to be collected (Payne, B.P. (2011). "X-ray Photoelectron Spectroscopy Studies on the Oxidation Processes of Nickel, Chromium and their Alloys" Ph.D. Dissertation, The University of Western Ontario).

These two advancements allow chemical state images to be collected over a range of photoelectron BE's. The image datasets can then be combined using analytical software (Fairley 2009) and converted into spectral datasets producing XPS spectra at each image pixel (Artyushkova and Fulghum 2004, Smith et al. 2006) Once the electrons exit the CHA they enter a channel plate detector which consists of several semiconducting glass tubes connected in series known as channel electron multipliers (CEMs). Electrons entering the CEMs collide with the walls of the tubes resulting in a cascade effect as secondary electrons are produced. The cascade effect results in an increase in the electron signal by a factor of $> 10^4$.

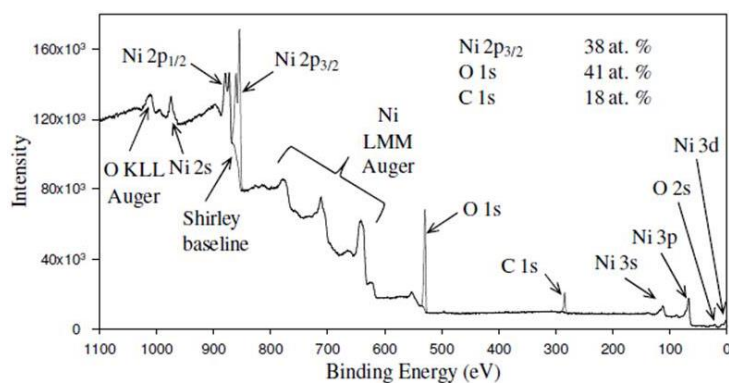
By convention XPS spectra are plotted as a function of photoelectron intensity vs. BE. Survey spectra, sometimes termed wide or broad scans, are collected using a high pass energy (> 120 eV), a high energy step (0.7 eV) and a large BE window (> 1000 eV). These spectra have low resolution, however, the large BE range allows for the photoelectron peaks for all elements present to be analyzed.

From the XPS survey spectrum the elemental concentration for a surface containing two or more elements (except for H and He) can be determined using the following formula:

$$X_A = \frac{\frac{I_A}{S_A}}{\sum_n \frac{I_n}{S_n}} \quad (2.14)$$

where X_A , I_A and S_A represent the atomic concentration (in at%), the peak area and the relative sensitivity factor (RSF) for element A, in a surface having n elements. Any contributions from the energy loss background to the photoelectron peak intensities are removed using a subtraction algorithm. In Fig. 2.24(a) all spectral background intensity was removed using a Shirley baseline. The RSF values correct for differences in peak intensities resulting from the probability a specific photoelectron transition will occur (cross-section), element IMFP, instrument transmission function and detector efficiency.

(a)



(b)

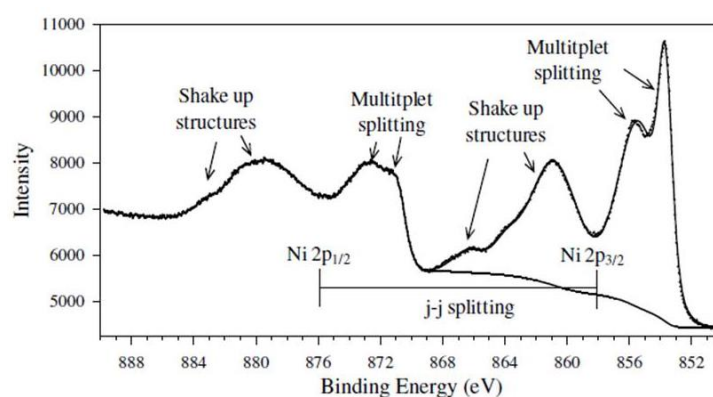


Figure 2.24 (a) The survey spectrum collected from a polycrystalline NiO powder sample containing a small C impurity. The elemental concentrations in at.% for the Ni, O and C species are also presented. (b) The high resolution Ni 2p spectrum taken for the same NiO sample. The electronic structural features arising from j-j coupling (Ni 2p_{3/2}, Ni 2p_{1/2}), multiplet splitting and shake up interactions are clearly visible (Payne, B.P. (2011). “X-ray Photoelectron Spectroscopy Studies on the Oxidation Processes of Nickel, Chromium and their Alloys” Ph.D. Dissertation, The University of Western Ontario).

The oxidation state and local bonding environments of atoms within a surface are monitored using high-resolution spectra. These scans are typically collected at a low pass energy (10 – 20 eV), a low energy step (0.1 – 0.05 eV) and BE windows ranging from 20 – 40 eV.

At the atomic level, absorption of a photon results in the expulsion of a photoelectron producing an atom in an excited state. The observed BE of this photoelectron is

defined as the difference in energy between the photoionized atom (final state) and the unexcited atom (initial state). The chemical shift refers to the small changes in photoelectron BE of an atom based on its local bonding environment and/or chemical state. These BE differences can be explained qualitatively using the charged sphere model. In this model the individual atoms of a surface are considered to be hard spheres having a valence charge q at a fixed radius of r . Inside the sphere the charge distribution is considered to be uniform and as a result any change in the valence charge density will shift the BE of all core electrons by:

$$\Delta BE = q/r \quad (2.15)$$

The cross-section (peak shape and intensity) for each core energy level photoelectron peak is defined by the principal quantum number n , the angular momentum quantum number l , and the electron spin angular momentum quantum number s . Following photoionization from an orbital where $l = 0$ (i.e. 1s shell) a singlet photoelectron peak is observed as only one final state is possible. For orbitals where $l > 0$ (i.e. 2p shells) the orbital angular momentum and spin angular momentum of the remaining electron can couple either in parallel (lower energy) or anti-parallel (higher energy), resulting in two possible final states. This gives rise to a doublet structure defined by the following relationship:

$$j = (l \pm s) \quad (2.16)$$

where j is the total angular momentum quantum number. This phenomenon is referred to as spin-orbit or j - j coupling (Fig. 2.24(b)). In the case of the 2p spectral line j values of $3/2$ ($2p_{3/2}$) and $1/2$ ($2p_{1/2}$) are obtained. The separation between the doublet ($2p_{3/2}$ & $2p_{1/2}$) peaks increases with atomic number z and is scaled by a factor of $1/r^3$, with r representing the radius of the orbital from which the photoelectron has been ionized. The relative electron populations of the respective doublet peaks are defined by $2j + 1$ resulting in a $2p_{3/2}:2p_{1/2}$ ratio of 2:1.

The 2p spectra for transition metal cationic species having unpaired d electrons are further complicated by additional fine structures resulting from multiplet splitting (Fig. 2.24(b)). These structures arise from the parallel or anti-parallel coupling of the spin angular momentum of an unpaired core electron with the spin angular momentum of unpaired 3d valence electrons. Exchange interactions between electrons with parallel spins are lower in energy than the interactions between electrons with

anti-parallel spins, producing a doublet structure. Additional contributions from atomic relaxation and ligand interactions also contribute to the multiplet structures observed. Other high BE spectral features common to many transition metals are shake up and/or shake off peaks (Fig. 2.24(b)). Shake up peaks arise from simultaneous loss of a photoelectron and excitation of a valence electron to a higher unoccupied bound state. Shake off are similar in origin only instead of the valence electron being excited to an unoccupied energy level it is lost to the continuum, resulting in a doubly ionized final state. The observed BE of the latter peaks are much higher than those for the former. In the mid 1970s Gupta and Sen (GS) used a Hartree-Fock free ion method to model the 2p core line final states for many of the transition metals (Gupta and Sen 1974, Gupta and Sen 1975). Their models produced a good approximation of the observed line shapes for most transition metals.

The core line shape of the photoelectron peaks collected for pure metal surfaces tend to have an asymmetric character that tail off to higher BE. The degree of asymmetry of the core line peak for any metal is related to its density of states at the Fermi level. In metals the valence and conduction bands overlap and as a result electrons are easily promoted above the Fermi level to any number of unoccupied energy levels. Moving valence electron density away from the nucleus effectively strengthens the “hold” the nucleus has on the core electrons, resulting in the ejection of photoelectrons having slightly less KE than the ground state atom. Some metal spectra also exhibit plasmon loss features, which arise from photoelectrons that have excited oscillations in valence electrons while passing through the surface. These collective oscillations require specific amounts of energy leading to set KE losses and the appearance of characteristic peaks at higher BE. XPS can also be employed to model the thickness of oxide films provided that the thickness of the oxide is less than the maximum photoelectron escape depth.

The thickness of an oxide overlayers can also be calculated using the intensities of the metal and oxide phases derived from fitted high-resolution XPS spectra. The overlayer equation shown here was first derived by Carlson (Carlson 1982) and later rearranged in terms of oxide thickness d by Strohmeier (Strohmeier 1990):

$$d = \lambda \sin \theta \left[\frac{N_m \lambda_m I_o}{N_o \lambda_o I_m} + 1 \right] \quad (2.17)$$

Where m and o represent the metal and oxide phases, respectively, λ is the IMFP, N stands for the volume density of metal atoms in either the metal or the oxide phase, I is the peak area for either the metal or the oxide, and θ is the take off angle of the electrons.

A third method for measuring oxide thickness was developed by Tougaard and is commercially available in a software package called QUASESTM (Tougaard 2000, Tougaard 1998). The basis for the Tougaard algorithms is the concept of inelastic scattering. When a photoelectron travels through a surface it may undergo one or more energy loss events. The probability that an electron will experience one or more energy loss interactions increases sharply with depth. From equation 2.12 a loss in KE due to scattering will result in an increase in the observed BE and leads to the formation of the extrinsic background located on the higher BE side of a photoelectron peak. The Tougaard algorithms model the photoelectron energy loss (extrinsic) backgrounds using material dependent IMFPs and energy loss cross-sections. The IMFP was previously described as the average distance a photoelectron can travel before undergoing an inelastic collision, while the energy loss cross-section represents the average amount of energy a photoelectron will lose per scattering event (20-30 eV). Based on the typical IMFP lengths QUASESTM has a maximum operational depth between 5 to 10 nm, depending on the surface being analyzed.

The QUASESTM software package is divided into two analytical programs 'Analyze' and 'Generate'. The 'Analyze' program calculates overlayer thicknesses by modeling the extrinsic background associated with any photoelectron peak by determining the depth from which photoelectrons originated. The 'Generate' program determines the surface structure of the oxide by modeling the distribution of atoms in the experimental spectrum using a combination of reference spectra whose extrinsic backgrounds have been modified for the depth from which they are situated in the surface. The advantage to the 'Generate' programs is that it allows for the near surface morphology to be modeled using five different profiles.

In this thesis work, All XPS analysis was performed at ACMS, Surface characterization lab, located at the Indian Institute of Technology Kanpur, India, using a PHI 5000 VersaProbe II, FEI Inc. as shown in Fig. 2.25. The PHI 5000 VersaProbe II spectrometer is equipped with a monochromatic Al K $_{\alpha}$ X-ray source having

characteristic excitation energy of 1486.6 eV and a line width between 0.3-0.4 eV. The base pressures in the analytical chamber are typically near 2×10^{-6} Pa prior to the introduction of the sample.



Figure 2.25 X-ray Photoelectron Spectrometer (Model: PHI 5000 Versaprobe II, FEI Inc.) (Image source: <https://www.iitk.ac.in/acms/spectroscopylab.html>).

CHAPTER 3

THE EFFECT OF ANNEALING TEMPERATURE ON THE STRUCTURAL, MORPHOLOGICAL, MECHANICAL AND SURFACE PROPERTIES OF INTERMETALLIC NITI ALLOY THIN FILMS

This chapter begins with a discussion of growth and characterization of DC magnetron sputtered intermetallic NiTi alloy thin films. Also, it contains the effect of annealing temperature on the structural, morphological, mechanical and surface properties of intermetallic NiTi thin films.

3.1 INTRODUCTION

NiTi thin films having shape memory effect (SME) have been extensively studied for MEMS (micro-electro-mechanical system) applications such as micro actuators due to their large recovery forces and good mechanical properties (Fu et al. 2004, Pan and Cho 2007, Sanjabi et al. 2009, Lehnert et al. 2000). Further, these shape memory alloys also possess several desirable properties like high power to weight ratio (force to volume), high damping capacity, good chemical resistance and biocompatibility (Zainal et al. 2015, Sonoda et al. 2004, Fu et al. 2005) It is well reported that shape memory effect, super elasticity and phase transformation temperatures of sputter deposited NiTi thin films are quite sensitive to the film composition, contamination, annealing temperature, aging time, thermo-mechanical treatment and deposition parameters (Kotnur and Janssen 2012). Sputtering is one of the popular methods used to deposit NiTi thin films with desired composition and high deposition rates (Sato et al. 1998). Co-sputtering is one of the best feasible method to prepare the NiTi thin films by varying the individual target powers (Ohta et al. 2000, Sanjabi and Barber 2010, Kumar et al. 2009). During the sputtering process, the processing variables such

as argon gas pressure, base pressure, substrate to target distance and substrate temperature were kept constant. The sputter deposited NiTi thin film exhibits amorphous nature at room temperature. To crystallize the NiTi thin films, these have to be vacuum annealed at appropriate crystallization temperature. This treatment promotes both shape memory effect and superelasticity.

Grain nucleation and growth are the direct consequence of crystallization process in thin films at elevated temperatures (Lee and Ramirez 2004, Wang and Vlassak 2006). As a result, shape memory effect, micro-structure and physical properties of NiTi thin films will be greatly influenced by the post-annealing temperature. The influence of post annealing conditions on film micro-structure, surface morphology and mechanical properties has been reported in literature (Geetha Priyadarshini et al. 2011, Kumar et al. 2006), but reports on the evolution of surface characteristics of sputtered Ni-60 at. pct and Ti-40 at. pct intermetallic NiTi thin films are not adequate. In the present work, the main objective is to study the impact of annealing temperature on structural, morphological, mechanical and surface properties of intermetallic NiTi thin films. This work mainly analyzes the influence of sputter deposition and post annealing conditions on intermetallic NiTi thin films when subjected to same annealing time but different annealing temperatures.

3.2 EXPERIMENTAL

3.2.1 Growth of intermetallic NiTi alloy thin films

Intermetallic NiTi thin films were grown on silicon (1 0 0) substrates of dimension 10 mm x 10 mm using DC magnetron sputtering system (incidence angle $\sim 45^\circ$), which is a two gun sputter down set up. The two separate circular targets Ni and Ti of target size (diameter x thickness): 50.8 mm x 3.18 mm with a purity of 99.99% were used to prepare the intermetallic NiTi thin films. Diffusion and rotary pump were used to evacuate the sputter chamber to a base pressure, lower than 5×10^{-6} mbar. Pirani-Penning gauge combination was used to measure pressure in the vacuum chamber. The Ar gas pressure with purity 99.99% was fed into the sputter chamber during the sputtering process using an MFC (Mass Flow Controller - AALBORG GFC 17) with a flow rate of 30 sccm. To remove the organic contaminants, the silicon substrates

were primarily cleaned sequentially in an ultrasonic bath with double distilled water and then washed with boiled acetone and later cleaned with 2-propanol. Before every sputter deposition process the targets were pre-sputtered for 15 minutes to remove the native surface oxide layer. The sample holder was rotated axially at 10 rpm to attain uniform film composition. The target to substrate distance in the vacuum chamber was maintained at approximately 50 mm for all depositions. As-deposited films have been vacuum annealed for 1 hour (base pressure of 5×10^{-6} mbar) at a temperature range of 350°C to 650°C and then furnace was cooled to room temperature before they were removed. The various deposition details of intermetallic NiTi thin films are shown in Table 3.1.

Table 3.1 Deposition conditions for intermetallic NiTi thin films

Substrate	Si (1 0 0)
Sputtering gas	Argon
Argon gas flow rate	30 sccm
Background pressure	5×10^{-6} mbar
Deposition pressure	0.15 mbar
Substrate-target distance	5 cm
Deposition time	60 min
Deposition temperature	Room temperature
Substrate rotation speed	10 rpm
Film thickness	300 nm
Composition (EDS, at.%)	Ti-40, Ni-60

3.2.2 Thin film characterization

The thickness of the film was measured using Surface Profilometer (Dektak 150, Arizona). The diffraction patterns were collected using a Rigaku MiniFlex-600 table top diffractometer with Cu-target ($\lambda = 1.54056 \text{ \AA}$). The X-ray tube was maintained at an accelerating voltage of 40 kV at a current of 15 mA. Energy dispersive X-ray spectroscopy (EDXA) was used to determine the elemental composition. The surface morphology was investigated using Field Emission Scanning Electron Microscope

(FESEM) using SUPRA 55, CARL ZEISS-GERMANY. Further film topography and roughness were examined using Atomic Force Microscope (AFM: Model NTMDT) under semi contact mode.

Nanoindentation tests were performed by ASMEC Universal Nanomechanical Tester (UNAT-ZHN) works as a depth sensing hardness tester in the micro range with a maximum indenter force of 2 N using UNAT-InspectorX version-3 software. Nanoindentation tests on thin films were executed with a Berkovich tip. To find the hardness and elastic modulus, load controlled indentation test was performed on each sample. During the nanoindentation test the maximum load set was at 2.5 mN and in each case the holding time was maintained for a period of 10 s. The surface characteristics of intermetallic NiTi thin films were described using X-ray photoelectron spectroscopy (Model: PHI 5000 VersaProbe II, FEI Inc.) with monochromatic Al K_{α} (1486.6 eV) X-ray source. The pressure inside the XPS vacuum chamber during analysis was maintained at 10^{-8} mbar. Survey spectra of annealed intermetallic thin films were recorded in the range of 0-1100 eV at constant pass energy of 20 eV. HRXPS (High Resolution X-ray Photoelectron Spectroscopy) were used to find the chemical state, concentrations (quantifications) and to assess for all the dominant elements present in the films surface viz. Ti (2p), Ni (2p), O (1s) and C (1s). The C (1s) peak was used to regulate the spectra during characterization for any charging effects. Gaussian peak fitting model was used on the experimental spectra of annealed thin films to achieve a better analysis of the data.

3.3 RESULTS AND DISCUSSION

3.3.1 Structural analysis

The intermetallic NiTi thin films are sensitive to substrate temperature, post-annealing temperature and annealing time (Petrovic et al. 2012). Figure 3.1(a-d) shows the X-ray diffraction measurements carried out on intermetallic NiTi thin films. In spite of similar film composition the annealed films showed crystallinity and revealed distinct film structure. It was already proposed that heat treatment should be carried out at lower temperatures for a minimum time to reduce the reaction between film and substrate to control film microstructure, mechanical properties and shape memory

effects (Kumar et al. 2009). In the present work, simple heat treatments were employed as they have the advantage of being relatively inexpensive and easily incorporated into a device manufacturing process. Heat treatments of NiTi are constrained to temperatures lower than the recrystallization temperature of 650°C. Therefore, the temperatures investigated in this study were 350, 450, 550 and 650°C. At low temperatures the diffusion rates are low, but the driving force for nucleation is high while at higher temperatures the reverse is true. Partial crystallization starts after 300°C in NiTi thin films. Pelton et al. studied that 300-500°C heat treatments result in the formation of the Ni₄Ti₃ precipitate; heat treatments at 500-600°C, however, result in the dissolution of the Ni₄Ti₃ precipitate followed by the eventual formation of the Ni₃Ti₂ and Ni₃Ti precipitates (Pelton et al. 2000). The time-temperature-transformation (TTT) diagram constructed by Nishida et al. had established that at the temperatures of 500-800°C the precipitation sequence of Ni₄Ti₃ → Ni₃Ti₂ → Ni₃Ti occurs (Nishida et al. 1986). Intermetallic NiTi thin films exhibited several diffraction peaks indicating the polycrystalline nature. From diffraction peaks we have concluded that Ni₃Ti was the major phase present in the grown films. A broad diffraction peak observed at $2\theta = 43.54^\circ$ was indexed for (0 0 4) reflections of the Ni₃Ti phase of intermetallic NiTi thin films (Geetha Priyadarshini et al. 2011). In addition to the major Ni₃Ti phase, XRD pattern exhibited existence of diffraction peaks located at 39.22°, 42.52°, 47.48° and 48.37° positions are assigned to (0 2 0), (4 1 0), (2 0 2) and (4 4 2) corresponding to Ni-rich precipitates which are identified as B19' (Martensite phase), Ni₄Ti₃ and NiTi₂. The Ni-rich precipitates evolution occurs due to high annealing temperatures, or high temperature holding time (Martins et al. 2006). During the crystallization of NiTi films non-equilibrium precipitation reactions occur, leading to the martensite phase, which is present in the films. During co-sputtering process of NiTi thin films various metallic phases such as Ni₃Ti, Ni₂Ti, and Ni₄Ti₃ are found to coexist due to incomplete alloying. There are two main properties extracted from peak width analysis viz. crystallite size and lattice strain. According to Williamson and Hall, the diffraction line broadening is due to crystallite size and strain contribution (Prabhu et al. 2014, Bindu and Thomas 2014, Monshi et al. 2012). The average nanocrystalline size was calculated using the Debye-scherrer's formula:

$$D = \frac{K\lambda}{\beta \cos\theta} \quad (3.1)$$

Where D = crystalline size, K = shape factor (0.9), β = integral half width, θ = Bragg angle, and λ = wavelength of $\text{CuK}\alpha$ radiation (1.5406 Å).

The strain induced broadening in film due to crystal imperfection and distortion was calculated using the formula:

$$\varepsilon = \frac{\beta}{4 \tan \theta} \quad (3.2)$$

Where ε = lattice strain, the peak width from crystallite size varies as $\frac{1}{\cos\theta}$ and strain varies as $\tan \theta$. The structural parameters of intermetallic NiTi thin films are shown in Table 3.2.

Table 3.2

Table 3.2 Structural parameters of intermetallic NiTi thin films.

Annealing temperature (°C)	Average crystallize size (nm)	Lattice strain (ε)
350	14.93	0.0064
450	18.65	0.0052
550	37.26	0.0026
650	2.45	0.0390

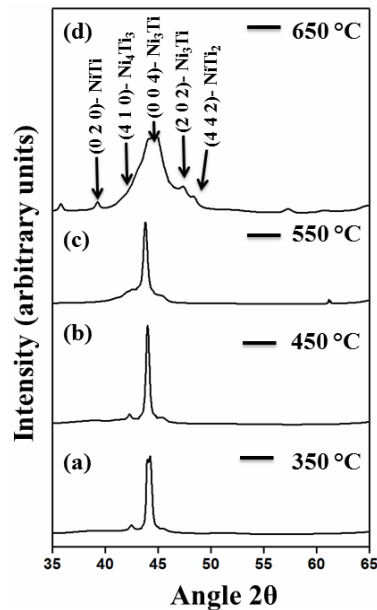


Figure 3.1 XRD patterns of intermetallic NiTi thin films annealed at (a) 350°C (b) 450°C (c) 550°C and (d) 650°C.

3.3.2 Surface morphology

The kinetic behavior of the deposited thin films varies drastically with respect to the annealing temperatures. The analysis of the thin films clearly showed that crystallite nucleation and growth were greatly influenced by the annealing temperature. Figure 3.2(a-d) shows the FESEM planar view of the intermetallic NiTi thin films. Fig. 3.2(a) (annealed at 350°C) shows crack free solid surface and there is no clear grain formation due to the non-initiation nature of atomic migration. Figure 3.2(b) indicates nucleation stage when several nuclei have just formed due to the initiation of atomic migration forming grains at 450°C. Along the grain boundaries a small percentage of porosity is found and the closed pores present under the film surface opened due to the swelling effect (Behera and Aich 2015). These types of pores are not interconnected. This change in the microstructure is due to the competing nature of the nucleation and the active growth rate of grains.

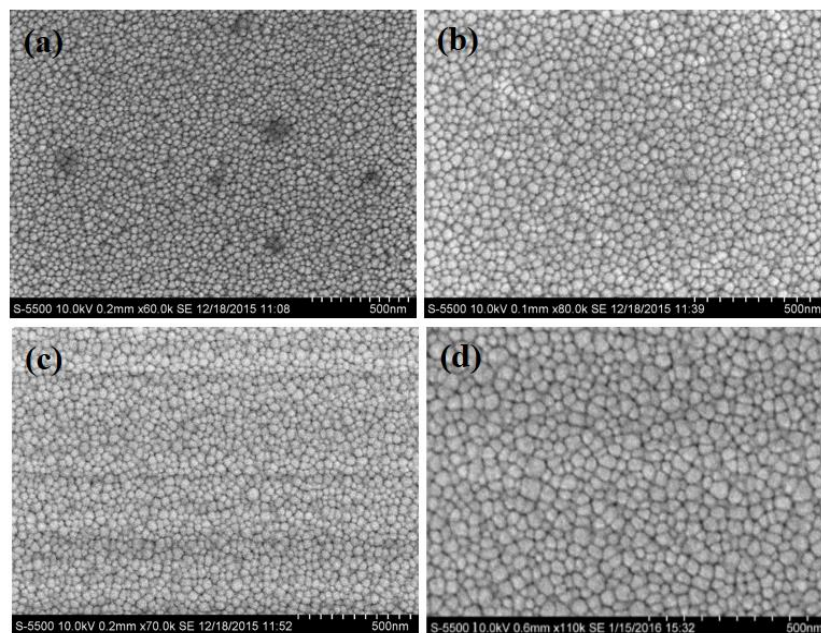


Figure 3.2 FESEM micrographs of intermetallic NiTi thin films annealed at (a) 350°C (b) 450°C (c) 550°C and (d) 650°C.

In general, the characteristics of grain growth are controlled by the amount of chemical, topographical disorder and the diffusion of atomic species (Huang and

Ramirez 2009). As the annealing temperature was changed further from 450°C to 550°C diffusion rate increased and the grains continued to grow rapidly due to the improved crystallization (Birnbaum et al. 2009). At higher temperatures (at 650°C) the crystallization is completed and the grains grow no further. Due to the crystallization a few grains have raised more than the surrounding grains leading to larger grain size confirming the decrease in the density of grain boundaries. As compared to the bulk materials the NiTi thin films exhibit porous nature with voids (voids link together to form a crack that eventually leads to failure in the neck region) (Geetha Priyadarshini et al. 2011).

3.3.3 Surface topography analysis

Figure 3.3(a-d) show three dimensional representations of intermetallic NiTi thin films accounted from atomic force microscopy (AFM) on the scan area of 1.5 μm x 1.5 μm. It is clear that the surface morphology show a slightly different morphology even though their elemental composition is the same. Fig. 3.3(a) shows the wavy topography formed by ribbon (undulating ridges) type structures bounded by shallow and wide depressions. At a lower annealing temperature, the deposited films are not having obvious crystallization. This surface morphology indicates featureless grain growth (unclear) indicating no clear grain formation.

Table 3.3 Various roughness parameters of the intermetallic NiTi thin films with same scan area.

Annealing temperature (°C)	Scan size (μm) ²	RMS roughness (nm)	Ra roughness (nm)	P-V roughness (nm)
			AFM	
350	1.5 x 1.5	3.08±0.06	2.40±0.13	20.04±0.06
450	1.5 x 1.5	3.20±0.09	2.60±0.09	22.48±0.22
550	1.5 x 1.5	3.79±0.31	3.06±0.32	24.07±0.35
650	1.5 x 1.5	5.57±0.27	4.41±0.38	45.61±0.89

However, as the annealing temperature of the film is increased further from 450°C to 650°C (Fig. 3.3(b-d)), the amorphous state like topographies disappeared and the

grains are seen to protrude further from the film surface indicating grain growth. This feature can be understood based on theories of surface diffusion, grain coalescence, and growth rate (thin film growth process) of the films. At 450°C (Fig. 3.3(b)) the grain structure changed from unclear grain growth (amorphous state) to crystalline state and film surface showed a larger number of randomly distributed large columnar grains formed by coalescence of adjacent grains.

At 550°C the grains agglomerated together and formed a few bigger grains. This agglomeration led to the irregular grain growth, making the height variance in the grains. At 650°C (Fig. 3.3(d)) the film surface reveals a bumpy topography formed by loosely packed columnar grains (formed by interfaces and grain boundaries on interdiffusion in thin films). During the secondary grain growth some of the grains grow extremely large compared to the neighboring ones. It results in the agglomeration of the few grains (Huang and Liu 2005).

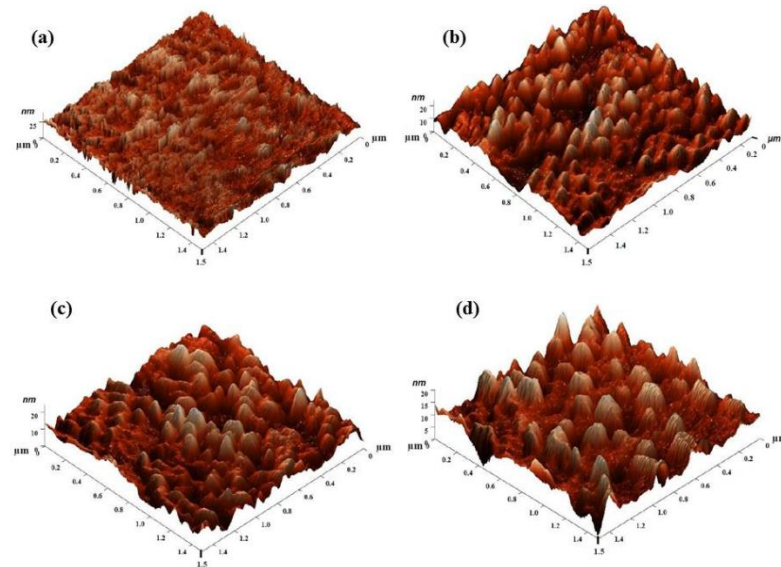


Figure 3.3 AFM (3D surface morphology) micrographs of sputter deposited intermetallic NiTi thin films vacuum annealed for 1 hour at (a) 350°C (b) 450°C (c) 550°C and (d) 650°C.

The surface morphology can be quantified by roughness parameters like RMS, Ra and P-V. Table 3.3 shows the values of surface roughness parameters obtained from AFM having scan size 1.5 μm x 1.5 μm. At the lower annealing temperature (Fig. 3.3(a))

RMS roughness of intermetallic NiTi films show 3.08 nm, this smaller surface roughness contributed by the shallower depressions exhibit the smoother film surface (featureless microstructure). As the annealing temperature was increased further, the formation of deeper channels and grains protruding from the film surface resulted in higher surface roughness values changing from 3.20 to 5.57 nm (Fig. 3.3(b-d)). The RMS roughness values were obtained by using the following equation (Choudhary et al. 2011):

$$RMS = \left[\frac{1}{N} \sum_{i=1}^N (Z_i - Z)^2 \right]^{1/2} \quad (3.3)$$

Where N is the number of surface height data in the examined area, Z_i is the height of the maximum (i^{th}) grain and Z is the average height of the all examined grains, respectively.

3.3.4 Nanoindentation

Nanoindentation is used to record the penetration depth of an indenter into the sample surface along with the applied load to measure the area of the contact and hardness of the test sample. In this study, nine indents were performed in intermetallic NiTi thin films at different regions, each spaced 4 μm apart, for each annealing condition. Each indent consisted of a 6-second loading, 10-second holding and a 6-second unloading segments. Usually, the hold periods were used to diminish the time dependent effects (creep effects) generated in the specimen. Figure 3.4(a-d) shows the load-displacement ($P-h$) curve obtained from the nanoindentation testing of the sputter deposited intermetallic thin films. To obtain the sample hardness (H) and elastic modulus (E_r) from the p-h curve the data were analyzed by the Oliver and Pharr method (Tall et al. 2007, Kan et al. 2013).

Nine nanoindentations were performed on each film at different locations with a peak load of 2.5 mN. The load displacement curves obtained for all the nine indents for each of the four samples were plotted in Fig. 3.4(a-d). The behavior of the samples was generally consistent from test to test, indicating that the samples were fairly homogeneous over the areas tested. The load displacement curves of deposited films shows overall elasto-plastic response (Kan et al. 2013). The plastic response

(unloading curve) is smooth indicating that it is purely the recovery on relaxation during indentation withdrawal. The annealing temperature has a significant amount of effect on the nanoindentation test performed on deposited films. Annealing leads to an increase in strength by grain boundaries and dislocation interactions in turn increases the average hardness and elastic moduli. This can be attributed to the combined effect of crystallization, nucleation and grain growth (Lee et al. 2006), which is also supported by XRD, FESEM and AFM (Fig. 3.1, Fig. 3.2 and Fig. 3.3). Table 3.4 shows the variation in hardness and elastic moduli values of intermetallic NiTi thin films sputter deposited at ambient temperature and vacuum annealed in the temperature range of 350°C to 650°C, respectively. At low penetration depth, due to the nucleation and propagation of dislocations which is presented in the films the hardness of the material increases. The elastic modulus and hardness are found using the equations (2.1), (2.7) and (2.8) (chapter-2). The strength of metallic films rises rapidly when the thickness of the film falls below about 0.3 μm and the Hall-Petch relation, generally obeyed by thin films, is also dependent on film thickness (Miyazaki et al. 1990). Both Ni and Ti are very sensitive to residual oxygen at higher temperatures even though the films were annealed in high vacuum.

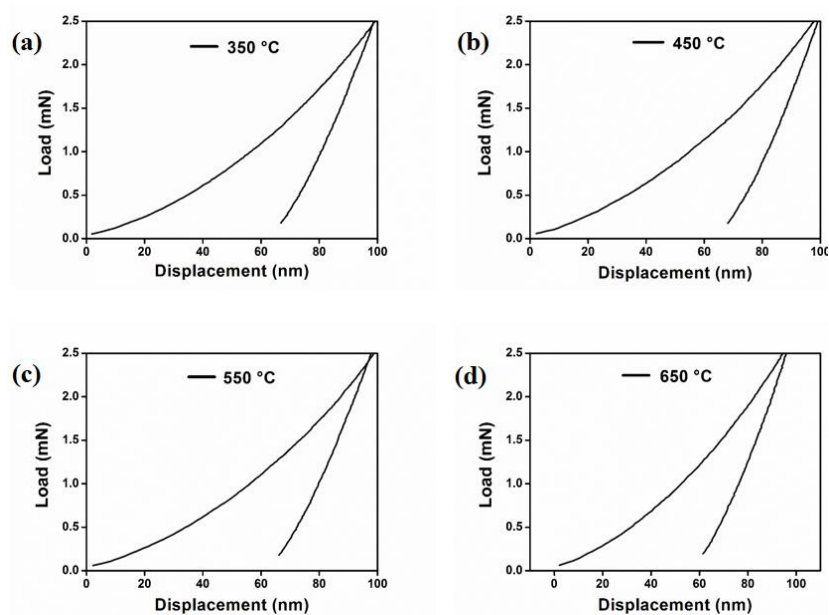


Figure 3.4 Load-displacement curves from nanoindentation experiments performed on the intermetallic NiTi thin films deposited at room temperature and vacuum annealed for 1 h at four different temperatures.

The observed increase in hardness and elastic modulus are likely to be affected by these oxide layers. Deeper indentations are required to limit the effects of oxide layers on the measured mechanical properties. The annealed films show a decrease in the mechanical hysteresis due to better crystallization by annealing. We have noticed a shift in the total *P-h* loop of the annealed intermetallic NiTi thin films. The acquired hardness and elastic modulus values show greater values for the higher annealing temperature and lesser values for lower annealing temperatures. This is mainly due to the grain nucleation and growth during phase transformations and phase segregation in the intermetallic NiTi thin films with respect to the annealing temperature. Even though the defect density is decreased by annealing, the phase segregation of Ni₃Ti causes precipitation hardening. This leads to an increase in the hardness and elastic modulus values (Kumar et al. 2006).

Table 3.4 The hardness and elastic modulus parameters of intermetallic NiTi thin films annealed at four different temperatures.

Annealing Temperature (°C)	Hardness (GPa)	Elastic Modulus (GPa)
350	8.32	154.60
450	8.36	160.46
550	8.80	163.75
650	10.24	164.49

3.3.5 X-ray photoelectron spectroscopy analysis

The surface characteristics of annealed intermetallic NiTi thin films recorded by XPS survey scan is shown in Fig. 3.5(a-d) and the dominant signals are from Titanium, Nickel, Carbon and Oxygen. The surface elemental composition of annealed intermetallic NiTi thin films is shown in Table 3.5. The Carbon content present in the thin films noticed in survey spectra was ascribed to the surface contamination from the environment. The presence of oxygen content in survey spectra is the reaction with residual gases in the XPS spectrometer chamber or the ionic transport via impurities in the Ar gas. Titanium content is decreasing significantly with annealing

temperature up to 550°C and increases at 650°C. HRXPS spectra are recorded for each of dominant element that appeared in the XPS survey spectrum and their binding energies are shown in Fig. 3.6(a-d), 3.7(a-d), 3.8(a-d) and 3.9(a-d). The individual chemical state and spectral information offered by HR-XPS for dominant elemental states Ni (2p), Ti (2p), O (1s) and C (1s) are described as follows.

3.3.5.1 Ni (2p) spectra

The surface characteristics of annealed intermetallic NiTi thin films for Nickel content, HR-XPS are noted in the binding energy region of Ni (2p). The Gaussian de-convolution of the HR-XPS was used to identify the binding energy peaks.

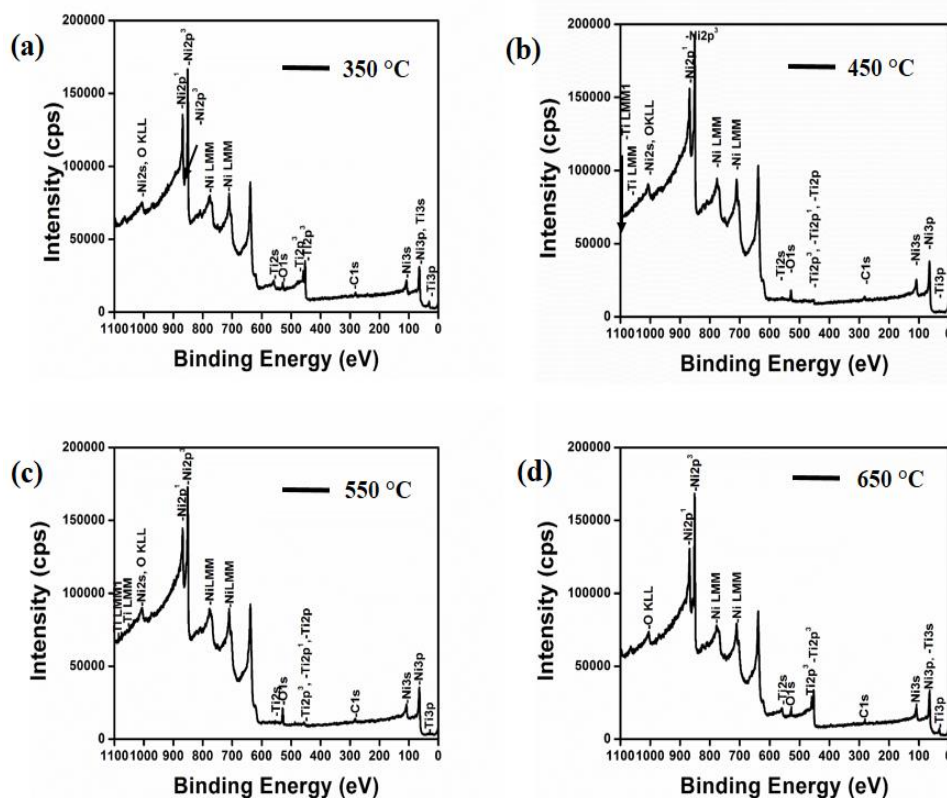


Figure 3.5 XPS survey spectrum obtained for intermetallic NiTi thin films annealed at (a) 350°C (b) 450°C (c) 550°C and (d) 650°C.

The de-convoluted Ni (2p) spectra consist of three binding energy peaks that are unchanged with annealing temperature. The binding energy peaks located at 867.5 eV and 850.5 eV are characterized by a 2-2.5 eV shift in binding energy over Ni species.

These binding energy shifts occur in the annealed thin films due to chemical effects and matrix effects such as differences in work function, crystal potential and relaxation energy (Kim and Winograd 1975). A small peak or satellite structure of binding energy at 857.1 eV can be seen in Fig. 3.6. The binding energy peaks positioned at 867.5 eV and 850.5 eV were attributed to a combination of two different metallic Ni states of Ni 2p_{1/2} and Ni 2p_{3/2}. However, another small peak or satellite structure at 857.1 eV arises due to the reorganization of the valence electrons as photoelectrons that are emitted from the core level corresponds to Ni₂O₃ or Ni(OH)₂ but this has been ascribed to Ni(OH)₂ because Ni₂O₃ is not likely to be present, as it is unstable (Kim and Winograd 1974). The existence of the additional satellite structure at 857.1 eV is consistent with experimental result reported in the literature (Shabalovskaya et al. 2008). Chan et al. studied NiTi alloys at reduced temperatures and observed a TiO₂ surface layer with metallic Nickel and Nickel oxide (NiO) (Chan et al. 1990). Nickel oxide such as NiO not observed in annealed intermetallic NiTi thin films, which were frequently reported in the literature (Green et al. 1997). Chu et al. reported that oxidation of NiTi alloys at temperatures up to 1000°C initiated the nickel species to be migrated from the surface regions into a deeper inner layer which consists of Ni₃Ti (Chu et al. 2006). It is proposed that there was an outer TiO₂ surface layer and inner Ni₃Ti layer and an intermediate layer consisting of TiO₂ and a phase of Ti in solid solution in Ni.

Table 3.5 Surface elemental composition evaluated from XPS survey spectrum of intermetallic NiTi thin films.

Annealing Temperature (°C)	Ti (2p)	Ni (2p)	C (1s)	O (1s)
350	34.7	44.6	2.4	18.3
450	3.7	45.7	26.5	24.1
550	1.7	43.8	13.8	40.7
650	31.6	46.2	5.6	16.6

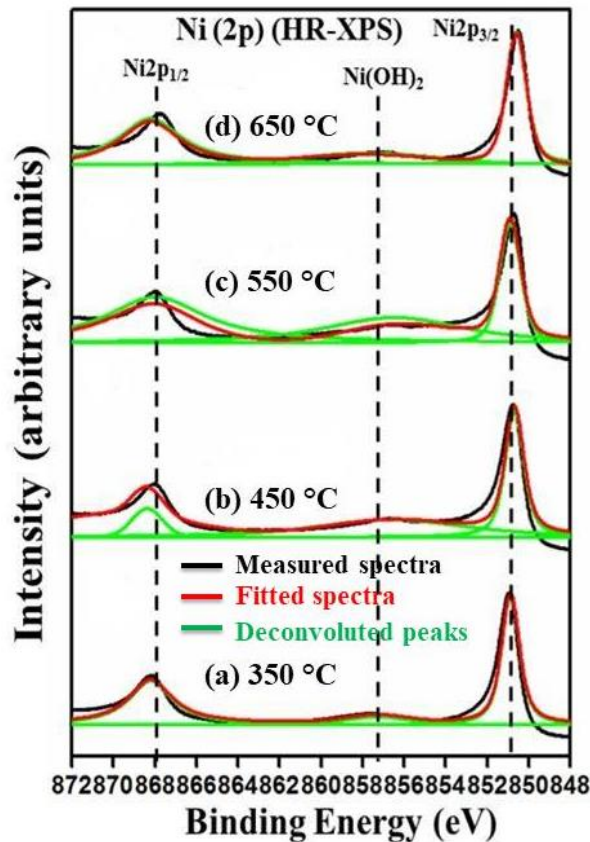


Figure 3.6 Gaussian de-convoluted HR-XPS spectrum for Ni (2p) of intermetallic NiTi thin films annealed at (a) 350°C (b) 450°C (c) 550°C and (d) 650°C.

3.3.5.2 Ti (2p) spectra

HR-XPS spectrum recorded in the binding energy regions of Titanium for annealed intermetallic NiTi thin films is shown in Fig. 3.7(a-d). The deconvoluted Ti (2p) high resolution XPS spectra in Fig. 3.7(a-d) show the variations in the Ti binding energy after annealing at different temperatures. At 350°C (Fig. 3.7(a)) four peaks situated at binding energies of 462.7 eV, 458.8 eV, 453.6 eV and 452.3 eV can be noticed. The binding energies 462.7 eV and 458.8 eV peaks match to $2p_{1/2}$ and $2p_{3/2}$ spin doublet states for Ti^{4+} (TiO_2), 453.6 eV and 452.3 eV peaks corresponds to metallic Ti (Pequegnat et al. 2015). The binding energy peaks located at 453.6 eV and 452.3 eV are characterized by a 2-2.5 eV shift in binding energy over Ti species. For Ti (2p) peak on the surface, apart from metallic peak, there is large content of TiO_2 peak present due to oxygen contamination. The binding energy peak located at 458.8 eV

has a strong affinity for oxygen and forms TiO_2 oxide layer on the film surface (Sharma and Mohan 2013). As the annealing temperature is increased from 350°C to 450°C (Fig. 3.7(b)) the deconvoluted Ti (2p) spectra had shown five binding energy peaks at 462.6 eV, 458.8 eV, 456.7 eV, 454.0 eV and 452.5 eV. The binding energy peaks 462.6 eV and 458.8 eV correspond to $2p_{1/2}$ and $2p_{3/2}$ spin doublet states for Ti^{4+} (TiO_2). The binding energy peaks located at 456.7 eV corresponds to Ti^{3+} metallic Titanium and 454.0 eV and 452.5 eV correspond to metallic Ti. The annealing temperature at 550°C (Fig. 3.7(c)) titanium had shown binding energy peaks located at 467.4 eV, 463.5 eV, 459.4 eV and 456.5 eV. The binding energy 467.4 eV corresponds to metallic Ti which is due to the shift in the binding energy over Ti species.

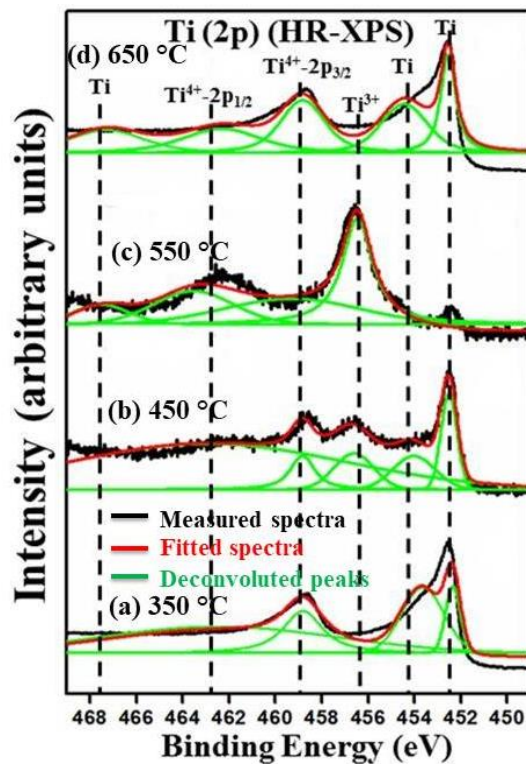


Figure 3.7 Gaussian de-convoluted HR-XPS spectrum for Ti (2p) of intermetallic NiTi thin films annealed at (a) 350°C (b) 450°C (c) 550°C and (d) 650°C .

The binding energy located at 463.5 eV and 459.4 eV correspond to $2p_{1/2}$ and $2p_{3/2}$ spin doublet states for Ti^{4+} (TiO_2). The binding energy 456.5 eV represents Ti^{3+} metallic Titanium. The deconvoluted Ti (2p) HR-XPS at 650°C (Fig. 3.7(d)) had

shown peaks at binding energies of 467.2 eV, 462.4 eV, 458.8 eV, 454.4 eV and 452.5 eV. The binding energies located at 467.2 eV, 454.4 eV and 452.5 eV corresponds to metallic Titanium. The binding energies 462.4 eV and 458.8 eV correspond to Ti^{2+} and Ti^{4+} metallic states.

In the case of films annealed at 350°C the Ti (2p) peak present on the film surface shows spin doublet states for Ti^{4+} (TiO_2) and metallic titanium. As the annealing temperature increased from 350°C to 450°C the Ti (2p) peak of the film surface, apart from spin doublet states for Ti^{4+} (TiO_2) and metallic Titanium, there exists a small content of Ti^{3+} metallic Titanium. Beneath the surface, Ti mainly exists in the metallic state due to the significant interdiffusion between the Ni and Ti. As the annealing temperature is increased from 450°C to 550°C the Ti (2p) peak of the film surface, apart from spin doublet states for Ti^{4+} (TiO_2) and metallic Titanium, the Ti^{3+} metallic Titanium content increases and the peaks are prominent due to higher interdiffusion of Ni and Ti. However, at lower temperatures the difference in activation energies leads to oxygen ion diffusion dominating with metal ion diffusion but increases with increase in temperature. The surface oxide growth relies on the diffusion of the metallic Nickel and Titanium species through the oxide. The films annealed at 650°C shows metallic Titanium, Ti^{2+} and Ti^{4+} metallic states. The possible oxidation behavior NiTi could be the decomposition of Ti oxide by the nearby metallic Ti at the oxide/alloy interface. The TiO_2 layer forms onto the film surface are prominent because Titanium is thermodynamically sensitive to oxygen, water and atmosphere.

3.3.5.3 O (1s) spectra

HR-XPS spectra recorded for thin films in the binding energy regions of Oxygen are shown in the Fig. 3.8(a-d). The Gaussian de-convolution of the HR-XPS was used to identify the binding energy peaks. The peaks are located at 529.5 eV and 528.5 eV. De-convoluted curve has shown the binding energy values that are consistent with reported binding energy values in literature (Bukhtiyarov et al. 2006). The binding energy peak in O (1s) spectrum located at 529.5 eV in annealed films, initiates from O^{2-} or TiO_2 (oxygen elements diffuse and reacts with Ti to form metal oxide) formation which is supported by the Ti (2p) high resolution spectra as discussed in the section 3.3.5.1.2. The other small peak observed at 528.5 eV in annealed films is

assigned to the nucleophilic oxygen C-H bond, is due to the nature of interaction oxygen from ethene content of the atmosphere (Du and Schuster 1998). From O (1s) de-convoluted curve it is clearly observed that oxygen has a strong tendency to form the TiO₂ metal oxide layer on the film surface.

3.3.5.4 C (1s) spectra

Similar to Ni (2p), Ti (2p) and O (1s) HR-XPS spectrum, high resolution spectra recorded in the binding energy regions of Carbon is shown in the Fig. 3.9(a-d). The binding energies recorded after Gaussian de-convolution of the experimental curve are at 281.1 eV, 282.5 eV and 285.1 eV. The binding energies at 281.1 eV and 282.5 eV were assigned for Ti-C. The heat of formation of Ti-C is $-184 \text{ kcal mol}^{-1}$ but that of Ni-C is not well established and the Ni-C phase diagram does not show stable carbides. The Ni concentration increases in the NiTi matrix by the presence of Ti-C particles and accounts for the lowering of transformation temperatures.

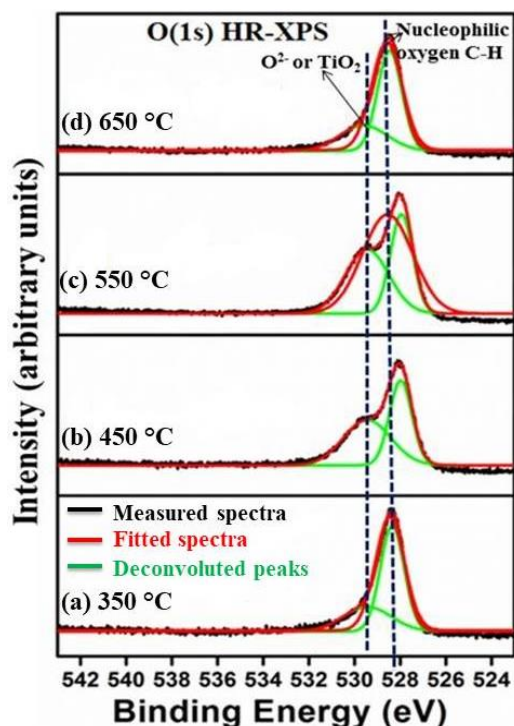


Figure 3.8 Gaussian de-convoluted HR-XPS spectrum for O (1s) of intermetallic NiTi thin films annealed at (a) 350°C (b) 450°C (c) 550°C and (d) 650°C.

Du and Schuster described that the formation of Ti-C in the carbon containing NiTi SMA's based on the quasi binary NiTi-TiC eutectic system (Du and Schuster 1998). The formation of Ti-C is favoured and Ni is segregated out of the Ti-C phase in annealed intermetallic NiTi thin films and this phenomenon was attributed to the high affinity of Titanium towards oxygen and carbon under high temperature annealing (Poon et al. 2005). The binding energy at 285.1 eV was assigned for carbon-carbon and carbon-hydrogen viz. C-C and C-H bond. The located binding energy values are well matched with reports available in the literature (Pequegnat et al. 2015). From X-ray photoelectron spectroscopy survey spectrum, it is clear that in the annealed intermetallic NiTi thin films due to their thermodynamic reasons Titanium has a strong affinity to form metal oxides (TiO₂) layer onto the film surface-atmosphere interface. TiO₂ has the larger unit cell and upon oxidation of Ti the larger titanium dioxide crystal structure is accommodated by Ti content relocate towards the film surface, leaving a Ni rich matrix behind. This phenomenon was proposed for study of oxidation scale on furnace cooled NiTi, and is supported by depth profiled auger studies on Oxygen exposed NiTi surfaces (Firstov et al. 2002, Tao et al. 2008).

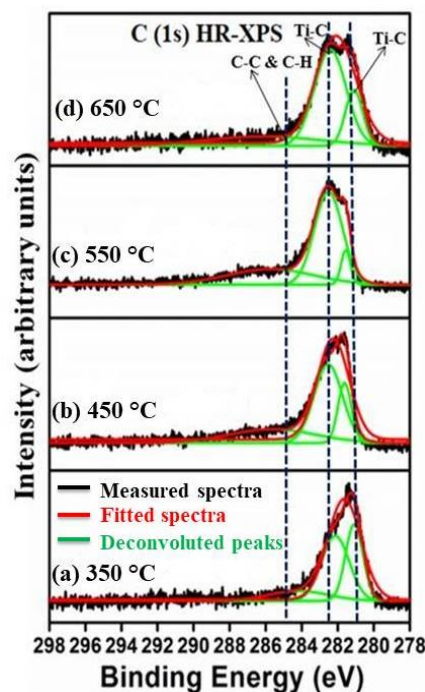


Figure 3.9 Gaussian de-convoluted HR-XPS spectrum for C (1s) of intermetallic NiTi thin films annealed at (a) 350°C (b) 450°C (c) 550°C and (d) 650°C.

The presence of high nickel content in NiTi based alloy thin films often causes suspicion of its suitability for medical applications. The TiO₂ layer formation on film surface prevents the release of Ni element, which is beneficial to bio-compatibility and corrosion resistance. The optimized preparation and modification processes for the metal oxide layer formation and prevention of surface layer degradation are more important if the NiTi thin films are considered for medical applications.

3.4 CONCLUSIONS

- Based on XRD, it was concluded that annealed intermetallic NiTi thin films were crystallized, resulting in the form of dominant Ni₃Ti phase along with intermetallic precipitates.
- The surface morphology of the investigated intermetallic NiTi thin films from FESEM characterization was found to vary significantly with respect to annealing temperature.
- Topographical structures can be altered by varying the annealing temperature. As the annealing temperature increases, the grain growth of the film changes from unclear to clear grain formation with larger crystal size and the transformation of microstructure from wavy topography to globular grain like type. The RMS, Ra and P-V roughness value increase with increase in annealing temperature.
- The hardness and elastic modulus values of deposited films increase probably due to formation of the intermediate metastable states by the incomplete alloying process.
- X-ray photoelectron spectroscopy (XPS) investigation indicated that the annealed intermetallic NiTi thin films possess strong ability to form natural TiO₂ as an outermost oxide layer on the film surface with Ni-rich matrix trapped behind most likely in the prior lattice sites of NiTi.

CHAPTER 4

AGING TIME CORRELATION IN DC MAGNETRON SPUTTERED Ni₆₀Ti₄₀ THIN FILMS

It is well known that shape memory effect, super elasticity and phase transformation temperatures of sputter deposited NiTi thin films are quite sensitive to the film composition, contamination, annealing temperature, aging time, thermo-mechanical treatment and deposition parameters (Kotnur and Janssen 2012). This chapter mainly consists of the effect of aging temperature on the structural, morphological, mechanical and surface properties of intermetallic NiTi thin films.

4.1 INTRODUCTION

Shape memory alloys (SMAs) are considered as the suitable candidate materials for MEMS (micro-electro-mechanical-systems) applications due to their large recovery strain and recovery force (Pan and Cho 2007). In addition to that shape memory alloys also possess pseudoelasticity (superelasticity), high force to volume (power to weight) ratio, good chemical resistance and biocompatibility (Sanjabi et al. 2009, Lehnert et al. 2000, Cho et al. 2005). These properties have made SMAs recognized as promising materials for research on functional and smart (or intelligent) system applications (Levi et al. 2008). In order to use the NiTi thin films for MEMS applications, it is essential to prepare them in micron level. Sputtering is one of the most preferred method to prepare NiTi based SMAs. The sputtered NiTi film composition could be controlled by metallurgical factors (annealing, aging process, film composition, contamination and thermo-mechanical treatment, etc.), sputtering conditions (deposition temperature, gas pressure, substrate bias, target power and target to substrate distance, etc.) and application conditions (heat dissipation, heating/cooling rate, room temperature and environment, strain rate, etc. (Krulvitch et al. 1996, Miyazaki and Ishida 1999, Ishida et al. 1996). Vacuum deposited intermetallic NiTi thin films generally show fine grained structure and high surface

reactive nature and sensitivity. Therefore, it is essential to understand the surface structure and its aging effect when exposed to air (ambient atmosphere). The film thickness required in MEMS applications is usually less than a few microns, a relatively thin reaction layer might have important effects on shape memory and adhesion properties.

The effect of deposition and post annealing conditions of intermetallic NiTi thin films on film micro-structure, surface morphology and mechanical properties are widely reported in the literature (Ohta et al. 2000). The effects of second phase segregation and super lattice formation and their implication on the electron diffraction patterns and also mechanical response (deformation behavior) of the films to nanoindentation was examined. Suzana Petrovic et al. (Petrović et al. 2012) studied the effects of thermal treatment and Ar-ion implantation on the composition and structure of the (Ni/Ti)_x5/Si multilayer system using TEM and XPS. Implantation of argon into Ni/Ti multi-layered thin films has induced intermixing and intermetallic NiTi phase formation. Green et al. (Green et al. 1997) examined the surface chemical composition of both N⁺ ions implanted and shot peened surface and amorphised Ni-Ti and unmodified Ni-Ti. The observations indicate that the surface of Ni-Ti contained dissociated Ni and Ti species. Ti existing as an outermost oxide with Ni trapped behind, most likely in the prior lattice sites of Ni-Ti. Firstov et al. examined mechanically polished NiTi alloy exposed to heat treatment in air in the temperature range 300-800°C. A smooth protective nickel-free oxide layer with a relatively small amount of Ni species at the air/oxide interface was produced by oxidation at 500°C (Firstov et al. 2002). Fu et al. (Fu et al. 2005) was employed to study the surface chemistry of the films and interfacial structure of the Si/TiNi system.

The proper understanding in the optimization of deposition conditions and aging time along with the knowledge of surface characteristics of intermetallic NiTi thin films play a vital role in the usage of micro-device applications. Moreover, reports on the influence of aging time on intermetallic NiTi thin films and evolution of surface property relationships of NiTi thin films are not reported earlier. The main objective of the present work is to study the impact of the aging time correlation on structural, morphological, mechanical and surface properties of intermetallic NiTi thin films. The surface characteristics of these films studied using XPS and the elemental

composition and presence of various chemical states have been discussed in detail in section 4.4.5. In our work, we focus on the influence of aging time on intermetallic NiTi thin films when subjected to same annealing temperature (600°C for 1 h) but different aging times (at 500°C for 2 h, 4 h and 6 h).

4.2 EXPERIMENTAL

The detailed experimental procedure for the preparation of intermetallic NiTi thin films have been discussed in the chapter-3, section 3.2. The NiTi thin films were prepared and were subsequently solution treated or annealed at 600°C for 1 hour. The annealing temperature was selected from the phase diagram that the Ni-Ti composition would lie in the single phase NiTi region. The temperature was raised to the solution treatment temperature at a ramp rate of 50°C/min. Cooling rate was kept to be at 2°C/min. After solution treatment the films were aged at 500°C for 2h, 4h and 6h and then cooled to room temperature. Nishida et al. (Nishida et al. 1986) proposed the aging temperature for bulk Ti-52 Ni alloys depending on the TTT (time-temperature-transformation) diagram.

4.3 THIN FILM CHARACTERIZATION

The detailed description regarding thin film characterization techniques carried out for intermetallic NiTi thin films have been discussed in chapter-3, section 3.3. Atomic force microscope (AFM Model: Bruker Innova) under tapping mode was used to examine the roughness and film topography.

4.4 RESULTS AND DISCUSSION

4.4.1 Structural analysis

The annealing temperature and aging time will influence the structure as well as properties of NiTi thin films and their shape memory behavior (Fu and Du 2003). As-deposited films do not show the crystalline state due to insufficient heat treatment. To make these films crystalline, high deposition temperature or post-annealing

temperature is required. To reduce the reaction between film and substrate, it is important that post-annealing should be done at the lowest annealing temperature for minimum duration, otherwise it could make dramatic changes in the structural, morphological, mechanical properties and shape memory effect (Fu et al. 2004). In order to study the effect of aging time on intermetallic NiTi thin films, the films are deposited at room temperature and the post-annealing (solution treatment) was executed on these films.

Figure 4.1(a-e) shows the XRD patterns of intermetallic thin films grown at room temperature, post-annealed at 600°C for 1 h and post-annealed at 600°C for 1 h followed by aging at 500°C for 2 h, 4 h and 6 h. In spite of similar film composition, the annealed and aged films showed crystallinity and revealed distinct microstructure. The annealed and aged films have shown the presence of several diffraction peaks indicating poly-crystalline nature of those films. XRD diffraction pattern confirmed that the dominant peak at $2\theta = 43.81^\circ$ is indexed for (0 0 4) planar reflection represents the Ni₃Ti phase of NiTi. The XRD pattern revealed the presence of Ni₃Ti phase as a major phase with some diffraction peaks corresponding to intermetallic precipitates which are identified as NiTi and NiTi₂. The diffraction peaks positioned at 35.15°, 38.76°, 41.40°, 42.81°, 46.85° and 47.79° are assigned to (1 1 0), (0 0 2), (5 1 1), (1 1 0), (2 0 2) and (5 3 1) planar reflections, respectively. The high temperature holding or high temperature post-annealing, or aging time leads to the evolution of Ni-rich precipitates (Kompatscher et al. 2002, Allafi et al. 2002, Martins et al. 2007). Interestingly, a few lower intensity diffraction peaks corresponding to NiTi₂ peaks are also observed. Sputter deposition of Ni-rich NiTi thin films, however, is able to create an unstable structure with a homogeneous distribution of excess Ni. The subsequent aging of these films causes precipitates to form within the NiTi grains at low annealing temperatures and times (Sato et al. 2010). The intermetallic NiTi thin films sputter deposited at room temperature shows amorphous nature (Fig. 4.1(a)). The intermetallic NiTi thin films were subsequently solution treated or annealed at 600°C for 1 hour. As the annealing temperature is increasing from room temperature to 600°C (Fig. 4.1(b)) the diffusion rate increases and grain formation occur due to atomic migration. In the case of films aged at 2 h (Fig. 4.1(c)) the initial nucleation of a meta stable, solid phase transforms e.g., amorphous solid particles that

crystallize with time. As the aging time is increasing from 2 h to 4 h (Fig. 4.1(d)) would allow for greater diffusion within the Ni-rich films, which could lead to greater precipitation in the NiTi matrix. These precipitates are coherent with the austenite matrix and their coherency strains strengthening the austenite phase.

Increasing the aging time from 4 h to 6 h (Fig. 4.1(e)) the degree of crystallinity increases due to the presence of intermetallic precipitates. An increase in the aging time causes the precipitates to become spherical in shape and lose their coherency with the austenite matrix. This observation qualitatively agrees with the present experimental data which shows an increase in crystallinity (larger spherical precipitates) with an increase in aging time. In the case of aged intermetallic thin films different phases such as NiTi, Ni₃Ti and Ni₂Ti co exists due to incomplete alloying process.

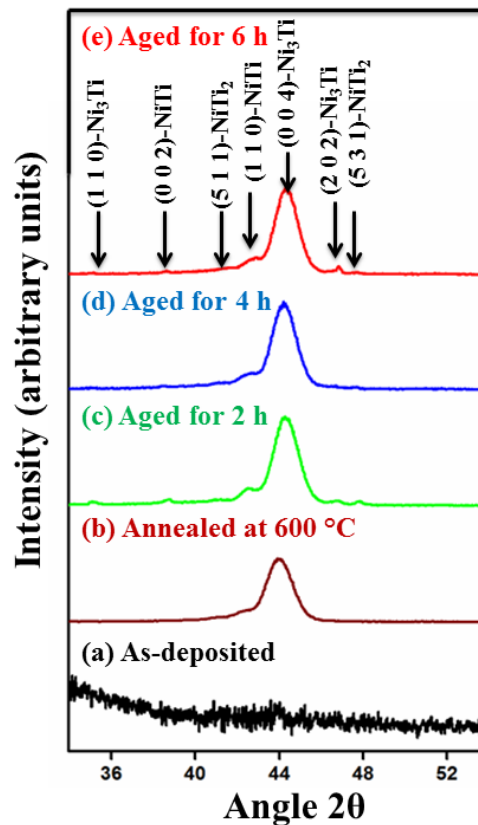


Figure 4.1 X-ray diffraction patterns of intermetallic NiTi thin films (a) as-deposited (b) vacuum annealed at 600°C for 1 h (c) vacuum annealed at 600°C for 1 h followed by aging at 500°C for 2 h (d) vacuum annealed at 600°C for 1 h followed by aging at

500°C for 4 h and (e) vacuum annealed at 600°C for 1 h followed by aging at 500°C for 6 h.

4.4.2 Surface morphology

Figure 2(a-c) and Figure 3(a-c) shows the planar and cross-sectional view of FESEM micrographs recorded for intermetallic NiTi thin films. These FESEM images clearly indicate the change in surface morphology of thin films annealed at 600°C for 1 h followed by aging at 500°C for 2 h, 4 h and 6 h. During crystallization process, nucleation and growth, initiate once an amorphous material is sufficiently heated. From a thermodynamic point of view, the driving force for an amorphous material to crystallize is the free energy difference between the amorphous and crystalline phases. The crystallization of amorphous material starts with a nucleation followed by growth process and it depends on annealing and/or aging temperature and time (Raju et al. 2008). The subsequent aging of intermetallic NiTi thin films causes precipitates to form within the NiTi grains, which initially form as thin plates or Guinier-Preston (GP) zones at low annealing temperatures and time ((Sato et al. 2010)). In the case of films aged at 2 h (Fig. 4.2(a)) the diffusion rate is low to have a significant effect on the NiTi matrix composition. Initial diffusion and precipitation rates are low due to the Ni content being lower than the solubility limit in NiTi. The GP zones were formed by the segregation of Ni atoms in NiTi grains. At low aging times, the solubility of Ni in NiTi will reduce the Ni₄Ti₃ forms to a lesser content. The Ni-rich phase Ni₄Ti₃ preferentially nucleated at the grain boundaries. The remaining excess Ni content would be in the form of Ni₃Ti precipitates. Further aging of these films allow for greater diffusion forms bigger precipitates within the NiTi grains (solid phases exists in equilibrium) are incoherent with the matrix, thus ineffective to the transformation behavior of the B2 matrix (Paryab et al. 2010). The diffusion rate increases due to higher temperatures and longer aging times allow for greater diffusion. The overall surface morphology in the case of films aged at 4 h and 6 h appears to be homogeneous. Long-term aging causes the precipitates become spherical in shape and lose their coherency with the austenite matrix and forms large precipitated particles within NiTi grains that we can notice in the case of film aging at 4 h and 6 h from Fig. 4.2(b) and Fig. 4.2(c).

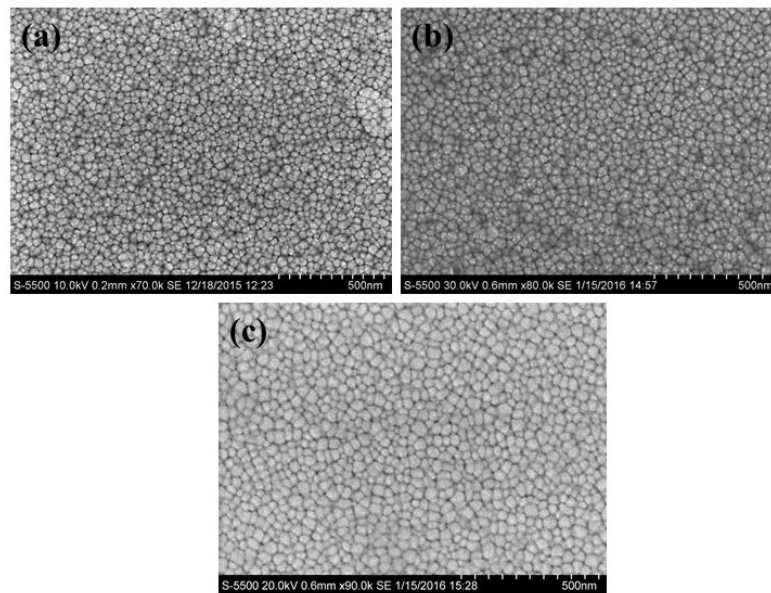


Figure 4.2 FESEM planar micrographs of intermetallic NiTi thin film vacuum annealed at 600°C for 1 h followed by aging at 500°C for (a) 2 h (b) 4 h and (c) 6 h.

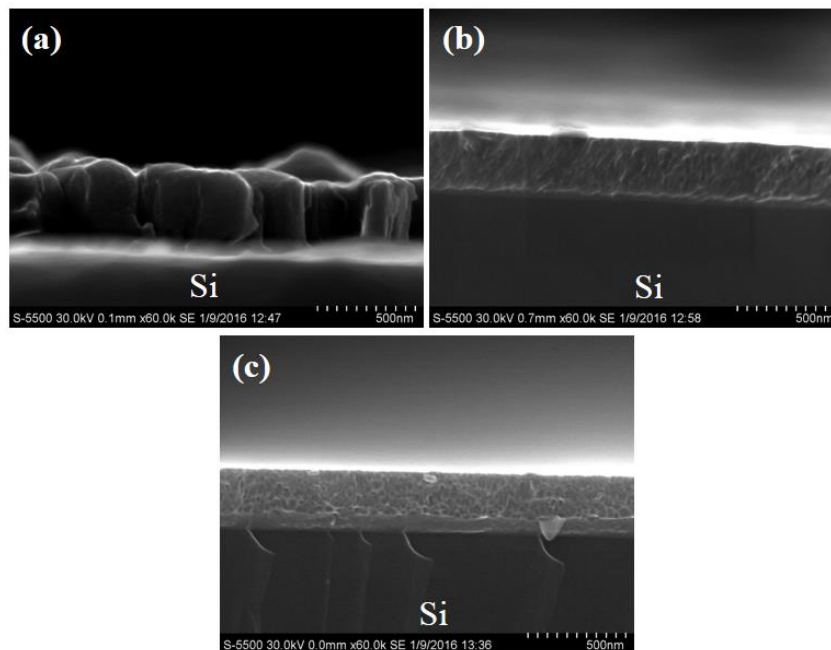


Figure 4.3 FESEM cross-sectional micrographs of intermetallic NiTi thin film vacuum annealed at 600°C for 1 h followed by aging at 500°C for (a) 2 h (b) 4 h and (c) 6 h.

The variance in the film microstructure is a direct consequence of the relation between the crystallization temperature, nucleation and growth. Fig. 4.3(a-c) shows

the cross-sectional images of the intermetallic thin films annealed at 600°C for 1 h followed by aging at 500°C for 2 h, 4 h and 6 h. As it can be seen in Fig. 4.3(a), the intermetallic NiTi thin films aged at 2 h exhibit finely packed (thick or dense) fibrous kind microstructure indicating the formation of precipitates (intermetallic particles). But in the case of film aged at 4 h and 6 h shown in Fig. 4.3(b-c) we have observed that the size of the precipitates increases with increasing aging time. Precipitation results into nucleation where the drifting atoms group together within the NiTi grains. This forms a microstructure usually comprising of two or more distinct phases.

4.4.3 Surface topography analysis

Figure 3(a-c) show a typical three dimensional image of intermetallic NiTi thin films deposited at room temperature and annealed at 600°C for 1 h followed by aging at 500°C for 2 h, 4 h and 6 h in the scan areas of 1 μm x 1 μm . The surface roughness variation can be clearly resolved from atomic force microscopy images for the films. The surface roughness parameters such as average roughness (R_{avg}), root mean square roughness (R_{rms}) and peak to valley roughness parameters are found from AFM scans for each sample at different location are presented in Table 4.1. The surface roughness values increase with increase in aging temperature. The surface topography changes can be clarified based on the theories such as surface diffusion, coalescence and grain growth (thin film growth process) of the films. The surface roughness is closely associated with the change in the films.

AFM measurements can be based on film structure, including roughness, defects, amorphous, crystalline phases, nucleation, and growth modes. The aggregation leads to an uneven growth of grains that result into the differences in the grain height. In the case of film aged at 2 h we have noticed unclear grain growth formed by precipitates. As the aging temperature increases from 2 h to 4 h the film topography shows a larger grain due to the increase in size of precipitates and loses their coherency in the matrix. Aging at 6 h the topography shows the extremely larger grain formation is due to increment in density of the precipitates within the NiTi grains. The AFM micrographs clearly revealed that the surface roughness parameters of the intermetallic NiTi thin films increases with increasing in aging time.

Table 4.1. Various roughness parameters of the intermetallic NiTi thin films with same scan area.

Aging time	Scan size (μm) ²	RMS roughness (nm)	Ra roughness (nm)	P-V roughness (nm)
		AFM		
2 h	1 x 1	0.3	0.2	3.66±0.09
4 h	1 x 1	0.4	0.3	3.76±0.07
6 h	1 x 1	0.7	0.4	4.85±0.12

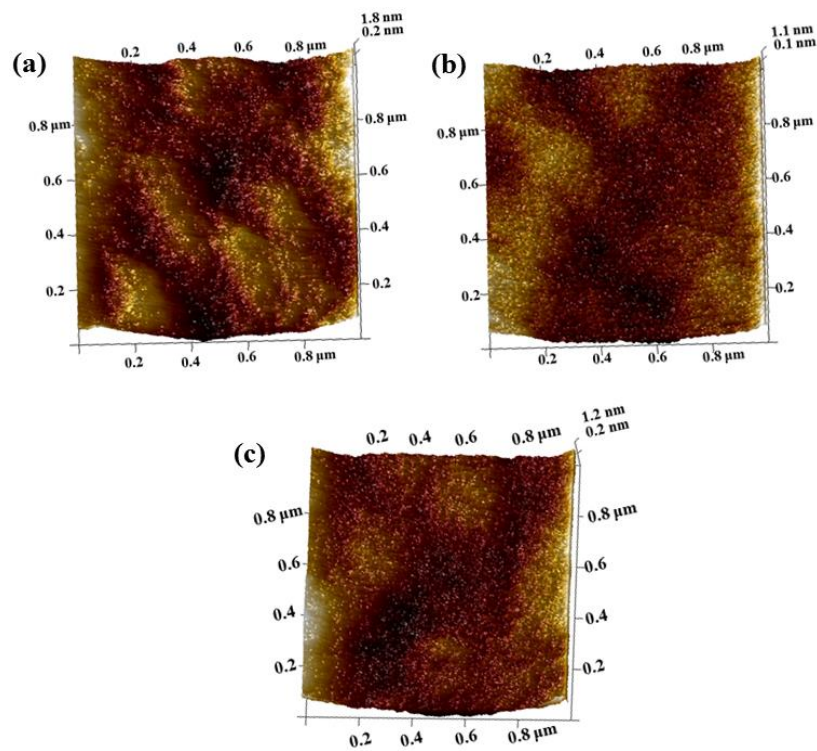


Figure 4.4 AFM (3D surface morphology) micrographs of sputter deposited intermetallic NiTi thin film vacuum annealed at 600°C for 1 h followed by aging at 500°C for (a) 2 h (b) 4 h and (c) 6 h.

4.4.4 Nanoindentation

The survey of the literature from the past two decades clearly shows that most of the mechanical tests on NiTi thin films were done using the Bulge tests (Makino et al. 2000, Makino et al. 2001). In all indentation tests, the indenter was applied over a

range of load for a period of time and the load was then held constant, while the displacement (depth) was examined. In this work, all indentation tests were carried out using an ASMEC nanoindenter with a Berkovich (a three sided pyramid shape tip) diamond indenter and the tip radius of curvature being 200 nm. The indentations were performed at different regions of the film. The indentation regions were ~100 nm apart, so that there were no interventions on the load-displacement curves at each indenter spot. The indentation tests were carried out at room temperature and the samples fixed firmly to the sample holder. The load displacement curves (P-h) obtained for the intermetallic NiTi thin films annealed at 600°C for 1 h followed by ageing at 500°C for 2 h, 4 h and 6 h are shown in Fig. 4.5(a-c).

Nine indents were made on each sample to obtain the load-displacement curve. The estimation of the elastic property parameters like hardness and elastic modulus, etc. was done from this curve. The load displacement curves of intermetallic NiTi thin films show overall elasto-plastic response (Mohri et al. 2015). During indentation withdrawal, the unloading curve, was smooth which indicated that it was purely recovery on relaxation. The aging temperature had a significant amount of effect on the nanoindentation test executed on intermetallic NiTi thin films. Aging leads to a metastable state of the solid solution which in turn produces intermetallic particles. As the aging time increases the density of the precipitates increases within the NiTi grains due to this the grain size increases. Table 4.2 shows the variation in hardness and elastic modulus values of intermetallic NiTi thin films annealed at a temperature of 600°C for 1 h followed by aging at 500°C for 2 h, 4 h and 6 h, respectively. The elastic modulus measurements were more strongly affected by the substrate compared to the hardness measurements because the elastic field under the tip was confined to a long range field that extended into the substrate but not confined to the film. It is essential to note that the indenter size should be less than 10 % of the films to avoid the substrate effects that play a major role in the deformation process that takes place around indenter (Tall et al. 2007). Saha and coworkers et al. have studied the influence of the substrate by including an additional term in the reduced modulus equation. Film modulus is reasonably well if the contact depths are less than 50% of the film thickness (Saha and Nix 2002). In the present work, the mechanical property

of thin films was reasonable because the contact depth was less than 50% film thickness.

Table 4.2 The hardness and elastic modulus parameters of intermetallic NiTi thin film vacuum annealed at 600°C for 1 h followed by aging at 500°C for different times.

Aging time	Hardness (GPa)	Elastic modulus (GPa)
2 h	8.32	148.92
4 h	9.12	154.46
6 h	9.41	163.13

The analytical method of Oliver and Pharr was used to determine the hardness and elastic modulus of the intermetallic NiTi thin films (Kan et al. 2013). This method is only applicable to the film-substrate system if the film is sufficiently thick or if the film and substrate have similar elastic properties. The maximum load P_{max} and the displacement at peak load, h_{max} are the major parameters that are used for analysis in this method.

Both Ni and Ti are highly reactive to residual oxygen even though the films annealed and aging is done in high vacuum. Deeper indentations were required to limit the effects of oxide layers on the measured mechanical properties. The hardness and elastic modulus were obtained from typical load-displacement curves shown in Fig. 4.5(a-c). The elastic modulus was determined from the slope in the initial unloading segments of the P-h curves. The hardness and elastic modulus of the intermetallic NiTi thin films increases with increase in aging time. The age-treated films show a decrease in the mechanical hysteresis due to increase in the density of precipitates within the NiTi grains.

In the present study the variation in elastic modulus obtained are also due to the stress-induced phase transformations phenomena. Possible variation in the elastic moduli, associated with stress induced phase transformations can be estimated by comparing the previously reported elastic moduli for bulk and thin films of NiTi alloys. The bulk NiTi alloy has been shown to have an elastic modulus of 65 GPa (Oliver and Pharr 2004). In contrast, austenite phases NiTi thin films have been reported to have a elastic modulus of 84 GPa. While elastic modulus of martensitic

NiTi thin films has shown ~60 GPa (Pelletier et al. 2002). Nanda Kumar et al. have been reported the elastic modulus of intermetallic NiTi thin films 150 GPa (Kumar et al. 2006). The other authors have reported the elastic moduli of 110 GPa and 20 GPa (bulging test), respectively (Fu et al. 2001). In the present work, the intermetallic NiTi thin films aged at 2 h, 4 h and 6 h has shown elastic modulus of 148.92, 154.46 and 163.13 GPa, respectively.

The hardness and elastic moduli values are shown in Table 4.2. The increasing trend in hardness and elastic moduli values can be attributed to the change in the formation of intermetallic precipitates that occur during aging at different time intervals. Although the defect density is reduced by annealing, increase in density of incoherent precipitates during aging leads to an increase in the hardness and elastic modulus. The strength of the metallic films increases vividly when the thickness falls below about 0.3 μm and the Hall Petch relation, obeyed by thin films, is also dependent of thickness (Moyné et al. 1999). The hardness and elastic moduli values of films aged at 2 h are 8.32 and 148.92 GPa respectively. These are low compared to the films aged at 4 h and 6 h respectively. The hardness and elastic moduli values of aged films at 4 h and 6 h are 9.12 and 9.41, 154.46 and 163.13 GPa respectively. It is clear that the films exposure to long term aging causes more incoherency in the Ni-rich NiTi matrix due to the larger precipitated particle formation. Due to this reason these films show differences in the hardness and elastic modulus and are ineffective to the transformation behavior of the B2 matrix.

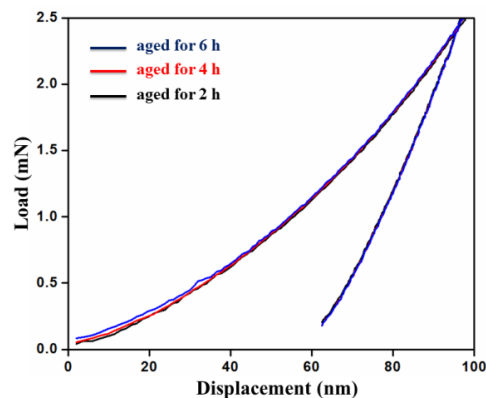


Figure 4.5 Load-displacement plots of intermetallic NiTi thin films deposited at room temperature and vacuum annealed at 600°C for 1 h followed by aging at 500°C for 2 h, 4 h and 6 h.

4.4.5 X-ray photoelectron spectroscopy analysis

The X-ray photoelectron spectroscopy mainly depends on the excitation process that makes peak shift analysis, interpretation of binding energy state investigations. The bonding of the atoms in the first few atomic layers of the surface material was determined by XPS. The experimental energy spectra were compared to standard values to identify the bond type and relative concentration of each bond type (Moulder et al. 1992). The physical and chemical composition of a NiTi alloy surface plays an important role in corrosion resistance and biocompatibility (Ratner et al. 2004). The good biocompatibility of NiTi alloys is attributed to the thin native titanium oxide surface layer. However, Nickel in oxidized or metallic state is noticed on the surface or sub-layers and its amount depends on the surface treatments like mechanical polishing, electrochemical polishing, heat treatments and shot peening (Armitage and Grant 2003). In the reported work, simple heat treatments and aging time were employed in intermetallic NiTi thin films. The surface oxidation occurs during heat treatment results into increased TiO₂ thickness, roughness and changes in the composition of the surface film. Heat treatments of intermetallic NiTi thin films are restricted to temperature lower than the recrystallization temperature of 650°C; therefore, the temperatures used in this study for annealing and aging were 600°C and 500°C, respectively.

The surface characteristics of as-deposited intermetallic NiTi thin films annealed at 600°C for 1 h followed by aging at 500°C for 2 h, 4 h and 6 h were recorded by XPS. The dominant surface elements were Nickel (Ni), Titanium (Ti), Oxygen (O), Carbon (C). The surface elemental composition of age treated films is shown in Table 4.3. Titanium has a high affinity towards oxygen and carbon (enthalpy or chemisorb barrier energy for Ti and Ni to react with oxygen at surface are 241 kJ/mol and 956 kJ/mol, respectively) due to this reason as soon as the as-deposited films are exposed to ambient conditions, oxygen and carbon get rapidly adsorbed on the film surface (Fu et al. 2005). The reduction of the Ni content of the film surface and also the presence of high Ni content in sub-layer is due to the preferential oxidation of Ti. The spectral information and individual chemical state offered by HR-XPS for each dominant element state are given below.

Table 4.3 Surface elemental composition evaluated from an XPS survey spectrum of intermetallic NiTi thin film vacuum annealed at 600°C for 1 h followed by aging at 500°C for different times.

Element	Concentration (at. %)		
	Aged for 2 h	Aged for 4 h	Aged for 6 h
O1s	51.6	57.1	55.5
C1s	< 1	5.0	< 1
Ni2p	1.1	0.3	1.3
Ti2p	47.3	37.7	43.2

4.4.5.1 Ni (2p) spectra

To study the surface characteristics of age-treated intermetallic thin films for Nickel content, HR-XPS noted in the binding energy region of Ni (2p). Fig. 4.6(a-c) shows the HR-XPS spectra recorded for age-treated films. Two broad peaks located at a binding energy of 868.1 eV and 850.8 eV observed, are characterized by a 2-2.5 eV shift in binding energy over Ni species. A small peak or satellite structure of binding energy at 857.5 eV can be seen in Fig. 4.6(a-c). The shift in binding energy in thin films arises due to the chemical effects and matrix effects such as differences in work function, crystal potential and relaxation energy (Kim and Winograd 1975). The binding energy peaks positioned at 868.1 eV and 850.8 eV were attributed to a combination of two different metallic Ni doublet spin states of Ni 2p_{1/2} and Ni 2p_{3/2}. Wang et al. studied the appearance of intermetallic Ni doublet spin states for NiTi bulk samples. The binding energy peak positioned at 857.5 eV corresponds to Ni(OH)₂ (Wang et al. 2007). This peak is supposed to be a shake-up satellite, which occurs due to reorganization of the valence electrons as photo electrons are emitted from the core levels (Chu et al. 2007). For the heat treatments (solution treated) a transition from logarithmic to parabolic oxidation (Logarithmic oxidation: Oxidations is initially rapid and then slows down and becomes negligible and Parabolic oxidation: Oxidation rate decreases with time) occurs between 400 and 600°C, while the oxidation tends to be parabolic (from above 600°C up to 900°C. Oxide growth occurs by diffusion of oxygen ion and metal ion. However, at lower temperatures the difference in activation energies leads to oxygen ion diffusion dominating with metal ion diffusion but increases with increase in temperature. The surface oxide growth

relies on the diffusion of the metallic Nickel and Titanium species through the oxide. The diffusion coefficient of Ni at 500°C is half that of Ti (Firstov et al. 2002).

The XPS measurements showed that the age-treated films were enclosed by an oxide layer a few nanometers thickness through which the metallic substrate (sub layer) was detectable. This oxide layer is composed fully of TiO₂ but few Ti sub-oxides and Ni oxidized species were detected and the surface was depleted in Ni. In the case of age-treated films the upper surface layer consists of the strong presence of TiO₂ and Ni₃Ti intermetallic phase (Sato et al. 2009). After a long aging time we have noticed the Ni depletion of the matrix due to enhanced growth of Ni-rich particles (precipitates). Longer aging treatments consist of large and widely spaced precipitates only affects the Ni-concentration in the matrix. It leads to heterogeneous precipitation of Ni-rich particles within NiTi grains (Ishida et al. 1997). It may be due to the fact that titanium being the highly reactive element, segregates to the film surface and is oxidized there forming titanium dioxide with Ni enriched alloy layers underneath. The lower Ni content is supported by the thicker surface metal oxide layer (titanium dioxide) (Firstov et al. 2002). The presence of titanium dioxide layer on intermetallic NiTi thin film surface can prevent Ni content releasing from the surface of age-treated films, which would be a suitable property for biomedical applications.

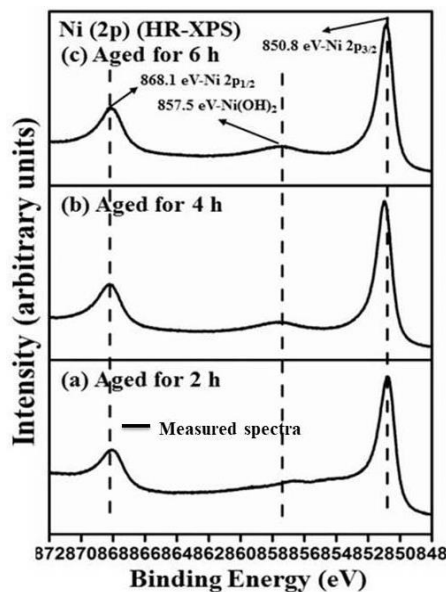


Figure 4.6 Ni (2p) HR-XPS spectrum recorded for intermetallic NiTi thin films annealed at 600°C for 1 h followed by aging at 500°C for (a) 2 h (b) 4 h and (c) 6 h.

4.4.5.2 Ti (2p) spectra

HR-XPS spectrum recorded for age-treated intermetallic NiTi thin films in their binding energies of Titanium is shown in Fig. 4.7(a-c). High resolution XPS spectra in Fig. 4.7(a-c) show the variations in the Ti binding energy after aging at different times. Films age-treated at 2 h two broad peaks located at binding energies of 462.4 eV and 456.6 eV can be seen in Fig. 4.7(a-c). These binding energy peaks correspond to Ti^{3+} metallic Titanium. We have also noticed a small satellite peak located at a binding energy of 452.4 eV corresponds to Ti (2p) metallic precipitates. As the aging time is increasing from 2 h to 4 h and 6h we have noticed two binding energy peaks that are positioned at 458.7 eV and 452.6 eV. These peaks are corresponding to $2p_{3/2}$ spin states for Ti^{4+} (TiO_2) and Ti (2p) metallic precipitates. In the case of films aged at 2 h the Ti 2p peak present on the film surface shows metallic Ti^{3+} and metallic Ti 2p peak but no traces of TiO_2 peaks found (Fig. 4.7(a)). As the aging time increased from 2 h to 4 h the Ti 2p peak on the film surface, apart from metallic Ti 2p peak, there exists a large content of TiO_2 peak due to oxygen contamination as shown in Fig. 4.7(b). The films aged at 6 h (Fig. 4.7(c)) shows the metallic Ti 2p peak and TiO_2 peak. As the aging time is increased from 2 h to 4 h and 6 h the TiO_2 peak is prominent and the Ti^{3+} peaks are disappeared. The possible oxidation behavior NiTi could be the decomposition of Ti oxide by the nearby metallic Ti at the oxide/alloy interface. Bui et al. studied such decomposition during oxidation of Ti at temperatures above 350°C (Duc et al. 1980). It creates a high density of vacancies allowing fast diffusion of oxygen leads to linear or quasi linear oxidation rate of Ti. The formation of TiO_2 layer on the film surface can prevent Ni being released from the surface of aging thin films and it would be a useful material property for corrosion resistance and bio-medical applications (Sharma and Mohan 2013). Titanium dioxide layer formation on the film surface is prominent due to the higher thermodynamic (Gibbs free energy) reactive nature of Titanium with oxygen, water and atmosphere.

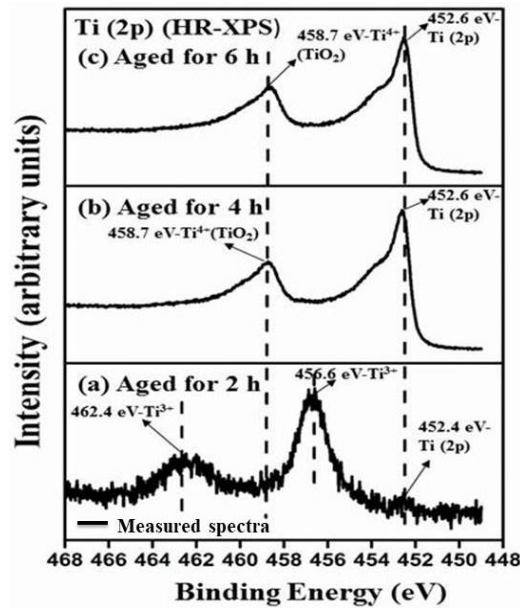


Figure 4.7 Ti (2p) HR-XPS spectrum recorded for intermetallic NiTi thin films annealed at 600°C for 1 h followed by aging at 500°C for (a) 2 h (b) 4 h and (c) 6 h.

4.4.5.3 O (1s) spectra

The reaction with residual gases in the spectrometer chamber or the ionic transport via impurities in the Ar gas causes the oxygen content in the intermetallic NiTi thin films. High resolution spectra recorded for the oxygen content of aging intermetallic NiTi thin films in their binding energies are shown in Fig. 4.8(a-c). Gaussian deconvolution is applied to the experimental curve to identify the exact location of the binding energy peaks. In films aged for 2 h the binding energy peaks positioned at 531.5 eV, 529.7 eV and 527.9 eV can be seen in Fig. 4.8(a). The binding energy peak located at 531.5 eV is assigned to the formation of metal hydroxide (-OH). The binding energy peak located at 529.7 eV initiates from O²⁻ or TiO₂ (metal oxide) formation. At 527.9 eV the binding energy peak corresponds to nucleophilic oxygen C-H bond, is due to the interaction of oxygen with ethene content of the atmosphere (Bukhtiyarov et al. 2006). As the aging time is increased from 2 h to 4 h and 6 h the binding energies are located at 530.9 eV, 529.3 eV and 528.4 eV as can be seen in Fig. 4.8(b-c). The binding energy located at 530.9 eV corresponds to metal hydroxide (-OH) formation. The binding energies positioned at 529.3 eV initiates from O²⁻ or TiO₂ (metal oxide) formation and the binding energy peak centered at 528.4 eV

assigned to nucleophilic oxygen C-H bond, is due to the nature of interaction of oxygen from ethene content of the atmosphere. It is evident from de-convoluted curves that O (1s) has the strong ability to form TiO₂ oxide layer on the film surface of aged intermetallic NiTi thin films. The deconvoluted curves of films aged at 2 h show the metal hydroxide, metal oxide and C-H bond formation (Fig. 4.8(a)). It is clear from Fig. 4.8(b) that the TiO₂ content is low compared to the films aged at 4 h and 6 h. This indicates that the oxygen content diffuse and react with titanium to form titanium dioxide deep into the film. The sputtered intermetallic NiTi thin films are easily contaminated with oxygen content. At the beginning the increase is very fast, but slows down with time after long-time exposure.

4.4.5.4 C(1s) spectra

The carbon bonds identified by XPS from intermetallic thin films are a result of surface contamination from the environment and organic solvents used for cleaning the samples. Fig. 4.9(a-c) shows the HR-XPS spectra recorded for aged intermetallic thin films recorded in the binding energy regions of carbon. The Gaussian de-convolution of the HR-XPS were used to identify the binding energy peaks.

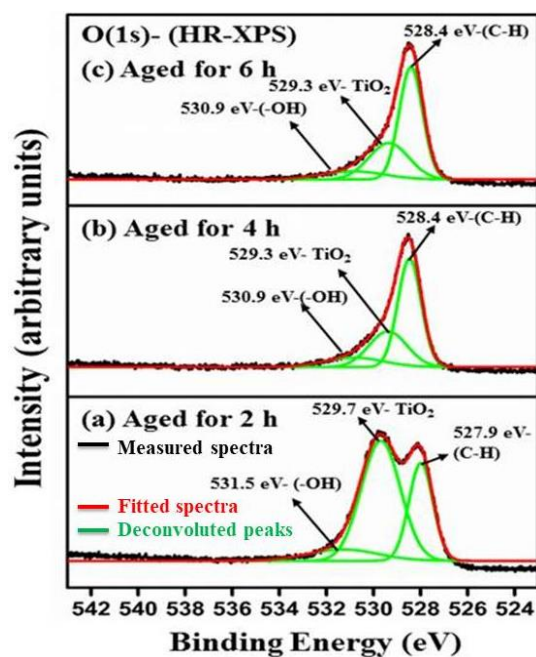


Figure 4.8 Gaussian de-convoluted HR-XPS spectrum for O (1s) of intermetallic NiTi thin films annealed at 600°C for 1 h followed by aging at 500°C for (a) 2 h (b) 4 h and (c) 6 h.

Films, aged at 2 h the binding energy peaks are located at 286.8 eV, 284.5 eV, 282.8 eV and 281.5 eV. The binding energy peaks positioned at 286.8 eV and 284.5 eV correspond to (C-O), carbon-carbon (graphitic carbon) and carbon-hydrogen viz. C-C and C-H respectively. The binding energy peaks located at 282.8 eV and 281.5 eV were assigned to Ti-C (Titanium-Carbide) particle formation. Carbon has no measurable solubility and forms entirely Ti-C. The presence of Ti-C particles (which is consuming Ti) increases the Ni concentration in the NiTi matrix and accounts for the lowering of transformation temperatures. Based on the quasi-binary NiTi-TiC eutectic system, the formation of Ti-C in the carbon-containing NiTi SMAs described which has been presented by Du and Schuster (Du et al. 2000). The low carbon content melts with eutectic composition the “eutectic” TiC forms at the eutectic temperature. The heat of formation of Ti-C is $-184 \text{ kcal mol}^{-1}$ but that of Ni-C is not well established and the Ni-C phase diagram does not show stable carbides. The formation of Ti-C is favoured and Ni is segregated out of the Ti-C phase in aged intermetallic NiTi thin films and this phenomenon was attributed to the high affinity of Titanium towards oxygen and carbon under high temperature annealing (Poon et al. 2005). As the aging time is increased from 2 h to 4 h, four binding energy peaks can be seen and these are located at 286.8 eV, 283.4 eV, 282.7 eV and 281.2 eV respectively. The binding energy peaks positioned at 286.8 eV and 283.4 eV correspond to (C-O) and Si-C formation (Ju et al. 2012, Hishita et al. 2003) The other two binding energies 282.7 eV and 281.2 eV are assigned to Ti-C particles. The films aged at 6 h four binding energy peaks are positioned at 284.9 eV, 282.7 eV, 281.4 eV and 280.9 eV respectively. The binding energy peak positioned at 284.9 eV is assigned to carbon-carbon (graphitic carbon) and carbon-hydrogen viz. C-C and C-H respectively. The binding energy peaks located at 282.7 eV, 281.4 eV and 280.9 eV are assigned to Ti-C species (particles). The deconvoluted curves of films aged at 2 h (Fig. 4.9(a)) has showed C-O, C-C, C-H and Ti-C bond formation, whereas the deconvoluted curves of films aged at 4 h (Fig. 4.9(b)) has exhibited C-O, Si-C and Ti-C bond formation. The deconvoluted curves of films aged at 6 h (Fig. 4.9(c)) have revealed C-C, C-H and Ti-C bond formation. It is clear from the above analysis that the Ti-C content is increased with respective to the aging time. This is due to the stable carbide formation of carbon in the quasi-binary NiTi-TiC eutectic system.

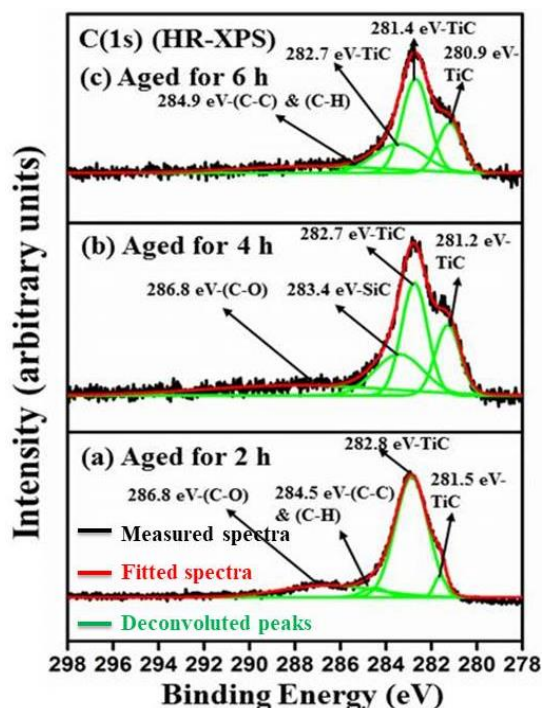


Figure 4.9 Gaussian de-convoluted HR-XPS spectrum for C (1s) of intermetallic NiTi thin films annealed at 600°C for 1 h followed by aging at 500°C for (a) 2 h (b) 4 h and (c) 6 h.

HR-XPS clearly indicated that the aged intermetallic NiTi thin films are highly sensitive to oxygen and carbon and forms TiO₂ oxide layer onto the film surface and Ti-C particles in the Ni-rich precipitates. The larger TiO₂ crystal structure is accommodated by Ti content that move towards the film surface upon oxidation of Titanium, leaving a Ni-rich matrix trapped behind. The TiO₂ layer present on the surface of aged intermetallic NiTi thin films are useful for the corrosion resistance and bio-medical applications (Chrzanowski et al. 2008, Hansen et al. 2015) Detailed investigations have to be done such as optimized preparation and modification processes for passivation layer (TiO₂) and prevention of film surface oxide layer from degradation to use these films in medical applications.

4.5 CONCLUSIONS

- As-deposited films were observed to be amorphous in nature. The films were crystallized by heat treatment at 600°C for 1 h and were studied for the aging effect on these films at 500°C for 2 h, 4 h and 6 h.

- The heat treated films were crystallized and age-treated films showed Ni₃Ti phase along with intermetallic precipitates.
- From FESEM and AFM analysis, it was found that the size of the precipitates increased with increase in aging time.
- The hardness and elastic moduli values are increasing with increase in aging time due to incoherency of the Ni-rich matrix.
- As soon as the films were exposed to the ambient atmosphere carbon and oxygen content increased on the surface and diffused into the surface and sub layers.
- It is clearly resolved from X-ray photoelectron spectroscopy (XPS) studies that aged films have the ability to form adherent and natural titanium dioxide protective layer on the film surface with Ni-rich matrix trapped behind most likely in the sub layers of NiTi along with TiC precipitates.

CHAPTER 5

INFLUENCE OF ANNEALING TEMPERATURE ON THE STRUCTURAL, MORPHOLOGICAL, MECHANICAL AND SURFACE PROPERTIES OF NEAR EQUIATOMIC NITI THIN FILMS

This chapter begins with a discussion of growth and characterization of DC magnetron sputtered near equiatomic NiTi alloy thin films. Also, it contains the effect of annealing temperature on the structural, morphological, mechanical and surface properties of near equiatomic NiTi thin films.

5.1 INTRODUCTION

Sputtered NiTi thin films have been widely investigated in microelectromechanical (MEMS) systems and miniature robotics due to their unique properties such as super elasticity, the shape memory effect, high damping capacity, high work output per unit volume and biocompatibility. They are promising and high performance materials for microfabrication facilitating integration in MEMS systems comprising of micro actuators and micro sensors (Fu et al. 2004, Tillmann and Momeni 2015). The load bearing capability and superelasticity make them appropriate materials for cavitation erosion coatings (Tillmann and Momeni 2015). NiTi thin films exhibit fast cooling rates in comparison to bulk materials due to their higher surface to volume ratio and significant increase in the heat transfer rate, and therefore possesses a lower response time (Tillmann and Momeni 2015). The theoretical and experimental predictions show that these films are suitable material for the thermomechanical data storage technology (Crone and Shaw 2004). NiTi thin films can be employed to engineer surface coatings with excellent tribological and self-healing properties (Tillmann and Momeni 2015) (Shih et al. 2001). Physical vapor deposition technique by magnetron sputtering seems to be the best method to fabricate NiTi alloy thin films. The phase

transformation temperatures of NiTi thin films are extremely sensitive to the Ni elemental content and a shift of 1 at.% Ni can decrease the transformation temperature by 100°C. The understanding and control of the mechanical and surface characteristics of these thin films are prominent issues in the application level. NiTi thin films can easily be exposed and show interaction with the atmosphere, irrespective of applications in micro-devices or functional surface coatings. The main objective of this work is to study the influence of annealing temperature on structural, morphological, mechanical and surface properties of near equiatomic NiTi thin films. Similar type of work have been reported in the literature for NiTi thin films (Tillmann and Momeni 2015, Surbled et al. 2001, Kumar et al. 2009, Fu and Du 2003, Sharma and Mohan 2013, Lee et al. 2006).

In the present work, we have investigated the crystallization, nucleation, grain growth and recrystallization phenomena in near equiatomic NiTi thin films during annealing at different temperatures. The influence of annealing on an intermediate R-phase (rhombohedrally distorted martensite phase) formation at different temperatures along with their mechanical properties (elastic modulus and hardness values) have also been studied. It may be noted that the main focus was on the surface characteristics of NiTi thin films obtained by XPS and their elemental composition and the presence of various chemical states. The mechanical and surface characteristics of near equiatomic NiTi thin films are strongly affected by the composition of the films, deposition parameters, annealing temperature and aging time.

5.2 EXPERIMENTAL

The detailed experimental procedure for the preparation of near equiatomic NiTi thin films have been discussed in the chapter-3, section 3.2. As-deposited films were annealed in vacuum at 350, 450, 550 and 650°C for 1 h. The annealing temperature was elevated at a ramp rate of 25°C/min. After annealing the samples were cooled to room temperature and the cooling rate was kept at 2°C/min. The annealing temperature was selected based on the Ni-Ti alloy phase diagram so that the alloy composition would exist in the single phase Ni-Ti region.

5.3 THIN FILM CHARACTERIZATION

The detailed description regarding thin film characterization techniques carried out for near equiatomic NiTi thin films have been discussed in chapter-3, section 3.3. Atomic force microscope (AFM Model: Bruker Innova) under tapping mode was used to examine the roughness and film topography. The elemental composition of these thin films was determined to be Ni-50.3 and Ti-49.7 at.%.

5.4 RESULTS AND DISCUSSIONS

5.4.1 Structural analysis

Figure 5.1(a-d) shows the X-ray diffraction patterns plotted for annealed thin films. After annealing, these thin films have exhibited sharp peaks indicating crystalline nature. The existence of several diffraction peaks indicates that the films are polycrystalline in nature. Moreover, in spite of similar film composition the samples have exhibited distinct microstructures at room temperature. The post-deposition heat treatment promoted changes in the film microstructure that played an important role on the phase transformation behavior of the films. By employing an annealing technique, NiTi thin films have shown a significantly higher nucleation and growth rates, leading to a higher amount of crystallized NiTi material or a higher degree of crystallization (Lee et al. 2006, Wang and Vlassak 2006). In case of the qualitative analysis of crystallization kinetics reaction, the reaction rate is directly related to the activation energy (Q) and the temperature (T) and proportional to $\exp(-Q/kT)$, where k is a Boltzmann constant in the Arrhenius exponential relationship (Tillmann and Momeni 2015). More thermal energy or higher atomic diffusion is required to initiate the crystallization process. Zhang et al. examined the NiTi thin films by employing an annealing technique at various temperatures and reported that the degree of crystallinity raises by increasing the temperature and causes enhancement in the precipitation (Zhang et al. 2007). The annealed films showed the presence of R-phase as a major constituent. Moreover, X-ray diffraction patterns exhibited various diffraction peaks corresponding to Ni-rich precipitates; they were identified as Ni_3Ti and Ni_4Ti_3 . These Ni-rich precipitates may be either due to high temperature

annealing, or high temperature holding (Allafi et al. 2002, Martins et al. 2006). The B19' phase (monoclinic martensite phase) was disappeared for samples which were annealed above 350°C. Martins et al. confirmed the presence of B19' at room temperature could be probably due to higher biaxial stress (Martins et al. 2010).

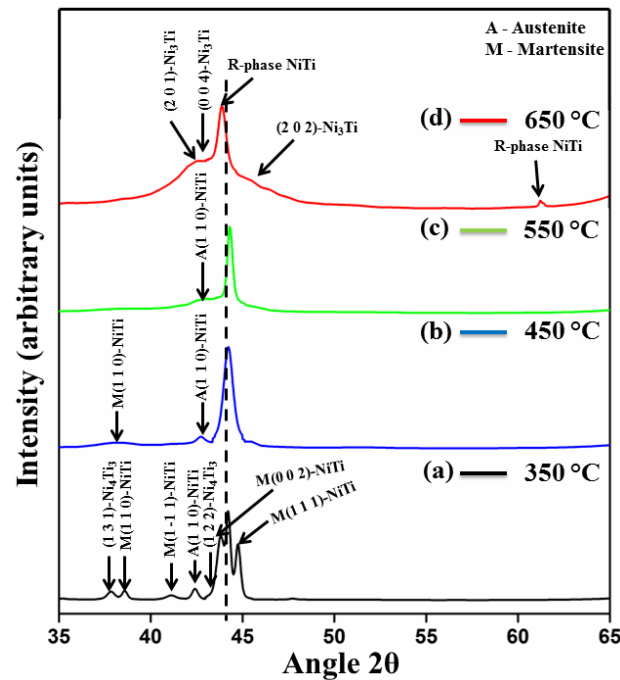


Figure 5.1 XRD patterns of near equiatomic NiTi thin films annealed at (a) 350°C (b) 450°C (c) 550°C and (d) 650°C.

In the present investigation, the diffraction peaks located at 42.48° and 43.41°, 46.42° positions were assigned to (2 0 1), (0 0 4) and (2 0 2) planes of Ni₃Ti precipitates. The diffraction peak located at 37.77° is assigned to (1 3 1) plane of Ni₄Ti₃ precipitate. A few diffraction peak matching of Martensite phase was also observed in annealed films, which were located at 38.22°, 38.61°, 41.19°, and 43.62° assigned to (1 1 0), (1 1 0), (1 -1 1) and (0 0 2) planes of martensite phase, respectively. The diffraction peaks located at 42.37°, 42.81° and 42.60° were assigned to (1 1 0) plane of Austenite phase, respectively. The small amount of Austenite phase, Martensite phase, Ni₄Ti₃ and Ni₃Ti precipitates present in the samples were probably due to incomplete material transformation nearby the substrate interface due to substrate constraints (Su et al. 1994, Martins et al. 2008).

The average crystalline size or particle size was calculated from the line broadening of the X-ray diffraction lines, using the Scherrer's formula (Smilgies 2009) after removing the instrumental broadening. The strain induced broadening in the film due to crystal imperfection and distortion was estimated using the Stokes-Wilson equation (Thool et al. 2014). Estimated crystallite size and lattice strain corresponding to the R-phase peak broadening of the films annealed at 350, 450, 550 and 650°C was found to be 14.8, 23.4, 32.8 and 25.2 nm and 0.0062, 0.0043, 0.0021 and 0.0094 respectively. The crystallite size increased as the temperature increases from 350-550°C but decreased at 650°C due to recrystallization and the strain values vice versa. At higher temperatures (at 650°C), the new strain free grains nucleate and grow inside the old distorted grains and at the grain boundaries to replace the deformed grains produced by the strain hardening. Recrystallization mainly depends on the temperature, time and the amount of strain hardening of the material. The more strain hardening, the lower is the temperature at which recrystallization occurs. The greater the strain hardening, the more nuclei for the new grains, resulting in small grain size. The crystallite size and strain values are shown in Table 5.1.

5.4.2 Surface morphology

Figure 5.2(a-d) shows cross sectional micrographs of the annealed NiTi thin films. The FESEM micrographs clearly show the distinct morphology with annealing. The films showed dense, a complete outward grain growth and flakes type formation in the cross-sectional surface morphology. The studies conducted by Zhang et al. revealed that increasing the annealing temperature can improve the movement of absorbed atoms and initiate the diffusion of atoms to the favorable energy positions (Zhang et al. 2007). The films annealed at 350°C (Fig. 5.2(a)) showed randomly grown fibrous type microstructure indicating the films were not fully crystallized. At low temperatures the diffusion rate was low, but the driving force for nucleation was high, but at higher temperature the reverse was true. There was no clear grain formation due to the non-initiation nature of atomic migration. At 450°C the morphology of the film changed to clear surface grain growth as it can be noticed from Fig. 5.2(b). This indicates nucleation stage when several nuclei that had just

formed due to the initiation of atomic migration forming grains. The change in the surface morphology occurred due to the competing nature of the nucleation and the active growth rate of grains. As the annealing temperature was changed further from 450°C to 550°C (Fig. 5.2(c)) the diffusion rate increased and grains tend to grow due to the improved crystallization (higher activation energy). The larger grain size confirmed the reduction in the grain boundaries. As the annealing temperature is raised further from 550°C to 650°C (Fig. 5.2(d)) interestingly, we have noticed a flake type of formation in the cross sectional morphology. At 650°C the deformation increased due to the recrystallization phenomenon. At higher temperatures, strain free grains are created during the restoration process of recrystallization. This occurs due to the short range diffusion enabled by the high temperatures (Weihnacht and Bruckner 2002). An increase in the deformation during the diffusion process increases the rate of nucleation faster than the growth rate. This type of behavior is supported by the XRD studies (crystallite size variation) as discussed earlier in section 5.1. Another reason for the flake type of film formation is due to the different type of fracture surface. Further, flake type of film morphology depends on the mechanical properties of the material. The grain size values are presented in Table 5.1.

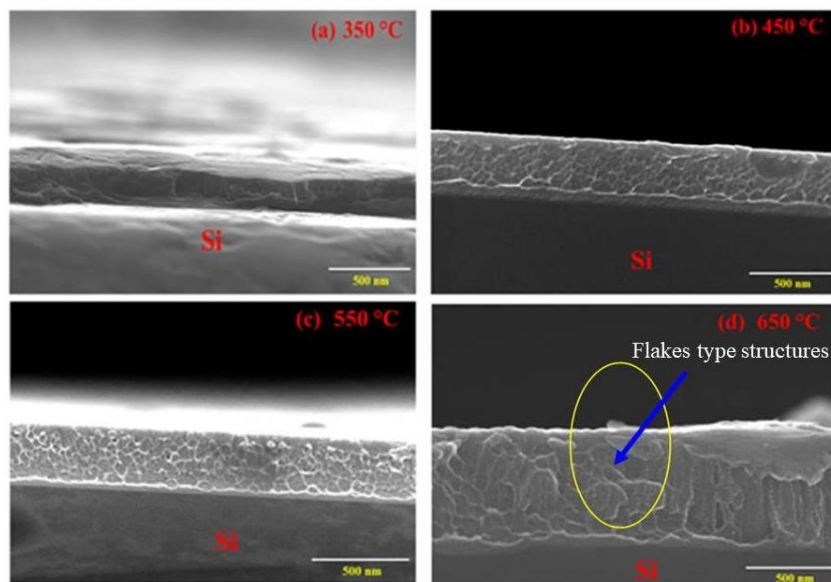


Figure 5.2 Cross sectional FESEM micrographs of near equiatomic NiTi thin films annealed at (a) 350°C (b) 450°C (c) 550°C and (d) 650°C.

5.4.3 Surface topography analysis

Fig. 3a-d show three dimensional representations of the annealed thin films deduced from atomic microscopy on the scan area of $0.5 \mu\text{m} \times 0.5 \mu\text{m}$. It is possible to distinguish the grain formation and confirm their nanometric character from the AFM topography. Table 1 shows the surface roughness parameters like R_q (root mean square), R_a (average roughness) and R_{max} (peak to valley difference) obtained from AFM. At a lower annealing temperature the roughness values were smaller when compared to the higher annealing temperatures.

The films annealed at 350°C (Fig. 5.3(a)) exhibits wavy topography formed by undulating ridges bound by shallow and wide depressions. At lower temperatures there was no clear grain formation due to partial crystallization of films. Fu et al. confirmed that the substantial increase in surface roughness is due to surface relief or self-accommodation caused by martensitic transformation (i.e., formation of twinning martensite structures, such as martensitic pins, rods, branches, plates, etc., upon cooling) (Fu et al. 2005a). As the annealing temperature increases from 350°C to 450°C (Fig. 5.3(b)) the wavy topography disappears and the surface morphology shows the grain formation due to the initiation of atomic migration (the activation energy increases with increase in annealing temperature). At 550°C (Fig. 5.3(c)) the agglomeration of the grains takes place and leads to the formation of larger grains. The irregularities (abnormal grain growth) in the grain growth make the height variance in the grains. As the annealing temperature is raised from 550°C to 650°C (Fig. 5.3(d)) the film surface topography is changed due to the recrystallization phenomena. When the annealing temperature increase, the film will start to yield and also the minimum strain energy will control the grain growth. Recrystallisation is the process in which deformed grains are replaced by strain-free (defects free) grains. In this process the initial strain free grains with certain volume (size) leads to finer recrystallized grains by nucleation (i.e. migration of pre-existing high angle boundaries induced by deformation). The driving force for recrystallisation is the stored strain energy in the thin film material. During recrystallisation, the stress-free grains nucleate and grow until the original grains fully consumed (Boulesteix et al. 1969).

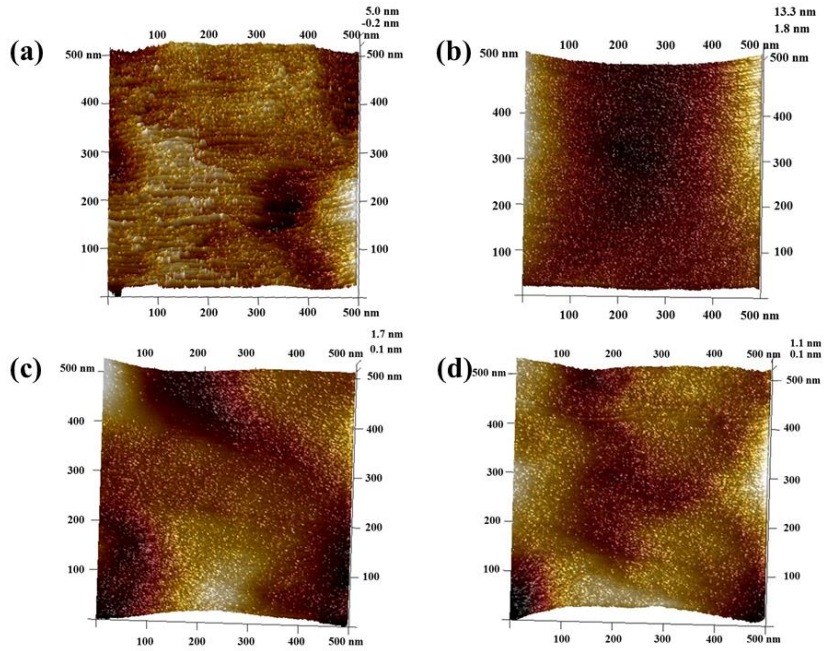


Figure 5.3 AFM (3D surface morphology) micrographs of sputter deposited near equiatomic NiTi thin film vacuum annealed for 1 h at (a) 350°C (b) 450°C (c) 550°C and (d) 650°C.

Table 5.1. Various parameters of the near equiatomic NiTi thin films annealed at 350, 450, 550 and 650°C.

Annealing temperature (°C)	Grain size (nm)		Strain	AFM			
	XRD along R-phase	FESEM		Scan size (μm^2)	Rq Roughness (nm)	Ra Roughness (nm)	Rmax Roughness (nm)
350	14.8	25.9	0.0062	0.5 x 0.5	3.15	2.49	26.7
450	23.4	43.2	0.0043	0.5 x 0.5	4.30	3.62	44.1
550	32.5	49.8	0.0021	0.5 x 0.5	6.40	4.50	51
650	25.2	19.3	0.0094	0.5 x 0.5	2.27	1.63	20.5

5.4.4 Nanoindentation

The nanoindentation tests provide the variation of indentation load, P , as a function of indentation penetration depth, h . For evaluation of mechanical properties, load-displacement ($P-h$) curves obtained from the nano indentation are shown in Fig. 5.4

(a-c). Nine indents were made in different regions, each spaced 4 μm apart, for each annealed condition with a peak load of 1.5, 2 and 2.5 mN. Each indent consisted of a 6-second loading, 10-second holding and a 6-second unloading segments. The hold segments were maintained to diminish the time dependent effects (creep effects) produced in the specimen. All nanoindentation tests were executed at room temperature with a Berkovich (a three sided pyramid shape tip) diamond indenter and the tip radius of curvature being 200 nm by fixing samples firmly to the sample holder.

The samples show consistent behavior over the areas tested indicated homogeneity. The load-displacement curves of annealed films exhibited overall elasto-plastic response. During indentation withdrawal the unloading curve (plastic response) is smooth showing that it is purely the recovery on relaxation. Annealing leads to an increase in strength by grain boundaries and dislocation interactions resulting in an increase in average hardness and elastic moduli. Phase segregation is also a cause of the increase in average hardness and elastic moduli (Geetha Priyadarshini et al. 2011). This can be attributed to the combined effects of crystallization, nucleation and grain growth phenomena and phase segregation which are supported by XRD, FESEM and AFM (Fig. 5.1, 5.2 and 5.3) analysis.

The hardness, elastic moduli, depth recovery ratio, and wear resistance values of these thin films are presented in Table 5.2. The indentation depth should be less than 10% of the film thickness that play an important role in the deformation process that take place around indenter. Oliver and Pharr method were used to estimate the hardness (H) and elastic modulus (E_r) from the $P-h$ curve. In case of annealed thin films, a large force is mandatory to reach the maximum indentation depth due to the higher hardness of the material. XRD analysis (section 5.1) revealed that the films were well crystallized and possesses dominantly R-phase. The measured elastic modulus values are strongly affected by the film substrate than hardness because the elastic field under the tip is confined to the long range field that extends into the substrate. The Oliver-Pharr method is well-known for monolithic materials. This method is appropriate to the film-substrate system if the film is having a suitable thickness or if the film and substrate have similar elastic properties.

Even though the films annealed in high vacuum Nickel and Titanium are highly sensitive to the residual oxygen. The measured hardness and elastic modulus values are expected to be affected by these oxide layers. To limit the oxide layer effects on the measured mechanical properties deeper indentations are required. In this work, the contact depth is maintained at ~30% of film thickness. The mechanical hysteresis follows the increasing trend when the films annealed from 350-550°C (Fig. 5.4(a-c)) at different loads owing to the high degree of crystallization dominantly R-phase, nucleation and grain growth. The films annealed at 650°C shows a decrease in the mechanical hysteresis and noticed a shift in the total $P-h$ loop of the films at different loads (Fig. 5.4(a-c)). This occurs due to the Ni_3Ti precipitation formation and also the recrystallization process that initiates change in grain deformation supported by XRD, FESEM and AFM studies (section 5.1, 5.2 and 5.3).

In this work, the stress-induced phase transformation phenomena are also a reason for the variation in elastic modulus. The possible variation in elastic moduli, associated with stress induced phase transformations can be measured by comparing the previously reported bulk and thin film elastic moduli of NiTi alloys. The bulk NiTi alloy has been shown to have an elastic modulus of 65 GPa (Fu et al. 2001). In contrast, the martensitic phase and austenitic NiTi thin films have been reported to have an elastic modulus 60 GPa and 84 GPa respectively (Fu et al. 2001). Kumar et al. have reported that NiTi thin films have an elastic modulus of ~115 GPa (Kumar et al. 2009). The elastic modulus of intermetallic NiTi thin films 150 GPa has been reported by Kumar et al. (Kumar et al. 2006). Mohri et al. investigated the bilayer NiTi thin films and reported an elastic modulus of 87.4 ± 1.2 GPa (Mohri et al. 2015). Thomasova et al. have been reported the elastic modulus (martensite phase) of 78 GPa for resonant ultrasound spectroscopy subjected NiTi thin films (Thomasova et al. 2015). Huang et al. have been reported the elastic moduli of 89.0 ± 2.1 GPa for Ti-48.3 at.% Ni (martensite) and 92.8 ± 3.1 GPa for Ti-50.8 at.% Ni (austenite) at 110°C, respectively (Huang et al. 2011).

The indentation induced superelasticity effect can be characterized by the depth recovery ratio by using the following equation (Huang et al. 2010):

$$\text{Depth recovery ratio} = \frac{(h_{\max} - h_r)}{h_{\max}} \quad (5.1)$$

Where h_{max} indicates the penetration depth at the maximum load and h_r is the residual depth when the load returns to zero during indentation withdrawal. The depth recovery ratio was increased from 350-550°C but decrease at 650°C as shown in Table 5.2. The increment in the depth recovery ratio could be due to the increase in higher degree of crystallization, nucleation and grain growth. At 650°C, the decrement is probably due to the presence of Ni_3Ti precipitation and also with the recrystallization phenomena.

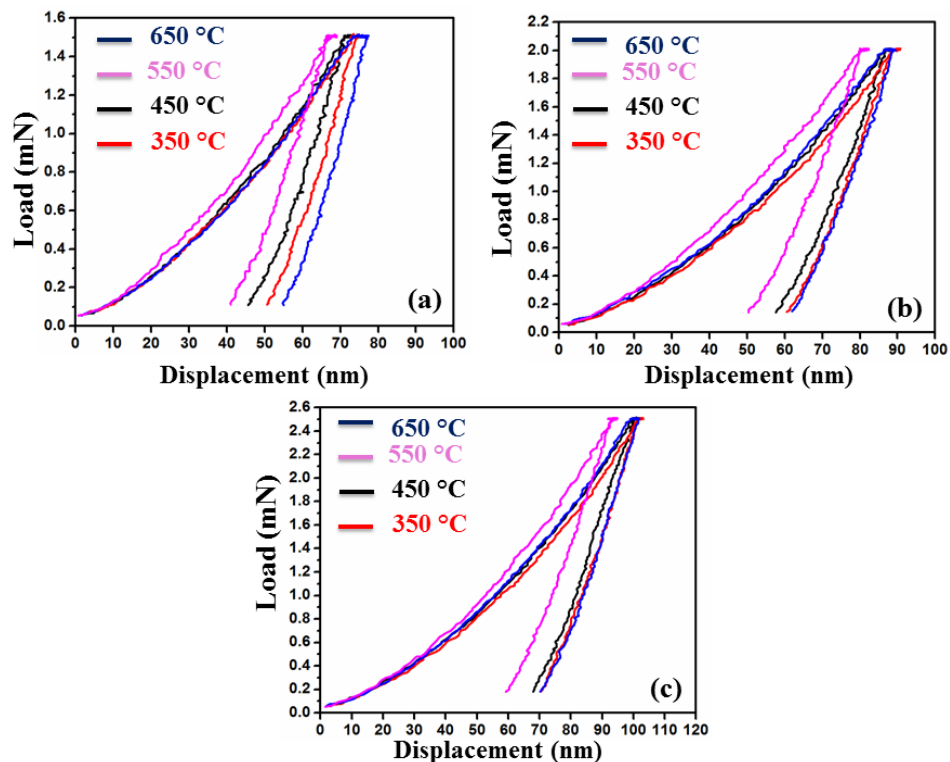


Figure 5.4 Load-displacement curves from nanoindentation experiments performed on the near equiatomic NiTi thin films deposited at room temperature and vacuum annealed for 1 hour at four different temperatures (a) 1.5 mN (b) 2 mN and (c) 2.5 mN.

The significant feature to determine the behavior of wear resistance of the thin film coatings is attributed to the ratio of hardness (H) and elastic modulus (E_r). Ni et al. revealed that the deformation around the indenter surface is due to piling-up and sinking-in and also the tendency of sinking-in increases with increasing H/E ratio (Ni et al. 2004). NiTi thin films consisting of a higher H/E ratio results in smaller

accumulative strain leading into better wear resistance. More fraction of work is consumed during plastic deformation at a relatively lower H/E ratio by which large plastic strain is predictable while contacting material (Sato et al. 2008). Near equiatomic NiTi thin films possess a dominant R-phase, Ni_4Ti_3 and Ni_3Ti precipitates. These precipitates are capable to increase the strength of R-phase, thereby limiting the degree of plastic deformation in load cycling.

Table 5.2 The hardness, elastic modulus, depth recovery ratio, and wear resistance parameters of near equiatomic NiTi thin films annealed at four different temperatures for different loads.

Load (mN)	Annealing temperature (°C)	Hardness (H) (GPa)	Elastic modulus (E_r) (GPa)	Depth recovery ratio	Wear resistance (H/E_r)
1.5	350	7.50±0.2	148.65±3.1	0.32±0.02	0.0504±0.0004
	450	8.58±0.4	162.47±1.0	0.36±0.01	0.0528±0.0002
	550	9.69±0.5	167.23±3.5	0.39±0.02	0.0579±0.0015
	650	6.85±0.3	142.36±1.3	0.29±0.04	0.0468±0.0003
2	350	7.43±0.4	147.42±3.5	0.32±0.01	0.0494±0.0006
	450	8.40±0.1	162.47±1.4	0.33±0.01	0.0504±0.0002
	550	9.50±0.5	164.16±2.7	0.37±0.02	0.0578±0.0012
	650	7.03±0.2	141.55±5.3	0.30±0.04	0.0483±0.0005
2.5	350	7.60±0.1	153.86±3.6	0.32±0.01	0.0519±0.0003
	450	8.57±0.3	158.55±2.4	0.33±0.01	0.0529±0.0004
	550	9.60±0.5	163.45±5.1	0.36±0.04	0.0587±0.0017
	650	7.26±0.4	144.32±3.2	0.31±0.03	0.0482±0.0008

5.4.5 X-ray photoelectron spectroscopy analysis

The surface characteristics of as deposited thin films annealed at various temperatures for 1 h were recorded by XPS as shown in Fig. 5.5(a-d). The dominant surface

elements are Nickel (Ni), Titanium (Ti), Carbon (C) and Oxygen (O). The surface elemental compositions of annealed films are shown in Table 5.3. As soon as the films exposed to ambient conditions, Oxygen and Carbon were adsorbed on the film surface. The spectral information and individual chemical state for each dominant element state are explained below.

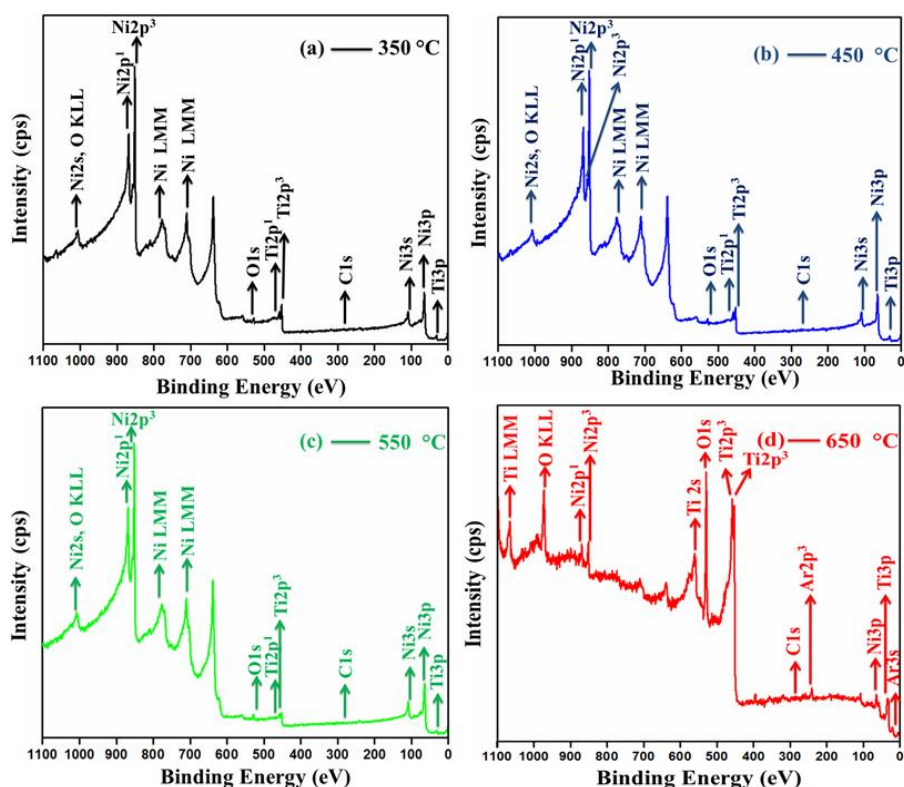


Figure 5.5 XPS survey spectrum obtained for near equiatomic NiTi thin films annealed at (a) 350°C (b) 450°C (c) 550°C and (d) 650°C.

Table 5.3 Surface elemental composition evaluated from an XPS survey spectrum of near equiatomic NiTi thin films.

Annealing Temperature (°C)	Ti (2p)	Ni (2p)	C (1s)	O (1s)
350	20.8	63.8	10.1	5.4
450	24	68.9	< 1	7.1
550	13.4	72.3	4.5	9.8
650	45	2.1	<1	52.9

5.4.5.1 Ni (2p) spectra

Figure 5.6(a-d) shows the HR-XPS spectra recorded for Ni (2p) spectra of annealed films. The binding energy peaks were identified by Gaussian deconvolution of the HR-XPS. The deconvoluted Ni (2p) of annealed films consists of four binding energy peaks that are located at different binding energy peaks. The binding energy peaks are characterized by a 2-2.5 eV shift in binding energy over Ni species. Due to chemical effects and matrix effects such as variances in crystal potential, relaxation energy and work function the shifts in binding energy occurs (Kim and Winograd 1975). The binding energy peak centered at 869.2 eV was corresponds to a metallic Ni state of Ni $2p_{1/2}$. Gao et al. reported that the binding energy peak at 869.2 eV with a spin orbital spectral line of Ni 2p, coincides with the appearance of the zero valence state of Ni (Gao et al. 2012). The binding energy peak centered at 858.4 eV was attributed to bulk nickel oxide (854.0 eV) explained based on the quantization effect reported in the literature (Uhlenbrock et al. 1992, Singh et al. 2014). However, another small binding energy peak or satellite structure located at post annealed temperatures, 350°C-851.9 eV, 450°C-852.8 eV, 550°C-852.4 eV and 650°C-852.2 eV occurs due to reorganization of the valence electrons as photoelectrons are emanated from the core levels attributed to the metallic Ni state. The binding energy peak located at 851.4 eV corresponds to metallic Ni spin states of Ni $2p_{3/2}$. It is observed from the HR-XPS studies that Ni content is increasing from 350°C to 550°C but decreases at 650°C as shown in the Table 5.3. The reduction in Ni content occurs due to the formation of TiO₂ surface layer with metallic Ni and Nickel Oxide (NiO). Chu et al. studied that oxidation of NiTi thin films initiated the Ni species to be drifting from the surface regions into a deeper inner layer which consists of Ni₃Ti phase (Chu et al. 2006). It was proposed that there exists an inner Ni₃Ti layer and outer TiO₂ and a phase of Ti in solid solution in Ni. Due to diffusion of oxygen ion and metal ion in thin films, there occurs oxide growth on the surface layer. The difference in activation energies is increasing with increasing temperature. The metal ion diffusion dominates oxygen ion diffusion and it also increases with increasing temperature. It is also proposed that Titanium, being a highly reactive element compared to Nickel, segregates to the film

surface and oxidizes to form a titanium dioxide layer with Ni species underneath the layer (Fu et al. 2005).

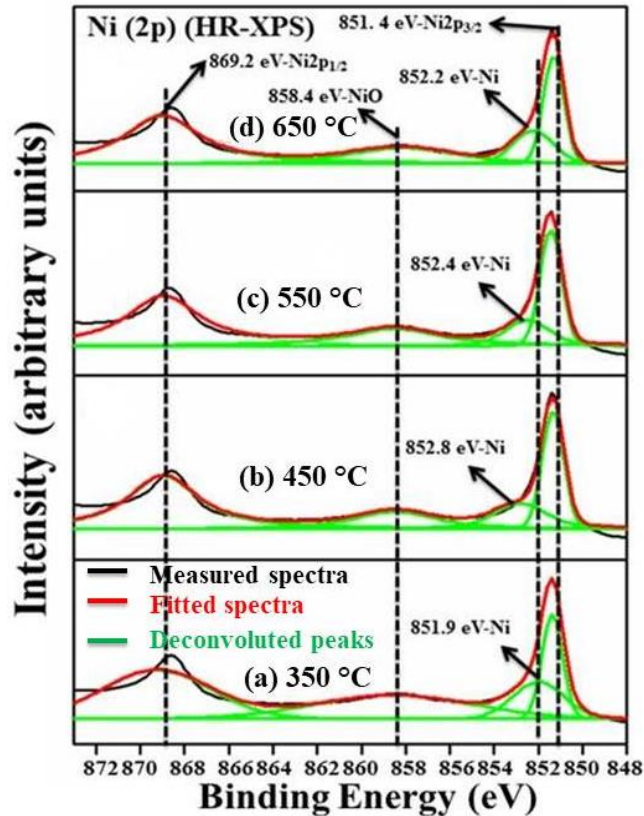


Figure 5.6 Gaussian de-convoluted HR-XPS spectrum for Ni (2p) of near equiatomic NiTi thin films annealed at (a) 350°C (b) 450°C (c) 550°C and (d) 650°C.

5.4.5.2 Ti (2p) spectra

Figure 5.7(a-d) shows the HR-XPS spectra recorded for Ti (2p) spectra of annealed films. The deconvoluted Ti (2p) spectra of annealed films consists of three binding energy peaks that are located at 458.8 eV, 453.5 eV and 452.8 eV. The binding energy located at 458.8 eV corresponds to $2p_{3/2}$ spin states for Ti^{4+} (TiO_2). Ti has a strong affinity for oxygen and forms TiO_2 oxide layer on the film surface (Chrzanowski et al. 2008, Cao et al. 2016). The binding energy peaks positioned at 453.5 eV and 452.8 eV were attributed to metallic Ti. The binding energy peaks positioned at 453.5 eV and 452.8 eV are characterized by a 2-2.5 eV shift in binding energy over Ti species. Titanium content increases from 350-450°C but it decreases at 550°C and then it

again increases at 650°C, as shown in Table 5.3. In case of NiTi thin film the diffusion process between Ni and Ti starts at 300°C. As the annealing temperature changes from 350°C to 450°C (Fig. 5.7(b)) diffusion starts and Titanium typically exists in the metallic state, due to the significant inter-diffusion between the Ni and Ti beneath the surface. As the temperature progress further from 450-550°C (Fig. 5.7(c)) the Titanium content is decreasing due to the higher inter-diffusion of Ni and Ti. Due to this reason it is clear that the oxygen ion diffusion dominates metal ion diffusion at lower temperatures, but increases with raise in temperature. At 650°C (Fig. 5.7(d)) the films show the increment in the metallic state of Titanium. The promising oxidation behavior of NiTi could be due to the decomposition of Ti oxide by the nearby metallic Ti at the oxide/alloy interface. The metal oxide formation is prominent because the Titanium reacts with water, oxygen and atmosphere.

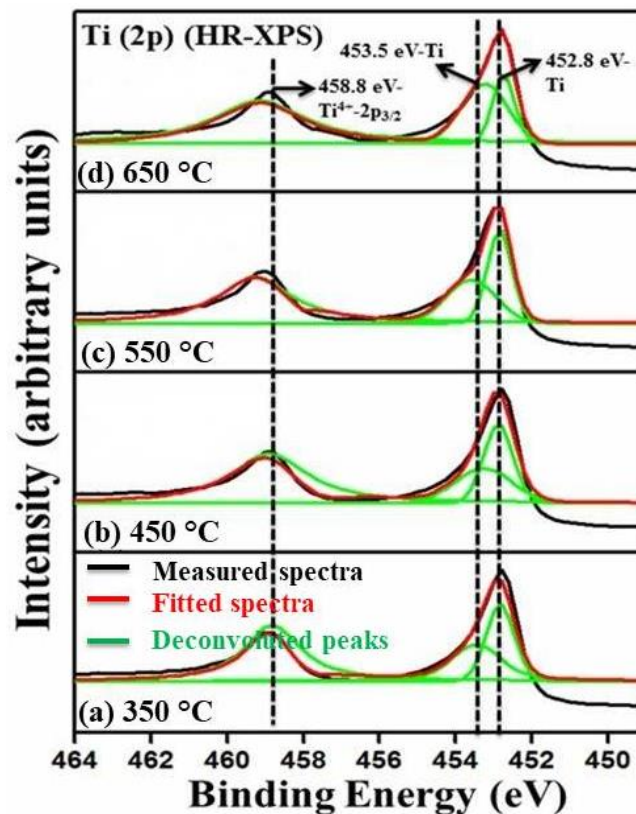


Figure 5.7 Gaussian de-convoluted HR-XPS spectrum for Ti (2p) of near equiatomic NiTi thin films annealed at (a) 350°C (b) 450°C (c) 550°C and (d) 650°C.

5.4.5.3 O (1s) spectra

The ionic transport through impurities in the Ar gas or the residual gases in the spectrometer chamber causes the oxygen content in the annealed films. HR-XPS spectra recorded in the binding energy regions of Oxygen are shown in the Fig. 5.8(a-d). The Gaussian deconvoluted binding energy values are consistent with the reported values in literature (Bukhtiyarov et al. 2006). The films annealed at 350°C exhibits four binding energies that are located at 531.1 eV, 530.4 eV, 529 eV and 528.5 eV as shown in Fig 5.8(a). The binding energy peak situated at 531.1 eV and 530.4 eV corresponds to metal hydroxide (-OH) formation (Armitage and Grant 2003). The binding energy peak positioned at 529 eV initiates from O^{-2} or TiO_2 (metal oxide) formation which is supported by the Ti (2p) high resolution spectra, as shown in the section 5.4.5.2. The binding energy peak located at 528.5 eV correspond to nucleophilic oxygen C-H bond which is due to the interaction of oxygen with ethene content of the atmosphere (Du and Schuster 1998). The films annealed at 450°C (Fig. 5.8(b)) shows the four binding energies that are positioned at 530.6 eV, 529.3 eV, 528.5 eV and 528.1 eV. The binding energy peak located at 530.6 eV is ascribed to the metal hydroxide formation. The binding energy located at 529.3 eV initiates from O^{-2} or TiO_2 formation. The lower binding energy located at 528.5 eV and 528.1 eV is assigned to nucleophilic oxygen C-H bond. As the annealing temperature increases from 450°C to 550°C (Fig. 5.8(c)), the films reveal four binding energies that are located at 530.9 eV, 530.6 eV, 529.3 eV and 528.8 eV. The binding energy peak located at 530.9 eV and 530.6 eV corresponds to metal hydroxide (-OH) formation. The binding energy peak located at 529.3 eV initiates from O^{-2} or TiO_2 formation. The lower binding energy peak located at 528.8 eV attributed to nucleophilic oxygen C-H bond. As the annealing temperature progress further from 550°C to 650°C (Fig. 5.8(d)) the binding energies are seen at 530 eV, 529.3 eV, 528.8 eV and 528.4 eV. The binding energy peak located at 530 eV corresponds to metal hydroxide (-OH) formation. The binding energy peak located at 529.3 eV initiates from O^{-2} or TiO_2 formation. The binding energies 528.8 eV and 528.4 eV correspond to nucleophilic oxygen C-H bond. From the deconvoluted curves it can be concluded that O (1s) has strong ability to form TiO_2 layer. The oxygen content is increasing from 350-650°C

indicating that increase in the diffusion of Oxygen content and also the reaction of titanium to form titanium dioxide. The increase is very slow at the beginning but increase with raise in annealing temperature due to higher thermodynamic reactive nature.

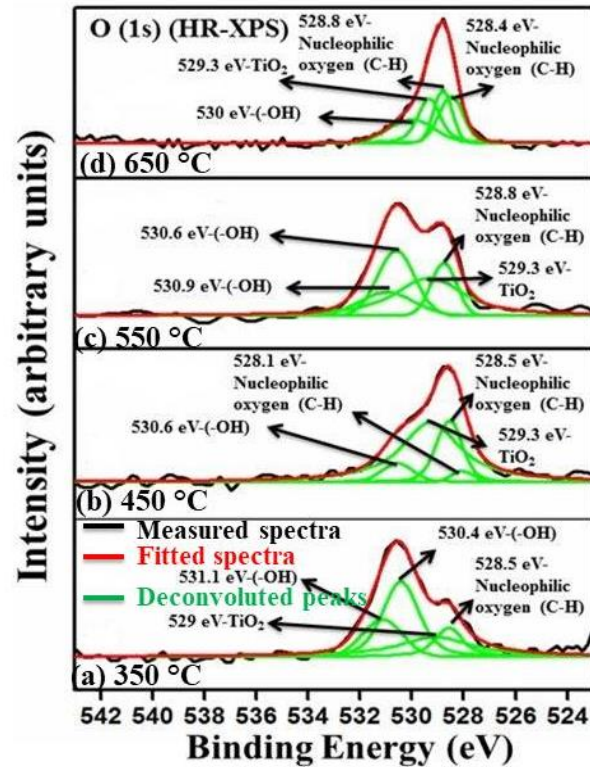


Figure 5.8 Gaussian de-convoluted HR-XPS spectrum for O (1s) of near equiatomic NiTi thin films annealed at (a) 350°C (b) 450°C (c) 550°C and (d) 650°C.

5.4.5.4 C (1s) spectra

Figure 5.9(a-d) shows the HR-XPS spectra recorded in the binding energy region of carbon. Films, annealed at 350°C (Fig. 5.9(a)) the binding energies are located at 284.4 eV, 283.8 eV, 283.4 eV and 283.2 eV. The binding energy peak located at 284.4 eV corresponds to carbon-carbon (graphitic carbon) and carbon-hydrogen viz. C-C and C-H. The binding energy peaks located at 283.8 eV and 283.4 eV are assigned to Si-C (Silicon-Carbide) formation (Ju et al. 2012, Hishita et al. 2003).

The binding energy peak located at 283.2 eV corresponds to Ti-C (Titanium-Carbide) particle formation. The Ni concentration increases due to the presence of Ti-C particles in the NiTi matrix and results in lowering the transformation temperatures.

The formation of Ti-C in the carbon containing NiTi SMA has been reported by Du and Schuster et al. based on the NiTi-TiC eutectic system (Du and Schuster 1998). The heat of formation of Ni-C is not well established, but the heat of formation of Ti-C is $-184 \text{ kcal mol}^{-1}$ and Ni-C phase diagram does not show stable carbides. The segregation of Ni out of NiTi matrix and high affinity of Titanium towards Oxygen and Carbon favored the formation of Ti-C under high temperature annealing (Poon et al. 2005). As the annealing temperature is changed from 350°C to 450°C (Fig. 5.9(b)) we have observed two binding energies that are located at 283.4 eV and 282.9 eV . The binding energy peak located at 283.4 eV and 282.9 eV assigned to Si-C and Ti-C formation. At 550°C (Fig. 5.9(c)), the observed binding energies are located at 284.1 eV , 283.8 eV and 283.4 eV . The binding energy peak at 284.1 eV corresponds to carbon-carbon (graphitic carbon) and carbon-hydrogen viz. C-C and C-H. The binding energy peaks located at 283.8 eV and 283.4 eV corresponds to Si-C formation. Films, annealed at 650°C (Fig. 5.9(d)) the observed binding energy peaks are at 283.7 eV , 283.4 eV and 283.2 eV . The binding energy peaks located at 283.7 eV and 283.4 eV corresponds to Si-C formation and 283.2 eV corresponds to Ti-C particle formation.

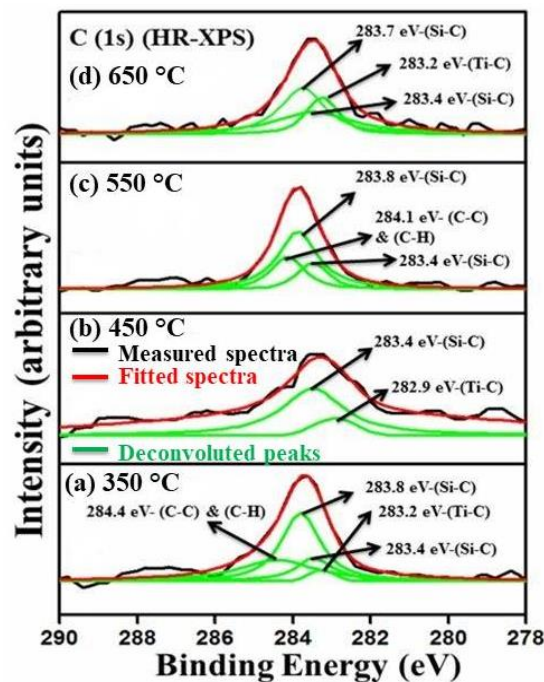


Figure 5.9 Gaussian de-convoluted HR-XPS spectrum for C (1s) of near equiatomic NiTi thin films annealed at (a) 350°C (b) 450°C (c) 550°C and (d) 650°C .

At 450°C the carbon content is decreased in comparison to 350°C due to the presence of an outer surface layer and inner Ni₃Ti layer formation. At 550°C the carbon content is increasing due to the Ti-C particle formation and Ni-C is segregated out of Ti-C. Titanium has a high affinity towards Oxygen and Carbon under high temperature annealing (Tao et al. 2008). Films, annealed at 650°C shows that the Carbon content decreases due to the thermodynamic sensitivity of Titanium and shows strong affinity towards Oxygen to form TiO₂ onto the film surface. TiO₂ has the large unit cell and upon oxidation of Ti, the crystal structure of TiO₂ is accommodated by the Ti content relocate towards the film surface leaving a Ni-rich matrix trapped behind.

5.5 CONCLUSIONS

- In the present investigation, the effect of annealing temperature on structural, morphological, mechanical and surface properties have been studied for the same annealing time at different temperatures.
- Annealed films were crystallized, resulting in the appearance of dominant R-phase along with precipitates. From XRD studies, it was clearly observed that the crystalline size increases from 350 to 550°C but decreases at 650°C due to recrystallization phenomenon.
- The average roughness value increases due to nucleation and grain growth from 350-550°C, but at 650°C it decreases due to the formation of secondary grain growth by recrystallization.
- Higher degree of crystallization, nucleation and grain growth could result in the increase in hardness and elastic modulus values, but decreases due to progression of the recrystallization process.
- Nickel appeared on the surface of the films reduces at higher temperature due to the high affinity of Titanium content. It is clearly resolved from HR-XPS studies that annealed films have strong tendency to form TiO₂ protective layer on the film surface along with Ti-C and Si-C particles (precipitates).

CHAPTER 6

AGING TIME CORRELATION IN DC MAGNETRON SPUTTERED NEAR EQUIATOMIC NITI THIN FILMS

This chapter begins with a discussion of growth and characterization of DC magnetron sputtered near equiatomic NiTi alloy thin films. Also, it contains the effect of aging time on the structural, morphological, mechanical and surface properties of near equiatomic NiTi thin films.

6.1 INTRODUCTION

During the last two decades NiTi shape memory alloy (SMA) thin films are potentially desirable for micro and nano electromechanical systems (MEMS & NEMS), smart sensors, actuators, aerospace, automobile, telecommunication, military and bio-medical fields, because they have a much higher work output per volume and also a significantly improved response speed due to a larger surface-to-volume ratio (Fu et al. 2004, Choudhary and Kaur 2016). NiTi is the most widely used and commercially available SMA for both active and passive applications due to their special ability to respond to stimuli. Because of their unique properties NiTi SMAs have been extensively used as smart and functional materials. Shape memory effect, superelasticity and transformation temperatures of the sputtered NiTi thin films are strongly influenced by metallurgical aspects such as contamination, thermo-mechanical treatment, annealing, aging process or alloy composition, etc. NiTi thin films are sensitive to all these factors and it is apparently an intrinsic disadvantage. However, this sensitivity also provides tremendous flexibility for intended engineering applications.

The effect of aging treatment on the R phase formation in near equiatomic NiTi thin films has been a focus of research for many years and a large volume of experimental information is available in the literature (Tomozawa et al. 2006, Olbricht et al. 2011, Ohkata and Tamura 1996, Khalil-Allafi et al. 2006, Khalil-Allafi et al. 2002, Zheng et

al. 2008, Wang et al. 2014, Dlouhy et al. 2003, Xue et al. 2011, Ravari et al. 2014). The main objective of the present thesis work is to investigate the influence of aging time correlation on structural, morphological, mechanical and surface properties of near equiatomic NiTi thin films. The influence of aging on R-phase formation at different time intervals along with their mechanical properties (elastic modulus and hardness values) have been studied. The presence of various chemical states and the elemental composition of these films have been studied using XPS. This work mainly focuses on the effect of aging time on near equiatomic NiTi thin films when subjected to same annealing temperature, i.e. 600°C for 1 h but at different aging times (at 500°C for 2 h, 4 h and 6 h).

6.2 EXPERIMENTAL

The detailed experimental procedure for the preparation of near equiatomic NiTi thin films have been discussed in the chapter-3, section 3.2. In this thesis work, the near equiatomic thin films were subsequently solution treated or annealed at 600°C for 1 h. The annealing temperature chosen from the Ni-Ti phase diagram in such a way that the Ni-Ti composition lies in the single phase NiTi region. Depending on the TTT (time-temperature-transformation) diagram Nishida et al. [31] studied the influence of aging temperature on bulk Ti-52 Ni alloys. The temperature was elevated to the solution temperature at a gradient speed of 50°C/min. Cooling rate was kept at 2°C/min. The films were aged at 500°C for 2 h, 4 h and 6 h and then cooled to room temperature. The deposition variables such as argon gas pressure, target to substrate distance, base pressure and substrate temperature were kept constant.

6.3 THIN FILM CHARACTERIZATION

The detailed description regarding thin film characterization techniques carried out for near equiatomic NiTi thin films have been discussed in chapter-3, section 3.3. Atomic force microscope (AFM Model: Bruker Innova) under tapping mode was used to examine the roughness and film topography. The elemental composition of these thin films was determined to be Ni-50.3 and Ti-49.7 at.%.

6.4 RESULTS AND DISCUSSIONS

6.4.1 Structural analysis

Figure 6.1(a-e) shows the X-ray diffraction patterns recorded for near equiatomic NiTi thin films deposited at room temperature, vacuum annealed at 600°C for 1 h, and followed by aging at 500°C for 2 h, 4 h and 6 h. In spite of similar elemental composition of the films, the annealed and aged films exhibited crystalline nature with dissimilar microstructure. To control the film microstructure, mechanical properties and the shape memory effect, the heat treatment has been carried out at low temperature for very short time to reduce the reaction between film and substrate. In this work, simple heat treatments were conducted for thin films as they have the benefit of being quite inexpensive and easily incorporated into a device fabrication. The partial crystallization starts at 300°C in NiTi alloy thin films. The annealing and/or aging temperatures has been constrained to a temperature lower than the recrystallization temperature 650°C. At higher temperatures the diffusion rates are high, driving force for nucleation is low where as the reverse is true with lower temperatures. Pelton et al. investigated that 300-500°C heat treatments result in the formation of the Ni₄Ti₃ precipitates and also heat treatments at 500-600°C results in the eventual formation of Ni₃Ti₂ and Ni₃Ti precipitates by dissolution of the Ni₄Ti₃ (Pelton et al. 2000). The time-temperature-transformation (TTT) diagram established by Nishida et al. revealed the precipitation sequence of Ni₄Ti₃ → Ni₃Ti₂ → Ni₃Ti at the temperatures of 500-800°C (Nishida et al. 1986). In the present thesis work, the annealed and aged films exhibited a number of diffraction peaks shown the polycrystalline nature. The dominant diffraction peak present at $2\theta = 44.25^\circ$ confirms the R-phase of NiTi. The XRD pattern revealed the presence of few diffraction peaks corresponding to precipitates named as NiTi-Austenite phase, NiTi-Martensite phase, Ni₃Ti, Ni₄Ti₃ and NiTi₂ respectively. The results of the present study are consistent with the literature which revealed the formation of various Ni-rich precipitates, such as Ni₄Ti₃, Ni₃Ti₂ and Ni₃Ti (Liu et al. 2004, Liu and Favier 2000, Carroll et al. 2004, Jiang et al. 2008, Wang et al. 2015b, Hara et al. 1997) along with R-phase transformation associated with formation of Ni₄Ti₃ (Kim et al. 2004, Zhou et al. 2005) and occurrence of multistage transformation behavior (Fan et al. 2004, Su and Wu

2004). Near equiatomic NiTi alloy thin films usually containing 49-51 at.% Ni, shows a single stage transformation between the B2 austenite and the B19' martensite under solution-treated conditions (Kim et al. 2004, Khalil-Allafi et al. 2004, Liu et al. 2006).

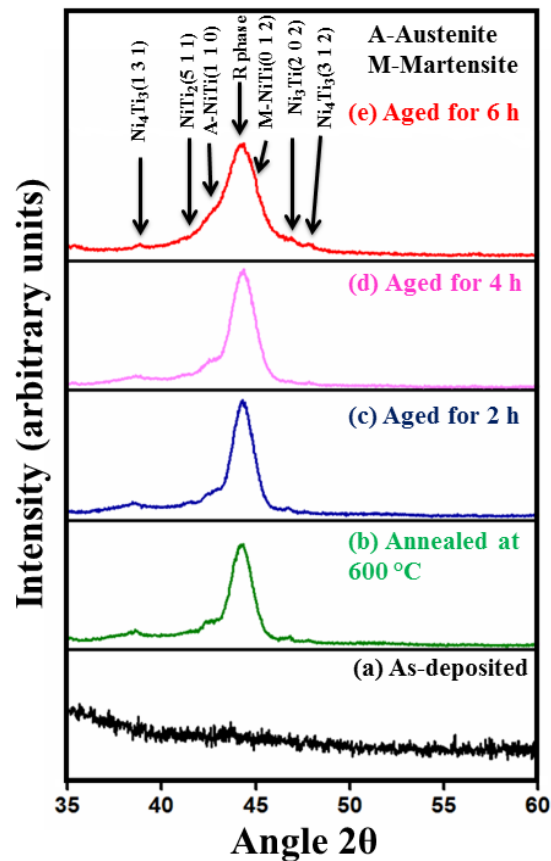


Figure 6.1 X-ray diffraction patterns of near equiatomic NiTi thin films (a) as-deposited (b) vacuum annealed at 600°C for 1 h (c) vacuum annealed at 600 °C for 1 h followed by aging at 500°C for 2 h (d) vacuum annealed at 600°C for 1 h followed by aging at 500°C for 4 h and (e) vacuum annealed at 600°C for 1 h followed by aging at 500°C for 6 h.

At lower annealing temperatures, near equiatomic NiTi thin films (typically below 723 K) results in multiple stage transformation sequences, involving double-stage A→R transformation or double stage R→M transformations. High temperature aging or longer duration generally exhibits single stage, i.e. M↔A transformation (Fan et al. 2004, Wang et al. 2015, Liu et al. 1997). The diffraction peaks located at 38.62°,

41.51°, 42.64°, 45.13°, 46.74° and 47.79° were assigned to (1 3 1), (5 1 1), (1 1 0), (0 1 2), (2 0 2) and (3 1 2) planes of Ni₄Ti₃, NiTi₂, NiTi (Austenite), NiTi (Martensite), Ni₃Ti and Ni₄Ti₃. Martins et al. studied the existence of R-phase in near equiatomic NiTi thin films and investigated that the increase in resistivity in the cooling and heating cycles are due to the lattice distortion and twinning, which are the dominant mechanisms in self-accommodation R-phase transformation (Martins et al. 2010). The presence of Austenite and Ni₄Ti₃ phases are well in agreement with Martins et al. (Martins et al. 2008). Bysakh et al. have reported the presence of Ni₃Ti phase along with Austenite phase of near equiatomic NiTi thin films (Bysakh et al. 2012). The presence of NiTi₂ phase is consistent with the literature supporting the fact that NiTi films form precipitates above 500°C (Sharma et al. 2010, Kumar et al. 2010).

The evolution of NiTi precipitates occurs by the high temperature holding or at high temperature annealing and/or aging time. At lower annealing temperatures and time, the subsequent aging causes precipitates to form within the NiTi grains. As-deposited film exhibits amorphous nature (Fig. 6.1(a)). The films were then solution treated or annealed at 600°C for 1 h. At 600°C the diffusion rate increases and due to atomic migration the grain formation occurs (Fig. 6.1(b)). In the case of films aged for 2 h (Fig. 6.1(c)) amorphous solid particles crystallize with time indicating the initial nucleation of a meta stable, solid phase transforms. As the aging time increases from 2 h to 4 h (Fig. 6.1(d)) the diffusion rate increases in films causing greater precipitation in the NiTi matrix. These Ni-rich precipitates are coherent with the austenite matrix in the NiTi and owing to the strength of this phase (Paryab et al. 2010). As the aging time increases from 4 h to 6 h (Fig. 6.1(e)) the degree of crystallinity increases due to the presence of Ni-rich precipitates, it also causes the precipitates to become spherical in shape and lose their coherency with the austenite matrix.

6.4.2 Surface morphology

Figure 6.2(a-c) shows the cross-sectional view of FESEM micrographs recorded for annealed and/or aged near equiatomic NiTi thin films. The micrographs clearly reveals the distinct microstructure of film annealed at 600°C for 1 h followed by aging at 500°C for 2 h, 4 h and 6 h. The investigation on these films clearly shows

that crystallite nucleation and grain growth were significantly influenced by the annealing and/or aging temperature. Figure 6.2(a) shows crack free solid surface and a clear grain formation due to the initiation of atomic migration. In general the characteristic grain growth is structured by the amount of chemical, the diffusion of atomic species and the topographical disorder (Huang and Ramirez 2009). Once an amorphous material is sufficiently heated, nucleation and grain growth occurs leading to crystallization process. The driving force for an amorphous sample to crystalline depends on the free energy difference between the amorphous and crystalline phases. Annealing and/or aging temperature and time plays a crucial role in thin film formation as it depends on nucleation and grain growth (Fu et al. 2005a, Reddy and Udayashankar 2017). These films primarily forms as thin plates or Guinier-Preston (GP) zones at low annealing temperatures and time, which later forms precipitates within NiTi grains on subsequent aging (Sato et al. 2010).

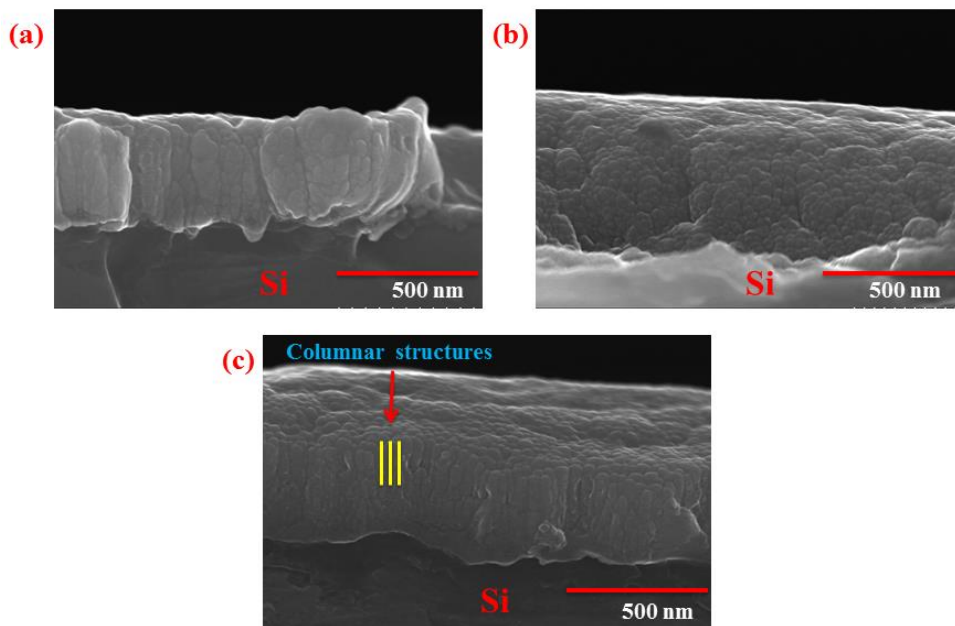


Figure 6.2 Cross sectional FESEM micrographs of near equiatomic NiTi thin film vacuum annealed at 600°C for 1 h followed by aging at 500°C for (a) 2 h (b) 4 h and (c) 6 h.

The thin films aged for 2 h (Fig. 6.2(a)) have low diffusion rate and it leads to lower precipitation rate. Due to the lower Initial diffusion and precipitation rates the Ni

content being lower than the solubility limit in NiTi. The GP zones were formed by the segregation of Ni atoms in NiTi grains. The Ni-rich phase Ni_4Ti_3 preferentially nucleated at the grain boundaries. At low aging times, the solubility of Ni in NiTi will reduce the Ni_4Ti_3 forms to a lesser content. The remaining excess Ni content would be in the form of Ni_3Ti precipitates. Further aging causes greater diffusion and forms bigger precipitates within the NiTi grains, which are incoherent with the NiTi matrix, making them ineffective to the transformation temperature of NiTi B2 matrix (Paryab et al. 2010). Higher temperatures and longer aging times cause greater diffusion. The surface morphology of the films aged for 4 h appears to be due to homogeneous grain growth. Due to the long term aging the precipitates become more spherical in shape and lose their coherency. More incoherency in the NiTi matrix with the austenite matrix forms larger precipitated particles. In the case of films aged at 6 h we have noticed columnar structures which are represented in the Fig. 6.2(c). Crystalline grains always nucleated primarily at the surface in the system, which grew laterally until impingement, and later grew inward to form columnar grains (Callisti et al. 2014, Petrov et al. 2003). The direct consequence of the relation between the crystallization temperature, nucleation and grain growth cause variance in the film surface morphology. The near equiatomic NiTi thin films aged at 2 h and 4 h shows the formation of intermetallic precipitates (From Fig. 6.1). The precipitates increase with increase in aging time. Precipitation results in to nucleation where the drifting atoms group together within the NiTi grains. After aging at 6 h the growth of surface nucleated crystals is rapidly in the lateral direction within the plane of the film followed by significantly slow growth normal to the surface.

6.4.3 Surface topography analysis

Figure 6.3(a-c) represents the typical three dimensional images of near equiatomic NiTi thin films recorded using atomic force microscopy (AFM) on the scan area of $0.5 \mu\text{m} \times 0.5 \mu\text{m}$. The surface roughness variation can be noticed clearly from the AFM images. The surface roughness parameters of thin films such as average roughness (R_{avg}), root mean square roughness (R_{rms}) and a peak to valley roughness parameters are found from AFM scans at different locations of each sample is presented in the Table 6.1. It is clearly observed that the roughness values are

increased with aging temperatures. The surface roughness values of thin films, mainly depends on the surface diffusion, coalescence of grain boundary movement and grain growth. These measurements are accounted for from film structure, roughness, amorphous and crystalline phases, defects, nucleation and growth modes. Usually in thin films the aggregation leads to an uneven growth of grains that makes the differences in grain height. The films aged for 2 h show unclear grain growth (abnormal or discontinuous grain growth) formation caused by precipitates. As the aging temperature raises from 2 h to 4 h the grain size increases due to increase in size of precipitates and lose their coherency in the matrix. In the case of samples aged for 6 h (Fig. 6.3(c)) we observed extremely larger incoherent precipitates uniformly distributed. Due to the increment in density of the precipitates within the NiTi grains the larger grain formation occurs. It is clear from AFM analysis that the grain size increases with respect to the aging time.

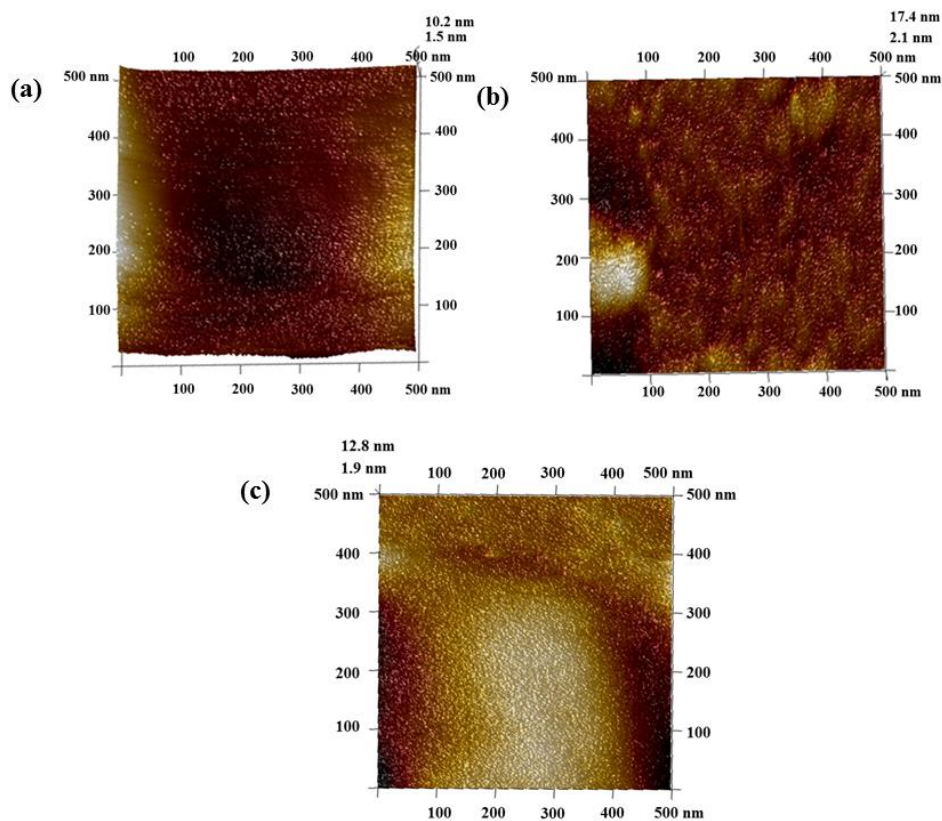


Figure 6.3 AFM (3D surface morphology) micrographs of sputter deposited near equiatomic NiTi thin film vacuum annealed at 600°C for 1 h followed by aging at 500°C for (a) 2 h (b) 4 h and (c) 6 h.

Table 6.1 Various roughness parameters of the near equiatomic NiTi thin films with same scan area.

Aging time	Scan size	AFM		
		RMS roughness (nm) R_q	R_a roughness (nm)	P-V roughness (nm)
2 h	0.5 x 0.5	2	1	16
4 h	0.5 x 0.5	4	3	32
6 h	0.5 x 0.5	7	4	37

6.4.4 Nanoindentation

Nanoindentation provides precise measurements of the variation of indentation load (P), as a function of penetration depth (h). The load-displacement curves obtained from the nanoindentation tests for evaluation of mechanical properties are shown in Fig. 6.4(a-c). Nanoindentation test was carried out using an ASMEC nanoindenter with a three sided pyramid shape tip (Berkovich diamond indenter) and the radius of curvature of the tip is 200 nm. The indentation tests were performed at room temperature and the samples were fixed firmly to the sample holder. Fig. 6.4(a-c) indicates the load displacement curves obtained for the near equiatomic NiTi thin films annealed at 600°C for 1 h followed by aging at 500°C for 2 h, 4 h and 6 h. In the present work, nine indents were performed on thin films at different regions, each spaced 4 μm apart, for each aging condition. Each indent comprised of a 6-second loading, 10-second holding and 6-second unloading segments. Typically the hold periods were maintained to reduce the time dependent effects (creep effects) produced in the specimen. The load-displacement curves of thin films indicates overall elasto-plastic response (Birnbbaum et al. 2009, Huang et al. 2011). The unloading curve is smooth during indentation withdrawal, which indicates that it is purely (elastic) recovered on relaxation. Aging cause metastable states of the solution which in turn yields intermetallic precipitates. The density of precipitates increases within the NiTi grains with increase in aging time because of which the grain size increases. Compared to the hardness, the elastic modulus measurements are strongly affected by the substrate because the elastic field under the indenter tip is restrained to a long range into the substrate not restricting to the film surface (i.e. the extent of the

plastic field is much smaller than the extent of the elastic field). In order to avoid the substrate effects that play a crucial role in the deformation process taking place around indenter, it is important to note that the indentation depth should be less than 10-20% of the film thickness (Tall et al. 2007). The influence of the substrate by including an additional term in the reduced modulus equation has been reported by Saha and Coworkers (Saha and Nix 2002). Film modulus is reasonably well if the contact depth is less than 50% of the film thickness. In this work, the mechanical properties of thin films are rational because the contact depth is less than 50% of film thickness. From the Hall Petch relation, it is clear that the strength of the metallic films increases rapidly when the thickness falls below about 0.3 μm (Moyné et al. 1999).

Based on Johnson's spherical cavity model Shaw et al. explained the deformation process involved in the martensitic and austenitic structures during nanoindentation (Shaw et al. 2003). According to this model, in the case of a martensitic structure the deformation of the solid under the indenter tip occurs by plastic deformation in the region nearest to the tip followed by martensite twin rearrangement where stresses are greatest. The stress induced phase transformation (pseudo elasticity) in the case of austenitic structure, the elastic deformation in the region is far from the indenter tip.

The hardness and elastic modulus of aged near equiatomic NiTi thin films were determined by using Oliver-Pharr analysis method (Kan et al. 2013). This method is valid to the film-substrate system if the film and substrate have similar elastic properties. Even though the films are annealed and aged in high vacuum, both Ni and Ti are highly reactive to residual oxygen. To limit the effects of oxide layers on the measured mechanical properties, deeper indentations are required. The elastic modulus was determined using slope in the initial unloading segments of the P-h curves. The hardness and elastic modulus of the near equiatomic NiTi thin films increases with increase in aging time. The mechanical hysteresis decreases due to increase in the density of precipitates within the NiTi grains.

In the present work, the variation in elastic modulus attained are also due to the stress induced phase transformation phenomena. The possible variation in the elastic moduli with respect to stress induced phase transformations can be assessed by comparing the reported literature for bulk and NiTi alloy thin films. Oliver et al. have reported that

bulk NiTi alloy has an elastic modulus of 65 GPa (Oliver and Pharr 2004). According to Xu Huang et al. at room temperature the elastic modulus of the martensite film (Ti-48.3 at.% Ni) is 73.7 ± 4.2 GPa and the elastic modulus of the austenite film is 80.1 ± 2.1 GPa (Huang et al. 2011). Ashvani Kumar et al. have reported that NiTi thin films have an elastic modulus of ~ 115 GPa (Kumar et al. 2009). Martina Thomosava et al. have reported that the elastic modulus of martensite phase as 78 GPa for resonant ultrasound spectroscopy subjected NiTi thin films (Thomasová et al. 2015). Fu et al. have reported that the elastic modulus of 84 and 60 GPa for austenitic phase and martensitic phase respectively (Fu et al. 2001).

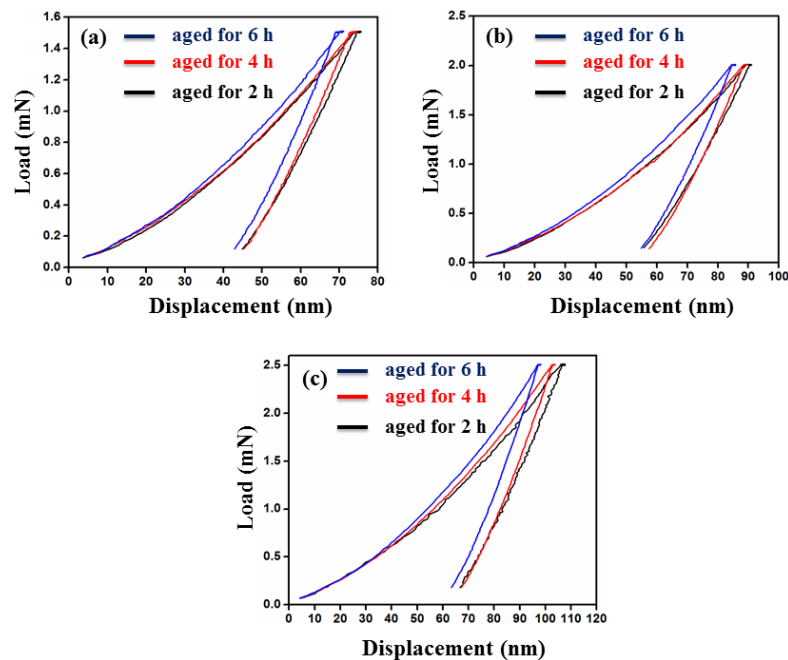


Figure 6.4 Load-displacement curves from nanoindentation experiments performed on the near equiatomic NiTi thin films deposited at room temperature and vacuum annealed at 600°C for 1 h followed by aging at 500°C for 2 h, 4 h and 6 h. (a) 1.5 mN (b) 2 mN and (c) 2.5 mN.

According to the XRD results, aged near equiatomic NiTi thin films dominantly possessed R-phase with a higher crystallization degree along with small amounts of precipitates like Ni_4Ti_3 , Austenite, Martensite, Ni_3Ti and NiTi_2 precipitates. Crone et al. investigated that Austenite phase is flexible and its superelasticity can lower the

hardness as a consequence of the load-induced reversible phase transformation (Austenite \leftrightarrow Martensite) (Crone and Shaw 2004). The Ni_4Ti_3 precipitation is capable of increasing the strength of the Austenite phase and limit the degree of plastic deformation during load cycling (Somsen et al. 1999). The presence of NiTi_2 precipitates induces hardness and brittle behavior which can initiate cracks upon loading (Paula et al. 2004). Although the defect density is reduced by annealing, increase in density of incoherent precipitates (Ni_3Ti) during aging leads to an increase in the hardness and elastic modulus (Geetha Priyadarshini et al. 2011). Gonzalez et al. studied the influence of heat treatments (at lower temperatures) on films and thermomechanical cycling on the R-phase and have shown that higher stress and strain values were possible for thin films (Gonzalez et al. 2010).

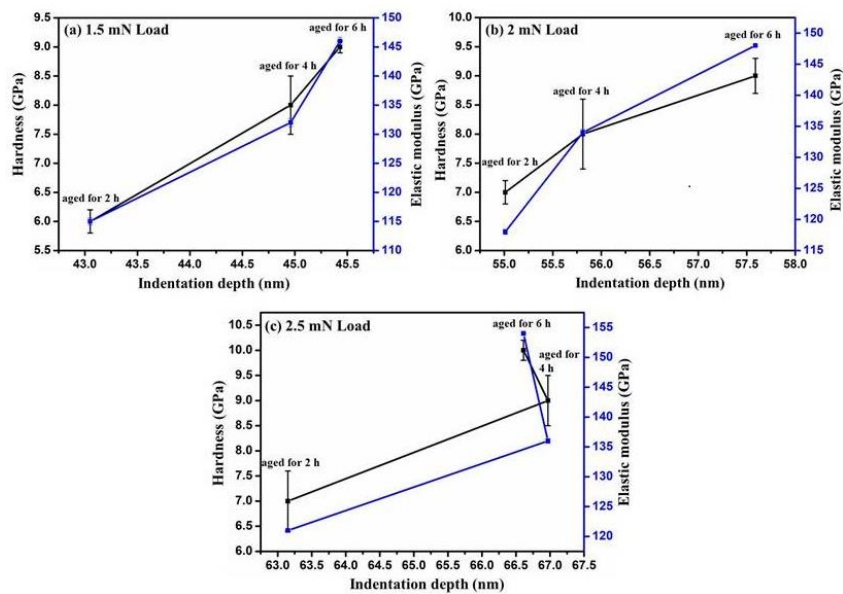


Figure 6.5 The average Hardness and Elastic modulus as a indentation depth of the near equiatomic NiTi thin films deposited at room temperature and vacuum annealed at 600°C for 1 h followed by aging at 500°C for 2 h, 4 h and 6 h. (a) 1.5 mN (b) 2 mN and (c) 2.5 mN.

Aging of Ni-rich NiTi alloy thin films induces variations in both the internal stress state and the chemical compositions by the formation of Ni-rich precipitates. The transformation behavior and mechanical properties of the alloys are affected by the coherent Ni_4Ti_3 in matrix (Jiang et al. 2009). The hardness and elastic moduli values of aged near equiatomic NiTi thin films are shown in Fig. 6.5(a-c). The increasing

tendency in hardness and elastic modulus values attributed to the change in the formation of intermetallic precipitates that occur during aging at different intervals of time. Increase in density of incoherent precipitates during aging leads to an increase in the hardness and elastic modulus.

6.4.5 X-ray photoelectron spectroscopy analysis

The X-ray photoelectron spectroscopy is a surface sensitive quantitative technique that mainly depends on the excitation process and measures the elemental composition, empirical formula, chemical state and electronic state of the elements that exists within a material. The bonding of the atoms and their binding energy states in the first few atomic layers of the surface material were estimated by XPS. The obtained experimental binding energy spectra were compared with standard values to identify the bond type and relative concentration of each bond type (Moulder et al. 1992, Naumkin et al. 2003). In this thesis work, simple heat treatments and aging time were employed in near equiatomic NiTi thin films. During heat treatment surface oxidation occurs that results in the increased TiO₂ thickness, roughness and changes in the composition of the film surface. The temperature maintained during annealing and aging were 600°C and 500°C, respectively.

The surface characteristics of near equiatomic NiTi thin films are recorded by XPS as shown in Fig. 6.6(a-c). The dominant surface elements identified are Nickel (Ni), Titanium (Ti), Oxygen (O), Carbon (C). It is clearly observed that the Oxygen content in the films is due to the reaction with residual gases in spectrometer chamber or the ionic transport via impurities in Ar gas. Oxygen and Carbon rapidly get adsorbed on the film surface whenever the as-deposited film is exposed to the ambient due to the high affinity of Titanium towards Oxygen and Carbon. XPS depth profile analysis of the aged near equiatomic NiTi thin films is shown in Fig. 6.7(a-c). A depth profile of the sample in terms of XPS quantities can be obtained by combining a sequence of ion gun etch cycles interleaved with XPS measurements from the current surface. Each ion gun etch cycle exposes a new surface and the XPS spectra provide the means of analyzing the composition of these surfaces.

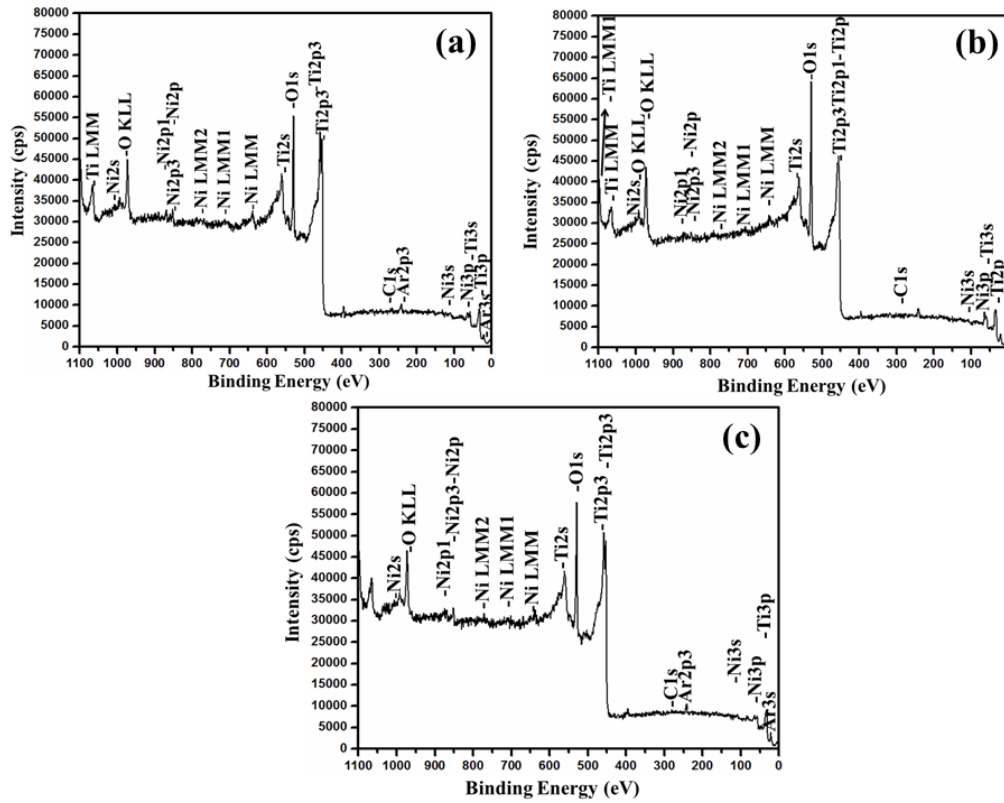


Figure 6.6 XPS survey spectrum obtained from near equiatomic NiTi thin film vacuum annealed at 600°C for 1 h followed by aging at 500°C for (a) 2 h (b) 4 h and (c) 6 h.

Table 6.2 Surface elemental composition evaluated from an XPS survey spectrum of near equiatomic NiTi thin film vacuum annealed at 600°C for 1 h followed by aging at 500°C for different times.

Element	Concentration (at.%)		
	Aged for 2 h	Aged for 4 h	Aged for 6 h
Ni (2p)	1.1	0.3	1.3
Ti (2p)	47.3	37.7	43.2
C (1s)	<1	5	<1
O (1s)	51.6	57.1	55.5

In the case of films aged at 2 h, the Oxygen and Carbon profiles show a lower (minimum) concentration at surface level and reduces to zero at the sputtering time for 1 min and then maintains stable concentration upto sputtering time for 17 min. Ti profile shows almost a marginal steady state concentration for 14 min (sputtering

time) and then decreases gradually to zero at sputtering for 17 min. The Ni profile increases gradually up to sputtering time of 1 min and thereafter it maintains a marginally steady state value up to 14 min and then decreases at sputtering for 17 min. The XPS depth profile of aged films for 4 h showed the Oxygen and Carbon profiles possess minimum concentration at surface level and it decreases to zero at the sputtering time for 1 min and thereafter it maintains a steady state up to the sputtering time of 17 min and gradually decreases to zero at sputtering for 17 min. Ti profile concentration starts at surface level and it marginally maintains a steady state concentration up to 14 min and gradually decreases to zero at sputtering for 17 min. Ni profile shows an increment up to a maximum level at the sputtering time for 1 min and maintains a marginal steady state value 3 min and thereafter it decreases to a minimum concentration at the sputtering time for 17 min.

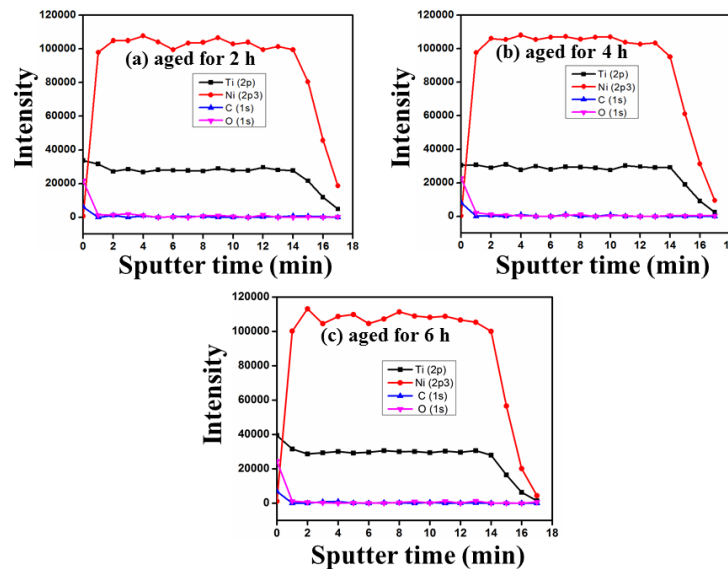


Figure 6.7 XPS depth profile analysis of the aged near equiatomic NiTi thin film vacuum annealed at 600°C for 1 h followed by aging at 500°C for (a) 2 h (b) 4 h and (c) 6 h.

Similarly, in the case of 6 h, the Oxygen and Carbon profiles showed a lower concentration at surface level and decreases to zero at the sputtering time for 1 min and thereafter it maintains a steady state up to the sputtering time of 14 min. Ti shows a minimum concentration at surface level and it decreases to 28% at the sputtering time for 2 min. Thereafter, it maintains a marginal steady state value up to the

sputtering time for 14 min and it gradually decreases to zero at the sputtering time of 17 min. The Ni profile shows an increment up to a maximum level at the sputtering time for 1 min. After that it decreases and maintains a marginal steady state value up to the sputtering time for 14 min. The Ni profile decreases thereafter and shows a zero at the sputtering time for 17 min. The elemental composition of near equiatomic NiTi thin films aged for 2 h, 4 h and 6 h are shown in Table 6.2. The spectral information and individual chemical state of each dominant element state offered by HR-XPS are described below.

6.4.5.1 Ni (2p) spectra

To study the surface characteristics of aged near equiatomic NiTi thin films for Nickel, the binding energy regions of Ni (2p) are noted by HR-XPS as shown in Fig. 6.8(a-c). Films, aged for 2 h showed two broad peaks located at a binding energy of 869.3 eV, 851.4 eV and one satellite peak can be seen at a binding energy of 856.7 eV. In the case of 4 h, the binding energy peaks are located at 868.6 eV, 851.4 eV and a lowest intensity peak at 858.2 eV. For 6 h age-treated films, the binding energy peaks are located at 868.6 eV, 851.4 eV and a small satellite peak was observed at 858.2 eV. The binding energy peaks are characterized by a 2-2.5 eV shift in binding energy over Ni content. In the case of thin films the shift in binding energy occurs due to the matrix effects such as the differences in work function, crystal potential, relaxation energy and chemical effects (Kim and Winograd 1975). The binding energy peaks that are unchanged with aging time located at 869.3 eV for 2 h, 868.6 eV (for 6 h and 4 h) and 851.4 eV (for 2 h, 4 h and 6 h) were attributed to a metallic Ni doublet spin states of Ni 2p_{1/2} and Ni 2p_{3/2}. For NiTi bulk samples the appearance of Ni doublet spin states has been reported by Wang et al. (Wang et al. 2007). Moreover, the small peak or the satellite structure at 856.7 eV for 2 h and 858.2 eV for 4 h and 6 h correspond to Ni 2p_{3/2} peaks of metallic Ni. The presence of the satellite structure is consistent with the experimental results reported in the literature (Fu et al. 2005). This shake-up satellite peak is arisen due to reorganization of valence electrons as photo electrons are emitted from the core levels (Chu et al. 2007). The enthalpy or chemisorb barrier energy for Titanium and Nickel to react with oxygen in the surface are 241 kJ/mol and 956 kJ/mol, respectively (Fu et al. 2005). Due to this

reason, whenever the as-deposited films are exposed to ambient, oxygen and carbon get swiftly adsorbed on the thin film surface. The presence of Ni content in sublayer is due to the preferential oxidation of Ti. For the heat treatments in the temperature range of 400 and 600°C a transition from logarithmic to parabolic oxidation occurs, while the oxidation tends to be parabolic from above 600°C upto 900°C. The difference in activation energies leads to oxygen ion diffusion dominating with metal ion diffusion, but increases with increase in temperature (Firstov et al. 2002). Chu et al. studied that oxidation of NiTi alloy at 1000°C instigated the nickel species to be migrated from the surface layer into a deeper inner layer which possess intermetallic precipitate Ni₃Ti (Chu et al. 2007).

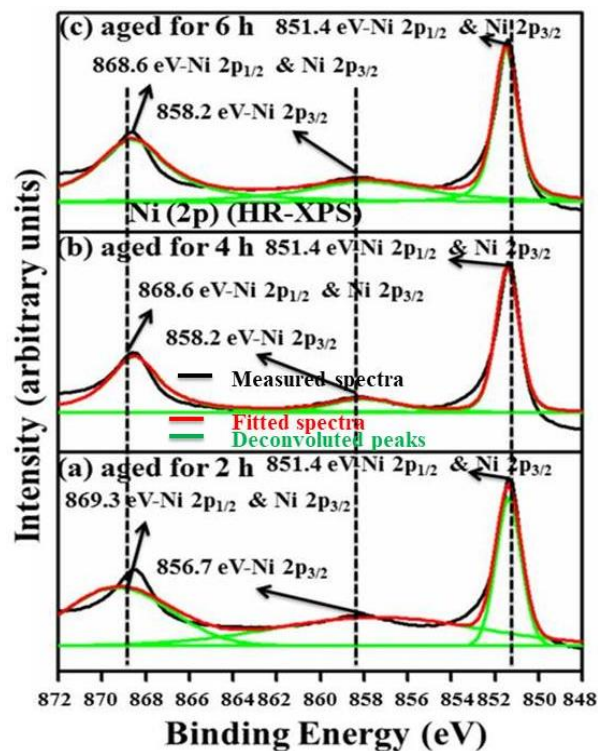


Figure 6.8 Gaussian de-convoluted HR-XPS spectrum for Ni (2p) of near equiatomic NiTi thin film vacuum annealed at 600°C for 1 h followed by aging at 500°C for (a) 2 h (b) 4 h and (c) 6 h.

The age-treated near equiatomic NiTi thin films were enclosed with a few nanometer thickness of oxide layers through which the metallic sub layers were detectable. The surface layer consists of the strong presence of TiO₂ and Ni₃Ti intermetallic phase

(Sato et al. 2009). Longer aging time comprises of large and widely spaced precipitates only effects the Ni-concentration in the matrix. It is noticed from the HR-XPS studies that Ni content is decreasing in 4 h compared to the 2 h but increases in 6 h age-treated films as shown in Table 6.2. The decrement in Nickel content is due to the formation of TiO₂ surface layer with metallic Ni. Chu et al. investigated that in the case of NiTi thin film oxidation, there exists an inner Ni₃Ti layer and outer TiO₂ and a phase of Ti in solid solution in Ni (Chu et al. 2007). The surface oxide layer formation relies on the diffusion of the metallic Nickel and Titanium species through the oxide. At 500°C the diffusion coefficient of Ni is half that of Ti. Higher aging duration lead to the growth of the size of the precipitates. At long aging times (6 h) the depletion of Ni matrix occurs due to enhanced growth of Ni-rich particles (precipitates).

6.4.5.2 Ti (2p) spectra

HR-XPS spectrum recorded in the binding energy regions of Titanium for aged near equiatomic NiTi thin films is shown in Fig. 6.9(a-c). The binding energy peaks which are located at 458.9 eV (for 2 h, 4 h and 6 h) and 453 eV - 2 h, 452.9 eV - 4 h and 453.2 eV - 6 h in aged films are shown in Fig. 6.9(a). These binding energy peaks are characterized by a 2-2.5 eV shift in binding energy over Ti species. The binding energy peak located at 458.9 eV corresponds to 2p_{3/2} spin state for Ti⁴⁺ (TiO₂). The binding energy peak centered at 453.2 eV- 2 h, 452.9 eV - 4 h and 453.0 eV - 6 h correspond to metallic Titanium or Ti (2p) metallic precipitates (Fu et al. 2005, Pequegnat et al. 2015). From HR-XPS studies, it is clear that the Titanium content is decreasing at 4 h when compared to 2 h and increases in the case of 6 h. The possible oxidation behavior of NiTi could be the decomposition of Titanium oxide by nearby metallic Ti at the oxide/alloy interface. This type of decomposition during oxidation of Ti at temperatures above 350°C has been reported by Bui et al. (Duc et al. 1980). It results in a high density of vacancies allowing fast diffusion of oxygen leads to linear or quasi linear oxidation of Ti. However, the differences in activation energies at lower temperatures lead to oxygen ion diffusion dominating with metal ion diffusion. The formation of Titanium dioxide onto the film surface is prominent because Ti is the thermodynamically reactive with Oxygen and water. The prevention of Ni from

the surface of aging thin films by formation of TiO_2 could be undertaken for enhancing corrosion resistance and bio-medical applications.

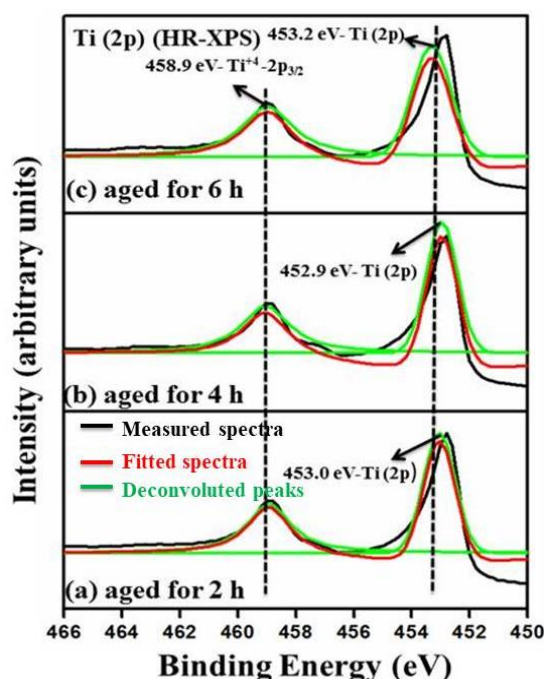


Figure 6.9 Gaussian de-convoluted HR-XPS spectrum for Ti (2p) of near equiatomic NiTi thin film vacuum annealed at 600°C for 1 h followed by aging at 500°C for (a) 2 h (b) 4 h and (c) 6 h.

6.4.5.3 O (1s) spectra

Figure 6.10(a-c) shows the HR-XPS spectra recorded for thin films in the binding energy regions of Oxygen. The binding energy peaks are identified by the Gaussian de-convolution of the HR-XPS. We have observed four binding energy peaks that are located at 529.5 eV, 529.1 eV, 528.7 eV and 528.3 eV for 2 h, 529.5 eV, 529.1 eV, 528.7 eV and 528.5 eV for 4 h and 529.9 eV, 529.3 eV, 529 eV and 528.6 eV for 6 h age-treated thin films. The binding energy peaks in age-treated thin films at 2 h, 4 h and 6 h are characterized by a 2-2.5 eV shift in binding energy over Oxygen species. In the case of 2 h age-treated film, the binding energy peaks located 529.5 eV and 529.1 eV initiates from O^{2-} or TiO_2 (metal oxide) formation which is supported by the Ti (2p) high resolution spectra as discussed earlier (section 6.4.5.2). The other binding

6.4.5.4 C (1s) spectra

Figure 6.11(a-c) shows the HR-XPS spectra recorded for aged near equiatomic NiTi thin films in the binding energy regions of carbon. Films, which are aged for 2 h, the binding energy peaks are located at 283.9 eV, 283.6 eV and 283.3 eV were assigned to Si-C (Silicon-Carbide) particle formation. In the case of films aged for 4 h the binding energy peaks are centered at 284.3 eV, 283.7 eV and 283.4 eV. The binding energy peak located at 284.3 eV corresponds to carbon-carbon (graphitic carbon) and carbon-hydrogen viz. C-C and C-H respectively. The other binding energy peaks located at 283.7 eV and 283.4 eV were assigned to Si-C particle formation.

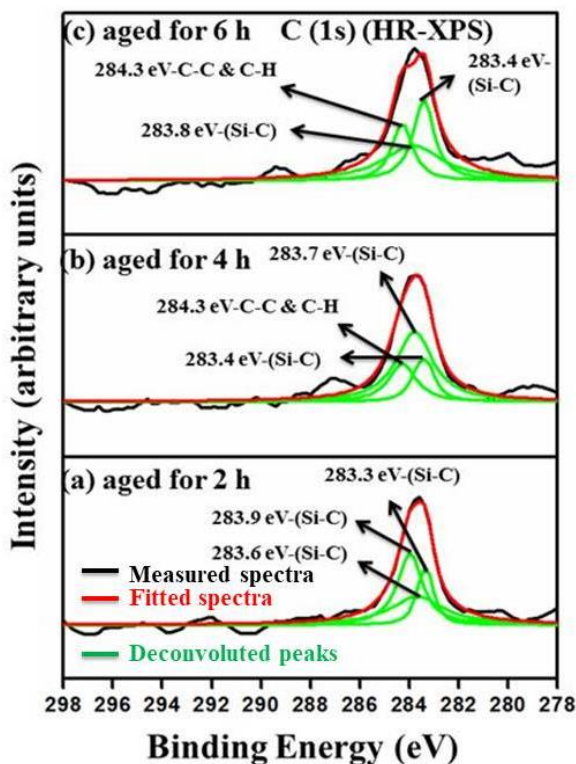


Figure 6.11 Gaussian de-convoluted HR-XPS spectrum for C (1s) of near equiatomic NiTi thin film vacuum annealed at 600°C for 1 h followed by aging at 500°C for (a) 2 h (b) 4 h and (c) 6 h.

As the aging temperature increased from 4 h to 6 h the resulting binding energy peaks are located at 284.3 eV, 283.8 eV and 283.4 eV. The binding energy peak located at

284.3 eV corresponds to carbon-carbon (graphitic carbon) and carbon-hydrogen viz. C-C and C-H respectively. The other low intensity binding energy peaks located at 283.8 eV and 283.4 were assigned to Si-C particle formation. The located binding energy values are well matched with available literature (Hishita et al. 2003, Ju et al. 2012, Poon et al. 2005). The carbon content increases as the aging temperature is increased from 2 h to 4 h but, it decreases at 6 h. The increment in carbon content at 4 h is due to the high affinity of Titanium towards Oxygen and Carbon. The decrease in the carbon content at 6 h is due to the formation of Ni₃Ti precipitates in the NiTi matrix sublayers. From HR-XPS studies, it is clear that the aged near equiatomic NiTi thin films are thermodynamically reactive to Oxygen and Carbon and forms TiO₂ oxide layer onto the film surface and Si-C particles in the NiTi matrix. Upon oxidation of Titanium, the larger TiO₂ crystal structure is accommodated Ti content that moves towards the film surface by leaving Ni-rich precipitates trapped behind (Ruperez et al. 2016).

6.5 CONCLUSIONS

- Near equiatomic NiTi thin films (Ni-50.3 and Ti-49.7 at.%) were prepared and the effect of aging time on the structural, morphological, mechanical and surface properties of these films were investigated.
- As-deposited films were amorphous. From XRD studies, it was observed that aged near equiatomic NiTi thin films possessed dominant R-phase along with intermetallic precipitates.
- FESEM and AFM characterizations revealed that the size of the precipitates increased as the aging time increased from 2 h to 6 h.
- The increase in hardness and elastic modulus values could be probably due to the precipitation incoherency in the NiTi matrix.
- X-ray photo electron spectroscopy studies clearly revealed that the aged near equiatomic NiTi thin films had a strong tendency to form TiO₂ layer as an outermost layer onto the film surface with intermetallic precipitates trapped behind most likely in the lattice sites of NiTi along with Si-C precipitates.

CHAPTER 7

SUMMARY AND FUTURE DIRECTIONS

The conclusions and future directions of intermetallic and near equiatomic NiTi thin films are presented in this chapter.

7.1 SUMMARY

In order to prepare the magnetron sputtered thin films for specific applications, knowledge of its dependence on the deposition parameters is essential. This includes an understanding of the phenomena that control the evolution of the film growth during subsequent processing. The sputtered NiTi film composition was easily affected by metallurgical factors (annealing, aging process, film composition, contamination and thermomechanical treatment, etc.), sputtering conditions (deposition temperature, gas pressure, substrate bias, target power and target to substrate distance, etc.) and application conditions (heat dissipation, heating/cooling rate, room temperature and environment, strain rate, etc.). This thesis mainly describes the growth and characterization of DC magnetron sputtered intermetallic, and near equiatomic NiTi alloy thin films. The correlation between deposition parameters and material properties has been characterized. In this thesis work, we have mainly investigated the influence of post-deposition conditions such as annealing temperature and/or aging time on NiTi thin film micro-structure, surface morphology, mechanical and surface properties.

7.1.1 The effect of annealing temperature on the structural, morphological, mechanical and surface properties of intermetallic NiTi alloy thin films

- Intermetallic NiTi thin films were grown on silicon (1 0 0) substrates using DC magnetron sputtering system with two separate circular elemental targets Ni and Ti.
- The influence of sputter deposition and post annealing conditions on intermetallic NiTi thin films was studied when subjected to same annealing time but different annealing temperatures.
- Heat treatments of NiTi thin films are limited to temperatures lower than the recrystallization temperature of 650°C. At low temperatures the diffusion rates are low, but the driving force for nucleation is high while at higher temperatures the reverse is true.
- From XRD studies it was clear that the intermetallic thin films were crystalline showing Ni₃Ti as a dominant phase along with NiTi, Ni₄Ti₃ and NiTi₂ phase.
- The surface morphology of the intermetallic NiTi thin films examined using FESEM and was found to vary significantly with respect to annealing temperature. It was observed that the change in the microstructure is due to the competing nature of the nucleation and the active growth rate of the grains.
- AFM studies indicated that the surface morphology showed a slightly different morphology even though their elemental composition is the same. As the annealing temperature increases, the grain growth of the film changes and the roughness parameters like RMS, Ra and P-V value increase.
- The acquired hardness and elastic modulus values show greater values for the higher annealing temperature and lesser values for lower annealing temperatures. This is mainly due to the nucleation, growth process of the grains and phase segregation in the intermetallic NiTi thin films with respect to the annealing temperature.
- From HR-XPS studies it was confirmed that in the annealed intermetallic NiTi thin films due to their thermodynamic reasons Titanium content show a strong affinity to form metal oxides (TiO₂) layer onto the film surface-atmosphere interface. TiO₂ has the larger unit cell and upon oxidation of Ti the larger titanium dioxide crystal structure is accommodated by Ti content relocate towards the film surface, leaving a Ni rich matrix trapped behind.

7.1.2 Aging time correlation in DC magnetron sputtered Ni60Ti40 thin films

- In this thesis work, we have investigated the influence of aging time on intermetallic NiTi thin films when subjected to same annealing temperature (600°C for 1 h) but different aging times (at 500°C for 2 h, 4 h and 6 h).
- From XRD it was cleared that increasing the aging time increases the degree of crystallinity due to the presence of intermetallic precipitates. An increase in the aging time causes the precipitates to become spherical in shape and lose their coherency with the austenite matrix. In the case of aged intermetallic thin films different phases such as NiTi, Ni₃Ti and Ni₂Ti co exists due to incomplete alloying process.
- FESEM characterization clearly showed that long term aging caused the precipitates become spherical in shape and lose their coherency. These spherical incoherent precipitates in the Ni-rich matrix combines with the austenite matrix and forms large precipitated particles within NiTi grains.
- The surface roughness increase with increase in aging temperature. The surface topography changes can be clarified based on the theories such as surface diffusion, coalescence and grain growth of the films.
- The hardness and elastic modulus of the intermetallic NiTi thin films increases with increase in aging time. The age-treated films show a decrease in the mechanical hysteresis due to increase in the density of precipitates within the NiTi grains.
- Longer aging treatments affects the Ni-concentration in the matrix. It leads to heterogeneous precipitation of Ni-rich particles within NiTi grains. From HR-XPS it was proposed that titanium being the highly reactive element, segregates to the film surface and is oxidized there forming titanium dioxide with Ni enriched alloy layers underneath.

7.1.3 Influence of annealing temperature on the structural, morphological, mechanical and surface properties of near equiatomic NiTi thin films

- Near equiatomic NiTi thin films were grown on silicon (1 0 0) substrates using DC magnetron sputtering system with two separate circular elemental targets Ni and Ti.
- In the present thesis work, we have investigated the crystallization, nucleation, grain growth and recrystallization phenomena in near equiatomic NiTi thin films during annealing at different temperatures.
- It was observed that recrystallization mainly depends on the temperature, time and the amount of strain hardening of the material. The more strain hardening, the lower is the temperature at which recrystallization occurs. The greater the strain hardening, the more nuclei for the new grains, resulting in small grain size.
- It was understood that the small amount of Austenite phase, Martensite phase, Ni₄Ti₃ and Ni₃Ti precipitates present in the samples were probably due to incomplete material transformation nearby the substrate interface due to substrate constraints.
- The FESEM micrographs clearly showed the distinct morphology with annealing. The films showed dense, a complete outward grain growth and flakes type formation in the cross-sectional surface morphology.
- At a lower annealing temperature the roughness values were smaller when compared to the higher annealing temperatures.
- It was revealed that the driving force for recrystallisation is the stored strain energy in the thin film material. During recrystallisation, the stress-free grains nucleate and grow until the original grains fully are consumed.
- Near equiatomic NiTi thin films possess a dominant R-phase, Ni₄Ti₃ and Ni₃Ti precipitates. These precipitates are capable of increasing the strength of R-phase, thereby limiting the degree of plastic deformation in load cycling.
- The difference in activation energies is increasing with increasing temperature. The metal ion diffusion dominates oxygen ion diffusion and it also increases with increasing temperature. It was also understood that Titanium segregates to the film

surface and oxidizes to form a titanium dioxide layer with Ni species underneath the layer along with Ti-C and Si-C particles.

7.1.4 Aging time correlation in DC magnetron sputtered near equiatomic NiTi thin films

- In this thesis work, we have investigated the effect of aging time on near equiatomic NiTi thin films when subjected to same annealing temperature, i.e. 600°C for 1 h but subjected to different aging times (at 500°C for 2 h, 4 h and 6 h).
- XRD studies revealed that as the aging time increases the degree of crystallinity increases due to the presence of Ni-rich precipitates, it also causes the precipitates to become spherical in shape and lose their coherency with the austenite matrix.
- The direct consequence of the relation between the crystallization temperature, nucleation and grain growth cause variance in the film surface morphology. It was observed that the precipitates increase with increase in aging time. Precipitation results into nucleation where the drifting atoms group together within the NiTi grains.
- The surface roughness values of thin films mainly depends on the surface diffusion, coalescence and grain growth. It is clear from AFM analysis that the grain size increases with respect to the aging time.
- Nanoindentation studies revealed that the increasing tendency in hardness and elastic modulus values attributed to the change in the formation of intermetallic precipitates that occur during aging at different intervals of time (Increase in the density of incoherent precipitates during aging leads to an increase in the hardness and elastic modulus).
- From HR-XPS studies, it was concluded that the aged near equiatomic NiTi thin films are thermodynamically reactive to Oxygen and Carbon and forms TiO₂ oxide layer onto the film surface and Si-C particles in the NiTi matrix.

7.2 Future directions

The current work has been an important step in the growth and characterization of the intermetallic and nearequiatomic NiTi thin films with nanometer dimensions. This can be further explored to understand the fundamental properties such as structural, morphological, mechanical and surface properties of intermetallic and near equiatomic NiTi alloy thin films for potential nanoscale device applications. The future directions that could bring high impact to the research community include the following:

1. The indentation recovery would be increased by using a spherical indenter that would not induce the high strain that a Berkovich indenter causes. Using a spherical indenter would also provide a standard to compare indentation recovery to other studies. The induced strain could be tailored by changing the radius of the indenter. The spherical indenter would remove the indenter blunting from a factor for indentation recovery. The optimal crystal structure orientation for maximum indentation recovery is a necessary parameter to be characterized.
2. Electrical resistance measurement is a promising technique to study the shape memory effects in near equiatomic thin film on substrates down to nanometer range. It is also easy to incorporate them with the cooling system so that the temperature studied can be easily extended to liquid nitrogen temperature.
3. In-situ TEM is a powerful tool to simultaneously observe the microstructural changes (precipitate formation) upon transformation in intermetallic and near equiatomic NiTi thin films. The in-situ investigation on nanosize materials will further extend the experimental work on size effect. Inclusion into the constitutive behavior model of various microstructural features will lead to more precise and predictive constitutive laws for shape memory alloy thin films.
4. NiTi thin films with nanometer grains (about tens or hundreds of nanometers) exhibits shape memory effect, then it is promising to fabricate nano-scale SMA thin film structures with the aid of precision tools (such as focused ion milling or FIB).
5. Successful implementation of NiTi micro actuators requires a good understanding of the relationship among processing, microstructure and properties of NiTi thin

films. NiTi film based microractuators will find potential applications in medicine, aerospace, automotive, and consumer products. Miniature TiNi actuated devices based on sputtered TiNi films are ready for the huge commercial market, especially for medical microdevices and orthopaedic implant applications.

REFERENCES

- Acar, E., Ozbulut, O. E., and Karaca, H. E. (2015). “Experimental investigation and modeling of the loading rate and temperature dependent superelastic response of a high performance shape-memory alloy.” *Smart Mater. Struct.*, 24(7), 075020.
- Allafi, J. K., Ren, X., and Eggeler, G. (2002). “The mechanism of multistage martensitic transformations in aged Ni-rich NiTi shape memory alloys.” *Acta Mater.*, 50(4), 793–803.
- Armitage, D. A., and Grant, D. M. (2003). “Characterisation of surface-modified nickel titanium alloys.” *Mater. Sci. Eng. A*, 349(1), 89–97.
- Artyushkova, K., and Fulghum, J. E. (2004). “Mathematical topographical correction of XPS images using multivariate statistical methods.” *Surf. Interface Anal.*, 36(9), 1304–1313.
- “Atomic force microscope and method for imaging surfaces with atomic resolution.” (1988).
- Behera, A., and Aich, S. (2015). “Characterisation and properties of magnetron sputtered nanoscale bi-layered Ni/Ti thin films and effect of annealing.” *Surf. Interface Anal.*, 47(8), 805–814.
- Bhushan, B., and Li, X. (2003). “Nanomechanical characterisation of solid surfaces and thin films.” *Int. Mater. Rev.*, 48(3), 125–164.
- Bindu, P., and Thomas, S. (2014). “Estimation of lattice strain in ZnO nanoparticles: X-ray peak profile analysis.” *J. Theor. Appl. Phys.*, 8(4), 123–134.
- Binnig, G., and Rohrer, H. (1987). “Scanning tunneling microscopy-from birth to adolescence.” *Rev. Mod. Phys.*, 59(3), 615.
- Binns, C. (2010). *Introduction to nanoscience and nanotechnology*. John Wiley & Sons.

Birnbaum, A. J., Satoh, G., and Yao, Y. L. (2009a). “Functionally grading the shape memory response in NiTi films: Laser irradiation.” *J. Appl. Phys.*, 106(4), 043504.

Birnbaum, A. J., Yao, Y. L., Chung, U.-J., Im, J. S., Huang, X., and Ramirez, A. G. (2009b). “On the lateral crystal growth of laser irradiated NiTi thin films.” *Appl. Phys. Lett.*, 94(26), 261908.

Bolshakov, A., Oliver, W. C., and Pharr, G. M. (1994). “An explanation for the shape of nanoindentation unloading curves based on finite element simulation.” *MRS Online Proc. Libr. Arch.*, 356.

Boulesteix, C., Devant, G., Marraud, A., and Rateau, R. (1969). “Structure and Recrystallization of Indium Thin Film.” *J. Vac. Sci. Technol.*, 6(4), 780–783.

Briggs, D., and Seah, M. P. (2003). *Practical surface analysis: by auger and x-ray photoelectron spectroscopy*. Wiley.

Buehler, W. J., Gilfrich, J. V., and Wiley, R. C. (1963). “Effect of low-temperature phase changes on the mechanical properties of alloys near composition TiNi.” *J. Appl. Phys.*, 34(5), 1475–1477.

Bukhtiyarov, V. I., Nizovskii, A. I., Bluhm, H., Hävecker, M., Kleimenov, E., Knop-Gericke, A., and Schlögl, R. (2006). “Combined in situ XPS and PTRMS study of ethylene epoxidation over silver.” *J. Catal.*, 238(2), 260–269.

Bull, S. J. (2002). “Extracting hardness and Young’s modulus from load–displacement curves.” *Z. Für Met.*, 93(9), 870–874.

Busch, J. D., and Johnson, A. D. (1990). “Prototype micro-valve actuator.” *Micro Electro Mech. Syst. 1990 Proc. Investig. Micro Struct. Sens. Actuators Mach. Robots IEEE, IEEE*, 40–41.

Busch, J. D., Johnson, A. D., Lee, C. H., and Stevenson, D. A. (1990). “Shape-memory properties in Ni-Ti sputter-deposited film.” *J. Appl. Phys.*, 68(12), 6224–6228.

- Bysakh, S., Kumar, A., Kamat, S. V., Sharma, S. K., and Mohan, S. (2012). "Influence of annealing on oxidation, microstructure and mechanical properties of Ni-49Ti films." *J. Mater. Res.*, 27(7), 1068–1079.
- Callister Jr, W. D., and Rethwisch, D. G. (2012). *Fundamentals of materials science and engineering: an integrated approach*. John Wiley & Sons.
- Callisti, M., Mellor, B. G., and Polcar, T. (2014). "Microstructural investigation on the grain refinement occurring in Cu-doped Ni–Ti thin films." *Scr. Mater.*, 77, 52–55.
- Cao, F., Munroe, P., Zhou, Z., and Xie, Z. (2016). "The microstructure and mechanical properties of thin film Ni (Ti) nanocomposite coatings containing both oxygen and nitrogen." *Surf. Coat. Technol.*, 304, 375–383.
- Carlson, T. A. (1982). "Basic assumptions and recent developments in quantitative XPS." *Surf. Interface Anal.*, 4(4), 125–134.
- Carroll, M. C., Somsen, C., and Eggeler, G. (2004). "Multiple-step martensitic transformations in Ni-rich NiTi shape memory alloys." *Scr. Mater.*, 50(2), 187–192.
- Chan, C.-M., Trigwell, S., and Duerig, T. (1990). "Oxidation of an NiTi alloy." *Surf. Interface Anal.*, 15(6), 349–354.
- Chang, L. C., and Read, T. A. (1950). *Plastic deformation and diffusionless phase changes in metals the bold-cadmium beta phase*. Columbia University.
- Chang, L., Hu-Simpsono, C., Grummon, D. S., Pratt, W., and others. (1990). "Structure and Phase Transformations in Thermoelastic Ni (1- x) TiCu x) Thin Films Prepared by DC Magnetron Sputtering." *MRS Online Proc. Libr. Arch.*, 187.
- Chen, C.-Q., and Shen, Y.-P. (1997). "Optimal control of active structures with piezoelectric modal sensors and actuators." *Smart Mater. Struct.*, 6(4), 403.
- Cheng, Y., Cai, W., Li, H. T., Zheng, Y. F., and Zhao, L. C. (2004). "Surface characteristics and corrosion resistance properties of TiNi shape memory alloy coated with Ta." *Surf. Coat. Technol.*, 186(3), 346–352.

Cheng, Y.-T., and Cheng, C.-M. (2000). “What is indentation hardness?” *Surf. Coat. Technol.*, 133, 417–424.

Cheng, Y.-T., and Cheng, C.-M. (2004). “Scaling, dimensional analysis, and indentation measurements.” *Mater. Sci. Eng. R Rep.*, 44(4), 91–149.

Cho, H., Kim, H. Y., and Miyazaki, S. (2005). “Fabrication and characterization of Ti–Ni shape memory thin film using Ti/Ni multilayer technique.” *Sci. Technol. Adv. Mater.*, 6(6), 678–683.

Chopra, I. (2002). “Review of state of art of smart structures and integrated systems.” *AIAA J.*, 40(11), 2145–2187.

Choudhary, N., and Kaur, D. (2016). “Shape memory alloy thin films and heterostructures for MEMS applications: a review.” *Sens. Actuators Phys.*, 242, 162–181.

Choudhary, N., Kharat, D. K., and Kaur, D. (2011). “Structural, electrical and mechanical properties of magnetron sputtered NiTi/PZT/TiO_x thin film heterostructures.” *Surf. Coat. Technol.*, 205(11), 3387–3396.

Chrzanowski, W., Neel, E. A. A., Armitage, D. A., and Knowles, J. C. (2008a). “Effect of surface treatment on the bioactivity of nickel–titanium.” *Acta Biomater.*, 4(6), 1969–1984.

Chrzanowski, W., Neel, E. A. A., Armitage, D. A., Lee, K., Walke, W., and Knowles, J. C. (2008b). “Nanomechanical evaluation of nickel–titanium surface properties after alkali and electrochemical treatments.” *J. R. Soc. Interface*, 5(26), 1009–1022.

Chu, C. L., Chung, C. Y., and Chu, P. K. (2006a). “Surface oxidation of NiTi shape memory alloy in a boiling aqueous solution containing hydrogen peroxide.” *Mater. Sci. Eng. A*, 417(1), 104–109.

Chu, C. L., Chung, C. Y., and Chu, P. K. (2006b). “Surface oxidation of NiTi shape memory alloy in a boiling aqueous solution containing hydrogen peroxide.” *Mater. Sci. Eng. A*, 417(1), 104–109.

Chu, C. L., Hu, T., Wu, S. L., Dong, Y. S., Yin, L. H., Pu, Y. P., Lin, P. H., Chung, C. Y., Yeung, K. W. K., and Chu, P. K. (2007a). "Surface structure and properties of biomedical NiTi shape memory alloy after Fenton's oxidation." *Acta Biomater.*, 3(5), 795–806.

Chu, C. L., Hu, T., Wu, S. L., Dong, Y. S., Yin, L. H., Pu, Y. P., Lin, P. H., Chung, C. Y., Yeung, K. W. K., and Chu, P. K. (2007b). "Surface structure and properties of biomedical NiTi shape memory alloy after Fenton's oxidation." *Acta Biomater.*, 3(5), 795–806.

Chung, C. Y., and Chan, P. M. (2011). "NiTi shape memory alloy thin film micro-cantilevers array." *Thin Solid Films*, 519(15), 5307–5309.

Crone, W. C., and Shaw, G. A. (2004). "Applying NiTi shape-memory thin films to thermomechanical data storage technology." *MRS Online Proc. Libr. Arch.*, 855.

Dao, M., Chollacoop, N. v, Van Vliet, K. J., Venkatesh, T. A., and Suresh, S. (2001). "Computational modeling of the forward and reverse problems in instrumented sharp indentation." *Acta Mater.*, 49(19), 3899–3918.

DeLong, C. M., Bragg, R., and Simmons, J. A. (2008). "Evidence for spatial representation of object shape by echolocating bats (*Eptesicus fuscus*)." *J. Acoust. Soc. Am.*, 123(6), 4582–4598.

Dlouhy, A., Khalil-Allafi, J., and Eggeler, G. (2003). "Multiple-step martensitic transformations in Ni-rich NiTi alloys—an in-situ transmission electron microscopy investigation." *Philos. Mag.*, 83(3), 339–363.

Doerner, M. F., and Nix, W. D. (1986). "A method for interpreting the data from depth-sensing indentation instruments." *J. Mater. Res.*, 1(4), 601–609.

DU, Y., and Schuster, J. C. (1998). "Experimental investigation and thermodynamic modeling of the Ni-Ti-C system." *Z. Für Met.*, 89(6), 399–410.

Du, Y., Schuster, J. C., Seifert, H. J., and Aldinger, F. (2000a). “Experimental investigation and thermodynamic calculation of the titanium–silicon–carbon system.” *J. Am. Ceram. Soc.*, 83(1), 197–203.

Du, Y., Schuster, J. C., Seifert, H. J., and Aldinger, F. (2000b). “Experimental Investigation and Thermodynamic Calculation of the TitaniumSiliconCarbon System.” *J. Am. Ceram. Soc.*, 83(1), 197–203.

Duc, B., Jardin, C., Gauthier, J. P., Thollet, G., and Michel, P. (1980a). “Oxidation mechanism, oxide decomposition and phase transition in industrial titanium studied by high-resolution low-energy electron spectrometry.” *Titanium '80*, 4, 2819–2827.

Duc, B., Jardin, C., Gauthier, J. P., Thollet, G., and Michel, P. (1980b). “Oxidation mechanism, oxide decomposition and phase transition in industrial titanium studied by high-resolution low-energy electron spectrometry.” *Titanium '80*, 4, 2819–2827.

Duwez, P., and Taylor, J. L. (1950). “The structure of intermediate phases in alloys of titanium with iron, cobalt, and nickel.” *Trans AIME*, 188, 1173–1176.

Einstein, A. (1905). “On the electrodynamics of moving bodies.”

Fairley, N. (2009). *CasaXPS Manual 2.3. 15: Introduction to XPS and AES*. Casa Software.

Fan, G., Chen, W., Yang, S., Zhu, J., Ren, X., and Otsuka, K. (2004). “Origin of abnormal multi-stage martensitic transformation behavior in aged Ni-rich Ti–Ni shape memory alloys.” *Acta Mater.*, 52(14), 4351–4362.

Fernandes, F. M. B., Martins, R., Nogueira, M. T., Silva, R. J., Nunes, P., Costa, D., Ferreira, I., and Martins, R. (2002). “Structural characterisation of NiTi thin film shape memory alloys.” *Sens. Actuators Phys.*, 99(1), 55–58.

Firstov, G. S., Vitchev, R. G., Kumar, H., Blanpain, B., and Van Humbeeck, J. (2002). “Surface oxidation of NiTi shape memory alloy.” *Biomaterials*, 23(24), 4863–4871.

- Fischer-Cripps, A. C. (2011). "Factors affecting nanoindentation test data." *Nanoindentation*, Springer, 77–104.
- Frantz, N., Dufour-Gergam, E., Grandchamp, J. P., Bosseboeuf, A., Seiler, W., Nouet, G., and Catillon, G. (2002). "Shape memory thin films with transition above room temperature from Ni-rich NiTi films." *Sens. Actuators Phys.*, 99(1), 59–63.
- Fu, Y., and Du, H. (2003). "Effects of film composition and annealing on residual stress evolution for shape memory TiNi film." *Mater. Sci. Eng. A*, 342(1), 236–244.
- Fu, Y., Du, H., Huang, W., Zhang, S., and Hu, M. (2004). "TiNi-based thin films in MEMS applications: a review." *Sens. Actuators Phys.*, 112(2), 395–408.
- Fu, Y., Du, H., Zhang, S., and Gu, Y. (2005a). "Stress and surface morphology of TiNiCu thin films: effect of annealing temperature." *Surf. Coat. Technol.*, 198(1), 389–394.
- Fu, Y., Du, H., Zhang, S., and Huang, W. (2005b). "XPS characterization of surface and interfacial structure of sputtered TiNi films on Si substrate." *Mater. Sci. Eng. A*, 403(1), 25–31.
- Fu, Y., Du, H., Zhang, S., and Ong, S. E. (2005d). "Effects of silicon nitride interlayer on phase transformation and adhesion of TiNi films." *Thin Solid Films*, 476(2), 352–357.
- Fu, Y., Huang, W., Du, H., Huang, X., Tan, J., and Gao, X. (2001a). "Characterization of TiNi shape-memory alloy thin films for MEMS applications." *Surf. Coat. Technol.*, 145(1), 107–112.
- Fu, Y., Huang, W., Du, H., Huang, X., Tan, J., and Gao, X. (2001b). "Characterization of TiNi shape-memory alloy thin films for MEMS applications." *Surf. Coat. Technol.*, 145(1), 107–112.
- Ganneau, F. P., Constantinides, G., and Ulm, F.-J. (2006). "Dual-indentation technique for the assessment of strength properties of cohesive-frictional materials." *Int. J. Solids Struct.*, 43(6), 1727–1745.

Gao, D., Yang, G., Zhu, Z., Zhang, J., Yang, Z., Zhang, Z., and Xue, D. (2012). “One-step synthesis of open-cell Ni foams by annealing the Ni²⁺-based precursor in air.” *J. Mater. Chem.*, 22(19), 9462–9465.

Geetha Priyadarshini, B., Aich, S., and Chakraborty, M. (2011). “An investigation on phase formations and microstructures of Ni-rich Ni-Ti shape memory alloy thin films.” *Metall. Mater. Trans. A*, 42(11), 3284–3290.

Giannakopoulos, A. E., Larsson, P.-L., and Vestergaard, R. (1994). “Analysis of Vickers indentation.” *Int. J. Solids Struct.*, 31(19), 2679–2708.

Giannakopoulos, A. E., and Suresh, S. (1999). “Determination of elastoplastic properties by instrumented sharp indentation.” *Scr. Mater.*, 40(10), 1191–1198.

Goldstein, J. I., Newbury, D. E., Echlin, P., Joy, D. C., Fiori, C., and Lifshin, E. (1981). “Electron-Beam-Specimen Interactions.” *Scanning Electron Microsc. X-Ray Microanal.*, Springer, 53–122.

Gonzalez, C. H., Oliveira, C. A. do N., Pina, E. A. C. de, Urtiga Filho, S. L., Araújo Filho, O. O. de, and Araújo, C. J. de. (2010). “Heat treatments and thermomechanical cycling influences on the R-phase in Ti-Ni shape memory alloys.” *Mater. Res.*, 13(3), 325–331.

Green, S. M., Grant, D. M., and Wood, J. V. (1997). “XPS characterisation of surface modified Ni-Ti shape memory alloy.” *Mater. Sci. Eng. A*, 224(1–2), 21–26.

Grothe, B., and Park, T. J. (2000). “Structure and function of the bat superior olivary complex.” *Microsc. Res. Tech.*, 51(4), 382–402.

Gupta, R. P., and Sen, S. K. (1974). “Calculation of multiplet structure of core p-vacancy levels.” *Phys. Rev. B*, 10(1), 71.

Gupta, R. P., and Sen, S. K. (1975). “Calculation of multiplet structure of core p-vacancy levels. II.” *Phys. Rev. B*, 12(1), 15.

Gyobu, A., Kawamura, Y., Horikawa, H., and Saburi, T. (1999). “Martensitic transformation and two-way shape memory effect of sputter-deposited Ni-rich Ti–Ni alloy films.” *Mater. Sci. Eng. A*, 273, 749–753.

Hainsworth, S. V., Chandler, H. W., and Page, T. F. (1996). “Analysis of nanoindentation load-displacement loading curves.” *J. Mater. Res.*, 11(8), 1987–1995.

Hallwachs, W. (1889). “Ueber den Zusammenhang des Electricitätsverlustes durch Beleuchtung mit der Lichtabsorption.” *Ann. Phys.*, 273(8), 666–675.

Hansen, A. W., Führ, L. T., Antonini, L. M., Villarinho, D. J., Marino, C. E. B., and Malfatti, C. de F. (2015). “The electrochemical behavior of the NiTi alloy in different simulated body fluids.” *Mater. Res.*, 18(1), 184–190.

Hara, T., Ohba, T., Otsuka, K., and Nishida, M. (1997). “Phase transformation and crystal structures of Ti₂Ni₃ precipitates in ti–ni alloys.” *Mater. Trans. JIM*, 38(4), 277–284.

Hay, J. C., Bolshakov, A., and Pharr, G. M. (1999). “A critical examination of the fundamental relations used in the analysis of nanoindentation data.” *J. Mater. Res.*, 14(6), 2296–2305.

Helmerson, U., Lattemann, M., Bohlmark, J., Ehiasarian, A. P., and Gudmundsson, J. T. (2006). “Ionized physical vapor deposition (IPVD): A review of technology and applications.” *Thin Solid Films*, 513(1), 1–24.

Hertz, H. (1887). “Ueber einen Einfluss des ultravioletten Lichtes auf die electriche Entladung.” *Ann. Phys.*, 267(8), 983–1000.

Hishita, S., Aizawa, T., Suehara, S., and Haneda, H. (2003). “2.2 FORMATION MECHANISM OF SIC IN C-SI SYSTEM BY ION IRRADIATION.” *JAERI-Conf*, 228.

Ho, K. K., and Carman, G. P. (2000). “Sputter deposition of NiTi thin film shape memory alloy using a heated target.” *Thin Solid Films*, 370(1), 18–29.

Hou, H., Hamilton, R. F., Horn, M. W., and Jin, Y. (2014). “NiTi thin films prepared by biased target ion beam deposition co-sputtering from elemental Ni and Ti targets.” *Thin Solid Films*, 570, 1–6.

Hou, L., and Grummon, D. S. (1995). “Transformational superelasticity in sputtered titanium-nickel thin films.” *Scr. Metall. Mater.*, 33(6), 989–995.

Huang, X., and Liu, Y. (2005a). “Surface morphology of sputtered NiTi-based shape memory alloy thin films.” *Surf. Coat. Technol.*, 190(2), 400–405.

Huang, X., and Liu, Y. (2005b). “Surface morphology of sputtered NiTi-based shape memory alloy thin films.” *Surf. Coat. Technol.*, 190(2), 400–405.

Huang, X., Nohava, J., Zhang, B., and Ramirez, A. G. (2011). “Nanoindentation of NiTi shape memory thin films at elevated temperatures.” *Int. J. Smart Nano Mater.*, 2(1), 39–49.

Huang, X., and Ramirez, A. G. (2009). “Structural relaxation and crystallization of NiTi thin film metallic glasses.” *Appl. Phys. Lett.*, 95(12), 121911.

Huang, X., San Juan, J., and Ramirez, A. G. (2010). “Evolution of phase transformation behavior and mechanical properties with crystallization in NiTi thin films.” *Scr. Mater.*, 63(1), 16–19.

Ikuta, K., Fujita, H., Ikeda, M., and Yamashita, S. (1990). “Crystallographic analysis of TiNi shape memory alloy thin film for microactuator.” *Micro Electro Mech. Syst. 1990 Proc. Investig. Micro Struct. Sens. Actuators Mach. Robots IEEE*, IEEE, 38–39.

Isalgue, A., Torra, V., Seguin, J.-L., Bendahan, M., Amigo, J. M., and Esteve-Cano, V. (1999). “Shape memory NiTi thin films deposited at low temperature.” *Mater. Sci. Eng. A*, 273, 717–721.

Ishida, A., and Martynov, V. (2002). “Sputter-deposited shape-memory alloy thin films: properties and applications.” *Mrs Bull.*, 27(2), 111–114.

- Ishida, A., and Miyazaki, S. (1999). "Microstructure and mechanical properties of sputter-deposited Ti-Ni alloy thin films." *J. Eng. Mater. Technol.*, 121(1), 2–8.
- Ishida, A., Ogawa, K., Sato, M., and Miyazaki, S. (1997). "Microstructure of Ti-48.2 at. pct Ni shape memory thin films." *Metall. Mater. Trans. A*, 28(10), 1985–1991.
- Ishida, A., and Sato, M. (2003). "Thickness effect on shape memory behavior of Ti-50.0 at.% Ni thin film." *Acta Mater.*, 51(18), 5571–5578.
- Ishida, A., Sato, M., and Miyazaki, S. (1999). "Mechanical properties of Ti–Ni shape memory thin films formed by sputtering." *Mater. Sci. Eng. A*, 273, 754–757.
- Ishida, A., Sato, M., Takei, A., Nomura, K., and Miyazaki, S. (1996a). "Effect of aging on shape memory behavior of Ti-51.3 At. pct ni thin films." *Metall. Mater. Trans. A*, 27(12), 3753–3759.
- Ishida, A., Takei, A., Sato, M., and Miyazaki, S. (1994). "Shape memory behavior of Ti-Ni thin films annealed at various temperatures." *MRS Online Proc. Libr. Arch.*, 360.
- Ishida, A., Takei, A., Sato, M., and Miyazaki, S. (1996b). "Stress-strain curves of sputtered thin films of Ti- Ni." *Thin Solid Films*, 281, 337–339.
- James, R. D., and Hane, K. F. (2000). "Martensitic transformations and shape-memory materials." *Acta Mater.*, 48(1), 197–222.
- Jardine, A. P., Zhang, H., and Wasielesky, L. D. (1990). "Investigation into the thin-film fabrication of intermetallic NiTi." *MRS Online Proc. Libr. Arch.*, 187.
- Jiang, F., Li, L., Zheng, Y., Yang, H., and Liu, Y. (2008). "Cyclic ageing of Ti–50.8 at.% Ni alloy." *Intermetallics*, 16(3), 394–398.
- Jiang, F., Liu, Y., Yang, H., Li, L., and Zheng, Y. (2009). "Effect of ageing treatment on the deformation behaviour of Ti–50.9 at.% Ni." *Acta Mater.*, 57(16), 4773–4781.

- Johnson, A. D. (1991). "Vacuum-deposited TiNi shape memory film: characterization and applications in microdevices." *J. Micromechanics Microengineering*, 1(1), 34–41.
- Jones, I. P. (2001). *Materials science for electrical and electronic engineers*. Oxford University Press.
- Ju, H., Feng, X., Ye, Y., Zhang, L., Pan, H., Campbell, C. T., and Zhu, J. (2012). "Ca carboxylate formation at the calcium/poly (methyl methacrylate) interface." *J. Phys. Chem. C*, 116(38), 20465–20471.
- Kahn, H., Huff, M. A., and Heuer, A. H. (1998). "The TiNi shape-memory alloy and its applications for MEMS." *J. Micromechanics Microengineering*, 8(3), 213.
- Kainuma, R., Matsumoto, M., and Honma, T. (1987). "Metallographic Study of Precipitation Processes in Nickel-Rich TiNi Alloys." *Bull Res Inst Min. Dress. Met.*, 43(2), 149–158.
- Kajiwara, S. (1996). "Strengthening of Ti-Ni shape-memory films by coherent subnanometric plate precipitates." *Philos. Mag. Lett.*, 74(3), 137–144.
- Kan, Q., Yan, W., Kang, G., and Sun, Q. (2013). "Oliver–Pharr indentation method in determining elastic moduli of shape memory alloys—a phase transformable material." *J. Mech. Phys. Solids*, 61(10), 2015–2033.
- Kauffmann-Weiss, S., Hahn, S., Weigelt, C., Schultz, L., Wagner, M. F.-X., and Fähler, S. (2017). "Growth, microstructure and thermal transformation behaviour of epitaxial Ni-Ti films." *Acta Mater.*, 132, 255–263.
- Kawamura, Y., Gyobu, A., Horikawa, H., and Saburi, T. (1995). "Martensitic transformations and shape memory effect in Ti-Ni sputter-deposited thin films." *J. Phys. IV*, 5(C8), C8–683.
- Kelly, P. J., and Arnell, R. D. (2000). "Magnetron sputtering: a review of recent developments and applications." *Vacuum*, 56(3), 159–172.

- Khalil-Allafi, J., Dlouhy, A., and Eggeler, G. (2002). "Ni₄Ti₃-precipitation during aging of NiTi shape memory alloys and its influence on martensitic phase transformations." *Acta Mater.*, 50(17), 4255–4274.
- Khalil-Allafi, J., Eggeler, G., Dlouhy, A., Schmahl, W. W., and Somsen, C. (2004). "On the influence of heterogeneous precipitation on martensitic transformations in a Ni-rich NiTi shape memory alloy." *Mater. Sci. Eng. A*, 378(1), 148–151.
- Khalil-Allafi, J., Schmahl, W. W., and Toebbens, D. M. (2006). "Space group and crystal structure of the R-phase in binary NiTi shape memory alloys." *Acta Mater.*, 54(12), 3171–3175.
- Kim, J. I., Liu, Y., and Miyazaki, S. (2004). "Ageing-induced two-stage R-phase transformation in Ti–50.9 at.% Ni." *Acta Mater.*, 52(2), 487–499.
- Kim, J. J., Moine, P., and Stevenson, D. A. (1986). "Crystallization behavior of amorphous Ni-Ti alloys prepared by sputter deposition." *Scr. Metall.*, 20(2), 243–248.
- Kim, K. S., and Winograd, N. (1974). "X-ray photoelectron spectroscopic studies of nickel-oxygen surfaces using oxygen and argon ion-bombardment." *Surf. Sci.*, 43(2), 625–643.
- Kim, K. S., and Winograd, N. (1975a). "X-ray photoelectron spectroscopic binding energy shifts due to matrix in alloys and small supported metal particles." *Chem. Phys. Lett.*, 30(1), 91–95.
- Kim, K. S., and Winograd, N. (1975b). "X-ray photoelectron spectroscopic binding energy shifts due to matrix in alloys and small supported metal particles." *Chem. Phys. Lett.*, 30(1), 91–95.
- King, R. B. (1987). "Elastic analysis of some punch problems for a layered medium." *Int. J. Solids Struct.*, 23(12), 1657–1664.
- Kompatscher, M., Deme, B., Kostorz, G., Somsen, C., and Wassermann, E. F. (2002). "Small-angle neutron scattering of precipitates in Ni–Ti shape memory alloys." *Acta Mater.*, 50(6), 1581–1586.

Koskimaki, D., Marcinkowski, M. J., and Sastri, A. (1969). "Solid state diffusional transformations in the near-equiatomic Ni-Ti alloys(Phase changes in Ni/Ti alloys with equiatomic composition, resolving discrepancy on nonMartensitic eutectoidal decomposition of B2 structure and intermediate precipitate)." *Metall. Soc. AIME Trans.*, 245, 1883–1890.

Kotnur, V. G., and Janssen, G. (2012a). "In situ stress measurements and mechanical properties of a composition range of NiTi thin films deposited at elevated temperature." *Surf. Coat. Technol.*, 211, 167–171.

Krulevitch, P., Lee, A. P., Ramsey, P. B., Trevino, J. C., Hamilton, J., and Northrup, M. A. (1996a). "Thin film shape memory alloy microactuators." *J. Microelectromechanical Syst.*, 5(4), 270–282.

Krulevitch, P., Ramsey, P. B., Makowiecki, D. M., Lee, A. P., Northrup, M. A., and Johnson, G. C. (1996b). "Mixed-sputter deposition of Ni-Ti-Cu shape memory films." *Thin Solid Films*, 274(1–2), 101–105.

Kumar, A. N., Nair, C. S., Kannan, M. D., and Jayakumar, S. (2006). "TEM and nanoindentation studies on sputtered Ti 40 Ni 60 thin films." *Mater. Chem. Phys.*, 97(2), 308–314.

Kumar, A., Sharma, S. K., Bysakh, S., Kamat, S. V., and Mohan, S. (2010a). "Effect of substrate and annealing temperatures on mechanical properties of Ti-rich NiTi Films." *J. Mater. Sci. Technol.*, 26(11), 961–966.

Kumar, A., Sharma, S. K., Bysakh, S., Kamat, S. V., and Mohan, S. (2010b). "Effect of substrate and annealing temperatures on mechanical properties of Ti-rich NiTi Films." *J. Mater. Sci. Technol.*, 26(11), 961–966.

Kumar, A., Singh, D., and Kaur, D. (2009). "Grain size effect on structural, electrical and mechanical properties of NiTi thin films deposited by magnetron co-sputtering." *Surf. Coat. Technol.*, 203(12), 1596–1603.

- Kumar, A., Singh, D., and Kaur, D. (2012). "Variation in phase transformation paths of NiTi films as a function of film thickness." *Sens. Actuators Phys.*, 178, 57–63.
- Kumar, P. K., and Lagoudas, D. C. (2008). "Introduction to Shape Memory Alloys." *Shape Mem. Alloys*, Springer, Boston, MA, 1–51.
- Kurdjumov, G. V., and Khandros, L. G. (1949). "First reports of the thermoelastic behaviour of the martensitic phase of Au-Cd alloys." *Dokl. Akad. Nauk SSSR*, 66, 211–213.
- Kuribayashi, K., Yoshitake, M., and Ogawa, S. (1990). "Reversible SMA actuator for micron sized robot." *Micro Electro Mech. Syst. 1990 Proc. Investig. Micro Struct. Sens. Actuators Mach. Robots IEEE*, IEEE, 217–221.
- Kurumada, M., Kimura, Y., Suzuki, H., Kido, O., Saito, Y., and Kaito, C. (2004). "TEM study of early Ni₄Ti₃ precipitation and R-phase in Ni-rich NiTi nanoparticles." *Scr. Mater.*, 50(11), 1413–1416.
- Laves, F., and Wallbaum, H. J. (1939). "Zur Kristallchemie von Titan-Legierungen." *Naturwissenschaften*, 27, 674–675.
- Lee, H.-J., Huang, X., Mohanchandra, K. P., Carman, G., and Ramirez, A. G. (2009). "Effects of crystallization temperature on the stress of NiTi thin films." *Scr. Mater.*, 60(12), 1133–1136.
- Lee, H.-J., Ni, H., Wu, D. T., and Ramirez, A. G. (2006). "A microstructural map of crystallized NiTi thin film derived from in situ TEM methods." *Mater. Trans.*, 47(3), 527–531.
- Lee, H.-J., and Ramirez, A. G. (2004). "Crystallization and phase transformations in amorphous NiTi thin films for microelectromechanical systems." *Appl. Phys. Lett.*, 85(7), 1146–1148.
- Lehnert, T., Crevoiserat, S., and Gotthardt, R. (2002). "Transformation properties and microstructure of sputter-deposited Ni-Ti shape memory alloy thin films." *J. Mater. Sci.*, 37(8), 1523–1533.

Lehnert, T., Grimmer, H., Böni, P., Horisberger, M., and Gotthardt, R. (2000a). “Characterization of shape-memory alloy thin films made up from sputter-deposited Ni/Ti multilayers.” *Acta Mater.*, 48(16), 4065–4071.

Lehnert, T., Grimmer, H., Böni, P., Horisberger, M., and Gotthardt, R. (2000b). “Characterization of shape-memory alloy thin films made up from sputter-deposited Ni/Ti multilayers.” *Acta Mater.*, 48(16), 4065–4071.

Levi, D. S., Kusnezov, N., and Carman, G. P. (2008). “Smart materials applications for pediatric cardiovascular devices.” *Pediatr. Res.*, 63(5), 552–558.

Li, H., and Vlassak, J. J. (2009). “Determining the elastic modulus and hardness of an ultra-thin film on a substrate using nanoindentation.” *J. Mater. Res.*, 24(3), 1114–1126.

Liu, Y., Blanc, M., Tan, G., Kim, J. I., and Miyazaki, S. (2006). “Effect of ageing on the transformation behaviour of Ti–49.5 at.% Ni.” *Mater. Sci. Eng. A*, 438, 617–621.

Liu, Y., Chen, X., and McCormick, P. G. (1997). “Effect of low temperature ageing on the transformation behaviour of near-equiatomic NiTi.” *J. Mater. Sci.*, 32(22), 5979–5984.

Liu, Y., and Favier, D. (2000). “Stabilisation of martensite due to shear deformation via variant reorientation in polycrystalline NiTi.” *Acta Mater.*, 48(13), 3489–3499.

Liu, Y., Kim, J. I., and Miyazaki, S. (2004). “Thermodynamic analysis of ageing-induced multiple-stage transformation behaviour of NiTi.” *Philos. Mag.*, 84(20), 2083–2102.

Makino, E., Mitsuya, T., and Shibata, T. (2000). “Micromachining of TiNi shape memory thin film for fabrication of micropump.” *Sens. Actuators Phys.*, 79(3), 251–259.

Makino, E., Mitsuya, T., and Shibata, T. (2001). “Fabrication of TiNi shape memory micropump.” *Sens. Actuators Phys.*, 88(3), 256–262.

Martins, R. M. S., Braz Fernandes, F. M., Silva, R. J. C., Pereira, L., Gordo, P. R., Maneira, M. J. P., Beckers, M., Mücklich, A., and Schell, N. (2006a). “The influence of a poly-Si intermediate layer on the crystallization behaviour of Ni-Ti SMA magnetron sputtered thin films.” *Appl. Phys. Mater. Sci. Process.*, 83(1), 139–145.

Martins, R. M. S., Schell, N., Beckers, M., Mahesh, K. K., Silva, R. J. C., and Fernandes, F. B. (2006b). “Growth of sputter-deposited Ni-Ti thin films: effect of a SiO₂ buffer layer.” *Appl. Phys. Mater. Sci. Process.*, 84(3), 285–289.

Martins, R. M. S., Schell, N., Beckers, M., Silva, R. J. C., Mahesh, K. K., and Fernandes, F. B. (2008a). “Role of the substrate on the growth of Ni–Ti sputtered thin films.” *Mater. Sci. Eng. A*, 481, 626–629.

Martins, R. M. S., Schell, N., Mücklich, A., Reuther, H., Beckers, M., Silva, R. J. C., Pereira, L., and Braz Fernandes, F. M. (2008b). “Study of graded Ni-Ti shape memory alloy film growth on Si (100) substrate.” *Appl. Phys. Mater. Sci. Process.*, 91(2), 291–299.

Martins, R. M. S., Schell, N., Reuther, H., Pereira, L., Mahesh, K. K., Silva, R. J. C., and Fernandes, F. B. (2010). “Texture development, microstructure and phase transformation characteristics of sputtered Ni–Ti Shape Memory Alloy films grown on TiN< 111.” *Thin Solid Films*, 519(1), 122–128.

Martins, R. M. S., Schell, N., Silva, R. J. C., Pereira, L., Mahesh, K. K., and Fernandes, F. B. (2007). “In-situ study of Ni–Ti thin film growth on a TiN intermediate layer by X-ray diffraction.” *Sens. Actuators B Chem.*, 126(1), 332–337.

McKelvey, A. L., and Ritchie, R. O. (2000). “On the temperature dependence of the superelastic strength and the prediction of the theoretical uniaxial transformation strain in Nitinol.” *Philos. Mag. A*, 80(8), 1759–1768.

Meyer, E. (1992). “Atomic force microscopy.” *Prog. Surf. Sci.*, 41(1), 3–49.

Miura, S., and Nakanishi, N. (1986). “Proc. Int. Conf. on Martensitic Transformations.” *Jpn. Inst Met. Nara*, 1015.

- Miyazaki, S., Duerig, T. W., Melton, K. N., and others. (1990). *Engineering aspects of shape memory alloys*. Butterworth-Heinemann, London.
- Miyazaki, S., and Ishida, A. (1994). "Shape memory characteristics of sputter-deposited Ti–Ni thin films." *Mater. Trans. JIM*, 35(1), 14–19.
- Miyazaki, S., and Ishida, A. (1999a). "Martensitic transformation and shape memory behavior in sputter-deposited TiNi-base thin films." *Mater. Sci. Eng. A*, 273, 106–133.
- Miyazaki, S., and Ishida, A. (1999b). "Martensitic transformation and shape memory behavior in sputter-deposited TiNi-base thin films." *Mater. Sci. Eng. A*, 273, 106–133.
- Miyazaki, S., No, V. H., Kitamura, K., Khantachawana, A., and Hosoda, H. (2000). "Texture of Ti–Ni rolled thin plates and sputter-deposited thin films." *Int. J. Plast.*, 16(10), 1135–1154.
- Mohri, M., Nili-Ahmadabadi, M., Ivanisenko, J., Schwaiger, R., Hahn, H., and Chakravadhanula, V. S. K. (2015). "Microstructure and mechanical behavior of a shape memory Ni–Ti bi-layer thin film." *Thin Solid Films*, 583, 245–254.
- Monshi, A., Foroughi, M. R., and Monshi, M. R. (2012). "Modified Scherrer equation to estimate more accurately nano-crystallite size using XRD." *World J. Nano Sci. Eng.*, 2(3), 154–160.
- Moss, C. F., and Sinha, S. R. (2003). "Neurobiology of echolocation in bats." *Curr. Opin. Neurobiol.*, 13(6), 751–758.
- Moulder, J. F., Stickle, W. F., Sobol, P. E., and Bomben, K. D. (1992). "Standard Spectra for Identification and Interpretation of XPS data." *Perkin Elmer Eden Prairie MN*.
- Moyne, S., Poilane, C., Kitamura, K., Miyazaki, S., Delobelle, P., and Lexcelent, C. (1999). "Analysis of the thermomechanical behavior of Ti–Ni shape memory alloy thin films by bulging and nanoindentation procedures." *Mater. Sci. Eng. A*, 273, 727–732.

- Musil, J., and Vlček, J. (1998). “Magnetron sputtering of films with controlled texture and grain size.” *Mater. Chem. Phys.*, 54(1–3), 116–122.
- Naumkin, A. V., Kraut-Vass, A., Gaarenstroom, S. W., and Powell, C. J. (n.d.). *NIST X-ray Photoelectron Spectroscopy Database 20. Version 4.1, 2012*.
- Nemat-Nasser, S., and Guo, W.-G. (2006). “Superelastic and cyclic response of NiTi SMA at various strain rates and temperatures.” *Mech. Mater.*, 38(5), 463–474.
- Ni, W., Cheng, Y.-T., Lukitsch, M. J., Weiner, A. M., Lev, L. C., and Grummon, D. S. (2004). “Effects of the ratio of hardness to Young’s modulus on the friction and wear behavior of bilayer coatings.” *Appl. Phys. Lett.*, 85(18), 4028–4030.
- Nishida, M., Wayman, C. M., and Honma, T. (1986). “Precipitation processes in near-equiatomic TiNi shape memory alloys.” *Metall. Mater. Trans. A*, 17(9), 1505–1515.
- Ohkata, I., and Tamura, H. (1996). “The R-phase transformation in the Ti-Ni shape memory alloy and its application.” *MRS Online Proc. Libr. Arch.*, 459.
- Ohring, M. (2002). “Materials Science of Thin Films 2nd edn (New York: Academic).”
- Ohta, A., Bhansali, S., Kishimoto, I., and Umeda, A. (2000). “Novel fabrication technique of TiNi shape memory alloy film using separate Ti and Ni targets.” *Sens. Actuators Phys.*, 86(3), 165–170.
- Olbricht, J., Yawny, A., Pelegrina, J. L., Dlouhy, A., and Eggeler, G. (2011). “On the stress-induced formation of R-phase in ultra-fine-grained Ni-rich NiTi shape memory alloys.” *Metall. Mater. Trans.*, 42(9), 2556.
- Oliver, W. C., and Pharr, G. M. (1992a). “An improved technique for determining hardness and elastic modulus using load and displacement sensing indentation experiments.” *J. Mater. Res.*, 7(6), 1564–1583.

Oliver, W. C., and Pharr, G. M. (1992b). “An improved technique for determining hardness and elastic modulus using load and displacement sensing indentation experiments.” *J. Mater. Res.*, 7(6), 1564–1583.

Oliver, W. C., and Pharr, G. M. (2004a). “Measurement of hardness and elastic modulus by instrumented indentation: Advances in understanding and refinements to methodology.” *J. Mater. Res.*, 19(1), 3–20.

Oliver, W. C., and Pharr, G. M. (2004b). “Measurement of hardness and elastic modulus by instrumented indentation: Advances in understanding and refinements to methodology.” *J. Mater. Res.*, 19(1), 3–20.

Otsuka, K., and Ren, X. (2005). “Physical metallurgy of Ti–Ni-based shape memory alloys.” *Prog. Mater. Sci.*, 50(5), 511–678.

Page, T. F., and Hainsworth, S. V. (1993). “Using nanoindentation techniques for the characterization of coated systems: a critique.” *Surf. Coat. Technol.*, 61(1–3), 201–208.

Pan, G., Cao, Z., Shi, J., Wei, M., Xu, L., and Meng, X. (2014). “Different mechanical response of TiNi film induced by the shape of indenter during nanoindentation.” *Sens. Actuators Phys.*, 217, 75–80.

Pan, Q., and Cho, C. (2007). “The investigation of a shape memory alloy micro-damper for MEMS applications.” *Sensors*, 7(9), 1887–1900.

Paryab, M., Nasr, A., Bayat, O., Abouei, V., and Eshraghi, A. (2010). “Effect of heat treatment on the microstructural and superelastic behavior of NiTi alloy with 58.5 wt% Ni.” *Metalurgija*, 16(2), 123–131.

Paula, A. S., Canejo, J., Martins, R. M. S., and Fernandes, F. B. (2004). “Effect of thermal cycling on the transformation temperature ranges of a Ni–Ti shape memory alloy.” *Mater. Sci. Eng. A*, 378(1), 92–96.

Payne, B.P. (2011). “X-ray Photoelectron Spectroscopy Studies on the Oxidation Processes of Nickel, Chromium and their Alloys” Ph.D. Dissertation, The University of Western Ontario.

Pelletier, H., Muller, D., Mille, P., and Grob, J. J. (2002). “Effect of high energy argon implantation into NiTi shape memory alloy.” *Surf. Coat. Technol.*, 158, 301–308.

Pelton, A. R., Dicello, J., and Miyazaki, S. (2000). “Optimisation of processing and properties of medical grade Nitinol wire.” *Minim. Invasive Ther. Allied Technol.*, 9(2), 107–118.

Pequegnat, A., Michael, A., Wang, J., Lian, K., Zhou, Y., and Khan, M. I. (2015). “Surface characterizations of laser modified biomedical grade NiTi shape memory alloys.” *Mater. Sci. Eng. C*, 50, 367–378.

Petrov, I., Barna, P. B., Hultman, L., and Greene, J. E. (2003). “Microstructural evolution during film growth.” *J. Vac. Sci. Technol. Vac. Surf. Films*, 21(5), S117–S128.

Petrović, S., Peruško, D., Mitrčić, M., Kovac, J., Dražić, G., Gaković, B., Homewood, K. P., and Milosavljević, M. (2012). “Formation of intermetallic phase in Ni/Ti multilayer structure by ion implantation and thermal annealing.” *Intermetallics*, 25, 27–33.

Pharr, G. M., Oliver, W. C., and Brotzen, F. R. (1992). “On the generality of the relationship among contact stiffness, contact area, and elastic modulus during indentation.” *J. Mater. Res.*, 7(3), 613–617.

Poole, D. M., and Hume-Rothery, W. (1955). “The equilibrium diagram of the system nickel-titanium.” *J Inst Met.*, 83.

Poon, R. W. Y., Liu, X. Y., Chung, C. Y., Chu, P. K., Yeung, K. W. K., Lu, W. W., and Cheung, K. M. C. (2005a). “Surface and corrosion characteristics of carbon

plasma implanted and deposited nickel-titanium alloy.” *J. Vac. Sci. Technol. Vac. Surf. Films*, 23(3), 525–530.

Poon, R. W. Y., Yeung, K. W. K., Liu, X. Y., Chu, P. K., Chung, C. Y., Lu, W. W., Cheung, K. M. C., and Chan, D. (2005b). “Carbon plasma immersion ion implantation of nickel–titanium shape memory alloys.” *Biomaterials*, 26(15), 2265–2272.

Powell, C. J., and Jablonski, A. (2005). “NIST Electron Inelastic-Mean-Free-Path Database, Version 1.1; National Institute of Standards and Technology: Gaithersburg, MD, 2000.” *There No Corresp. Rec. This Ref.*

Prabhu, Y. T., Rao, K. V., Kumar, V. S. S., and Kumari, B. S. (2014). “X-ray analysis by Williamson-Hall and size-strain plot methods of ZnO nanoparticles with fuel variation.” *World J. Nano Sci. Eng.*, 4(01), 21.

Priyadarshini, B. G., Aich, S., and Chakraborty, M. (2016). “Nano-crystalline Ni Ti alloy thin films fabricated using magnetron co-sputtering from elemental targets: Effect of substrate conditions.” *Thin Solid Films*, 616, 733–745.

Raju, K. E., Bysakh, S., Sumesh, M. A., Kamat, S. V., and Mohan, S. (2008). “The effect of ageing on microstructure and nanoindentation behaviour of dc magnetron sputter deposited nickel rich NiTi films.” *Mater. Sci. Eng. A*, 476(1), 267–273.

Rajathadripura. (2014). "Characterization of Hybrid Electronic Materials Using Atomic Force Microscopy" (2014). LSU Master's Theses. 1172.

Ramirez, A. G., Ni, H., and Lee, H.-J. (2006). “Crystallization of amorphous sputtered NiTi thin films.” *Mater. Sci. Eng. A*, 438, 703–709.

Ratner, B. D., Hoffman, A. S., Schoen, F. J., and Lemons, J. E. (2004). *Biomaterials science: an introduction to materials in medicine*. Academic press.

Ravari, B. K., Farjami, S., and Nishida, M. (2014). “Effects of Ni concentration and aging conditions on multistage martensitic transformation in aged Ni-rich Ti–Ni alloys.” *Acta Mater.*, 69, 17–29.

- Reddy, B. N. K., and Udayashankar, N. K. (2017). "Aging time correlation in DC magnetron sputtered Ni₆₀Ti₄₀ thin films." *Vacuum*, 135, 124–134.
- Rupérez, E., Manero, J. M., Bravo-González, L.-A., Espinar, E., and Gil, F. J. (2016). "Development of Biomimetic NiTi Alloy: Influence of Thermo-Chemical Treatment on the Physical, Mechanical and Biological Behavior." *Materials*, 9(6), 402.
- Saha, R., and Nix, W. D. (2002). "Effects of the substrate on the determination of thin film mechanical properties by nanoindentation." *Acta Mater.*, 50(1), 23–38.
- San Paulo, A., and García, R. (2001). "Tip-surface forces, amplitude, and energy dissipation in amplitude-modulation (tapping mode) force microscopy." *Phys. Rev. B*, 64(19), 193411.
- Sanjabi, S., and Barber, Z. H. (2010). "The effect of film composition on the structure and mechanical properties of NiTi shape memory thin films." *Surf. Coat. Technol.*, 204(8), 1299–1304.
- Sanjabi, S., Naderi, M., Bidaki, H. Z., and Sadrnezhaad, S. K. (2009). "Characterization of sputtered NiTi shape memory alloy thin films." *Sci. Iran. Trans.*, 16(3), 248–252.
- Sanjabi, S., Sadrnezhaad, S. K., Yates, K. A., and Barber, Z. H. (2005). "Growth and characterization of Ti_xNi_{1-x} shape memory thin films using simultaneous sputter deposition from separate elemental targets." *Thin Solid Films*, 491(1), 190–196.
- Sato, M., Ishida, A., and Miyazaki, S. (1998). "Two-way shape memory effect of sputter-deposited thin films of Ti 51.3 at.% Ni." *Thin Solid Films*, 315(1), 305–309.
- Satoh, G., Birnbaum, A., and Yao, Y. L. (2008). "Effect of annealing parameters on the shape memory properties of NiTi thin films." *Proc. ICALEO*.
- Satoh, G., Birnbaum, A., and Yao, Y. L. (2009). "Shape Memory Property Alteration of Amorphous NiTi Thin Films Through Aging Heat Treatment." *ASME 2009 Int. Manuf. Sci. Eng. Conf.*, American Society of Mechanical Engineers, 637–646.

Satoh, G., Birnbaum, A., and Yao, Y. L. (2010). "Annealing effect on the shape memory properties of amorphous NiTi thin films." *J. Manuf. Sci. Eng.*, 132(5), 051004.

Schuh, C. A. (2006). "Nanoindentation studies of materials." *Mater. Today*, 9(5), 32–40.

Sekiguchi, Y., Funami, K., Funakubo, H., and Suzuki, Y. (1982). "Study on the hot pressed powder metallurgy of a TiNi shape memory alloy." *J. Phys. Colloq.*, 43(C4), C4–279.

Shabalovskaya, S., Anderegg, J., and Van Humbeeck, J. (2008). "Critical overview of Nitinol surfaces and their modifications for medical applications." *Acta Biomater.*, 4(3), 447–467.

Sharma, S. K., and Mohan, S. (2013a). "Influence of annealing on structural, morphological, compositional and surface properties of magnetron sputtered nickel–titanium thin films." *Appl. Surf. Sci.*, 282, 492–498.

Sharma, S. K., and Mohan, S. (2013b). "Influence of annealing on structural, morphological, compositional and surface properties of magnetron sputtered nickel–titanium thin films." *Appl. Surf. Sci.*, 282, 492–498.

Sharma, S. K., Vijaya, H. S., and Mohan, S. (2010). "Influence of substrate temperature and deposition rate on structural and mechanical properties of shape memory NiTi films." *Phys. Procedia*, 10, 44–51.

Shaw, G. A., Stone, D. S., Johnson, A. D., Ellis, A. B., and Crone, W. C. (2003). "Shape memory effect in nanoindentation of nickel–titanium thin films." *Appl. Phys. Lett.*, 83(2), 257–259.

Shih, C.-L., Lai, B.-K., Kahn, H., Phillips, S. M., and Heuer, A. H. (2001). "A robust co-sputtering fabrication procedure for TiNi shape memory alloys for MEMS." *J. Microelectromechanical Syst.*, 10(1), 69–79.

- Siegbahn, K., Gelius, U., Siegbahn, H., and Olson, E. (1970). "Angular distribution of electrons in ESCA spectra from a single crystal." *Phys. Scr.*, 1(5–6), 272.
- Singh, J., Kaurav, N., Lalla, N. P., and Okram, G. S. (2014). "Naturally self-assembled nickel nanolattice." *J. Mater. Chem. C*, 2(42), 8918–8924.
- Smilgies, D.-M. (2009). "Scherrer grain-size analysis adapted to grazing-incidence scattering with area detectors." *J. Appl. Crystallogr.*, 42(6), 1030–1034.
- Smith, E. F., Briggs, D., and Fairley, N. (2006). "Further developments in quantitative X-ray photoelectron spectromicroscopy: preliminary results from the study of germanium corrosion." *Surf. Interface Anal.*, 38(2), 69–75.
- Sneddon, I. N. (1965). "The relation between load and penetration in the axisymmetric Boussinesq problem for a punch of arbitrary profile." *Int. J. Eng. Sci.*, 3(1), 47–57.
- Somsen, C. H., Zähres, H., Kästner, J., Wassermann, E. F., Kakeshita, T., and Saburi, T. (1999). "Influence of thermal annealing on the martensitic transitions in Ni–Ti shape memory alloys." *Mater. Sci. Eng. A*, 273, 310–314.
- Sonoda, T., Watazu, A., Zhu, J., Shi, W., Kato, K., and Asahina, T. (2004). "Structure and mechanical properties of pure titanium film deposited onto TiNi shape memory alloy substrate by magnetron DC sputtering." *Thin Solid Films*, 459(1), 212–215.
- Sreekumar, M., Nagarajan, T., Singaperumal, M., Zoppi, M., and Molfino, R. (2007). "Critical review of current trends in shape memory alloy actuators for intelligent robots." *Ind. Robot Int. J.*, 34(4), 285–294.
- Stemmer, S., Duscher, G., Scheu, C., Heuer, A. H., and Rühle, M. (1997). "The reaction between a TiNi shape memory thin film and silicon." *J. Mater. Res.*, 12(7), 1734–1740.
- Strohmeier, B. R. (1990). "An ESCA method for determining the oxide thickness on aluminum alloys." *Surf. Interface Anal.*, 15(1), 51–56.

Su, P. C., and Wu, S. K. (2004). “The four-step multiple stage transformation in deformed and annealed Ti 49 Ni 51 shape memory alloy.” *Acta Mater.*, 52(5), 1117–1122.

Su, Q., Hua, S. Z., and Wuttig, M. (1994a). “Martensitic transformation in Ni50Ti50 films.” *J. Alloys Compd.*, 211, 460–463.

Su, Q., Hua, S. Z., and Wuttig, M. (1994b). “Martensitic transformation in Ni50Ti50 films.” *J. Alloys Compd.*, 211, 460–463.

Surbled, P., Clerc, C., Le Pioufle, B., Ataka, M., and Fujita, H. (2001). “Effect of the composition and thermal annealing on the transformation temperatures of sputtered TiNi shape memory alloy thin films.” *Thin Solid Films*, 401(1), 52–59.

Tabor, D. (2000). *The hardness of metals*. Oxford university press.

Tall, P. D., Ndiaye, S., Beye, A. C., Zong, Z., Soboyejo, W. O., Lee, H.-J., Ramirez, A. G., and Rajan, K. (2007). “Nanoindentation of Ni–Ti thin films.” *Mater. Manuf. Process.*, 22(2), 175–179.

Tanuma, S., Powell, C. J., and Penn, D. R. (1988). “Calculations of electron inelastic mean free paths for 31 materials.” *Surf. Interface Anal.*, 11(11), 577–589.

Tao, J. G., Pan, J. S., Huan, C. H. A., Zhang, Z., Chai, J. W., and Wang, S. J. (2008). “Origin of XPS binding energy shifts in Ni clusters and atoms on rutile TiO₂ surfaces.” *Surf. Sci.*, 602(16), 2769–2773.

Tesfai, A., El-Zahab, B., Bwambok, D. K., Baker, G. A., Fakayode, S. O., Lowry, M., and Warner, I. M. (2008). “Controllable formation of ionic liquid micro- and nanoparticles via a melt–emulsion–quench approach.” *Nano Lett.*, 8(3), 897–901.

Thomas, G., Mori, H., Fujita, H., and Sinclair, R. (1982). “Electron irradiation induced crystalline amorphous transitions in Ni-Ti alloys.” *Scr. Metall.*, 16(5), 589–592.

Thomasová, M., Sedlák, P., Seiner, H., Janovská, M., Kabla, M., Shilo, D., and Landa, M. (2015). “Young’s moduli of sputter-deposited NiTi films determined by resonant ultrasound spectroscopy: Austenite, R-phase, and martensite.” *Scr. Mater.*, 101, 24–27.

Thool, G. S., Singh, A. K., Singh, R. S., Gupta, A., and Susan, M. A. B. H. (2014). “Facile synthesis of flat crystal ZnO thin films by solution growth method: a microstructural investigation.” *J. Saudi Chem. Soc.*, 18(5), 712–721.

Tillmann, W., and Momeni, S. (2015a). “Tribological performance of near equiatomic and Ti-rich NiTi shape memory alloy thin films.” *Acta Mater.*, 92, 189–196.

Tillmann, W., and Momeni, S. (2015b). “Influence of in-situ and postannealing technique on tribological performance of NiTi SMA thin films.” *Surf. Coat. Technol.*, 276, 286–295.

Tillmann, W., and Momeni, S. (2015c). “In-situ annealing of NiTi thin films at different temperatures.” *Sens. Actuators Phys.*, 221, 9–14.

Tillmann, W., and Momeni, S. (2015d). “Comparison of NiTi thin films sputtered from separate elemental targets and Ti-rich alloy targets.” *J. Mater. Process. Technol.*, 220, 184–190.

Tomozawa, M., Kim, H. Y., and Miyazaki, S. (2006). “Microactuators using R-phase transformation of sputter-deposited Ti-47.3 Ni shape memory alloy thin films.” *J. Intell. Mater. Syst. Struct.*, 17(12), 1049–1058.

Tougaard, S. (2000). *QUASESTM, Software for Quantitative XPS/AES of Surface Nano-Structures by Analysis of the Peak Shape and Background*. Version.

Tougaard, S., and others. (1998). “Accuracy of the non-destructive surface nanostructure quantification technique based on analysis of the XPS or AES peak shape.” *Surf. Interface Anal.*, 26(4), 249–269.

Tsuchiya, K., and Davies, S. T. (1998). “Fabrication of TiNi shape memory alloy microactuators by ion beam sputter deposition.” *Nanotechnology*, 9(2), 67.

Tsui, T. Y., Oliver, W. C., and Pharr, G. M. (1996). "Influences of stress on the measurement of mechanical properties using nanoindentation: Part I. Experimental studies in an aluminum alloy." *J. Mater. Res.*, 11(3), 752–759.

Uhlenbrock, S., Scharfschwerdt, C., Neumann, M., Illing, G., and Freund, H.-J. (1992). "The influence of defects on the Ni 2p and O 1s XPS of NiO." *J. Phys. Condens. Matter*, 4(40), 7973.

Van Humbeeck, J. (1999). "Non-medical applications of shape memory alloys." *Mater. Sci. Eng. A*, 273, 134–148.

VanLandingham, M. R. (2003). "Review of instrumented indentation." *J. Res. Natl. Inst. Stand. Technol.*, 108(4), 249.

Varadan, V. K., and Varadan, V. V. (2000). "Microsensors, microelectromechanical systems (MEMS), and electronics for smart structures and systems." *Smart Mater. Struct.*, 9(6), 953.

Wagner, M. F., Nayan, N., and Ramamurty, U. (2008). "Healing of fatigue damage in NiTi shape memory alloys." *J. Phys. Appl. Phys.*, 41(18), 185408.

Walker, J. A., Gabriel, K. J., and Mehregany, M. (1990). "Thin-film processing of TiNi shape memory alloy." *Sens. Actuators Phys.*, 21(1–3), 243–246.

Wang, R. M., Chu, C. L., Hu, T., Dong, Y. S., Guo, C., Sheng, X. B., Lin, P. H., Chung, C. Y., and Chu, P. K. (2007). "Surface XPS characterization of NiTi shape memory alloy after advanced oxidation processes in UV/H₂O₂ photocatalytic system." *Appl. Surf. Sci.*, 253(20), 8507–8512.

Wang, R. X., Zohar, Y., and Wong, M. (2001). "The effects of process-induced stress on the microstructures and the phase transformation characteristics of sputtered titanium-nickel thin-film shape-memory alloys." *J. Micromechanics Microengineering*, 11(6), 686.

Wang, X., Kustov, S., Li, K., Schryvers, D., Verlinden, B., and Van Humbeeck, J. (2015a). "Effect of nanoprecipitates on the transformation behavior and functional

properties of a Ti–50.8 at.% Ni alloy with micron-sized grains.” *Acta Mater.*, 82, 224–233.

Wang, X., Kustov, S., Verlinden, B., and Van Humbeeck, J. (2015b). “Fundamental development on utilizing the R-phase transformation in NiTi shape memory alloys.” *Shape Mem. Superelasticity*, 1(2), 231–239.

Wang, X., Li, K., Schryvers, D., Verlinden, B., and Van Humbeeck, J. (2014). “R-phase transition and related mechanical properties controlled by low-temperature aging treatment in a Ti–50.8 at.% Ni thin wire.” *Scr. Mater.*, 72, 21–24.

Wang, X., and Vlassak, J. J. (2006a). “Crystallization kinetics of amorphous NiTi shape memory alloy thin films.” *Scr. Mater.*, 54(5), 925–930.

Wang, X., and Vlassak, J. J. (2006b). “Crystallization kinetics of amorphous NiTi shape memory alloy thin films.” *Scr. Mater.*, 54(5), 925–930.

Wasilewski, R. J., Butler, S. R., Hanlon, J. E., and Worden, D. (1971). “Homogeneity range and the martensitic transformation in TiNi.” *Metall. Trans.*, 2(1), 229–238.

Weihnacht, V., and Brückner, W. (2002). “Abnormal grain growth in {111} textured Cu thin films.” *Thin Solid Films*, 418(2), 136–144.

Winzek, B., Schmitz, S., Rumpf, H., Sterzl, T., Hassdorf, R., Thienhaus, S., Feydt, J., Moske, M., and Quandt, E. (2004). “Recent developments in shape memory thin film technology.” *Mater. Sci. Eng. A*, 378(1), 40–46.

Wolf, R. H., and Heuer, A. H. (1995). “TiNi (shape memory) films silicon for MEMS applications.” *J. Microelectromechanical Syst.*, 4(4), 206–212.

Wu, M. H., and Schetky, L. M. (2000). “Industrial applications for shape memory alloys.” *Proc. Int. Conf. Shape Mem. Superelastic Technol.*, 171–182.

Wuttig, M., Slutsker, J. S., Mori, K., and Li, J. (1999). “Stress-Induced Martensite in NiTi Corrugated Films.” *MRS Online Proc. Libr. Arch.*, 604.

Xue, D., Zhou, Y., and Ren, X. (2011). “The effect of aging on the B2-R transformation behaviors in Ti-51at% Ni alloy.” *Intermetallics*, 19(11), 1752–1758.

Zainal, M. A., Sahlan, S., and Ali, M. S. M. (2015). “Micromachined shape-memory-alloy microactuators and their application in biomedical devices.” *Micromachines*, 6(7), 879–901.

Zhang, L., Xie, C., and Wu, J. (2007). “Effect of annealing temperature on surface morphology and mechanical properties of sputter-deposited Ti–Ni thin films.” *J. Alloys Compd.*, 427(1), 238–243.

Zheng, Y., Jiang, F., Li, L., Yang, H., and Liu, Y. (2008). “Effect of ageing treatment on the transformation behaviour of Ti–50.9 at.% Ni alloy.” *Acta Mater.*, 56(4), 736–745.

Zhou, Y., Zhang, J., Fan, G., Ding, X., Sun, J., Ren, X., and Otsuka, K. (2005). “Origin of 2-stage R-phase transformation in low-temperature aged Ni-rich Ti–Ni alloys.” *Acta Mater.*, 53(20), 5365–5377.

LIST OF PUBLICATIONS

Refereed International Journals

1. **Naveen Kumar Reddy, B.**, Udayashankar, N.K. (2015). “The effect of annealing temperature on the optical and mechanical properties of intermetallic NiTi thin films using DC magnetron sputtering technique.” *International Journal of Advance Research in Science and Engineering (IJARSE)*, Vol. No.4, Issue No. 02.
2. **Naveen Kumar Reddy, B.**, Udayashankar, N.K. (2016). “The effect of annealing temperature on the structural, morphological, mechanical and surface properties of intermetallic NiTi alloy thin films.” *Surfaces and Interfaces*, 5, 62-71.
3. **Naveen Kumar Reddy, B.**, Udayashankar, N.K. (2017). “Aging time correlation in DC magnetron sputtered Ni₆₀Ti₄₀ thin films.” *Vacuum*, 135, 124-134.
4. **Naveen Kumar Reddy, B.**, Udayashankar, N.K. (2017). “Influence of annealing temperature on the structural, morphological, mechanical and surface properties of near equiatomic NiTi thin films.” *Vacuum*, 142, 186-196.
5. **Naveen Kumar Reddy, B.**, Udayashankar, N.K. “The effect of aging on structural, morphological, mechanical and surface properties of near equiatomic NiTi thin films.” (*Manuscript under review- Vacuum*).

Papers Presented in International Conferences

1. **Naveen Kumar Reddy, B.**, Udayashankar, N.K. (2014). “Structural Characterisation of Intermetallic Nanocrystalline Nickel-Titanium Thin Films Prepared by Oblique Angle DC Unbalanced Magnetron Sputtering.” 2nd *International Conference on Advanced Functional Materials (ICAFM 2014)*, CSIR-National Institute for Interdisciplinary Science and Technology, Trivandrum in association with The Indian Institute of Metals, Materials Research Society of India and Indian Ceramic Society, Trivandrum. (Poster presented).

2. **Naveen Kumar Reddy, B.,** Udayashankar, N.K. (2014) “Structural and Morphological Studies on Oblique Angle DC Unbalanced Magnetron Sputtered Intermetallic Nanocrystalline NiTi Thin Films for Biomedical Applications.” 6th *International Conference on NanoScience and Technology (ICONSAT 2014)*, Nano Mission, Department of Science and Technology (DST), Panjab University, Chandigarh, India. (Poster presented).

CURRICULUM VITAE

Address for correspondence:

B. Naveen Kumar Reddy
Research Scholar,
Department of Physics,
National Institute of Technology Karnataka,
Surathkal, Mangalore – 575 025.
Phone: +91-9845204742
E-mail: bussireddynaveen@gmail.com



Career Objective

To be a part of academic/research organization where I can have ample opportunities and get a chance to prove my abilities, strive for the development of the organization and make an impact in the field of teaching/research.

Research Interests

- ❖ Synthesis and characterization of thin films and their applications at device level
- ❖ Synthesis and characterization of smart or functional materials and it's applications
- ❖ Development of nanomaterials and devices for energy applications
- ❖ Synthesis and characterization of nanomaterials for bio-medical applications.

Educational Qualifications

- ❖ Doctor of Philosophy (Ph.D) (2011-2017)
Thesis title: Growth and Characterization of DC Magnetron Sputtered NiTi Shape Memory Alloy Thin Films
Department of Physics
National Institute of Technology Karnataka, Surathkal, Mangalore-575025, India.
- ❖ Master of Technology (M. Tech – Nanotechnology) (2009-2011)

Thesis title: “Synthesis and Characterization of Doped Nanocrystalline ZnO Powders by High Energy Ball Milling (ZoZ-Mill) for Varistor Applications”

Centre for Nanotechnology Research, VIT University, Vellore – 632 014, India.

Aggregate: (CGPA-7.63/10)

❖ **Master of Science in Physics (Specialization: Electronics & Instrumentation)**

Department of Physics

Loyola Academy Degree and P.G College,

Osmania university, Secunderabad, Telangana – 500 010, India.

Research Exposure

1. Characterization Techniques:

XRD, FESEM, AFM, TEM, XRD, BET, Optical microscope, UV-Visible Spectroscopy, Nanoindentation, XPS and Hall probe measurements.

2. Electrochemical Work Station

3. Thermal Evaporation Unit (metal coating)

4. Mechanical Alloy process (High Energy Ball Milling)

5. Combustion synthesis

Academic Credits

1. Thesis guiding for Postgraduates

2. Teaching fellow for undergraduate physics labs

3. Teaching tutorial classes for Post graduate students

Technical Skills

❖ P-spice, T-CAD

Computer Skills

Windows, Linux, MS-Office, Origin, MATLAB

Declaration

I hereby declare that the statements made above are true, complete and correct to the best of my knowledge.

Date:

Place: Mangalore

B. Naveen Kumar Reddy